

ԱՍՏՐՈՖԻԶԻԿԱ

ՏՈՄ 66

ԱՎԳՈՒՍՏ, 2023

ՎԵՐԱՎՐԱՄ

2023

ՎԵՐԱՎՐԱՄ 3

ՏՈՄ 66

ԱՍՏՐՈՖԻԶԻԿԱ

ՊՈՎԵՐԽՆՈՏՆԱ ՖՈՏՈՄԵՏՐԻԱ 50 ԿԱՐԼԻԿՈՎՈՒՄ ԳԱԼԱԿՏԻԿ
Վ ՄԵԾՆՈՄ ՕԲՅԵՄԵ

Կ.Ա.Կրյանովսկի, Մ.Ե.Շարինա, Ի.Դ.Կարաչենցև,

Գ.Մ.Կարամայա 317

Օ ՎՈՅՄՈՂՈ ՄԵԽԱՆԻԶՄԵ ՆԱՉԱԼԱ ԻԼԻ ՎՈՅԲՆՈՎԼԵՆԻԱ
ԱԿՏԻՎՆՈՒԹԻ ՌԱԴԻՕԳԱԼԱԿՏԻԿ Վ ՏԿՈՓԼԵՆԻՅԱ ԳԱԼԱԿՏԻԿ

Ռ.Ռ.Անդրեասյան, Ա.Վ.Աբրամյան, Գ.Մ.Պարոնյան,

Գ.Ա.Միկայլյան, Ա.Մ.Միկայլյան 331

ՊԵՐԵՍՄՈՒՐԵՆՆԱ ԴԻԱԳՐԱՄՄԱ ՎՐԴ Վ ՊԱՄԿԱՆ ՍԱՄՕ-
ՍՈՂԱՍՈՎԱՆՆՈՂ ԱՆԱԼԻԶԱ

Պ.Պրիվատուս, Չ.Պապպալարդո, Պ.Վ.Ռաօ, Ջ.Տ.Մազենցո 339
ՕԲՆՈՎԼԵՆԻԱ ԷՖԵՄԵՐԻԴ Վ ՍԵՄԻ ՎԵՐԱԲՐԱՆՆԻ ՏՐԱՆԶԻ-
ՏԻՐՈՒՅՈՒՆԻ ԷԿՑՈՊԼԱՆԵՏ ՕԲՅՈՐԱ ՀԱՏՆԵ

Ա.Պօրո, Փ.Ա.Փարահանի, Է.Ճշահանգիրի, Ա.Սարօստած,

Մ.Գոզարանդի, Մ.Խագցու, Փ.Աբոլխասսանի, Ա.Փախրաբադի,

Յ.Յոնցեն, Ա.Վյոնշե, Ռ.Նավես, Պ.Ղուէրրա, Ա.Մարկինի,

Մ.Սոլսբերի, Ռ.Էրենբերգը, Վ.Պ.Խենտւուն 353

ԱԿՏԻՎՆՈՒԹԻ ՄՈԼՈԴՈՅ ՅԵՆԴԵ ԵՊԻС 204376071 Վ ԱՍՏ-
ԿԱՑԱԿԻ ԱՌԱՋԱԿԱՑՈՒՅՈՒՆ

Ի.Ս.Սավանով 373

(Պրոջեկտ առ 4-րդ կազմի առաջնաշարքի առաջնաշարքի)

ԵՐԵՎԱՆ

Выходит с 1965г.
на русском и английском языках

Խմբագրական կողեզրական

Գլխավոր խմբագիր՝ Ա.Գ.Նիկոլոսյան (Հայաստան)
Գլխավոր խմբագրի տեղակալներ՝ Վ.Պ.Գրինին (Ուստաստան), Հ.Ա.Հարությունյան (Հայաստան)
Պատասխանատու քարտուղար՝ Ա.Ա.Հակոբյան (Հայաստան)

Ժ.Ալեքսյան (Ֆրանսիա), Գ.Ս.Բիսնովայի-Կոգան (Ուստաստան), Ի.Դ.Կարաչենցև (Ուստաստան),
Տ.Յու.Մաղարյան (Հայաստան), Ա.Մ.Սիրայելյան (Հայաստան), Բ.Ա.Շուտով (Ուստաստան),
Յու.Ա.Շենկելին (Ուստաստան), Ա.Ա.Չերեպաշով (Ուստաստան), Ե.Պ.Պավլենկո (Ուստաստան),
Է.Ս.Պարսամյան (Հայաստան), Վ.Պ.Ռեշետնիկով (Ուստաստան), Գ.Ն.Սարգսյան (Վրաստան),
Ա.Ա.Սահարյան (Հայաստան), Գ.Տ.Տեր-Ղազարյան (Հայաստան), Մ.Տիրատոս (Իտալիա),
Ա.Դ.Օղինցով (Իսպանիա)

Редакционная коллегия

Главный редактор: А.Г.Никогосян (Армения)

Заместители главного редактора: Г.А.Арутюнян (Армения), В.П.Гринин (Россия)

Ответственный секретарь: А.А.Акопян (Армения)

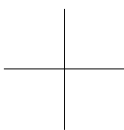
Ж.Алесян (Франция), Г.С.Бисноватый-Коган (Россия), И.Д.Караченцев (Россия),
Т.Ю.Магакян (Армения), А.М.Микаелян (Армения), С.Д.Одинцов (Испания),
Е.П.Павленко (Россия), Э.С.Парсамян (Армения), В.П.Решетников (Россия),
А.А.Саарян (Армения), Г.Н.Салуквадзе (Грузия), Г.Т.Тер-Казарян (Армения),
М.Туратто (Италия), А.М.Черепашук (Россия), Б.М.Шустов (Россия), Ю.А.Щекинов
(Россия)

"АСТРОФИЗИКА" - научный журнал, издаваемый Национальной академией наук Республики Армения. Журнал печатает оригинальные статьи по физике звезд, физике туманностей и межзвездной среды, по звездной и внегалактической астрономии, а также статьи по областям науки, сопредельным с астрофизикой. Журнал предназначается для научных работников, аспирантов и студентов старших курсов.

"ԱՍԴՎՖԻԶԻԿԱ"-ն գիտական հանդես է, որը հրատարակում է Հայաստանի Հանրապետության Գիտությունների Ազգային Ակադեմիան: Հանդեսը տպագրում է ինքնատիպ հոդվածներ աստղերի ֆիզիկայի, միզամածությունների և միջաստղային միջավայրի ֆիզիկայի, աստղաբաշխության և արտագալակտիկական աստղագիտության, ինչպես նաև աստղաֆիզիկային սահմանակից բնագավառների գծով: Հանդեսը նախատեսված է գիտական աշխատակիցների, ասպիրանտների և բարձր կուրսերի ուսանողների համար:

Адрес редакции: Республика Армения, Ереван 19, пр. Маршала Баграмяна 24^г
Редакция ж. "Астрофизика", тел. 56 81 38
e-mail: astrofiz@sci.am

© Издательство "Гитутюн" НАН Республики Армения, Астрофизика, 2023



АСТРОФИЗИКА

ТОМ 66

АВГУСТ, 2023

ВЫПУСК 3

DOI: 10.54503/0571-7132-2023.66.3-317

ПОВЕРХНОСТНАЯ ФОТОМЕТРИЯ 50 КАРЛИКОВЫХ ГАЛАКТИК В МЕСТНОМ ОБЪЕМЕ

К.А.КРЫЖАНОВСКИЙ¹, М.Е.ШАРИНА², И.Д.КАРАЧЕНЦЕВ²,
Г.М.КАРАТАЕВА¹

Поступила 28 апреля 2023

Представлены результаты поверхностной фотометрии 50-ти галактик в Местном объеме на основе архивных изображений, полученных на космическом телескопе Хаббла. Для выборки галактик приводятся интегральные величины в полосах V и I , а также профили яркости и цвета. Проведено сравнение полученных фотометрических параметров с измерениями других авторов.

Ключевые слова: *галактики:карликовые галактики:фотометрические параметры - галактики*

1. *Введение.* Стандартная космологическая модель Λ CDM успешно объясняет основные свойства крупномасштабной структуры Вселенной. Однако при переходе на мелкие шкалы порядка 1 Мпк возникают известные расхождения между предсказаниями теории и наблюдательными данными. Наиболее подходящим полигоном для сравнения выводов теории и наблюдений является Местный объем (МО) радиусом 10–12 Мпк вокруг Млечного Пути, для которого плотность наблюдательных данных больше, чем для далеких областей. Выбор указанного радиуса обусловлен тем, что расстояние каждой галактики внутри него может быть измерено с точностью около 5% на космическом телескопе Хаббла всего за один орбитальный период. Первый список галактик Местного объема содержал только 179 объектов [1]. Целенаправленные поиски близких галактик привели к созданию каталогов "A Catalog of Neighboring Galaxies" [2] с числом членов $N=450$ и "Updated Nearby Galaxy Catalog" [3] с $N=869$. За последние годы цифровые обзоры больших участков неба в оптическом диапазоне и в линии водорода 21 см (SDSS, DECaLS, HIPASS, ALFALFA etc.) значительно увеличили популяцию галактик МО. Последняя версия Local Volume Galaxy Database ([4]; www.sao.ru/lv/lvgdb) содержит более 1300 объектов. Значительная часть из них имеет аккуратные оценки расстояний и лучевых скоростей, что особенно важно для анализа распределения темной материи в МО. Интегральная светимость галактики, наряду с ее лучевой скоростью и расстоянием, является одной из самых важных параметров галактики. Из-за быстрого роста популяции

МО многие близкие карликовые галактики низкой поверхностной яркости оказались без надежной фотометрии, имея только грубые визуальные оценки видимых величин. Стала очевидной необходимость существенного укрепления фотометрической базы для галактик МО.

Основной целью данной работы является получение фотометрических параметров галактик с последующим анализом результатов в виде сравнения их со значениями, которые были взяты из других публикаций, а также из обзоров и каталогов. В данной работе не ставится задача исследования свойств галактик, подробной интерпретации результатов и построения различных зависимостей, а лишь дается возможность использовать эти результаты в последующих работах. Наблюдения за галактиками проводились в 2019–2020гг. с помощью Advanced Camera for Surveys (ACS), установленной на борту космического телескопа Хаббла (HST), в фильтрах F606W и F814W, в рамках проекта SNAP 15922 ("Every Known Nearby Galaxy", PI R.B Tully). В результате наблюдений были получены диаграммы цвет–величина для звездного населения 80-ти галактик. Из них для 63-х галактик были определены расстояния по светимости вершины ветви красных гигантов. Изображения наблюдавшихся галактик, диаграммы цвет–величина и измеренные расстояния приведены в "Extragalactic Distance Database" (EDD, [5]) с дополнениями в [6].

2. *Фотометрия.* Процесс поверхностной фотометрии был аналогичен таковому в статьях [7,8]. Для выполнения фотометрии использовался пакет программ *SURFPHOT*. Это часть большого пакета программ по анализу астрономических данных *MIDAS* (Munich Image Data Analysis System) [9], разрабатываемого в ESO. Был написан соответствующий скрипт, выполняющий различные команды и программы указанного пакета. Для получения интегральных величин использовались круговые и эллиптические апертуры. Процедура поиска центров галактик и моделирование распределения интенсивности по площади объекта были выполнены с помощью процедуры вписывания эллипсов *FIT/ELL3*. Фон неба оценивался и вычитался из изображения с помощью процедуры *FIT/FLAT SKY*, создающей двумерный полином с использованием метода наименьших квадратов. С помощью *SExtractor 2.5.0* ([10,11]) выделялись фоновые объекты. В полученных апертурах интегрировался поток (процедуры *INTEGRATE/APERTURE* и *INTEGRATE/ELLIPS*) и рассчитывались азимутально-усредненные поверхностные яркости.

Результаты фотометрии переводились в стандартную фотометрическую систему Джонсона–Казинса *BVRI* с помощью эмпирических формул:

$$V = V_i + 0.236(V_i - I_i) + 26.325; \quad (V - I) = 1.309(V_i - I_i) + 0.83; \quad I = I_i + 25.495, \quad (1)$$

где величины с подстрочным индексом *i* измерены в инструментальной фотометрической системе (см. [12]). С помощью полученных интегральных

звездных величин были вычислены величины в фильтре B по соотношению из [13]:

$$B' = V + 0.85(V - I) - 0.20. \quad (2)$$

Параметры профилей для галактик были получены с использованием модели на основе экспоненциальной функции [14]: $\mu(r) = \mu_0 + 1.086(r/h)$, где μ_0 - центральная поверхностная яркость и h - экспоненциальная масштабная длина.

3. Результаты. Основные результаты представлены в табл.1¹.

Табл.1 содержит список фотометрируемых галактик с именами в колонках 1 и 2 и с координатами на эпоху J2000.0 в колонке 3. Морфологические типы галактик и расстояния до них в Мпк из литературы [3] даны в колонках 4 и 5. В колонках 6, 7 и 8 содержатся результаты фотометрии и

Таблица 1

ПОВЕРХНОСТНАЯ ФОТОМЕТРИЯ 50-ТИ ГАЛАКТИК МЕСТНОГО ОБЪЕМА, КОТОРЫЕ НАБЛЮДАЛИСЬ С HST В ОБЗОРЕ SNAP 15922

Название	PGC	RA (2000.0) DEC	Тип	D	SBv0	V	I	B'	B _{lit}	A _B	Лит.
1	2	3	4	5	6	7	8	9	10	11	12
UGC 064	000591	000744.0+405232	dIrr	8.16	21.49	15.44	14.97	15.65	15.5	0.34	LV
WOC2017-07	-	005501.0-231009	dIrr	3.62	24.78	17.90	17.37	18.15	18.1	0.07	[16]
AGC 122226	086806	024638.9+274335	BCD	7.71	21.24	15.75	15.03	16.17	17.1	0.53	LV
ESO 300-016	011842	031010.5-400011	dIrr	9.33	22.04	15.92	15.52	16.06	15.6	0.08	LV
UGC 2716	012719	032407.2+174515	Sm	6.66	21.47	14.07	13.36	14.47	14.6	0.59	LV
KKH 22	2807114	034456.6+720352	dTr	3.12	25.00	16.22	15.04	17.02	18.0	1.66	LV
HIPASSJ0517	4078612	051721.6-324535	dIm	9.32	21.13	15.57	15.11	15.76	15.7	0.07	[17]
KKH 34	095594	055941.2+732539	Irr	7.28	24.04	17.02	16.20	17.52	17.1	1.08	LV
ESO 006-001	023344	81923.3-850844	dTr	2.70	22.32	14.68	13.65	15.36	-	0.83	-
KKH 46	2807128	090836.6+051732	dIrr	6.70	23.65	16.45	15.99	16.65	17.0	0.20	[18]
ESO 373-007	027104	093245.4-331444	dIrr	9.77	23.48	15.15	14.32	15.66	16.4	0.58	LV
UGC 5086	027115	093248.9+212754	dSph	8.49	22.67	15.97	15.16	16.44	15.9	0.14	[19]
6dFJ0944201	807172	094420.1-225458	BCD	10.47	21.42	17.12	16.73	17.23	16.8	0.33	[20]
2MASXJ0957	154449	095708.9-091548	BCD	10.13	20.17	15.27	14.45	15.77	15.8	0.29	[20]
MCG -01-26	029033	100138.4-081456	dIrr	9.94	22.24	14.97	14.22	15.40	15.4	0.15	LV
2dFGRS-N21	1099440	100932.5-021058	BCD	10.42	20.92	15.58	15.16	15.75	15.8	0.19	[21]
UGC 5918	032405	104936.5+653150	dIrr	8.50	23.68	14.81	14.06	15.25	15.0	0.05	[13]
Mrk 1265	032413	104940.4+225019	BCD	9.55	20.63	15.13	14.68	15.31	17.0	0.09	LV
KKH 68	2807141	113053.3+140846	dIrr	12.47	23.29	16.12	15.37	16.56	16.6	0.17	[22]
HIPASSJ1131	5060432	113135.2-314020	dIrr	6.90	22.43	18.06	17.59	18.14	18.2	0.30	[23]
KKH 69	2807142	113453.3+110112	dIrr	7.40	23.53	16.80	16.13	17.17	16.6	0.10	[22]

¹ Другие детальные данные нашей фотометрии доступны по индивидуальному запросу к контактному автору статьи.

Таблица 1 (Окончание)

1	2	3	4	5	6	7	8	9	10	11	12
LBTJ115205	[Grapes]	115205.6+544732	dIrr	5.96	23.75	18.10	17.64	18.27	18.5	0.04	LV
EVCC 67	4304796	115840.4+153534	dIrr	16.5	21.12	17.71	17.02	18.10	18.2	0.08	[24]
ESO 379-024	038252	120456.7-354435	dIrr	5.46	22.34	16.44	16.22	16.43	16.6	0.33	LV
SDSSJ1205	4310323	120531.0+310434	Sdm	16.0	21.49	17.20	16.34	17.73	17.6	0.08	[25]
KK 135	166130	121934.7+580234	dIrr	5.46	24.03	17.50	17.33	17.45	18.1	0.05	LV
MCG+09-20	040750	122652.6+530619	BCD	6.12	21.67	15.74	15.25	15.95	15.9	0.10	LV
MCG+00-32	041395	123103.8+014033	dIm	9.42	21.81	15.40	14.31	16.13	15.9	0.08	[26]
WSRT-CVN43	-	123109.0+420539	dIrr	8.13	23.15	17.55	17.48	17.41	17.8	0.08	LV
MCG+07-26	041749	123352.7+393733	dIm	9.94	22.34	15.42	15.04	15.54	16.5	0.06	[27]
KUG1234+29	042115	123714.0+293751	BCD	8.44	20.16	15.35	14.67	15.73	16.3	0.07	[24]
KKSG 30	3097708	123735.9-085202	dIrr	9.73	23.55	16.17	15.56	16.47	16.3	0.14	LV
UGC 7827	042380	123938.9+444915	dIrr	9.09	22.73	15.11	14.78	15.19	16.0	0.08	LV
KDG 178	042413	124010.0+323931	dIrr	13.0	22.80	16.06	15.61	16.22	17.1	0.06	LV
SDSSJ1240	4074723	124029.9+472204	dIrr	7.63	23.93	17.97	17.72	17.97	18.2	0.07	LV
NGC 4627	042620	124159.7+323425	E	6.93	20.32	12.74	11.88	13.27	13.1	0.07	[28]
BTS 151	2832120	124324.6+322856	dSph	7.60	23.01	16.85	16.10	17.29	17.6	0.07	[25]
UGC 7903	042832	124345.0+535732	dIrr	9.66	23.52	16.32	15.87	16.50	16.6	0.06	LV
ESO 219-010	044110	125609.6-500838	dSph	4.29	22.51	15.32	14.19	16.08	16.4	0.96	LV
MCG+07-27	045889	131251.8+403235	BCD	8.99	20.42	14.24	13.58	14.60	14.9	0.06	LV
KK 195	166163	132108.2-313147	dIrr	5.62	23.63	17.03	16.60	17.20	17.1	0.27	LV
NGC 5229	047788	133402.9+475455	Sdm	8.95	21.09	13.51	12.71	13.99	14.3	0.08	[13]
KKs 58	2815824	134600.8-361944	dSph	3.75	23.06	16.39	15.55	16.90	17.4	0.27	LV
ESO 222-010	052125	143503.0-492518	dIrr	3.15	22.34	14.87	14.13	15.31	16.3	1.11	LV
Mrk 475	052358	143905.4+364822	BCD	11.53	20.06	15.56	15.35	15.54	16.3	0.05	[29]
ESO 272-025	052591	144325.5-444219	dIrr	3.91	21.28	13.88	13.05	14.39	14.8	0.69	LV
KK 242	4689184	175248.4+700814	dTr	6.46	24.99	18.38	17.40	19.02	18.6	0.14	[30]
AGC 322463	5067080	225935.3+164611	dIrr	7.97	22.05	17.41	16.95	17.60	17.2	0.58	LV
ESO 347-017	071464	232656.1-372049	dIm	8.42	21.52	14.00	13.48	14.25	14.7	0.07	LV
2DFGRS-S43	704814	235840.7-312803	dIrr	3.66	22.22	15.85	14.90	16.47	16.2	0.07	[16]

анализа профилей яркости в данной работе: центральные поверхностные яркости в фильтре V и интегральные видимые звездные величины в фильтрах V и I фотометрической системы Джонсона-Казинса. В колонке 9 даны звездные величины в фильтре B системы Джонсона-Казинса, вычисленные по измеренным V и I звездным величинам по соотношению (2). Все приведенные в табл.1 звездные величины являются неисправленными за поглощение. Колонка 10 содержит звездные величины галактик в фильтре B системы Джонсона-Казинса из литературы. В колонке 11 приведены значения поглощения света в Галактике в фильтре B в звездных величинах. Литературные ссылки на данные, приведенные в колонке 10, даны в колонке 12. "LV" означает ссылку на последнюю версию базы данных [4] (и ссылки в ней), либо на индивидуальные глазомерные оценки звездной величины

И.Д.Караченцевым.

На рис.1² представлены полученные при фотометрии профили поверхностной яркости. Для каждой галактики приведены следующие панели: вверху слева - кривые роста интегральной звездной величины в фильтрах V (темная линия) и I (светлая линия); внизу слева - соответствующая разница между V и I кривыми роста; вверху справа - V и I профили яркости в зв. вел./кв. с; внизу справа - соответствующая разница между V и I профилями яркости. Диапазон ошибок фотометрии показан светлыми барами. Подробнее об определении ошибок фотометрии см. в статье [15].

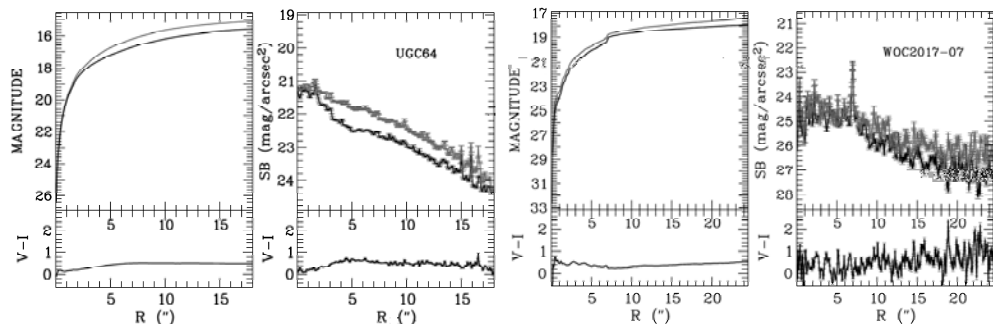


Рис.1. Профили поверхностной яркости и кривые роста интегральной звездной величины 50-ти галактик.

Сравнение результатов фотометрии, переведенных в величину B' (соотношение 2) с литературными фотометрическими оценками (табл.1, колонка 10), дает среднее значение различия $\Delta B = \langle B' - B_{lit} \rangle = +0^m.06 \pm 0^m.07$ и стандартную погрешность $\sigma(\Delta B) = 0^m.30$. После учета ошибок фотометрии в наших и литературных данных, погрешность наших измерений составляет $0^m.2$.

4. Заключительные замечания. В данной работе представлены результаты поверхностной фотометрии 50-ти галактик Местного объема с расстояниями $D < 12$ Мпк. Фотометрия основана на снимках галактик, полученных на космическом телескопе Хаббла в полосах V и I в рамках программы SNAP 15922. Для измерений отбирались объекты, чей диаметр не превышал угловые размеры камеры ACS HST. Определены интегральные V и I величины галактик и построены профили поверхностной яркости в обеих полосах. Сравнение полученных интегральных величин галактик с имеющимися данными из других источников показывает, что погрешность представленных нами оценок интегральных величин составляет около $0^m.2$. Большинство исследованных галактик являются объектами низкой поверхностной яркости

² Продолжение рис.1 см. в конце статьи. Из-за маленьких размеров панелей рис.1 бары диапазонов ошибок четко не видны.

с медианной величиной $SB_{OV} \simeq 22.2$ зв. вел./кв. с.

Авторы признательны Л.Н.Макаровой и Д.И.Макарову за полезные дискуссии. Работа основана на наблюдениях, сделанных с помощью космического телескопа NASA/ESA Hubble Space Telescope и полученных из Hubble Legacy Archive, созданного в сотрудничестве между Space Telescope Science Institute (STScI/NASA), the Space Telescope European Coordinating Facility (ST-ECF/ESAC/ESA) и the Canadian Astronomy Data Centre (CADC/NRC/CSA). Поддержка программы SNAP-15922 (PI R.B.Tully) была предоставлена НАСА через грант Научного института космического телескопа, находящийся в ведении Ассоциации исследовательских университетов в области астрономии, по контракту НАСА NASb5-26555.

Работа выполнена при частичной поддержке гранта Министерства науки и высшего образования РФ № 075-15-2022-262 (13.МНПМУ.21.0003).

¹ Санкт-Петербургский государственный университет, Санкт-Петербург, Россия

² Специальная астрофизическая обсерватория Российской академии наук, Нижний Архыз, Россия, e-mail: idkarach@gmail.com sme@sao.ru

SURFACE PHOTOMETRY OF 50 DWARF GALAXIES IN THE LOCAL VOLUME

K.A.KRYZHANOVSKY¹, M.E.SHARINA², I.D.KARACHENTSEV²,
G.M.KARATAEVA¹

The results of surface photometry of 50 galaxies in the Local Volume based on archival images obtained with the Hubble Space Telescope are presented. For the sample of galaxies, the integrated magnitudes in the V and I bands are given, as well as the brightness and color profiles. The obtained photometric parameters are compared with the measurements of other authors.

Keywords: *galaxies: dwarf galaxies: photometric parameters - galaxies*

ЛИТЕРАТУРА

1. *R.C.Kraan-Korteweg, G.A.Tammann*, Astron. Nachr., **300**, 181, 1979.
2. *I.D.Karachentsev, V.E.Karachentseva, W.K.Huchtmeier et al.*, Astron. J., **127**, 2031, 2004.
3. *I.D.Karachentsev, D.I.Makarov, E.I.Kaisina*, Astron. J., **145**, 101, 2013.
4. *E.I.Kaisina, D.I.Makarov, I.D.Karachentsev et al.*, Astrophys. Bull., **67**, 115, 2012.
5. *G.S.Anand, L.Rizzi, R.B.Tully*, Astron. J., **162**, 80, 2021.
6. *I.D.Karachentsev, N.A.Tikhonov*, Astrophysics, **66**, 1, 2023.
7. *R.A.Swaters, M.Balcells*, Astron. Astrophys., **390**, 863, 2002.
8. *V.A.Taylor, R.A.Jansen, R.A.Windhorst et al.*, Astrophys. J., **630**, 784, 2005.
9. *K.Banse, P.Crane, P.Grosbol et al.*, The Messenger, **31**, 26, 1983.
10. *D.O.Cook, D.A.Dale, B.D.Johnson et al.*, Mon. Not. Roy. Astron. Soc., **445**, 881, 2014.
11. *L.C.Ho, Z.-Y.Li, A.J.Barth et al.*, Astrophys. J. Suppl. Ser., **197**, 21, 2011.
12. *M.Sirianni, M.J.Jee, N.Benitez et al.*, Publ. Astron. Soc. Pacif., **117**(836), 1049, 2005.
13. *L.Makarova*, Astron. Astrophys., **139**, 491, 1999.
14. *G. de Vaucouleurs*, in S.Flugge, ed., Handbuch der Physik 53, Springer-Verlag, Berlin, p.275, 1959.
15. *M.E.Sharina et al.*, Mon. Not. Roy. Astron. Soc., **384**, 1544, 2008.
16. *S.J.Maddox, G.Efstathiou, W.J.Sutherland*, Mon. Not. Roy. Astron. Soc., **246**, 433, 1990.
17. *M.T.Doyle, M.J.Drinkwater, D.J.Rohde et al.*, Mon. Not. Roy. Astron. Soc., **361**, 34, 2005.
18. *L.N.Makarova, I.D.Karachentsev, E.K.Grebel et al.*, Astron. Astrophys., **384**, 72, 2002.
19. *L.N.Makarova*, Astron. Astrophys. Suppl., **128**, 459, 1998.
20. *D.H.Jones, W.Saunders, M.Read et al.*, Publ. Astron. Soc. Australia, **22**, 277, 2005.
21. *M.Colless, B.A.Peterson, C.Jackson et al.*, eprint arXiv:astro-ph/0306581, 2003.
22. *M.E.Sharina*, Astrophysics, **62**, 9, 2019.
23. *I.D.Karachentsev, L.N.Makarova, B.S.Koribalski et al.*, Mon. Not. Roy. Astron. Soc., **518**, 5893, 2023.
24. *S.Alam, F.D.Albareti, C.A.Prieto et al.*, Astrophys. J. Suppl. Ser., **219**, 12, 2015.
25. *J.K.Adelman-McCarthy, M.A.Agueros, S.S.Allam et al.*, Astrophys. J. Suppl. Ser., **175**, 297, 2008.
26. *C.D.Impey, D.Sprayberry, M.J.Irwin et al.*, Astrophys. J. Suppl. Ser., **105**, 209, 1996.
27. *H.Aihara, P.McGehee*, Astrophys. J. Suppl. Ser., **193**, 2011.
28. *G. de Vaucouleurs, A. de Vaucouleurs, H.Jr.Corwin et al.*, Third Reference Catalogue of Bright Galaxies. Springer-Verlag, New York, 1991.
29. *A. Gil de Paz, B.F.Madore, O.Pevunova*, Astrophys. J. Suppl., **147**, 29, 2003.
30. *J.Koda, M.Yagi, Y.Komiyama et al.*, Astrophys. J., **802**, L24, 2015.

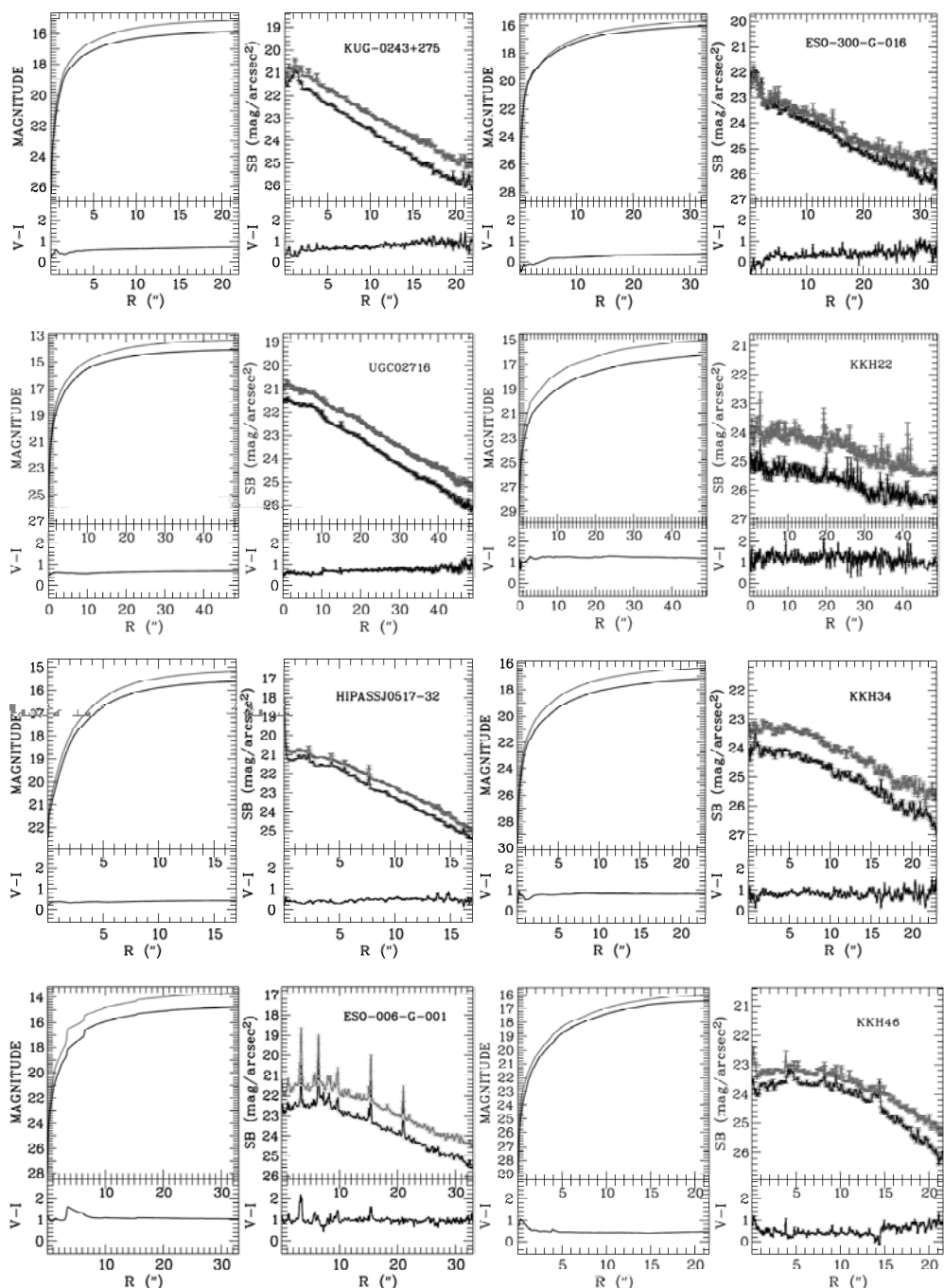


Рис.1. (Продолжение).

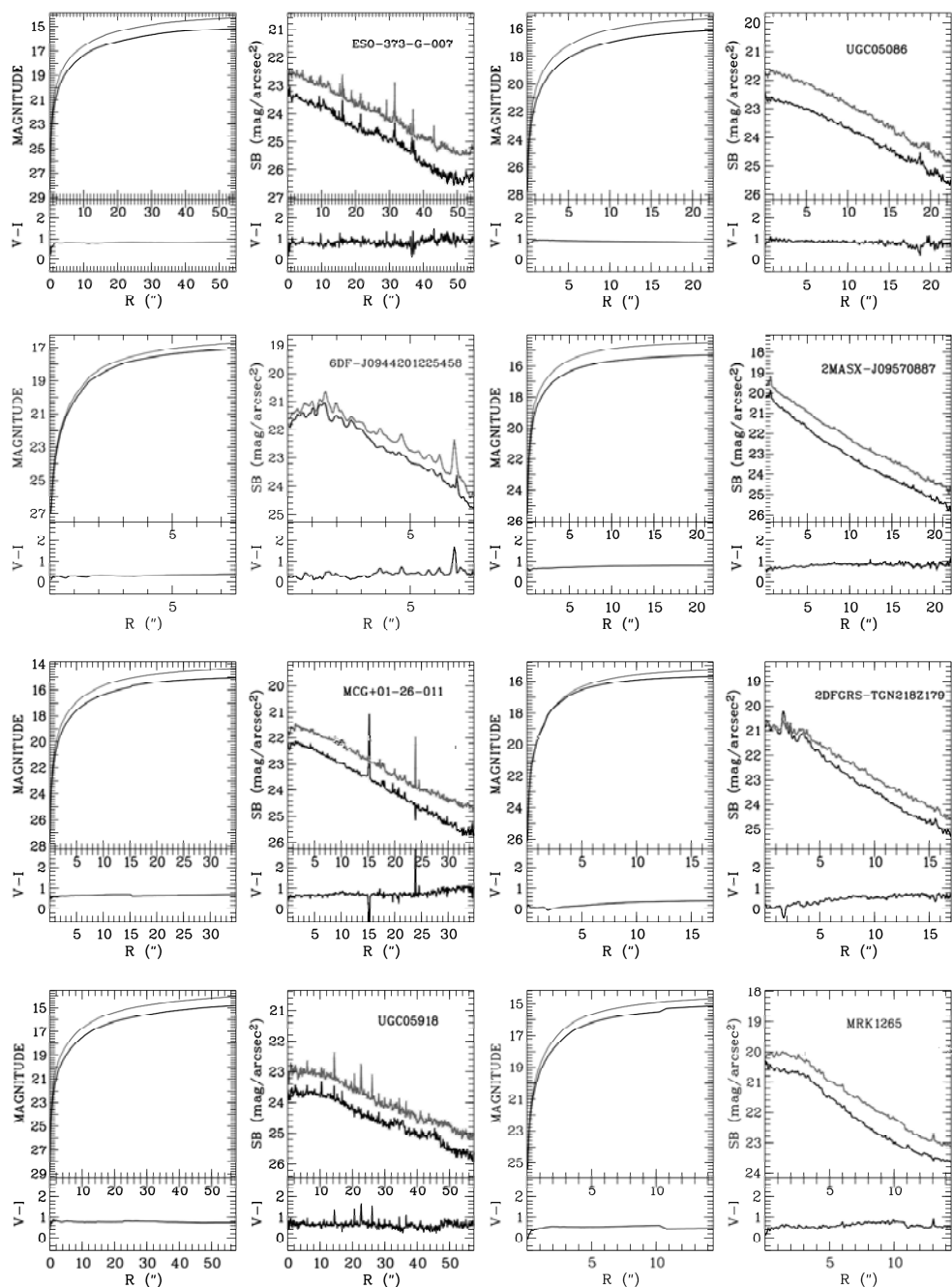


Рис.1. (Продолжение).

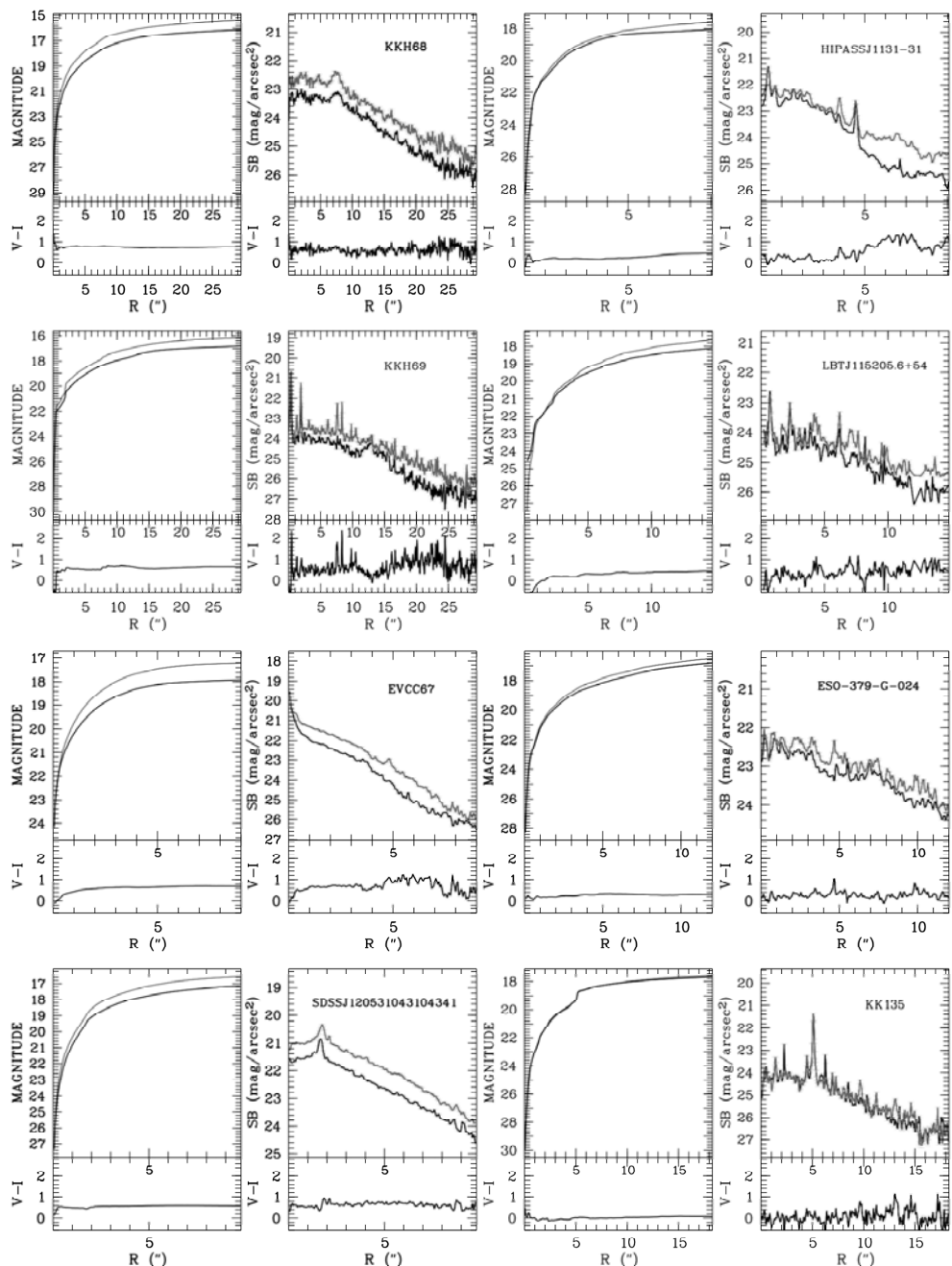


Рис.1. (Продолжение).

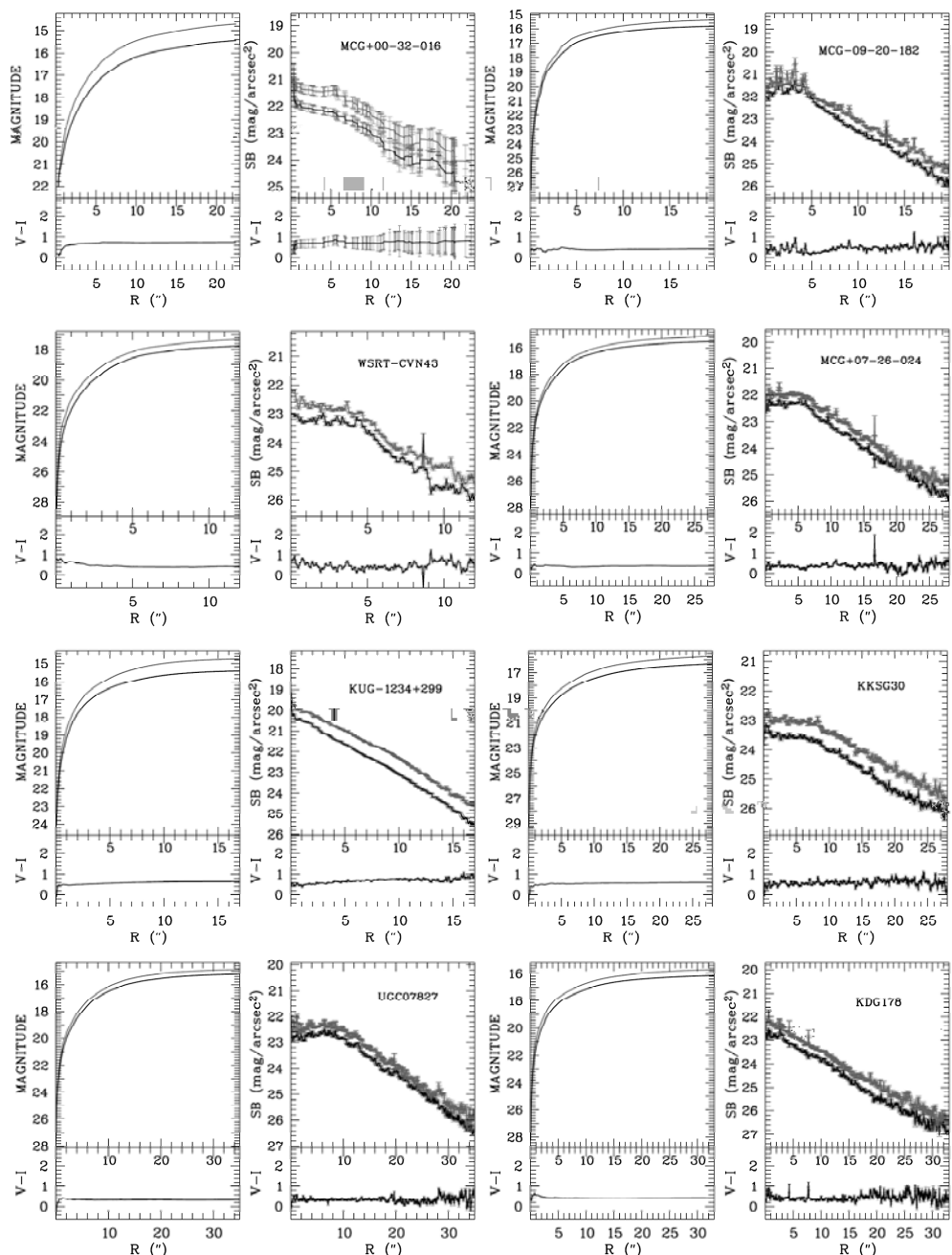


Рис.1. (Продолжение).

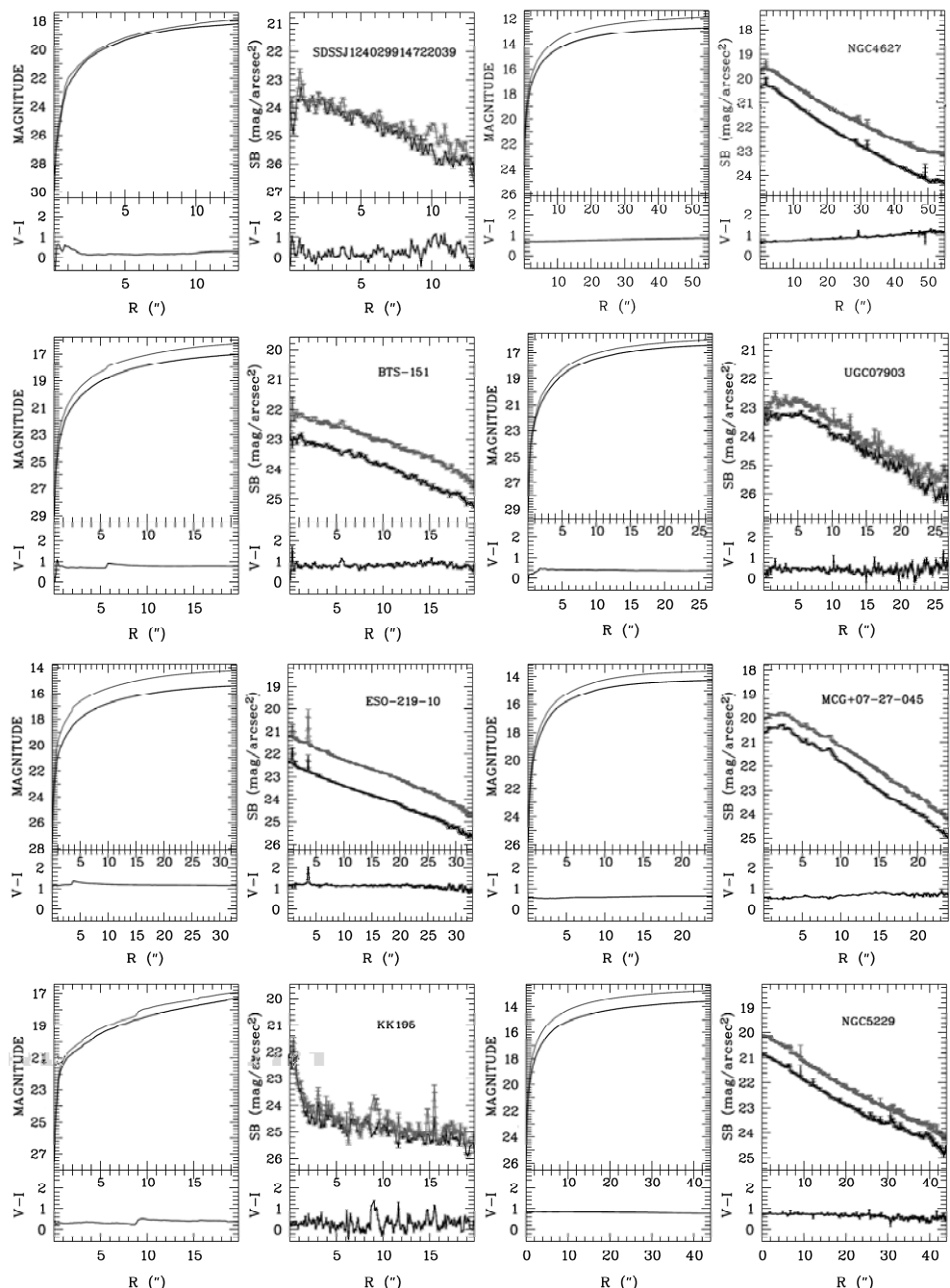


Рис.1. (Продолжение).

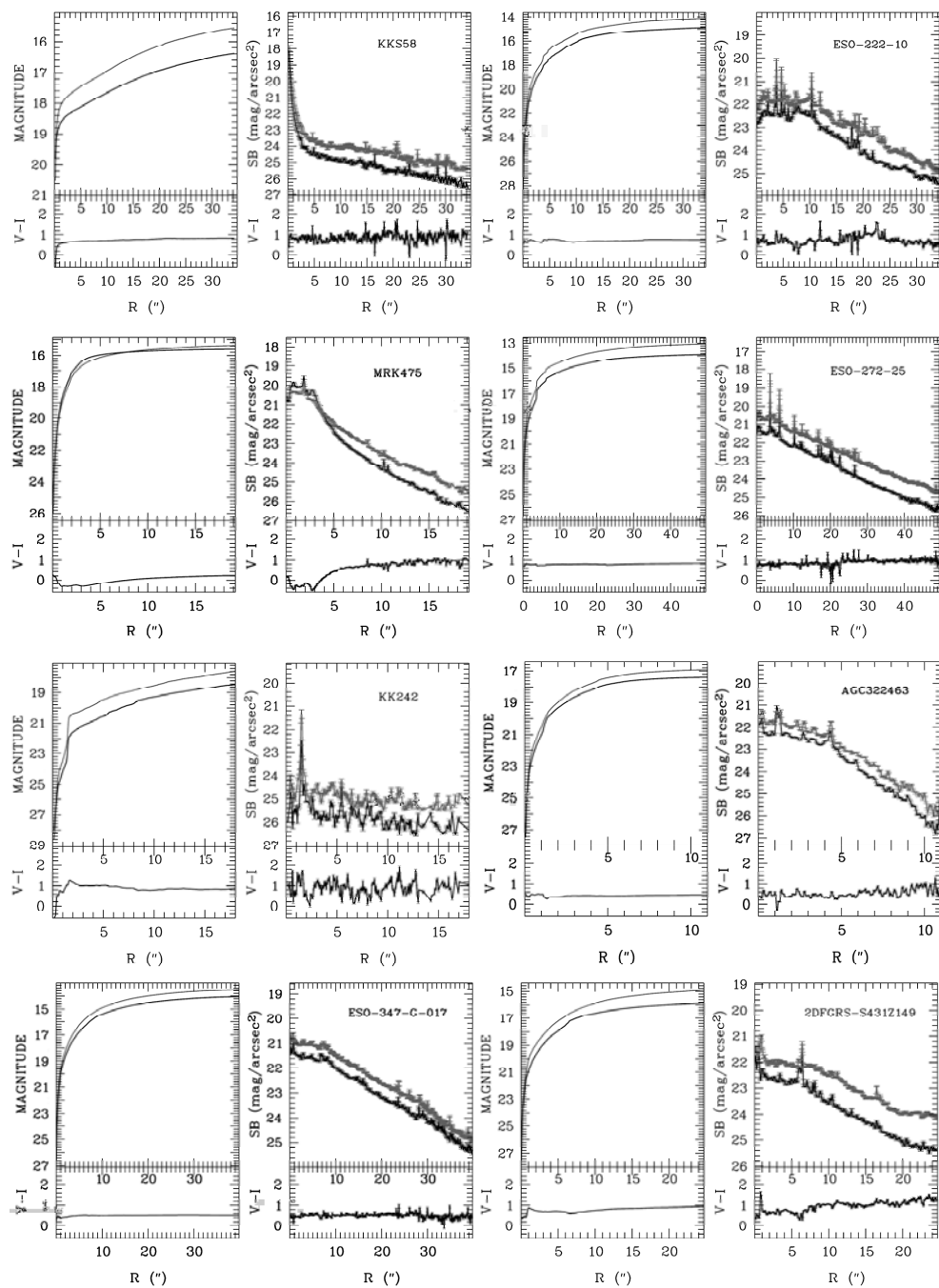


Рис.1. (Окончание).

АСТРОФИЗИКА

ТОМ 66

АВГУСТ, 2023

ВЫПУСК 3

DOI: 10.54503/0571-7132-2023.66.3-331

ON A POSSIBLE MECHANISM FOR THE START OR RESUMPTION OF ACTIVITY OF RADIO GALAXIES IN CLUSTERS OF GALAXIES

R.R.ANDREASYAN, H.V.ABRAHAMYAN, G.M.PARONYAN,
G.A.MIKAYELYAN, A.M.MICKAELIAN

Received 11 June 2023

We study the close proximity of the well-known and well-studied 3C31 class FRI radio galaxy in order to reveal the influence of the environment on an extragalactic radio source. It was shown that about 110 million years ago the galaxies NGC 380 and NGC 386 were located near the galaxy NGC 383 (the parent galaxy of 3C31). On the other hand, the modeling of the spectral characteristics of the radio emission of the central part of the radio galaxy 3C31 gives an estimate of the age of the central jet of about 100 million years. Therefore, it can be assumed that one of the possible reasons for the appearance or resumption of the radioactivity of the galaxy NGC 383 may be a triple close passage of galaxies.

Keywords: *galaxies - radio galaxies - clusters of galaxies - environment of galaxies*

1. *Introduction.* The environment surrounding the galaxy can play an important role in the formation and evolution of various types of activity in galaxies. In particular, this applies to extragalactic radio sources and activity in radio emission [1]. It is known that radio galaxies are often members of clusters of galaxies, and AGN activity is much higher in the central parts of clusters than in the rest of the metagalactic space [2,3]. This can be partly explained by the fact that the host galaxy of radio galaxies is usually massive galaxy ($M > 10^{12}$ solar masses), and they are often the central objects of clusters.

However, the relationship between AGN activity and galaxy clusters is still not fully explained. In this regard, it is very important to study the relationship between the physical and morphological features of radio galaxies and the characteristics of galaxy clusters in which these radio galaxies are located. Such characteristics can be the number, concentration and morphological composition of galaxies in clusters, the presence of hot and cold gas and dust in clusters, the presence of background radiation in different frequency ranges, and others.

Radio galaxies are divided into different types according to their physical and morphological features. One of the well-known classifications of extended radio galaxies is the (FR) classification of Fanaroff and Riley [4], which is based on the radio brightness distribution over the radio image. Radio galaxies with relatively

lower radio luminosity, in which the radio brightness decreases from the center to the edges, are classified as I class radio galaxies (FRI), and radio galaxies with higher radio luminosity, in which the radio brightness increases from the center to the edges of the II class (FRII). At present, the Fanaroff-Riley dichotomy has been studied quite well and many other differences in physical and morphological features have been found for different classes of radio galaxies. In particular, in our works, we studied the correlations between the physical and morphological features of extragalactic radio sources for different Fanaroff-Riley classes. A correlation was found between the optical and radio axes of nearby radio galaxies [5], a correlation of the ellipticity of parent optical galaxies associated with radio galaxies of different classes [6], a correlation of the average radio polarization angles with the radio axes [7], etc.

In [8] it was shown that the radio activity of FRIs are mostly triggered by different mechanisms than in FRIIs. One can probably expect some connection also between the FR class and the physical and morphological features of the cluster in which these radio galaxies are located. It can be due to the interaction between galaxies when they randomly pass close to each other. There are lot of papers where the activity of galaxies in the radio range is trying to be explained by merging processes [9,10]. In particular it was shown that in galaxy systems where traces of close interaction (merging) are observed, the percentage of active galactic nuclei is higher [11]. All of this may suggest that close transits of galaxies may be the cause (be a trigger) for the start of radio activity.

In this work, in order to reveal the influence of the environment on an extragalactic radio source, we study the close proximity of the well-known and well-studied 3C31 class FRI radio galaxy.

2. *Observational data.* The 3C31 class FRI radio source has been identified with the NGC 383 galaxy, which is the central object of the group of galaxies, which in turn is a member of the Perseus-Pisces supercluster [12] and has been studied quite well. Numerous results and useful data have now been obtained for these objects [13-18]. Of these, here we highlight some of the data of interest to us, which can be used in the present work.

Fig.1 and 2 show optical images of the region with the central galaxy NGC 383 overlaid on the radio maps. On figures there are maps of the radio image of the FRI class 3C31 radio galaxy at different frequencies, 145, 360, 615, and 1400 MHz corresponding to LOFAR, VLA, GMRT and FIRST observations, respectively. It must be noted that the Fig.2 is taken from the paper [19].

It can be seen from the Fig.1 that the group of galaxies with the central object NGC 383 has the form of a chain whose direction coincides well with the direction of the radio image of the 3C31 radio galaxy. High-resolution radio

observations have detected two oppositely directed jets within 10 kpc from the galaxy's core (Fig.2). Radio jet simulations [16] have shown that the direction of

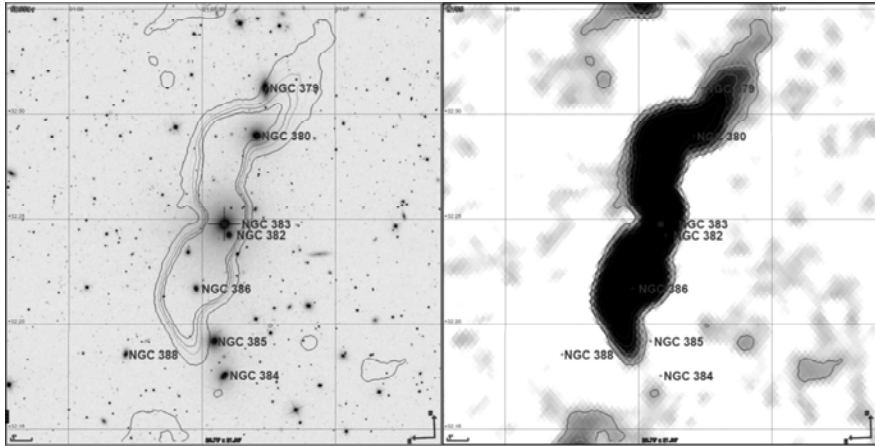


Fig.1. The region of a group of galaxies with the central object NGC 383 and overlaid radio Source 3C31 of the FRI class at the frequency of 1400 MHz.

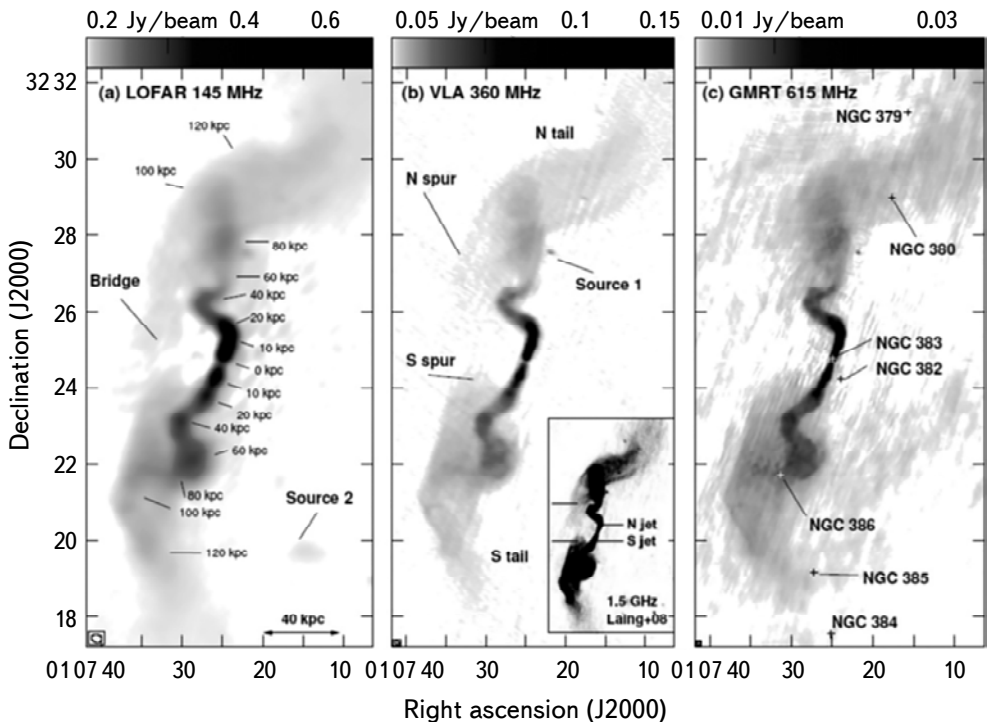


Fig.2. Radio image maps of the FRI class radio galaxy 3C31 at three different frequencies (from [19]).

the jet is approximately 52° with the line of sight. Moreover, the northern part of the jet approaches the observer, while the southern part moves away.

3. Data analysis. In Table 1 we bring the coordinates, redshifts and types of galaxies included in the galaxy group with central galaxy NGC383 from database NED.

From the analysis of the coordinates and redshift data of galaxies, as well as from Fig.1 and also Fig.2 from [19], it can be seen that the elliptical galaxies NGC380 and NGC386 are located respectively in the northern and southern parts of the 3C31 radio image. These galaxies, together with the central SA0 type galaxy of the group NGC383 (which is the parent galaxy of the radio galaxy 3C31), are on the same line, the direction of which coincides with the direction of inner part of the radio jet with great accuracy. Moreover, the relative radial velocity of the NGC380 galaxy with respect to the central galaxy NGC383 is directed towards the observer as the velocity of northern part of the jet, when the relative radial velocity of NGC386 is directed away from the observer as the velocity of southern part of the jet. If we assume that the galaxies NGC380 and NGC386 are not

Table 1

OBSERVATIONAL DATA OF GALAXIES INCLUDED IN THE GROUP WITH THE CENTRAL OBJECT NGC 383 FROM DATABASE NED

Name	RA deg	DEC deg	Redshift z	Morphology
NGC 379	16.815375	32.520361	0.01861	S0
NGC 380	16.823296	32.482922	0.01476	E2
NGC 382	16.849463	32.403864	0.01744	E
NGC 383	16.853995	32.412559	0.01700	SA0
NGC 384	16.854596	32.29245	0.01412	E3
NGC 385	16.863524	32.319533	0.01659	SA0
NGC 386	16.880387	32.361994	0.01853	E3
NGC 388	16.946442	32.309963	0.01816	E3

only projected onto radio images, but are located inside the radio-emitting region, then we can make the following plausible assumption that not only the directions of the relative radial velocities of these galaxies, but also the directions of spatial velocities coincide with the directions of motion of the northern and southern radio jets. Hence, the galaxies NGC380 and NGC386 are moving away from the central galaxy NGC383 along the directions of the radio jets of the 3C31 radio galaxy. It is interesting to determine the approximate time for which these galaxies covered the distance from NGC383.

In this study will be used standard cosmology, applying the values

$H_0 = 70 \text{ km s}^{-1} \text{ Mpc}^{-1}$, $\Omega_m = 0.3$ and $\Omega_\Lambda = 0.7$. At the redshift of the radio galaxy 3C31 ($z = 0.0169$; [16]), its distance will be $D = 73.3 \text{ Mpc}$, which corresponds to an angular scale of 0.344 kpc per arcsecond [19].

The data given in Table 1 were used to calculate the distance projections of the galaxies NGC380 and NGC386 from NGC383 on the image plane. To do this, using the coordinates of the galaxies, the corresponding angular distances were calculated, and then the projections of the distances of the galaxies were calculated using the above-mentioned angular scale of 0.344 kpc per arc second. Given the values of these projections and the fact that, as was assumed above, the real distances, as well as the direction of the radio jets, are 52° with the line of sight [16], it is possible to determine the real distances of the galaxies NGC380 and NGC386 from NGC383.

The relative radial velocities of the galaxies NGC380 and NGC386 compared to NGC383 can be calculated from the relative redshifts. The relative real velocities are also based on the assumption that they are 52° with the line of sight. The results of these calculations are shown in Table 2. We give the following data in Table 2: respectively in column 1 the name of the galaxy, 2 - redshift difference between the given galaxy and NGC383, 3 - corresponding relative radial velocities, 4 - real relative velocities, 5 - distances of the galaxies from the central NGC383 galaxy on the picture plane, 6 - the real distances of the galaxies, 7 - the time of the removal of the galaxies from the central object.

Table 2

RESULTS OF CALCULATIONS

Galaxies	Δz	ΔV	ΔV_0	d	d_0	T
		km/s	km/s	kpc	kpc	My
NGC380	-0.00224	-672	-1092	97.07	123.2	110
NGC386	+0.00153	+459	745.5	70.64	89.64	118

4. Discussion of the results. Table 2 shows that the galaxies NGC380 and NGC386 were near the galaxy NGC383 about 110 million years ago. A very close passage of these three galaxies then probably occurred, after which the recession of the galaxies NGC380 and NGC386 from the more massive central galaxy NGC383 began. A natural question arises whether such a close passage can be the cause (trigger) of the beginning of radioactivity of the central galaxy. Note that the question of the cause of the start or recurrence of radioactivity is studied in many works (see, for example, [20]), but there is still no clarity in this issue. Based on the results of our calculations, the reason for the resumption of radio activity of 3C31 radio galaxy can be considered the close passage of the three

above-mentioned galaxies about 110 million years ago. A reliable argument for this assumption can be considered that the modeling of the spectral characteristics of the radio emission of the central part of the radio galaxy 3C31 gives an estimate of the age of the central jet of about 100 million years [19]. Mentioned estimation agrees very well with the age of the triple transit of galaxies. This result with the good coincidence of the direction of the central jet with the direction of the removal of the galaxies NGC380 and NGC386 from the central galaxy NGC383 can be taken as an indirect argument for above-mentioned consideration.

As another indirect argument can be the assumption that elliptical galaxies NGC380 and NGC386 in the result of triple close passage of galaxies probably loss their gas component by the accretion to the central SA0 type galaxy NGC383 which is rich in gas and dust component [15].

Thus, from all of above-mentioned arguments it can be assumed that one of the possible reasons for the appearance or resumption of the radio activity of galaxies may be the triple close passage of galaxies.

Of course, for such an important assumption, the given single example is not enough, but we believe that it makes sense to continue investigating in this direction.

Acknowledgements. This research was partly accomplished by the Republic of Armenia Science Committee for the Advanced Research Grant 21AG-1C053 Revelation of Early Stages of Galaxy Evolution by Means of MW Study of Active Galaxies (2021-2026) and ANSEF grant PS-astroex-2597 Search and Studies of High Luminosity X-ray Galaxies (2022-2023).

NAS RA V.Ambartsumian Byurakan Astrophysical Observatory (BAO),
Byurakan 0213, Aragatzotn Province, Armenia, e-mail: randreasyan@gmail.com

О ВОЗМОЖНОМ МЕХАНИЗМЕ НАЧАЛА ИЛИ ВОЗОБНОВЛЕНИЯ АКТИВНОСТИ РАДИОГАЛАКТИК В СКОПЛЕНИЯХ ГАЛАКТИК

Р.Р.АНДРЕАСЯН, А.В.АБРАМЯН, Г.М.ПАРОНЯН,
Г.А.МИКАЕЛЯН, А.М.МИКАЕЛЯН

С целью выявления влияния окружающей среды на внегалактические радиоисточники, мы исследовали близкое окружение известной и хорошо изученной радиогалактики класса FRI 3C31. Показано, что около 110 млн лет

назад галактики NGC 380 и NGC 386 располагались вблизи галактики NGC 383 (родительской галактики 3C31). С другой стороны, моделирование спектральных характеристик радиоизлучения центральной части радиогалактики 3C31 дает оценку возраста центрального джета примерно в 100 млн лет. Поэтому можно предположить, что одной из возможных причин появления или возобновления радиоактивности галактики NGC 383 может быть тройное близкое прохождение галактик.

Ключевые слова: галактики - радиогалактики - скопления галактик - окружение галактик

REFERENCES

1. *N.Miller, F.Owen, J.Burns et al.*, *Astrophys. J.*, **118**, 1998, 1999.
2. *E.Bufanda, D.Hollowood, T.Jeltema et al.*, *Mon. Not. Roy. Astron. Soc.*, **465**, 2531, 2017.
3. *W.Mo, A.Gonzalez, D.Stern et al.*, *Astrophys. J.*, **869**, 131, 2018.
4. *B.Fanaroff, J.Riley*, *Mon. Not. Roy. Astron. Soc.*, **167**, 31P, 1974.
5. *R.R.Andreasyan, H.Sol*, *Astrophysics*, **42**, 275, 1999.
6. *R.R.Andreasyan, H.Sol*, *Astrophysics*, **43**, 413, 2000.
7. *R.R.Andreasyan, S.Appl, H.Sol*, *Astrophysics*, **45**, 198, 2002.
8. *E.Bernhard, C.Tadhunter, J.Pierce et al.*, *Mon. Not. Roy. Astron. Soc.*, **512**, 86, 2022.
9. *C.Duggal, C.O'Dea, S.Baum et al.*, *Astron. Nachr.*, **342**, 1087, 2021.
10. *C.Tadhunter, D.Dicken, R.Morganti et al.*, *Mon. Not. Roy. Astron. Soc.*, **445**, L51, 2014.
11. *M.Chiaberge, R.Gilli, J.Lotz et al.*, *Astrophys. J.*, **806**, 147, 2015.
12. *S.Sakai, R.Giovanelli, G.Wegner*, *Astrophys. J.*, **108**, 335, 1994.
13. *R.Strom, R.Fanti, P.Parma et al.*, *Astron. Astrophys.*, **122**, 305, 1983.
14. *P.Parma, M.Murgia, R.Morganti et al.*, *Astron. Astrophys.*, **344**, 7, 1999.
15. *A.Martel, S.Baum, W.Sparks et al.*, *Astrophys. J. Suppl. Ser.*, **122**, 81, 1999.
16. *R.Laing, A.Bridle*, *Mon. Not. Roy. Astron. Soc.*, **336**, 328, 2002.
17. *M.Hardcastle, D.Worrall, M.Birkinshaw et al.*, *Mon. Not. Roy. Astron. Soc.*, **334**, 182, 2002.
18. *J.Croston, M.Hardcastle*, *Mon. Not. Roy. Astron. Soc.*, **438**, 3310, 2014.
19. *V.Heesen, J.Croston, R.Morganti et al.*, *Mon. Not. Roy. Astron. Soc.*, **474**, 5049, 2018.
20. *C.Tadhunter, T.Robinson, R.G.Delgado et al.*, *Mon. Not. Roy. Astron. Soc.*, **356**, 480, 2005.

АСТРОФИЗИКА

ТОМ 66

АВГУСТ, 2023

ВЫПУСК 3

DOI: 10.54503/0571-7132-2023.66.3-339

THE REVISITED BPT DIAGRAM FROM THE SELF-CONSISTENT ANALYSIS

P.PRIVATUS^{1,4}, C.PAPPALARDO^{2,3}, P.V.K.RAO¹, D.T.MAZENGO¹

Received 12 June 2023

Accepted 18 August 2023

Galaxies' spectral energy distribution has been explored through the use of spectral synthesis codes, and these techniques have been essential in identifying many aspects of the current galaxy evolution model. Most of the spectral synthesis codes that have been developed so far are solely stellar and assume a negligible nebular contribution to the overall continuum. FADO (Fitting Analysis using Differential Evolution Optimisation) is the first spectral synthesis code to fit self-consistently stellar and nebular components. Diagnostic diagrams are powerful tools for classifying galaxies based on the emission line ratio of collisionally excited lines such as [OIII] λ 5007 , [NII] λ 6584 , [SII] λ 6716 , 6731, [OI] λ 6300 , and the Balmer recombination lines such as H α , H β . This paper explores the impact of including nebular components on diagnostic diagrams. We investigated the results of the application of FADO to the Sloan Digital Sky Survey Data Release 8 using the data analysed by MPA-JHU, the Max Planck Institute for Astrophysics, and Johns Hopkins University. We found that in all diagnostic diagrams, the fluxes for FADO are higher than those for MPA-JHU; the difference is significant compared to the error in the flux measurement. FADO overestimates the flux ratio of all three diagnostic diagrams over MPA-JHU, but the overestimation is comparable with the line flux ratio errors. The results indicate that the inclusion of a nebular continuum is very important when fitting the spectral energy distribution as it increases the fluxes of all galaxies. However, there is a mild impact from the inclusion of nebular component analysis in the diagnostic diagrams used to classify the ionisation state of galaxies' interstellar medium.

Keywords: *galaxies: diagnostic diagram: nebular*

1. *Introduction.* Diagnostic diagrams are powerful and helpful tools to identify the source of ionisation of the gas by comparing the ratio of collisionally excited lines ([OIII] λ 5007 , [NII] λ 6584 , [SII] λ 6716 , 6731, [OI] λ 6300) and the Balmer recombination lines (i.e. H α , H β). The emission-line diagnostic diagram, known as the BPT diagram, named after Baldwin, Phillips, and Terlevich, has been used to classify galaxies based on their emission line ratios [OIII]/H β versus [NII]/H α in which the star-forming, the composite and the active galactic nucleus (AGN) occupied specific regions [1]. Further modifications to the BPT diagrams were proposed in the works of [2,3]. They included [OIII]/H β versus [SII]/H α called the SII-diagnostic diagram, and [OIII]/H β versus [OI]/H α called the OI-diagnostic diagram, where the star-forming regions, the Seyfert, and the LINER occupy specific regions.

A galaxy's nuclear spectrum is made up of the individual spectra of billions of stars and the nebular emission excited by their radiative output. It may further comprise thermal and non-thermal emission components arising from an active galactic nucleus, heated dust, and large-scale shocks in the multi-phase interstellar medium, all of which combine into a panchromatic spectral energy distribution (SED) that encodes the energy production mechanisms and history of galaxies' assembly [4,5]. Population Spectral Synthesis (PSS) has been a fundamental tool in extragalactic astronomy that aims at deriving galaxies' physical and evolutionary characteristics across cosmic time [6]. Its goal is to obtain from the SED of a galaxy its star formation history and chemical enrichment history, SFH and CEH, respectively [7]. The PSS method, also known as the inverse, semi-empirical evolutionary, or fossil record technique, is used to infer from a galaxy's spectrum the mass, age, and metallicity of its stellar populations. This method has been widely applied to massive spectroscopic data sets, particularly the Sloan Digital Sky Survey (SDSS), yielding crucial insights into the history of galaxy assembly [6]. The galaxies' physical properties related to galaxies' formation and evolution are extracted from the spectra, such as star formation rates (SFRs), stellar masses (M_*), and gas phase metallicity [8-10].

The main shortcoming of all state-of-the-art PSS codes is that they exclude nebular emission (ne). This results in a deficiency in the physical interpretation of the observed emission line ratios, which introduces biases in the obtained physical properties of the galaxy, like the stellar mass, mass-weighted stellar age, and specific star formation rate [11,12]. The biases in purely stellar (PS) codes have relevant astrophysical implications, including an increased dispersion or change of the slope of the Star Formation main Sequence (SFMS) and other scaling relations, such as the stellar mass (M_*) versus metallicity relation [7]. Fitting Analysis using Differential evolution Optimisation (FADO) is a PSS method that has the unique capacity to identify in a spectrum the underlying stellar and nebular components simultaneously [12-14]. This so-far unique self-consistency code allows us to significantly alleviate degeneracy in current spectral synthesis, thereby opening a new avenue to the exploration of the history of galaxies' assembly [7,12]. FADO uses artificial intelligence and genetic optimisation algorithms to derive chemical enrichment and star formation histories of galaxies based on two elements in spectral fitting models: self-consistency between the best-fitting star formation history and the galaxy's nebular emission [12].

In the comparison of FADO with purely stellar codes Pappalardo et al. [14] observed that, even in the presence of high signal-to-noise (S/N) spectra, when a galaxy enters a phase of high specific star formation rate (sSFR), the exclusion of the nebular continuum emission in the fitting process has a significant impact on the estimation of its stellar population ages. Cardoso et al. [15] carried a similar

analysis to that of Cardoso et al. [7] to compare FADO with STARLIGHT by applying these tools to a set of synthetic spectra of galaxies with different star formation histories (SFHs). The consideration of different SFHs allowed the comparison of the results between FADO and STARLIGHT as a function of the level of the nebular contribution. They compared stellar masses, light- and mass-weighted stellar ages, and metallicity of the two tools, finding relevant differences. For galaxies with a significant nebular contribution, STARLIGHT can overestimate the stellar mass and mass-weighted mean stellar age up to ~ 2 dex and ~ 4 dex, respectively. On the other hand, STARLIGHT underestimates the mean metallicity and light-weighted mean stellar age by up to ~ 0.6 dex. Compared to these results, FADO obtains significantly better estimates, with a precision of ~ 0.2 , even for evolutionary stages where the nebular contribution is highly prominent.

Miranda et al. [16] applied FADO to the spectral database of the SDSS to derive the physical properties of galaxies and compare them with the MPA-JHU (Max Planck Institute for Astrophysics and Johns Hopkins University) analysis, which contains the properties of SDSS galaxies derived without the nebular contribution. The Star Forming (SF) galaxies sample was used in this study, the nebular extinction was collected through the Balmer decrement, then calculated the H α luminosity to estimate the SFR. Then, by combining the stellar mass and SFR estimates from FADO and MPA-JHU, the SFMS was obtained. The results showed an agreement between the SFR of FADO and MPA-JHU because of the consistency between the H α flux measurements used to estimate the SFR in the two datasets. The stellar mass estimates were slightly higher for FADO than for MPA-JHU on average. However, considering the uncertainties, the differences were negligible. With similar SFR and stellar mass estimates, the derived SFMS was also comparable between FADO and MPA-JHU. The additional modelling of the nebular contribution does not affect the retrieved fluxes and consequently does not influence SFR estimators based on the extinction-corrected H α luminosity. For the stellar masses, the results point to the same conclusion. These results were a consequence of the fact that the vast majority of normal SF galaxies in the SDSS have a low nebular contribution. However, the obtained agreement might only hold for local SF galaxies, but higher redshift galaxies might show different physical properties using FADO. This would then be an effect of the expected increased nebular contribution [16].

As a follow-up to this work, in this paper, we investigate the impact of including the nebular continuum for the nearby galaxies studied in SDSS data release 8 in the diagnostic diagrams. This paper is organised as follows: Section 2 presents the survey from which we get the data, the MPA-JHU and FADO analysis. Sections 3 and 4 present the results and their discussion. Section 5 concludes.

2. Data sample and analysis. The galaxies investigated in this paper have been extracted from the spectroscopic sample of the SDSS, a multi-spectral imaging and spectroscopic redshift survey conducted with the 2.5 m f/5 wide-angle optical modified Ritchey-Chretien altitude azimuth telescope [17,18]. The telescope is located at Apache Point Observatory, in south-east New Mexico at an elevation of 2.788 m [18]. The SDSS has collected data of objects covering over 14.500 deg² for galaxies up to a magnitude limit of 23 in *g*-band magnitude [17]. This release contains data for 1472581 objects, each with a single-fibre integrated spectrum in the wavelength range of 3800-9200 Å at a resolution of $R \sim 1800$ -2200. At an average redshift of ~ 0.1 , the fibre covers ~ 5.5 kpc of the central region of an object [15]. The SDSS spectra are classified as stars, galaxies, or quasars. Redshifts are determined with an automated routine, done using two independent pipelines, one (*spectro1d*) that worked by cross-correlation with a family of templates and emission-line fits, followed by eyeball inspection of problematic cases, and another (*idlspec2d* or *specBS*) which does direct χ^2 fitting of templates to the spectra [19]. Galaxies' emission line fluxes are derived from spectra. In measuring the nebular emission lines of galaxies, it is important to properly account for the galaxy continuum, which is rich in stellar absorption features. The following two sections describe the method used to build the MPA-JHU and the FADO datasets, respectively.

2.1. MPA-JHU. In SDSS, a stellar population synthesis model fits the stellar continuum, subtracted from the spectra to get the emission line measurements. The code applied to the 8th data release of SDSS (DR8), and the resulting measurements are used for various scientific analyses [8-10]. The MPA-JHU provided measurements for all objects that *idlspec2d* identified as galaxies [19]. We used this data set due to its photometric completeness, uniform spectral calibration, wide redshift coverage ($0.02 \leq z \leq 0.6$) and a range of emission line properties related to galaxy formation and evolution that have been analysed [8-10].

The Bayesian approach and model grids from Kauffmann et al. [8] are used to determine stellar masses. Since the spectra were obtained using a 3 arcsec aperture, they do not accurately depict the entire galaxy. In the SDSS spectroscopic fibre aperture, the stellar mass has been calculated using fibre magnitudes, and the overall stellar mass has been calculated using model magnitudes. The stellar mass output corresponds to the probability distribution functions at the median, 2.5%, 16%, 84%, and 97.5% values. Based on the information provided by Brinchmann et al. [9], SFRs are calculated within the galaxy fibre aperture using nebular emission lines. The galaxy photometry found by Salim et al. [20] is used to estimate SFRs outside of the fibre. For AGN and galaxies with weak emission lines, SFRs are estimated from the SED. They presented both the fibre SFR and

the total SFR at the median, 2.5%, 16%, 84%, and 97.5% of the probability distribution function. The strong optical emission lines ([OII] $\lambda 3727$, H β , [OIII] $\lambda 5007$, [NII] $\lambda 6548$, 6584, and [SII] $\lambda 6717$, 6731) are used to estimate the nebular oxygen abundances using the Bayesian approach described in Tremonti et al. [10]. Oxygen abundances are only computed for objects classified as "star forming". The output value of 12+log(O/H) is given at the median and 2.5%, 16%, 84%, and 97.5% of the probability distribution function.

2.2. FADO. FADO is the first population spectral synthesis code capable of fitting the optical SED due to the stellar and nebular components being self-consistently. The usage of FADO and its novel approach to SED fitting could play a critical role in determining the impact of nebular contribution when spectroscopic data are analysed and how this might have influenced our current understanding of the processes taking place in galaxies. A series of benchmark publications [7,14,16,21] tested FADO capabilities in simulated and actual data by applying it to the SDSS DR8. As detailed in Gomes and Papaderos [12], the main task of FADO is to reproduce the observed SED through a linear combination of spectral components representative of the individual stellar (SSP) and a nebular continuum as expressed by

$$F_\lambda = \sum_{i=1}^{N_*} M_{i,\lambda_0} L_{i,\lambda} 10^{-0.4 A_v q_\lambda} \otimes S(v_*, \sigma_*) + \Gamma_\lambda(n_e, T_e) 10^{-0.4 A_v^{neb} q_\lambda} \otimes N(v_\eta, \sigma_\eta), \quad (1)$$

where: F_λ is the flux observed from the spectrum; N_* is the number of unique spectral components in the adopted base library; M_{i,λ_0} is the stellar mass of the spectral component i at the normalization wavelength λ_0 ; $L_{i,\lambda}$ is the luminosity contribution of the i^{th} spectral component; A_v is the V-band extinction; q_λ is the ratio of A_λ over A_v ; $S(v_*, \sigma_*)$ denotes a Gaussian kernel simulating the effect of stellar kinematics on the spectrum, with v_* and $v\sigma_*$ representing the stellar shift and dispersion velocities, respectively; $\Gamma_\lambda(n_e, T_e)$ is the nebular continuum computed assuming that all stellar photons with $\lambda \leq 911.76\text{\AA}$ are absorbed and reprocessed into nebular emission, under the assumption of case B recombination, A_v^{neb} is the nebular V-band extinction, and $N(v_\eta, \sigma_\eta)$ denotes the nebular kinematics kernel, with v_η and σ_η representing the nebular shift and dispersion, respectively [15].

It is important to note that all publicly available population synthesis codes before FADO aimed to reconstruct the observed continuum using only the first term of Eq. 1, using a purely-stellar scheme to construct the overall observed SED [12,13,21]. One of FADO's novel features is the second term of Eq.1, which represents the relative rate of spectral contribution due to the ionizing photons produced by the young stellar component and scales with the intensity of the Balmer lines.

2.3. Selection criteria. The galaxies used in this study were obtained by cross-correlating MPA-JHU and FADO, resulting in 922951 galaxies. The galaxies were classified using the three diagnostic diagrams defined in Kewley et al. [3]: NII-BPT, SII, and OI. To accurately classify the galaxies into star-forming or AGN, we selected all galaxies with the $S/N > 3$ for all the emission lines used in this study. Assuming an electron density $n_e = 10^2 \text{ cm}^{-3}$ and electron temperature at $T = 10^4 \text{ K}$ for the case when the gas is optically thick for ionising radiation, meaning that the photon emitted after recombination is absorbed locally (this is the case for nearly all nebulae), then the theoretical value flux ratios $F(\text{H}\alpha/\text{H}\beta)$ are equal to 2.86 and 3.1 for star-forming and AGNs, respectively [22–25]. When an intrinsically low reddening is paired with inaccuracies in the stellar absorption

Table 1

MEDIAN DIFFERENCE BETWEEN THE LINE FLUXES USED

Median of the fluxes					
Emission line	MPA-JHU log(erg/s/cm ²)	FADO log(erg/s/cm ²)	Δ dex	MPA-JHU errors log(erg/s/cm ²)	FADO errors log(erg/s/cm ²)
[NII]	4.38	4.42	0.04 (10%)	0.02 (5%)	0.01 (2%)
[SII]	4.29	4.37	0.08 (20%)	0.03 (7%)	0.01 (2%)
[OI]	2.70	2.89	0.19 (55%)	0.06 (15%)	0.01 (2%)
[OIII]	3.33	3.51	0.18 (51%)	0.04 (10%)	0.01 (2%)
H α	5.31	5.32	0.01 (2%)	0.01 (2%)	0.001 (0.2%)
H β	3.89	3.93	0.04 (10%)	0.01 (2%)	0.004 (1%)

Columns: 1 - line, 2, 3 - median fluxes obtained with MPA-JHU and FADO, 4 - median differences of the emission line flux between FADO and MPA-JHU, 5, 6 - median of the emission line flux error in the MPA-JHU and FADO measurements.

Table 2

TOTAL NUMBER OF GALAXIES FOR BOTH MPA-JHU AND FADO CLASSIFICATION OF 400133, 380299, 228793 GALAXIES SAMPLE FOR NII, SII AND OI DIAGNOSTIC DIAGRAMS RESPECTIVELY

Galaxy type	[NII]		[SII]		[OI]	
	MPA JHU	FADO	MPA-JHU	FADO	MPA-JHU	FADO
Sample	400133	400133	380299	380299	228793	228793
SF	253163	231132				
Composite	76411	75810				
SF+Composite			322039	294945	182333	147981
Seyfert	17607	23309	18937	22989	19593	20936
LINER	20376	21357	25690	28444	18106	28643
Low S/N SF	32576	48525	13633	33921	8761	31233

correction and/or errors in the calibration and measurement of the line flux, a Balmer decrement smaller than the theoretical value can be obtained [3]. On the other hand, Balmer decrements lower than the theoretical value can indicate a higher nebular temperature [22]. For this reason, the objects with $F(\text{H}\alpha/\text{H}\beta) < 2.86$ for star-forming galaxies and with $F(\text{H}\alpha/\text{H}\beta) < 3.1$ for AGNs were removed from the sample. The median redshift of the objects used in this study is at $z \sim 0.1$. The number of galaxies obtained after applying all the selection criteria are shown in Table 2.

3. Results. In this section, we compare the fluxes obtained with MPA-JHU and FADO for all the emission lines used in this paper and also compare the generated diagnostic diagrams.

3.1. Flux comparisons for the sample. Fig.1 and Table 1 show the median differences between the line fluxes used to draw the diagnostic diagrams obtained with FADO and MPA-JHU for the total sample. Overall, FADO recovers higher fluxes than the MPA-JHU data: the differences are higher for collisionally excited lines, 0.18 dex (51%) for [OIII] $\lambda 5007$, 0.06 dex (15%) for [NII] $\lambda 6548$, 0.08 dex (20%) for [SII] $\lambda 6716$, 6731 and 0.19 dex (55%) for [OI] $\lambda 6300$. The differences are lower for H α recombination lines between 0.01 dex (2%) against 0.04 dex (10%) for H β (see Table 1). For the H α line, the differences between

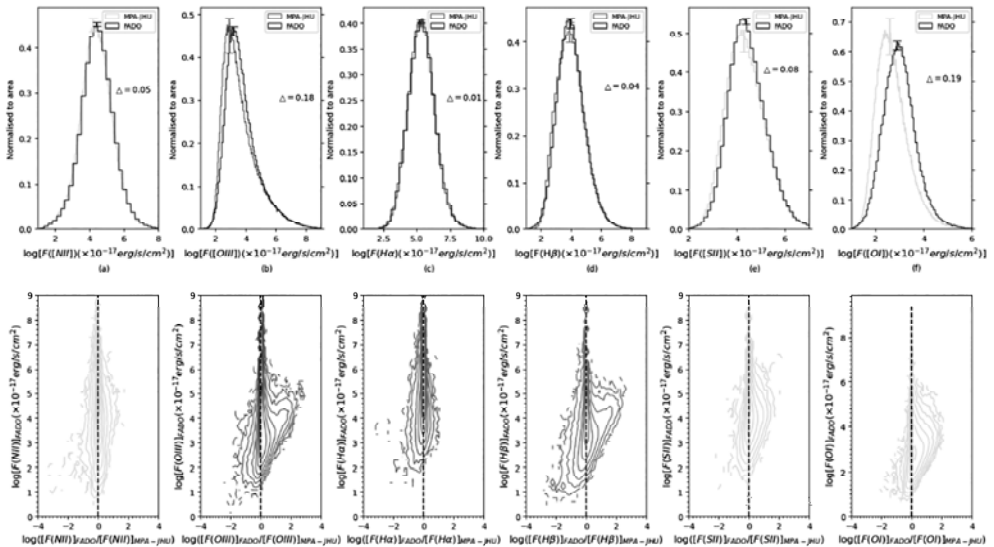


Fig.1. Flux comparison for MPA-JHU and FADO of the total sample. Top panels: histograms. Bottom panels: contour plots showing the fluxes estimated with FADO versus the ratio between the fluxes obtained with FADO and the MPA-JHU catalogue. The contour plots show 20%, 40%, 60%, 80% and 100% of the sample.

the fluxes measured by MPA-JHU and FADO and the median errors are comparable because of the higher fluxes of these emission lines. Fluxes are in 10^{17} erg/s/cm 2 unit to be consistent with the MPA-JHU measurements.

3.2. The NII diagnostic diagram. This subsection compares the NII diagnostic diagrams between MPA-JHU and FADO for Star-forming (SF), composite (COMP), Seyfert and LINER galaxies. The number of galaxies was obtained by adopting Kewley et al. [3] classification. For NII diagnostic SF galaxies using Eq. 2. The results from this classification are shown in Table 2: the median log values of $[\text{NII}]/\text{H}\alpha$ are -0.34 and -0.30 for MPA- JHU and FADO, respectively, for $[\text{OIII}]/\text{H}\beta$ are -0.49 and -0.48 for MPA-JHU and FADO, respectively, as shown in Fig.2.

The Composite galaxies were obtained by adopting Kewley et al. [3] classification, according to Eq. 3, as shown in Table 2. The median log value of $[\text{NII}]/\text{H}\alpha$ are -0.14 and -0.08 for MPA-JHU, and FADO respectively, and $[\text{OIII}]/\text{H}\beta$ is -0.26, and -0.25 for MPA-JHU, and FADO, respectively as shown in Fig.2.

Seyfert galaxies were obtained by selecting galaxies above Eq. 5, as shown in

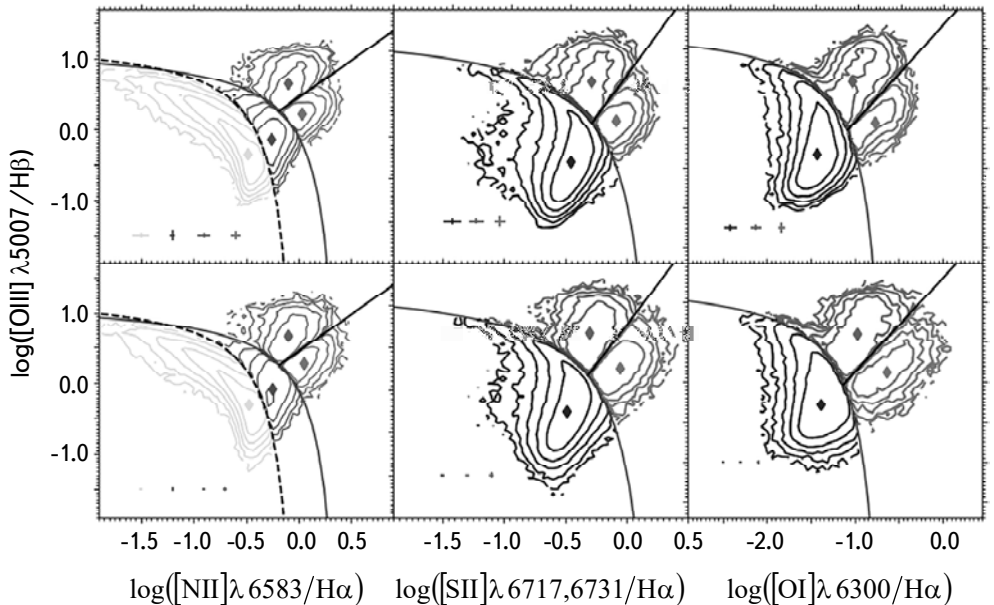


Fig.2. Contour plot showing the distribution of sources in the NII-BPT (left panels), SII(Middle panel) and OI (right panels) classification diagrams for MPA-JHU (upper panels) and FADO (bottom panel). The dashed line, and curved solid line, represent Kauffmann et al. [8], Kewley et al. [26], respectively. The straight solid line in NII BPT represents Schawinski et al. [27], and in SII and OI classification diagrams represent Kewley et al. [3] classification line. The contour plots show the sample's 20%, 40%, 60%, 80% and 100%. The small diamonds indicate the median values of the line ratios, and the + symbols are error bars for the measurements of the line ratios.

Table 2. The median log values of $[\text{NII}]/\text{H}\alpha$ are 0.65, 0.68 for MPA-JHU and FADO, respectively, and $[\text{OIII}]/\text{H}\beta$ are -0.10 and -0.10 for MPA-JHU and FADO, respectively.

The LINER galaxies were obtained by adopting Kewley et al. [3] relation, the galaxies the values given by Eq. 5 as shown in Table 2. The position of LINER galaxies in the $[\text{NII}]/\text{H}\alpha$ versus $[\text{OIII}]/\text{H}\beta$ diagnostic diagram for both MPA-JHU and FADO is shown in Fig.2. The median log values of $[\text{NII}]/\text{H}\alpha$ are 0.22, and 0.28 for MPA-JHU and FADO, respectively, and $[\text{OIII}]/\text{H}\beta$ are 0.03 and 0.04 for MPA-JHU and FADO, respectively.

$$\log([\text{OIII}]/\text{H}\beta) = 0.61/\log([\text{NII}]/\text{H}\alpha) - 0.05 + 1.3 \quad (2)$$

$$0.61/\log([\text{NII}]/\text{H}\alpha) - 0.47 + 1.19 = \log([\text{OIII}]/\text{H}\beta) \quad (3)$$

and

$$\log([\text{NII}]/\text{H}\alpha) = 3 \quad (4)$$

$$1.05 \log([\text{NII}]/\text{H}\alpha) + 0.45 = \log([\text{OIII}]/\text{H}\beta). \quad (5)$$

3.3. The SII diagnostic diagram. In this subsection, we compare the SII-diagnostic diagrams for star-forming, composite, Seyfert, and LINER galaxies. Galaxies are considered star-forming + Composite if they lie below Eq. 6, as shown in Table 2. The median log values of $[\text{SII}]/\text{H}\alpha$ are -0.50, and -0.48 for MPA-JHU and FADO, respectively, and $[\text{OIII}]/\text{H}\beta$ are -0.30, and -0.25 for MPA-JHU and FADO, respectively.

Seyfert galaxies were obtained by adopting Kewley et al. [3] relation, using Eq. 8, as shown in Table 2. The median log values of $[\text{SII}]/\text{H}\alpha$ are -0.33 and -0.30 for MPAJHU and FADO, respectively, and $[\text{OIII}]/\text{H}\beta$ are 0.65 and 0.67 for MPA-JHU and FADO, respectively.

LINER galaxies lie below Eq. 8, as shown in Table 2. The median log values of $[\text{SII}]/\text{H}\alpha$ are -0.11 and -0.05 for MPA-JHU and FADO, respectively, and $[\text{OIII}]/\text{H}\beta$ is 0.18 and 0.25 for MPA-JHU and FADO, respectively.

$$\log([\text{OIII}]/\text{H}\beta) = 0.72/\log([\text{SII}]/\text{H}\alpha) - 0.32 \quad (6)$$

and

$$1.3 \log([\text{SII}]/\text{H}\alpha) = 0.1 \quad (7)$$

$$\log([\text{SII}]/\text{H}\alpha) - 0.32 + 1.30 = \log([\text{OIII}]/\text{H}\beta). \quad (8)$$

3.4. The OI diagnostic diagram. In this subsection, we compare the OI diagnostic diagrams for star-forming, composite, Seyfert, and LINER galaxies. The galaxies are said to be star-forming + Composite if they are below the line (9), the number of galaxies is shown in Table 2. The median log values of $[\text{OI}]/\text{H}\alpha$ are -1.49, and -1.39 for MPA-JHU, and FADO respectively, and for

$[\text{OIII}]/\text{H}\beta$ are -0.32, and -0.28 for MPA-JHU, and FADO, respectively.

The galaxies above Eq. 11 were selected for OI Seyfert galaxies, and the number of galaxies is shown in Table 2. The median log values of $[\text{OI}]/\text{H}\alpha$ are -1.07, and -0.98 for MPA-JHU and FADO, respectively, and $[\text{OIII}]/\text{H}\beta$ is 0.59, and 0.61 for MPA-JHU and FADO, respectively.

OI LINER galaxies are found by selecting galaxies below Eq. 11, the galaxies obtained are shown in Table 2. The median log values of $[\text{OI}]/\text{H}\alpha$ are -0.69, and -0.64 for MPA-JHU and FADO, respectively, and $[\text{OIII}]/\text{H}\beta$ are 0.06, and 0.12 for MPA-JHU and FADO, respectively.

$$\log([\text{OIII}]/\text{H}\beta) = 0.73 / [\log([\text{OI}]/\text{H}\alpha) + 0.59] \quad (9)$$

and

$$1.33 \log([\text{OI}]/\text{H}\alpha) = -0.75 \quad (10)$$

$$\log([\text{OI}]/\text{H}\alpha) + 1.3 = \log([\text{OIII}]/\text{H}\beta). \quad (11)$$

The galaxies with $\text{S/N} > 2$ in $\text{H}\alpha$ are considered as low S/N star forming [9].

4. Discussion. Fig.1 and column 4 of Table 1 show how FADO obtain higher fluxes than the MPA-JHU. The overestimation is between 2-50% for Balmer and forbidden lines, which is slightly higher than the typical errors in the same lines, which is between 2-10%. The differences are larger for forbidden lines and less evident for Balmer lines, in particular for $\text{H}\alpha$, where the differences (2%) are comparable with the typical errors in this strong emission line.

Tables 3, 4, and 5 compare the differences in the median of the flux ratio between FADO and MPA-JHU (Δ) and the difference in flux ratio errors between MPA-JHU and FADO (ΔER) for NII, SII and OI diagnostic diagrams, respectively. It is observed that FADO results in the shifting of the emission line ratio of all three diagnostic diagrams. The deviation in the measurement for $[\text{NII}]/\text{H}\alpha$ is between 7-12%, that is 0.04 dex (10%), 0.06 dex (10%), 0.03 dex (7%), 0.05 dex

Table 3

COMPARISON OF THE DIFFERENCE OF THE MEDIAN OF THE
FLUX RATIO BETWEEN FADO AND MPA-JHU (Δ), AND THE
DIFFERENCE OF FLUX RATIO ERRORS BETWEEN MPA-JHU AND
FADO (ΔER) FOR NII DIAGNOSTIC DIAGRAM

Flux Ratio	SF		Composite		Seyfert		LINER	
	Δ	ΔER	Δ	ΔER	Δ	ΔER	Δ	ΔER
$[\text{NII}]/\text{H}\alpha$	0.04	0.02	0.06	0.02	0.03	0.02	0.05	0.03
$[\text{OIII}]/\text{H}\beta$	0.01	0.04	0.01	0.06	0.01	0.03	0.01	0.07

Table 4

COMPARISON OF THE DIFFERENCE IN THE MEDIAN OF THE FLUX RATIO BETWEEN FADO AND MPA-JHU (Δ), AND THE DIFFERENCE IN FLUX RATIO ERRORS BETWEEN MPA-JHU AND FADO (ΔER) FOR THE SII DIAGNOSTIC DIAGRAM

	SF+Composite		Seyfert		LINER	
Flux Ratio	Δ	ΔER	Δ	ΔER	Δ	ΔER
[NII]/H α	0.02	0.01	0.03	0.01	0.06	0.02
[OIII]/H β	0.05	0.04	0.02	0.03	0.07	0.08

Table 5

COMPARISON OF THE DIFFERENCE OF THE MEDIAN OF THE FLUX RATIO BETWEEN FADO AND MPA-JHU (Δ), AND THE DIFFERENCE OF FLUX RATIO ERRORS BETWEEN MPA-JHU AND FADO (ΔER) FOR OI DIAGNOSTIC DIAGRAM

	SF+Composite		Seyfert		LINER	
Flux Ratio	Δ	ΔER	Δ	ΔER	Δ	ΔER
[OI]/H α	0.1	0.07	0.09	0.05	0.05	0.03
[OIII]/H β	0.04	0.04	0.02	0.02	0.06	0.06

(12%) for star-forming, composite, Seyfert, and LINER galaxies in columns 2, 4, 6, and 8 of Tables 3, 4, and 5, respectively. For [SII]/H α , the deviation of the flux ratio is between 5-15%. For [OI]/H α , the deviation of the flux ratio is between 12-26%. For [OIII]/H β , the deviation of the flux ratio is between 2-20%.

From Tables 3, 4, and 5, it is observed that in all three diagnostic diagrams, the difference in the flux ratio between FADO and MPA-JHU is comparable to the difference in the error in the measurement of the flux ratio. The overestimation of the flux ratio is less significant when compared to the errors in the flux ratio for all the diagnostic diagrams.

5. *Conclusion.* In this work, we studied the results of the unique spectral synthesis code FADO applied to the SDSS-DR8 data set. The results are compared to the MPA-JHU catalogue, which performed a similar study using purely stellar codes for the analysis. We have applied the $S/N > 3$ condition for all emission lines used to draw diagnostic diagrams. The galaxies were classified based on the activity of the nucleus into Star-forming, Composite, Seyfert, and LINER by

applying the methods of Kewley et al. [3]. We compared the emission line fluxes and generated NII, SII and OI diagnostic diagrams using MPA-JHU and FADO. We show the three diagnostic diagrams for MPA-JHU and FADO in Fig.2. The significant findings of this study are:

- The inclusion of the nebular component increases the emission line fluxes of starforming, composite, Seyfert, and LINER galaxies. The differences are higher for collisionally excited lines, between 15-51%, 0.18 dex (51%) for $[\text{OIII}] \lambda 5007$, 0.06 dex (15%) for $[\text{NII}] \lambda 6548$, 0.08 dex (20%) for $[\text{SII}] \lambda 6716$, 6731 and 0.19 dex (55%) for $[\text{OI}] \lambda 6300$. These differences are slightly larger than the typical error measurements of such lines. The differences are less significant for Balmer lines, where for the $\text{H}\alpha$ line the median differences are comparable to the median errors, around 2%. At least for forbidden lines, including the nebular component in the analysis can impact the measured fluxes, even considering the measurement errors.
- Taking into account the nebular continuum by FADO results in the shifting of the median of the emission line ratio towards higher values. The deviation in the measurement for $[\text{NII}]/\text{H}\alpha$ is between 7-12%, for $[\text{SII}]/\text{H}\alpha$ between 5-15%, for $[\text{OI}]/\text{H}\alpha$ between 12-26%, and the $[\text{OIII}]/\text{H}\beta$ differences are between 2-20%. The difference in the emission line flux ratio between FADO and MPA-JHU is less significant when compared to the median error in the measurement of the emission line flux ratios which lie around 2-20%.

This indicates that the usual diagnostic diagrams used to classify the ionisation state of the galaxies' interstellar medium are mildly affected by the inclusion of the nebular component in the analysis.

Acknowledgments. We acknowledge the Max Planck Institute for Astrophysics and Johns Hopkins University for providing the data necessary for this study. C.P. acknowledges support from DL57/2016 (P2460) from the "Departamento de Física, Faculdade de Ciências da Universidade de Lisboa".

¹ Department of Physics, The University of Dodoma, Iyumbu, Dodoma, 41218, Tanzania, e-mail: privatuspius08@gmail.com

² Instituto de Astrofísica e Ciências do Espaço, Universidade de Lisboa - OAL, Tapada da Ajuda, Lisboa, PT1349-018, Portugal

³ Departamento de Física,, Faculdade de Ciências da Universidade de Lisboa, Edifício C8, Campo Grande,, Lisboa, PT1749-016, Portugal

⁴ Department of Natural Science, Mbeya University of Science and Technology, Iyunga, Mbeya, 53119, Tanzania

ПЕРЕСМОТРЕННАЯ ДИАГРАММА ВРТ В РАМКАХ САМОСОГЛАСОВАННОГО АНАЛИЗА

П.ПРИВАТУС^{1,4}, Ч.ПАППАЛАРДО^{2,3}, П.В.К.РАО¹, Д.Т.МАЗЕНГО¹

Спектральное распределение энергии галактик было исследовано с использованием кодов спектрального синтеза, которые важны для выявления многих аспектов современных моделей эволюции галактик. Большинство кодов спектрального синтеза, разработанных до сих пор, в основном учитывают звездную компоненту и предполагают незначительный небулярный вклад в общий континуум. FADO (Fitting Analysis using Differential Evolution Optimisation) - первый код спектрального синтеза, который самосогласованно учитывает обе компоненты. Диагностические диаграммы являются мощным инструментом для классификации галактик на основе отношений ударно возбуждаемых эмиссионных линий, таких как [OIII] $\lambda 5007$, [NII] $\lambda 6584$, [SII] $\lambda 6716, 6731$, [OI] $\lambda 6300$, а также рекомбинационных линий Бальмера, таких как H α , H β . В данной статье исследуется влияние небулярного компонента на диагностические диаграммы. Приведены результаты применения FADO к данным Sloan Digital Sky Survey Data Release 8, в сравнении с данными, проанализированными MPA-JHU (Max Planck Institute for Astrophysics и Johns Hopkins University). Обнаружено, что на всех диагностических диаграммах потоки для FADO выше, чем для MPA-JHU; разница значительна по сравнению с ошибкой измерения потока. FADO переоценивает отношение потоков во всех трех диагностических диаграммах по сравнению с MPA-JHU, но переоценка сопоставима с ошибками измерения потоков линий. Результаты указывают на то, что включение небулярного континуума является важным при подгонке спектрального распределения энергии, поскольку это увеличивает потоки всех галактик. Однако включение анализа небулярного компонента оказывает незначительное влияние на диагностические диаграммы, используемые для классификации ионизационного состояния межзвездной среды галактик.

Ключевые слова: галактики: диагностическая диаграмма: небулярное излучение

REFERENCES

1. J.A.Baldwin, M.M.Phillips, R.Terlevich, Publ. Astron. Soc. Pacif., **93**(551), 5, 1981.
2. S.Veilleux, D.E.Osterbrock, Astrophys. J. Suppl. Ser., **63**, 295, 1987.

3. *L.J.Kewley, B.Groves, G.Kauffmann et al.*, Mon. Not. Roy. Astron. Soc., **372**(3), 961, 2006.
4. *J.Walcher, B.Groves, T.Budavári et al.*, Astrophys. Space Sci., **331**(1), 1-51, 2011.
5. *C.Conroy*, Ann. Rev. Astron. Astrophys., **51**, 393, 2013.
6. *B.Panter, R.Jimenez, A.F.Heavens et al.*, Mon. Not. Roy. Astron. Soc., **391**(3), 1117, 2008.
7. *L.S.Cardoso, J.M.Gomes, P.Papaderos*, Astron. Astrophys., **622**, 56, 2019.
8. *G.Kauffmann, T.M.Heckman, C.Tremonti et al.*, Mon. Not. Roy. Astron. Soc., **346**(4), 1055, 2003.
9. *J.Brinchmann, S.Charlot, S.D.White et al.*, Mon. Not. Roy. Astron. Soc., **351**(4), 1151, 2004.
10. *C.A.Tremonti, T.M.Heckman, G.Kauffmann et al.*, Astrophys. J., **613**(2), 898, 2004.
11. *C.Pacifici, E.Cunha, S.Charlot et al.*, Mon. Not. Roy. Astron. Soc., **447**(1), 786, 2015.
12. *J.M.Gomes, P.Papaderos*, Astron. Astrophys., **603**, 63, 2017.
13. *J.M.Gomes, Fado*, Proceedings of the International Astronomical Union, **15**(S352), 108, 2019.
14. *C.Pappalardo, L.S.Cardoso, J.M.Gomes et al.*, arXiv preprint arXiv:2105.08082, 2021.
15. *L.S.Cardoso, J.M.Gomes, P.Papaderos*, arXiv preprint arXiv:2208.14036, 2022.
16. *H.Miranda, C.Pappalardo, P.Papaderos et al.*, arXiv preprint arXiv:2212.01293, 2022.
17. *D.G.York, J.Adelman, J.E.Anderson Jr et al.*, Astron. J., **120**(3), 1579, 2000.
18. *R.Suszyn'ski, P.Poczekajło*, Procedia Computer Science, **192**, 4386, 2021.
19. *H.Aihara, C.A.Prieto, D.An et al.*, Astrophys. J. Suppl. Ser., **193**(2), 29, 2011.
20. *S.Salim, J.C.Lee, R.Davé et al.*, Astrophys. J., **808**(1), 25, 2015.
21. *L.S.M.Cardoso*, PhD thesis, Universidade do Porto (Portugal), 2017.
22. *D.E.Osterbrock, G.J.Ferland*, Astrophysics Of Gas Nebulae and Active Galactic Nuclei. University science books, Sansalito, 2006.
23. *M.A.Dopita, R.S.Sutherland*, Astrophysics of the Diffuse Universe, Berlin, New York, Springer, 2003.
24. *B.Groves, J.Brinchmann, C.J.Walcher*, Mon. Not. Roy. Astron. Soc., **419**(2), 1402, 2012.
25. *I.G.Momcheva, J.C.Lee, C.Ly et al.*, Astron. J., **145**(2), 47, 2013.
26. *L.J.Kewley, M.Dopita, R.Sutherland et al.*, Astrophys. J., **556**(1), 121, 2001.
27. *K.Schawinski, D.Thomas, M.Sarzi et al.*, Mon. Not. Roy. Astron. Soc., **382**(4), 1415, 2007.

АСТРОФИЗИКА

ТОМ 66

АВГУСТ, 2023

ВЫПУСК 3

DOI: 10.54503/0571-7132-2023.66.3-353

EPHEMERIS UPDATES FOR SEVEN SELECTED HATNet SURVEY TRANSITING EXOPLANETS

A.PORO¹, F.A.FARAHANI², E.JAHANGIRI², A.SAROSTAD²,
M.GOZARANDI², M.HAGHGOU^{2,3}, F.ABOLHASSANI², A.FAKHRABADI²,
Y.JONGEN⁴, A.WÜNSCHE⁵, R.NAVES⁶, P.GUERRA⁷, A.MARCHINI⁸,
M.SALISBURY⁹, R.EHRENBERGER¹⁰, V-P.HENTUNEN¹¹

Received 30 March 2023

Accepted 18 August 2023

We refined the ephemeris of seven transiting exoplanets HAT-P-6b, HAT-P-12b, HAT-P-18b, HAT-P-22b, HAT-P-32b, HAT-P-33b, and HAT-P-52b. We observed 11 transits from eight observatories in different filters for HAT-P-6b and HAT-P-32b. Also, the Exoplanet Transit Database (ETD) observations for each of the seven exoplanets were analyzed, and the light curves of five systems were studied using Transiting Exoplanet Survey Satellite (TESS) data. We used Exofast-v1 to simulate these ground- and space-based light curves and estimate mid-transit times. We obtained a total of 11, 175 and 67 mid-transit times for these seven exoplanets from our observations, ETD and TESS data, respectively, along with 155 mid-transit times from the literature. Then, we generated transit timing variation (TTV) diagrams for each using derived mid-transit times as well as those found in the literature. The systems' linear ephemeris was then refined and improved using the Markov Chain Monte Carlo (MCMC) method. All of the studied exoplanets, with the exception of the HAT-P-12b system, displayed an increasing trend in the orbital period in the TTV diagrams.

Keywords: *planetary systems - planets and satellites*

1. Introduction. The number of exoplanets discovered and characterized each year has been increasing since the results of the first exoplanet detection [1]. "Hot Jupiters" are an important type of planetary gas giant with masses and radii similar to Jupiter but orbiting their host stars with short orbital periods (most less than 10 days), making them a good target system to discover and study [2,3]. The transit technique is the most efficient way to improve our understanding of exoplanets through ground- and space-based surveys. Furthermore, photometric transit surveys combined with radial velocity data have become one of the most successful methods for detecting transiting exoplanets over the past decade [4]. High-precision transit observations provide information to refine planetary parameters such as the planet's size, mass, atmosphere, and orbital ephemerides [5,6]. Moreover, photometric transit surveys allow us to study the variations of the orbital periods through TTV analysis. Space telescopes have longer available observational time, and they are not affected by the Earth's atmosphere as well. TESS is one of the most significant space-based survey missions for the discovery and observation of transiting exoplanets. TESS

was launched in 2018 to observe new exoplanets orbiting bright nearby stars that are brighter than Kepler mission stars [7]. Furthermore, when combined with previous work, this space mission provides precise transit timing for discovered exoplanets, which is critical for obtaining a better transit ephemeris [8].

Based on our observations, TESS, ETD¹, and literature observations, we updated orbital ephemeris for the HAT-P-6b, HAT-P-12b (TESS ID 198108326), HAT-P-18b (TESS ID 21744120), HATP-22b (TESS ID 252479260), HAT-P-32b, HAT-P-33b (TESS ID 239154970), and HAT-P-52b (TESS ID 436875934). These exoplanets were discovered by the Hungarian-made Automated Telescope Network (HATNet) survey.

2. *Observations and method.*

2.1. Observation and data reduction. Observations in this study have been made regarding exoplanets HAT-P-6b and HAT-P-32b during the years 2018 to 2022. A total of nine observation nights have been done for these two exoplanets; five and four nights for HAT-P-6b and HAT-P-32b, respectively. All these photometric observations have been done with small telescopes at eight observatories. We used CCD and standard filters in these observations. The information about the observatories, telescopes, CCDs, and data reduction software that we used is listed in Table 1. In Table 1, an abbreviated name has been determined for each observatory just to identify them in this study. The basic data reduction for the dark, bias, and flat field of each CCD image was carried out in accordance with the standard technique.

Table 1

THE OBSERVATORIES OF THIS STUDY AND THE INSTRUMENTS THAT WERE EMPLOYED

Observatory	Telescope	CCD	Data reduction Software
Rasteau Observatory, France (RO) Montcabrer private observatory, Spain (MO) Observatori Astronomic Albanyà, Spain (AA)	PlaneWave CDK 17" SCT 12" Meade ACF 16"	SBIG STXL11004 SBIG ST8-XME Moravian Instruments G4-9000	Muniwin/C-munipack Fotodif Fotodif
Astronomical Observatory, University of Siena (K54), Italy (AO)	MCT 300 mm	SBIG STL-6303	Muniwin/C-munipack
Observatoire des Baronnies Provençales, France (BO)	Cassegrain 430 mm	Zwo ASI6200 Pro mono	Muniwin/C-munipack
Private Observatory, Czech Republic (PO) Crow-Observatory Vranová, Czech Republic (CO)	400 mm NWT 300 mm	SBIG ST-10 XME Moravian Instruments G2-3200	AstroImageJ 3.2.10 Muniwin/C-munipack
Taurus Hill Observatory, Finland (TO)	SCT 14"	SBIG ST-8 XME	AIP4Win v2.4.10

¹ <http://var2.astro.cz/ETD/>

2.2. ETD data. To obtain the refined orbital ephemeris of selected HATNet exoplanets, we also collected also light curves, which were sourced from astronomers through the ETD archive [9]. Light curves were obtained from various filters and time scales. We used data in ETD that we were confident enough to be appropriate; for example, we did not use data whose declared time was less than three digits. We used those which generally have a quality index (DQ) of less than three [9]. All times in the data were converted from JD or HJD to BJD_{TDB} based on the geographic location of observation and RA(J2000) and DEC(J2000) from the Simbad² astronomical database.

In some ETD light curves, the airmass effect has been ignored, so airmass must be calculated based on the observers' location, which influences and improves the measured mid-transit times of related light curves. Therefore, we computed the airmass using the Astropy package in Python [10].

2.3. TESS data. Five of these exoplanets were observed by TESS, and HAT-P-6b, and HAT-P-32b have no TESS data yet. TESS observed the five host stars at 120-second cadences. We collected TESS data from the Mikulski space telescope archive (MAST). TESS style curves were extracted by LightKurve³ code from the MAST Python package.

2.4. Method. We relied on the AstroImageJ software [11] to normalize all of the data. Fig.1 shows the folded TESS light curves for five selected exoplanets.

Table 2

EXTRACTED GROUND-BASED TRANSIT TIMES FOR HAT-P-6b
AND HAT-P-32b IN THIS STUDY

Exoplanet	Observatory	T_c (BJD_{TDB})	Error	Filter	Eopch	O-C
HAT-P-6b	MO	2455430.46458	0.00110	Optec R cousins	362	0.0075
HAT-P-6b	RO	2458312.50536	0.00063	Baader imaging J	1110	0.0155
HAT-P-6b	AA	2458389.56389	0.00101	Baader $J-CV$	1130	0.0143
HAT-P-6b	AO	2459441.43053	0.00101	Johnsons-Cousins I	1403	0.0161
HAT-P-6b	RO	2459441.43128	0.00095	Baader imaging R	1403	0.0168
HAT-P-6b	RO	2459468.40283	0.00124	Baader imaging R	1410	0.0175
HAT-P-32b	CO	2459107.46235	0.00097	Johnsons-Cousins R_c	2180	-0.0015
HAT-P-32b	TO	2459191.31427	0.00034	Baader Bessel photometric R	2219	0.0001
HAT-P-32b	BO	2459507.36578	0.00017	Johnsons-Cousins V	2366	0.0005
HAT-P-32b	PO	2459593.36707	0.00024	Johnsons-Cousins R_c	2406	0.0015
HAT-P-32b	BO	2459593.37024	0.00041	Johnsons-Cousins R_c	2406	0.0046

² <http://simbad.u-strasbg.fr/simbad/>

³ <https://docs.lightkurve.org/>

Finally, all ground- and space-based light curves were applied to Exofast-v1 [12] for modeling purposes; as a consequence, the output mid-transit times and associated uncertainties were employed. Fig.2 provides an example of a modeled

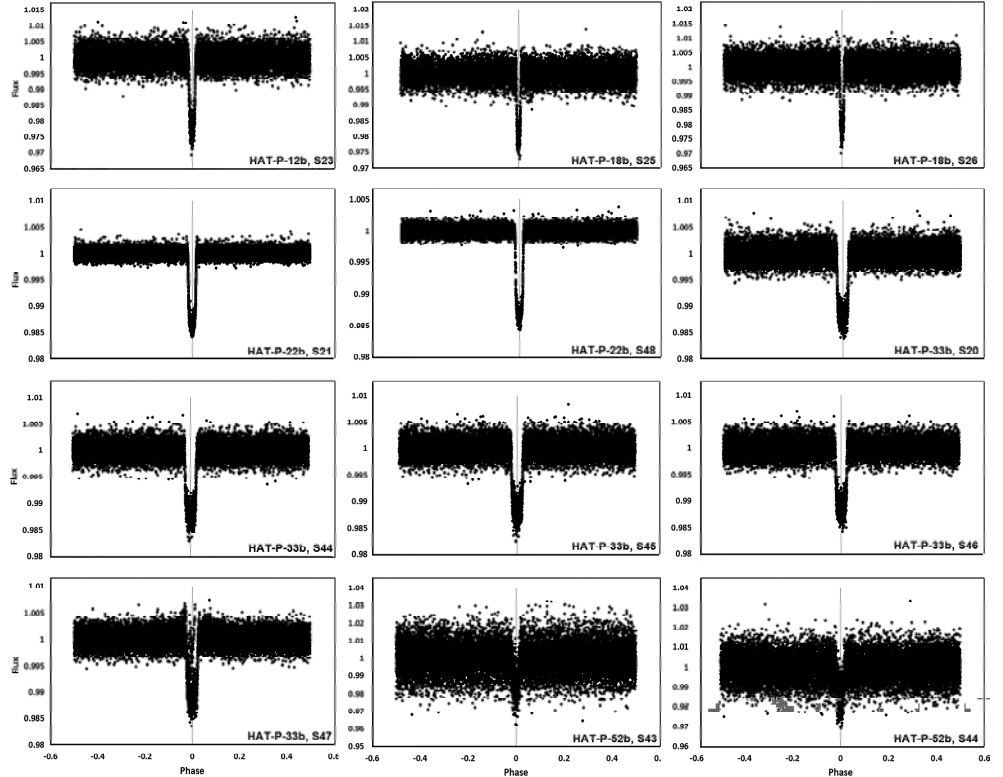


Fig.1. Folded TESS light curves in each sector of all selected exoplanets were obtained from the LightKurve code.

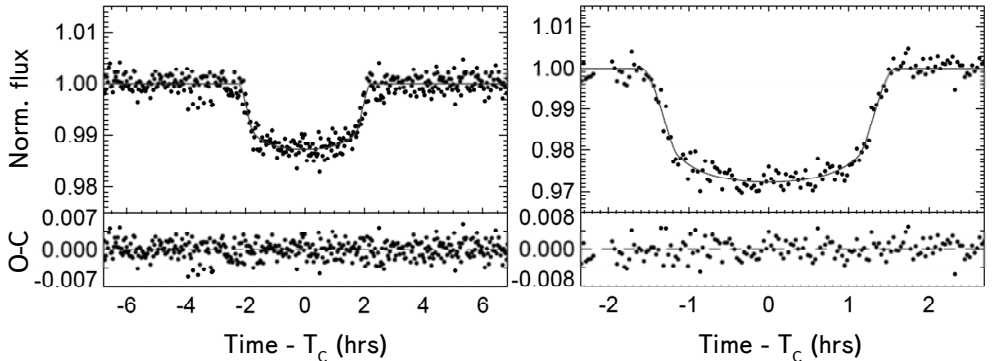


Fig.2. Left: HAT-P-33b observational and theoretical light curves using TESS sector 45 data; Right: The observational light curve of HAT-P-32b from this study in the V filter and the theoretical light curve.

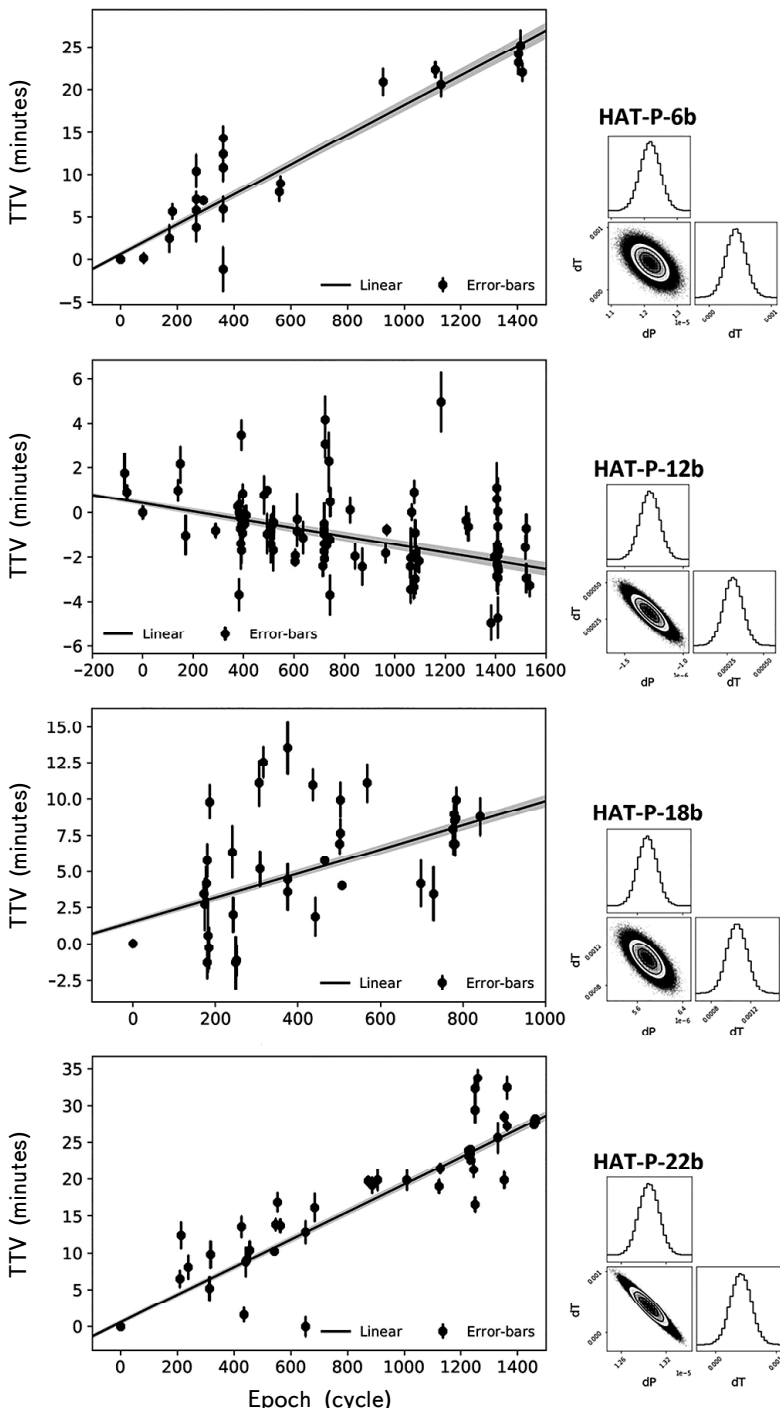


Fig.3. The TTV diagrams of seven studied exoplanets with the linear fit on the data points and posterior distributions for the fitted parameters using MCMC (dT and dP).

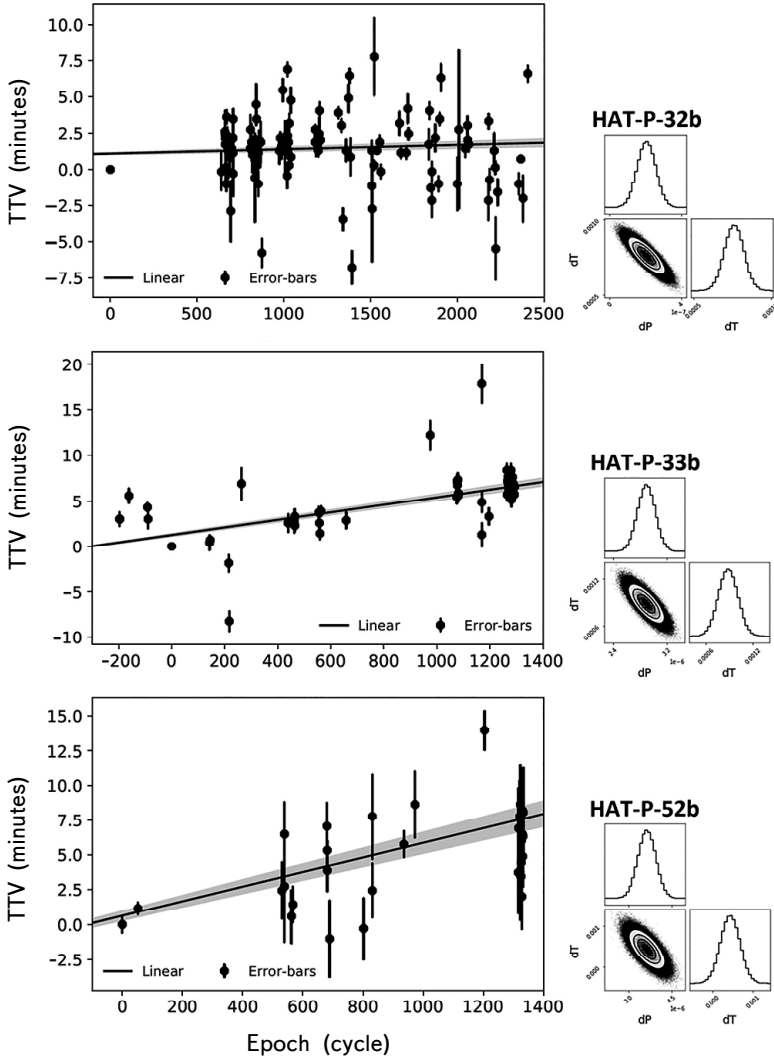


Fig.3. (The end).

probability distributions of the coefficients (100 walkers, 10000 step number, and 1000 burn-in) using the Pymc3 package in Python [13]. Fig.3 shows all TTV-diagrams of studied exoplanets and also displays the posterior distributions for the fitted parameters using the MCMC method (dT and dP).

3. Refined transit ephemeris. Follow-up observations of known transiting exoplanets, either with photometry or high-resolution spectroscopy, are an important issue. Accordingly, a growing quantity of this data provides the refined physical planetary properties, formation, and evolution processes of these exoplanets. Since the orbital ephemeris of exoplanets demonstrates their places in their orbits,

refinement of the exoplanet's ephemeris would be a key factor for the prediction of future transit events.

Based on the reference ephemeris for each exoplanet, epochs, and O-Cs are calculated. According to extracted mid-transit times, we can compute a new ephemeris by a well-known linear relation (1),

$$T_c = T_0 + E \times P, \quad (1)$$

where T_0 is considered as the reference mid-transit time, P and E are the orbital period and the number of epochs passed since T_0 , respectively. New ephemeris and reference ephemeris for exoplanets are given in Table 4.

Table 4

**THE NEW EPHEMERIS DERIVED BY A LINEAR FIT ON THE TTV
DIAGRAM OF EACH EXOPLANET AND REFERENCE EPHEMERIS
FOR COMPUTING EPOCHS AND THE TTV VALUES**

Exoplanet	New ephemeris (BJD_{TDB})	Reference ephemeris (BJD_{TDB})
HAT-P-6b	$2454035.6769526(3) + 3.85300(15)E$	$2454035.67652(28) + 3.852985(5)E$ [14]
HAT-P-12b	$2454419.19585(6) + 3.21305852(8)E$	$2454419.19556(20) + 3.2130598(21)E$ [15]
HAT-P-18b	$2454715.022802(97) + 5.5080288(2)E$	$2454715.02174(20) + 5.508023(6)E$ [16]
HAT-P-22b	$2454930.22043(16) + 3.2122330(1)E$	$2454930.22001(25) + 3.212220(9)E$ [17]
HAT-P-32b	$2454420.44713(6) + 2.15000821(5)E$	$2454420.44637(9) + 2.150008(1)E$ [16]
HAT-P-33b	$2455110.92683(12) + 3.4744769(1)E$	$2455110.92595(22) + 3.474474(1)E$ [16]
HAT-P-52b	$2455852.10370(23) + 2.7535989(3)E$	$2455852.10326(41) + 2.7535953(94)E$ [18]

3.1. *HAT-P-6b*. The exoplanet HAT-P-6b is a "hot Jupiter" with a radius of $1.33 \pm 0.06 R_J$ and a mass of $1.06 \pm 0.12 M_J$ [14], which was based on the primary transit method's results. According to a report by [14] on the characteristics of the planet and its host star, $e=0.046 \pm 0.031$ indicates that the planet's orbit is almost circular. Transit light curves for this exoplanet and refitted available photometry data with their new and literature mid-transit times collected in [19]. The discovery of these objects was announced in the study [14]. A revised orbital period and mid-transit time for this exoplanet were also updated by [20].

We collected the high-quality mid-transit times that were previously published in the literature, and the mid-transit times resulted from the modeling of ETD light curves for plotting an updated TTV diagram. We extracted a total of six mid-transit times from our observations and 13 mid-transit from ETD. We note that this exoplanet has not had TESS data.

3.2. *HAT-P-12b*. In [15] the transit method is used to discover the exoplanet HAT-P-12b, which orbits a dwarf star. According to the results of the discovery paper, HAT-P-12b is one of the least massive gas giant planets that was

Table 5

TRANSIT TIMES OF HAT-P-6b

T_c (BJD _{TDB})	Error	Epoch	O-C	Ref./ETD	Observer	T_c (BJD _{TDB})	Error	Epoch	O-C	Ref./ETD	Observer
2454035.67648	0.00027	0	0.0000	[19]		2455160.75292	0.00034	292	0.0048	KPNO 2.1m	
2454035.67652	0.00028	0	0.0000	[14]		2455430.45630	0.00180	362	-0.0008	[20]	
2454347.76839	0.00042	81	0.0001	[19]		2455430.46118	0.00100	362	0.0041	R.Dřevěný	
2454698.39160	0.00110	172	0.0017	[19]		2455430.46570	0.00130	362	0.0086	TRESCA	
2454740.77668	0.00063	183	0.0039	UDEM		2455430.46701	0.00100	362	0.0099	P.Véres	
2455064.42616	0.00119	267	0.0026	L.Brát		2456193.35362	0.00077	560	0.0055	Poddaný, Moudrá	
2455064.42751	0.00089	267	0.0040	J.Trnka, M.Klos		2456208.76626	0.00063	564	0.0062	J.Garlitz	
2455064.42843	0.00061	267	0.0049	Brát et al.		2457603.55511	0.00111	926	0.0145	J.L.Salto	
2455064.43067	0.00134	267	0.0072	R.Dřevěný, T.Kalisch		2459495.37153	0.00076	1417	0.0153	M.Raetz	

Table 6

TRANSIT TIMES OF HAT-P-18b

T_c (BJD _{TDB})	Error	Epoch	O-C	Ref./ETD	Observer	T_c (BJD _{TDB})	Error	Epoch	O-C	Ref./ETD	Observer
2454715.02174	0.00020	0	0.0000	[29]		2456455.56573	0.00075	316	0.0087	R.Naves	
2455662.40408	0.00054	172	0.0024	V.P.Hentunen		2456780.53283	0.00089	375	0.0025	F.G.Horta	
2455673.41967	0.00124	174	0.0019	[31]		2456780.53350	0.00073	375	0.0031	CAAT	
2455695.45273	0.00081	178	0.0029	A.Ayiomamitis		2456780.53981	0.00128	375	0.0094	A.Carreno	
2455706.46499	0.00077	180	-0.0009	C.Lopresti		2457116.52736	0.00073	436	0.0076	J.Gonzalez	
2455706.46993	0.00080	180	0.0040	[31]		2457149.56917	0.00092	442	0.0013	M.Deldem	
2455717.48233	0.00177	182	0.0004	A.L.Marrero		2457276.25646	0.00010	465	0.0040	[35]	
2455728.49780	0.00100	184	-0.0002	V.Benishek		2457474.54607	0.00046	501	0.0048	Signoret, Pioppa	
2455739.52081	0.00080	186	0.0068	F.C.Pecharromán		2457485.56256	0.00067	503	0.0053	Molina, Sureda	
2456042.45973	0.00124	241	0.0044	F.G.Horta		2457485.56424	0.00084	503	0.0069	D.Molina	
2456053.47276	0.00084	243	0.0014	[31]		2457507.59220	0.00019	507	0.0028	[32]	
2456086.51856	0.00125	249	-0.0009	[31]		2457843.58653	0.00090	568	0.0077	Scaggiante, Zardin	
2456097.53468	0.00074	251	-0.0008	T.Scarmato		2458559.62466	0.00111	698	0.0029	S.Dufoer	
2456400.48452	0.00108	306	0.0077	V.Popov		2458730.37292	0.00129	729	0.0024	B.Andreas	
2456411.49638	0.00084	308	0.0036	[31]		2459352.78320	0.00090	842	0.0061	[33]	

found until its discovery and is an exoplanet of the sub-Saturn type. The J band photometry study by [21] of this exoplanet obtained the precise mid-transit time to constrain the transit-time variations of the HAT-P-12b system. Lee et al. [22] observed three new transit light curves of HAT-P-12b, and with existing literature data, they came up with an improved ephemeris. Lee et al. [22] also refined the absolute physical properties of the star-planet system. Sada et al. [23] updated the ephemeris of HAT-P-12b according to six transits for this system by applying a least-squares linear fit to all available transit times. According to their results, no long-term TTVs were apparent. Mallonn et al. [24] studied HATP-12b in bands V and I to investigate the transmission spectrum of this system. Mallonn et al. [24] observed 23 new photometric transit light curves, and analysis showed no indication of star-spot influence on the calculated transit parameters. Alexoudi et al. [25] studied this exoplanet's atmosphere. In fact, the goal of this research was to specify an appropriate solution for future studies of other exoplanetary

Table 7

TRANSIT TIMES OF HAT-P-22b

T_e (BJD _{TDB})	Error	Epoch	O-C	Ref./ETD Observer	T_e (BJD _{TDB})	Error	Epoch	O-C	Ref./ETD Observer
2454930.22001	0.00025	0	0.0000	[17]	2457734.50182	0.00044	873	0.0137	V.P.Hentunen
2455601.57849	0.00079	209	0.0045	L.Brát	2457779.47248	0.00075	887	0.0133	D.Molina
2455614.43147	0.00126	213	0.0086	L.Brát	2457840.50512	0.00099	906	0.0138	M.Raetz
2455694.73397	0.00112	238	0.0056	S.Shadic, M.Butler	2458171.36382	0.00094	1009	0.0138	V.P.Hentunen
2455935.64851	0.00113	313	0.0036	S.Shadic	2458537.55631	0.00064	1123	0.0132	F.Campos
2455948.50056	0.00126	317	0.0068	G.Marino	2458550.40688	0.00053	1127	0.0149	J.Gaitan
2456298.63509	0.00098	426	0.0094	G.M.Schteinman	2458929.44872	0.00075	1245	0.0148	M.Theusner
2456327.53684	0.00066	435	0.0011	J.Lozano de Haro	2458945.50651	0.00071	1250	0.0115	M.Theusner
2456346.81517	0.00140	441	0.0061	[38]	2458945.51538	0.00117	1250	0.0204	A.Wunsche
2456356.45198	0.00059	444	0.0063	A.Ayiomamitis	2458945.51541	0.00055	1250	0.0204	Y.Jongen
2456391.78736	0.00088	455	0.0072	S.Shadic	2458945.51741	0.00106	1250	0.0224	M.Raetz
2456671.25040	0.00020	542	0.0071	[36]	2458974.42843	0.00083	1259	0.0234	Scaggiante, Zardin V.Perroud
2456687.31391	0.00055	547	0.0096	V.P.Hentunen	2459202.49043	0.00142	1330	0.0178	Scaggiante, Zardin M.Raetz
2456706.58936	0.00090	553	0.0117	[37]	2459276.36752	0.00079	1353	0.0138	Scaggiante, Zardin M.Bachschmidt
2456738.70941	0.00062	563	0.0095	[38]	2459276.37348	0.00044	1353	0.0198	Y.Jongen
2457024.58745	0.00090	652	0.0000	CAAT	2459308.49480	0.00049	1363	0.0189	
2457024.59630	0.00105	652	0.0089	R.N.Nogues	2459308.49839	0.00110	1363	0.0225	
2457127.38972	0.00132	684	0.0112	A.Valdera					

atmospheres. Spectroscopic observations using the Large Binocular Telescope (LBT) were done by [26] to obtain an atmosphere transmission spectrum of this exoplanet. They found no evidence of *Na* or *K* absorption features in the relatively flat transmission spectrum, which is in agreement with the HST transmission spectrum. Furthermore, Sariya et al. [27] included six new mid-transit times to determine a new ephemeris by a linear fit to a satisfactory level. Baxter et al. [28] also reported an infrared transmission photometry of HAT-P-12b with the other 48 exoplanets with the largest analysis of Spitzer/IRAC observations to study the influence of infrared photometry on atmospheric chemical properties.

We used mid-transit times conducted from the modeling of ETD light curves and TESS in association with data published in previous literature for plotting a new TTV diagram. We extracted 27 mid-transit times from ETD and 6 mid-transit times from sector 23 of TESS for HAT-P-12b.

3.3. *HAT-P-18b*. HAT-P-18b is a low-density Saturn-mass exoplanet orbiting a supersolar metallicity K2 dwarf star [29]. The discovery observations of this exoplanet have been made by [29] using the transit method to obtain the orbital and physical properties of the system. Authors [29] reported a non-zero ($e=0.084\pm0.048$) eccentricity for HAT-P-18b. Complementary new photometric observations of the full transit were also analyzed by [30] in order to independently estimate the parameters of the host star and HAT-P-18b. Seeliger et al. [31] performed the TTV study of HAT-P-18b with a limited number of existing high-

Table 9

TRANSIT TIMES OF HAT-P-52b

T_c (BJD _{TDB})	Error	Epoch	O-C	Ref./ETD	Observer	T_c (BJD _{TDB})	Error	Epoch	O-C	Ref./ETD	Observer
2455852.10326	0.00041	0	0.0000	[18]		2457727.30532	0.00049	681	0.0037	M.Bretton	
2455995.29102	0.00031	52	0.0008	[47]		2457749.32972	0.00193	689	-0.0007	[48]	
2457311.51042	0.00142	530	0.0017	[48]		2458060.48649	0.00155	802	-0.0002	[48]	
2457336.29302	0.00277	539	0.0019	[48]		2458140.34268	0.00137	831	0.0017	[48]	
2457336.29562	0.00164	539	0.0045	M.Bretton		2458140.34636	0.00214	831	0.0054	[48]	
2457399.62421	0.00133	562	0.0004	[48]		2458429.47243	0.00066	936	0.0040	P.Guerra	
2457413.39279	0.00091	567	0.0010	[48]		2458531.35748	0.00170	973	0.0060	M.Raetz	
2457724.55292	0.00121	680	0.0049	R.Naves		2459167.44167	0.00098	1204	0.0097	S.Gudmundsson	
2457727.30439	0.00107	681	0.0027	[48]		2459514.39070	0.00048	1330	0.0057	A.Wünsche	

over, Kokori et al. [35] derived the refined ephemeris from observations provided by the ExoClock network in combination with previous literature data.

For HAT-P-18b, we obtained seven mid-transit times from sectors 25 and 26 of TESS, and 21 mid-transit times from ETD.

3.4. HAT-P-22b. Bakos et al. [17] reported the discovery of the exoplanet HAT-P-22b. It is among the moderately massive and compact "hot Jupiters", orbiting a fairly metal-rich dwarf star with a $V=9.732$ magnitude. Hinse et al. [36] presented the first photometric follow-up observation of bright transiting exoplanets by using a defocusing technique. Following this, Baştürk et al. [37] performed a follow-up transit observation using a defocusing technique and they derived one complete transit and computed the mid-transit times for HAT-P-22b. The near-UV and optical photometric observations of HAT-P-22b were made by Turner et al. [38] to study the atmosphere of this exoplanet. Turner et al. [38] also refined the planetary parameters and ephemerides of HAT-P-22b "hot Jupiter". Accordingly, all derived parameters were in agreement with the discovery values by [17], and any non-spherical asymmetries were not seen in their data.

In order to plot a TTV diagram for this exoplanet, we extracted 30 and 14 mid-transit times resulting from the modeling of ETD and TESS light curves (sectors 21 and 48), respectively, as well as data from previous publications.

3.5. HAT-P-32b. The planet HAT-P-32b was discovered by the HATNet survey in 2011 and it is a "hot Jupiter" exoplanet orbiting a late-F-early-G dwarf star with $V=11.289$ magnitude. In this discovery, radial velocity measurements were taken with High-Resolution Echelle Spectrometer and transit model [39] was used in order to describe the HATNet photometry [16]. Sada et al. [21] presented a JH-band photometry observation of HAT-P-32b and extracted precise mid-transit times. Sada et al. [21] declared that HAT-P-32b system parameters were in agreement with those reported in the [16] study and derive a period of this exoplanet with improved uncertainty. Following this, Gibson et al. [40] reported

Table 11

TRANSIT TIMES OF HAT-P-33b

T_e (BJD _{TD_B})	Error	Epoch	O-C	Ref./ETD Observer	T_e (BJD _{TD_B})	Error	Epoch	O-C	Ref./ETD Observer
2454429.93117	0.00055	-196	0.0021	[16]	2456723.08352	0.00047	464	0.0016	[44]
2454551.53949	0.00058	-161	0.0039	[16]	2456723.08417	0.00059	464	0.0023	[44]
2454794.75180	0.00037	-91	0.0030	[16]	2457039.26162	0.00046	555	0.0026	[44]
2454801.69988	0.00074	-89	0.0021	[16]	2457046.20981	0.00046	557	0.0018	[44]
2455110.92595	0.00022	0	0.0000	[16]	2457053.15793	0.00047	559	0.0010	[44]
2455607.77606	0.00060	143	0.0003	[16]	2457067.05749	0.00043	563	0.0027	[44]
2455614.72513	0.00036	145	0.0005	[16]	2457397.13183	0.00066	658	0.0020	[44]
2455857.93657	0.00067	215	-0.0013	S.Shadick	2458498.54660	0.00113	975	0.0085	P.Guerra
2455864.88110	0.00078	217	-0.0057	S.Shadick	2459172.58691	0.00093	1169	0.0009	V.Ferrando
2456024.71746	0.00120	263	0.0048	[46]	2459172.58950	0.00078	1169	0.0034	Y.Jongen
2456636.22181	0.00072	439	0.0018	[44]	2459172.59843	0.00148	1169	0.0124	A.Wünsche
2456716.13465	0.00069	462	0.0017	[44]	2459266.39915	0.00068	1196	0.0023	M.Raetz
2456716.13498	0.00065	462	0.0020	[44]					

two primary transits of HAT-P-32b during Gemini-North Gemini Multi-Object Spectrograph observations. They used white light curve analysis in order to refine the parameters of this exoplanet and derive new ephemeris. Seeliger et al. [41] updated the system properties by analyzing the results of 45 transit observations, which were observed by using the young exoplanet transit initiative (YETI) network. Moreover, Seeliger et al. [41] studied the TTV diagram to investigate the existence of an additional planet in the HT-P-32b system. Wang et al. [42] performed a global fit for the HAT-P-32b system based on their new photometric observations and previously published RV data in order to update the system parameters. Wang et al. [42] also analyzed the TTV diagram for this system and according to the results, there was no significant TTV signals. Some follow-up high-quality observations of this exoplanet were done with small observatories operated by citizen scientists in 2020 [43].

The accurate mid-transit times for HAT-P-32b were obtained from the available data for plotting an updated TTV diagram. We extracted a total of five and 72 mid-transit times from our observations and the ETD, respectively.

3.6. HAT-P-33b. The planet HAT-P-33b was among the first exoplanets discovered by the HATNet survey in 2011 and was confirmed by high-precision photometry and additional radial velocity measurements [16]. HATP-33b is an inflated hot Jupiter orbiting a late-F dwarf star with a short orbital period. Authors reported that HAT-P-33b has a radius of $\sim 1.7R_J$, which is among one of the largest measured radius for all transiting exoplanets. HAT-P-33b also has an equilibrium temperature of more than 1600 K, which is the result of the high luminosity of its host star. The TTV study of HAT-P-33b was analyzed by the transiting exoplanet monitoring project (TEMP) in [44]. Wang et al. [44] refined HAT-

P-33b orbital ephemerides and the system parameters through R-band photometric observations. Furthermore, the extended radial velocity measurements of this planet have been made by [45]. Their obtained transit parameters were consistent with the resulting parameters from [16], but smaller values for the ingress/egress duration, and the planet to star radius ratio (R_p/R_*) were deduced. These differences were because of derived complete light curves, which led to shorter and shallower transit shapes. However, they found no sign of anomalies in the TTV diagram. Turner et al. [46] performed additional follow-up ground-based photometric observations to confirm the HAT-P-33b planetary parameters through TEP modeling methods. Turner et al. [46] used a weighted linear least-squares analysis to update the reference ephemeris for this planet. Moreover, they found that the *R*-band transit depth in HAT-P-33b is larger than its discovery value [16] when discussing the variation in planetary radius against wavelength. Photometric data revealed no evidence of star-spot for this exoplanet.

We used the mid-transit times collected from the modeling of ETD and TESS light curves to prepare a new TTV diagram for HAT-P-33b. For this exoplanet, 30 mid-transit times from TESS sectors 20, 44, 45, 46, and 47 were extracted, also with seven mid-transit times from ETD observations.

3.7. *HAT-P-52b*. HAT-P-52b is a short-period gas-giant "hot Jupiter" discovered and characterized in 2015 by the transit method [18]. Wang et al. [47] reported new photometric light curves for HAT-P-52b and refined this system's parameters by analyzing their light curves, previous photometric, and Doppler velocimetric data. Wang et al. [47] also performed the TTV study for HAT-P-52b and their results represented no significant trend in the TTV diagram and the measured mid-transit time was consistent with their updated linear ephemerides.

We plotted the updated TTV diagram based on the seven midtransit times from the modeling of ETD and 10 mid-transit times from the TESS light curves (sectors 43 and 44), along with published data in previous literature.

4. Summary and conclusion. We conducted a study on seven HATNet survey-selected transiting exoplanets and plotted the TTV diagrams. The goal of this study is to improve the planetary systems' reference ephemerides and to discuss the reasons for the period variations in these systems for future studies.

We have presented a new ephemeris for each of the seven exoplanets. For this purpose, we utilised the mid-transit times found in the literature as well as the light curves observed by ETD, TESS, and our ground-based observations. We used 11 mid-transit times from our observations in this study, which were made at eight observatories from 2018 to 2022.

Exofast-v1 was used to model the available light curves and extract the mid-transit times. We used the MCMC method to plot new TTV diagrams and refine

exoplanets' ephemeris. The TTV diagrams show the orbital periods of exoplanets HAT-P-6b, HAT-P-18b, HAT-P-22b, HAT-P-32b, HAT-P-33b, and HAT-P-52b are increasing, whereas exoplanet HAT-P-12b has a declining tendency. It is probable that the six exoplanets' orbital periods increased since their ephemeris accuracy has become inaccurate over time.

According to the new ephemeris for exoplanet HAT-P-6b, it seems that the uncertainties of t and P should be more carefully considered in future investigations and observations.

Acknowledgments. We made use of the ETD data for this investigation. ETD is maintained by the Czech Astronomical Society (CAS), an old astronomical organization in the Czech Republic with more than hundreds of members (amateur and professional astronomers included).

This work includes data from the TESS mission observations. Funding for the TESS mission is provided by the NASA Explorer Program.

¹ Astronomy Department of the Raderon AI Lab., BC., Burnaby, Canada, e-mail: poroatila@gmail.com

² BSN Project, Transiting Exoplanets Department, Tehran, Iran

³ Department of Chemistry, Faculty of Science, University of Guilan, Rasht, Iran

⁴ Observatoire de Vaison-La-Romaine, Departementale 51, 84110 Vaison-La-Romaine, France

⁵ Observatoire des Baronnies Provençales, Route de Nyons, F-05150 Moydans, France

⁶ Observatorio Montcabrer, Cabrils, Spain

⁷ Observatori Astronòmic Albanyà, Camí de Bassegoda S/N, Albanyà E-17733, Girona, Spain

⁸ University of Siena - Astronomical Observatory, Via Roma 56, 53100 Siena, Italy

⁹ British Astronomical Association, 25 Farringdon Street, London EC4A 4AB, England

¹⁰Czech Astronomical Society, Fričova 298, 251 65 Ondřejov, Czech Republic

¹¹Taurus Hill Observatory, 79480 Varkaus, Finland

ОБНОВЛЕНИЯ ЭФЕМЕРИД ДЛЯ СЕМИ ВЫБРАННЫХ ТРАНЗИТИРУЮЩИХ ЭКЗОПЛАНЕТ ОБЗОРА HATNet

А.ПОРО¹, Ф.А.ФАРАХАНИ², Э.ДЖАХАНГИРИ², А.САРОСТАД²,
 М.ГОЗАРАНДИ², М.ХАГГОУ^{2,3}, Ф.АБОЛХАССАНИ², А.ФАХРАБАДИ²,
 Ю.ЙОНГЕН⁴, А.ВЮНШЕ⁵, Р.НАВЕС⁶, П.ГУЭРРА⁷, А.МАРКИНИ⁸,
 М.СОЛСБЕРИ⁹, Р.ЭРЕНБЕРГЕР¹⁰, В.П.ХЕНТУНЕН¹¹

Уточнены эфемериды семи транзитирующих экзопланет HAT-P-6b, HAT-P-12b, HAT-P-18b, HAT-P-22b, HAT-P-32b, HAT-P33b и HAT-P-52b. В восьми обсерваториях наблюдено 11 транзитов в различных фильтрах для HAT-P-6b и HAT-P-32b. Также были проанализированы наблюдения базы данных транзитов экзопланет (ETD) для каждой из семи экзопланет, а кривые блеска пяти систем были исследованы с использованием данных космического телескопа TESS. Мы использовали Exofast-v1 для моделирования этих наземных и космических кривых блеска и оценки времени середины транзита. В общем получены 11, 175 и 67 времен середины транзита для этих семи экзопланет из наших наблюдений, ETD и TESS данных, соответственно, а также 155 времен середины транзита из литературы. Составлены диаграммы вариации времени транзита (TTV) для каждой из них, используя полученные времена середины транзита, а также те, которые были найдены в литературе. Затем линейные эфемериды систем были уточнены и улучшены с использованием метода Марковской цепи Монте-Карло (МCMC). Все изученные экзопланеты, за исключением системы HAT-P-12b, показали тенденцию увеличения орбитального периода на диаграммах TTV.

Ключевые слова: *планетарные системы - планеты и спутники*

REFERENCES

1. *M.Mayor, D.Queloz*, Nature, **378**, 355, 1995.
2. *S.Gunther, E.F.Guinan*, AAS, 2021.
3. *J.J.Fortney, R.I.Dawson, T.D.Komacek*, Journal of Geophysical Research (Planets), **126**, e06629, 2021.
4. *D.Charbonneau, T.M.Brown, D.W.Latham et al.*, Astrophys. J., **529**, L45, 2000.
5. *S.Hoyer, M.López-Morales, P.Rojo et al.*, Mon. Not. Roy. Astron. Soc., **434**, 46, 2013.
6. *S.R.Kane, S.Mahadevan, K. von Braun et al.*, Publ. Astron. Soc. Pacif., **121**,

- 1386, 2009.
7. *G.R.Ricker, J.N.Winn, R.Vanderspek et al.*, Proc. SPIE, **9143**, 914320, 2014.
 8. *R.L.Akeson, X.Chen, D.Ciardì et al.*, Publ. Astron. Soc. Pacif., **125**, 989, 2013.
 9. *S.Poddaný, L.Brát, O.Pejcha*, New Astron., **15**, 297, 2010.
 10. Astropy Collaboration, *T.P.Robitaille, E.J.Tollerud et al.*, Astron. Astrophys., **558**, A33, 2013.
 11. *K.A.Collins, J.F.Kielkopf, K.G.Stassun et al.*, Astron. J., **153**, 77, 2017.
 12. *J.Eastman, B.S.Gaudi, E.Agol*, Publ. Astron. Soc. Pacif., **125**, 83, 2013.
 13. *J.Salvatier, T.V.Wieckiä, C.Fonnesbeck*, Astrophysics Source Code Library, 2016.
 14. *R.W.Noyes, G.Á.Bakos, G.Torres et al.*, Astrophys. J., **673**, L79, 2008.
 15. *J.D.Hartman, G.Á.Bakos, G.Torres et al.*, Astrophys. J., **706**, 785, 2009.
 16. *J.D.Hartman, G.Á.Bakos, G.Torres et al.*, Astrophys. J., **742**, 59, 2011.
 17. *G.Á.Bakos, J.Hartman, G.Torres et al.*, Astrophys. J., **742**, 116, 2011.
 18. *J.D.Hartman, W.Bhatti, G.Á.Bakos et al.*, Astron. J., **150**, 168, 2015.
 19. *G.M.Szabo, O.Haja, K.Szatmary et al.*, IBVS, **5919**, 1, 2010.
 20. *G.Hébrard, D.Ehrenreich, F.Bouchy et al.*, Astron. Astrophys., **527**, L11, 2011.
 21. *P.V.Sada, D.Deming, D.E.Jennings et al.*, Publ. Astron. Soc. Pacif., **124**, 212, 2012.
 22. *J.W.Lee, J.-H.Youn, S.-L.Kim et al.*, Astron. J., **143**, 95, 2012.
 23. *P.V.Sada, F.G.Ramón-Fox*, Publ. Astron. Soc. Pacif., **128**, 024402, 2016.
 24. *M.Mallonn, V.Nascimbeni, J.Weingrill et al.*, Astron. Astrophys., **583**, A138, 2015.
 25. *X.Alexoudi, M.Mallonn, C.von Essen et al.*, Astron. Astrophys., **620**, A142, 2018.
 26. *F.Yan, N.Espinoza, K.Molaverdikhani et al.*, Astron. Astrophys., **642**, A98, 2020.
 27. *D.P.Sariya, I.-G.Jiang, L.-H.Su et al.*, Research in Astron. Astrophys., **21**, 097, 2021.
 28. *C.Baxter, J.-M.Désert, S.-M.Tsai et al.*, Astron. Astrophys., **648**, A127, 2021.
 29. *J.D.Hartman, G.Á.Bakos, B.Sato et al.*, Astrophys. J., **726**, 52, 2011.
 30. *M.Esposito, E.Covino, L.Mancini et al.*, Astron. Astrophys., **564**, L13, 2014.
 31. *M.Seeliger, M.Kitze, R.Errmann et al.*, Mon. Not. Roy. Astron. Soc., **451**, 4060, 2015.
 32. *J.Kirk, P.J.Wheatley, T.Louden et al.*, Mon. Not. Roy. Astron. Soc., **468**, 3907, 2017.
 33. *B.Edwards, C.Ho, H.Osborne et al.*, Astronomy: Theory, Observations and Methods, **2**, 25, 2021.
 34. *K.Paragas, S.Vissapragada, H.A.Knutson et al.*, Astrophys. J., **909**, L10, 2021.
 35. *A.Kokori, A.Tsiaras, B.Edwards et al.*, ApJS, **258**, 40, 2022.
 36. *T.C.Hinse, W.Han, J.-N.Yoon et al.*, Astron. Space Sci., **32**, 21, 2015.
 37. *Ö.Baştürk, T.C.Hinse, İ.Özavcı et al.*, Living Together: Planets, Host Stars and Binaries, **496**, 370, 2015.
 38. *J.D.Turner, K.A.Pearson, L.I.Biddle et al.*, Mon. Not. Roy. Astron. Soc., **459**, 789, 2016.
 39. *K.Mandel, E.Agol*, Astrophys. J., **580**, L171, 2002. doi:10.1086/345520.

40. *N.P.Gibson, S.Aigrain, J.K.Barstow et al.*, Mon. Not. Roy. Astron. Soc., **436**, 2974, 2013.
41. *M.Seeliger, D.Dimitrov, D.Kjurkchieva et al.*, Mon. Not. Roy. Astron. Soc., **441**, 304, 2014.
42. *Y.-H.Wang, S.Wang, T.C.Hinse et al.*, Astron. J., **157**, 82, 2019.
43. *R.T.Zellem, K.A.Pearson, E.Blasier et al.*, Publ. Astron. Soc. Pacif., **132**, 054401, 2020.
44. *Y.-H.Wang, S.Wang, H.-G.Liu et al.*, Astron. J., **154**, 49, 2017.
45. *H.A.Knutson, B.J.Fulton, B.T.Montet et al.*, Astrophys. J., **785**, 126, 2014.
46. *J.D.Turner, R.M.Leiter, L.I.Biddle et al.*, Mon. Not. Roy. Astron. Soc., **472**, 3871, 2017.
47. *X.-Y.Wang, Y.-H.Wang, S.Wang et al.*, ApJS, **255**, 15, 2021.
48. *M.Mallonn, C. von Essen, E.Herrero et al.*, Astron. Astrophys., **622**, A81, 2019.

АСТРОФИЗИКА

ТОМ 66

АВГУСТ, 2023

ВЫПУСК 3

DOI: 10.54503/0571-7132-2023.66.3-373

АКТИВНОСТЬ МОЛОДОЙ ЗВЕЗДЫ EPIC 204376071 ИЗ АССОЦИАЦИИ UPPER SCO

И.С.САВАНОВ

Поступила 19 апреля 2023

Принята к печати 18 августа 2023

По наблюдениям миссии K2 космического телескопа Кеплер выполнено исследование активности EPIC 204376071-молодого объекта, члена ассоциации Upper Sco с возрастом 11 ± 3 млн лет, кривая блеска которого обладает единичным затмением суточной продолжительности с глубиной около 80%. EPIC 204376071 является маломассивным M-карликом с массой $0.16 M_{\odot}$. По наблюдениям кампании C15 миссии K2 мы уточнили период вращения и амплитуду переменности блеска звезды, а также по стандартной методике оценили величину параметра запятненности A в абсолютной мере. Величина периода вращения звезды P равна 1.6270 ± 0.030 сут. Площадь пятен на поверхности EPIC 204376071 превосходит максимальную площадь пятен на Солнце и составляет величину порядка 7900 м.д.п. Представлены результаты восстановления температурных неоднородностей на поверхности EPIC 204376071. На построенной карте хорошо различимы две холодные области, разделенные по долготе примерно на 150° . Для оценки свойств вспышечной активности EPIC 204376071 была рассмотрена одна наиболее достоверная вспышка с амплитудой блеска около 4%. Измеренная относительная энергия вспышки RE составила 212 с. Вычислена энергия вспышки E_g оказалась равной $1.1 \cdot 10^{34}$ эрг ($\log E_g = 34.05$). Соответствующая ей вероятная величина массы коронального выброса может достигать $4.1 \cdot 10^{20}$ г. Рассмотрены литературные сведения о возможной природе единичного затмения суточной продолжительности с глубиной около 80% на кривой блеска EPIC 204376071.

Ключевые слова: звезды: активность: пятна: фотометрия: переменность: вспышки: затмения

1. *Введение.* В настоящее время, благодаря высокоточным квазинепрерывным фотометрическим наблюдениям с космическими телескопами, у широкого круга звезд стало возможным проведение исследований явления ослабления блеска (затмений), вызванных пылевой материей. К их числу, например, можно отнести объекты, получившие название дипперов (dippers) (см. [1] и ссылки в этой статье). Их затмения могут носить периодический, квазипериодический или даже непериодический характер. Длительность затмений может составлять несколько часов, а глубина доходить до 10-50%. Причиной затмений служит пылевое вещество, находящееся, например, у внутреннего края околозвездного диска или связанное с магнитосферой звезды. Как правило, большинство дипперов являются звездами спектрального класса M, для них характерно наличие избытка ИК излучения, многие из них принадлежат молодым ассоциациям Upper Scorpius и ρ Ophiuchus.

Уникальным объектом, на кривой блеска которого имеются свидетельства затмений, вызванных пылью, является объект KIC 8462852 (известный как звезда Бояджяна). В литературе имеются результаты многочисленных исследований (см., например ссылки в [2]), содержащих подробное обсуждение свойств объекта, периодичности затмений и проч. Основное отличие KIC 8462852 от дипперов состоит в том, что этот объект является звездой главной последовательности (ГП) спектрального класса F.

К числу других объектов (их список достаточно многочислен) с пылевыми затмениями можно отнести молодые звезды типа Т Тельца, объекты с возможными эзокометами (KIC 3542116, KIC 11084727 и др.), звезды с различной глубиной транзитов экзопланет, возможно имеющих пылевое окружение, уникальный белый карлик WD 1145+017 с затмениями глубиной около 1%, еще один уникальный объект 1SWASP J140747.93-394542.6 с затмением глубиной в 3^m и длительностью 45 сут и многие другие. Более подробные сведения об этих и других аналогичных объектах можно найти в [2] и в других статьях авторов.

В частности авторами [2] было обнаружено единичное затмение суточной продолжительности с глубиной около 80% у звезды EPIC 204376071 - молодого объекта - члена ассоциации Upper Sco. Цель нашего исследования заключается в изучении проявлений активности этой звезды.

2. EPIC 204376071 - молодая звезда - член ассоциации Upper Sco. В [2] опубликованы результаты анализа фотометрических наблюдений миссии Кеплер (K2) звезды EPIC 204376071 ($V=16^m.3$), принадлежащей ассоциации Upper Sco с возрастом 11 ± 3 млн лет, одной из самых молодых звездных ассоциаций. Молодость звезды подтверждается в [1,2] по ее кинематическим, спектральным и фотометрическим характеристикам, таким как быстрое вращение и значительная фотометрическая модуляция. Наблюдения объекта выполнялись миссией K2 в течение кампаний 2 (C2) и 15 (C15). В данных C15 авторы [2] обнаружили единичное событие значительного ослабления блеска EPIC 204376071 для даты 3168.5 BKJD (в шкале наблюдений миссии K2 BJD - 2454833) глубиной порядка 80% и продолжительностью около суток (рис.1а, с).

С учетом отсутствия аналогичного ослабления блеска в ходе кампании C2 и интервала времени между кампаниями C2 и C15 авторы [2] сделали заключение о величинах возможных интервалов периодов ослаблений блеска. Форма наблюдаемого явления ассиметрична, по длительности вход в ослабление происходил примерно в два раза быстрее, чем выход из него. В остальном изменения блеска характеризуются вращательной модуляцией с амплитудой около 1% и периодом около 1.6 сут (см. также [1]).

Согласно [2] масса звезды составляет $M=0.161\pm0.028$ массы Солнца. Объект отождествлен с источником Gaia EDR3 6243166527355588608, его параллакс составляет π (mas) = 7.1711 ± 0.0577 . На основе анализа кинематических свойств подтверждено, что EPIC 204376071 принадлежит ассоциации Upper Sco [2].

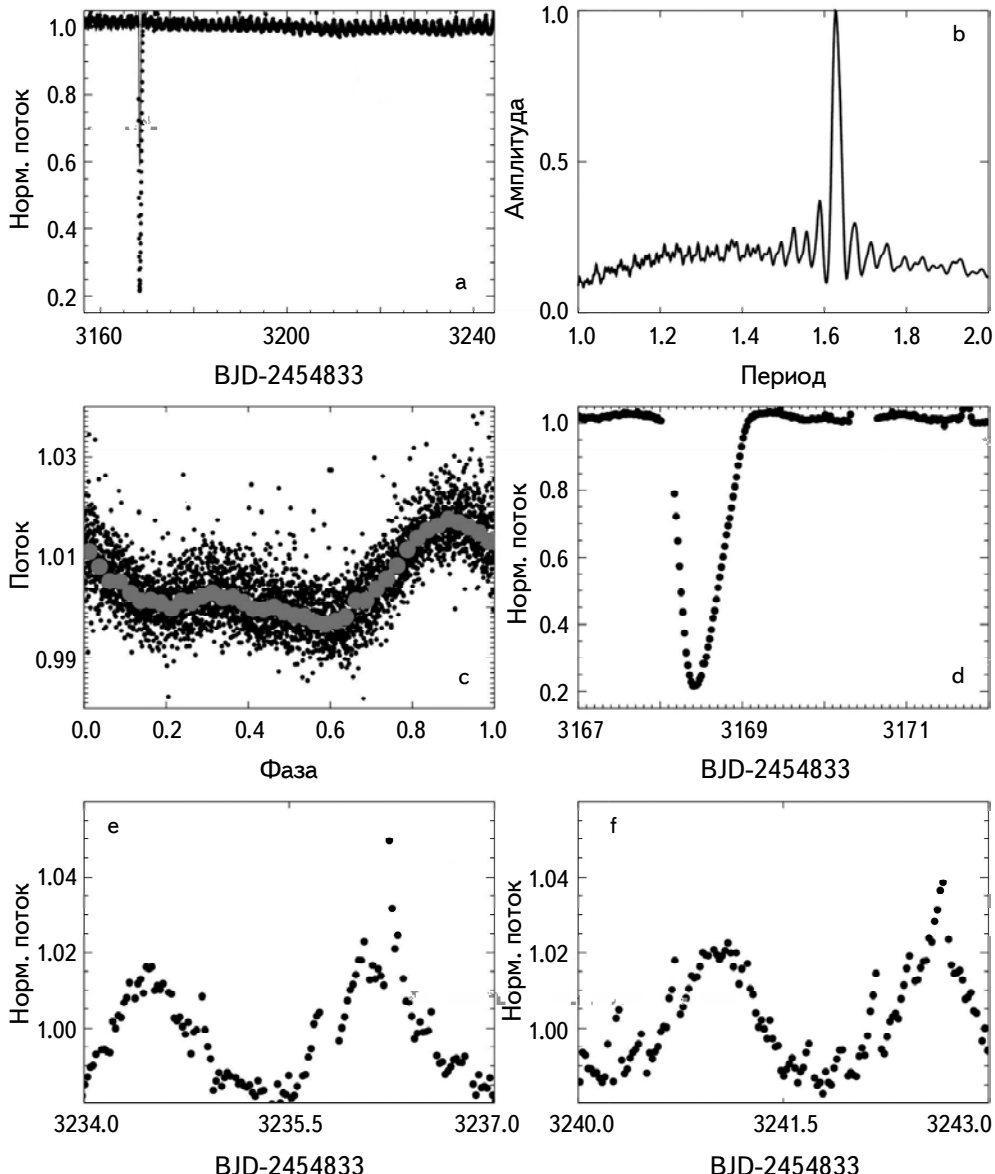


Рис.1. Кривая блеска для EPIC 204376071 (a), спектр мощности переменности блеска (b), фазовая диаграмма переменности блеска (светлые кружки соответствуют усредненным по бинам величинам) (c), суточное ослабление блеска (d), фрагменты кривой блеска (e,f). Данные приведены для наблюдений в кампании C15.

Эффективная температура звезды равна 2960 ± 75 К. Данные каталога Gaia EDR3 содержат более высокое значение оценки $T_{\text{эфф}} = 3861 \pm 450$ К. Отметим, что перечисленные нами свойства EPIC 204376071 приводятся согласно данным, указанным в [2] (табл.3) и в астрономической базе данных Simbad.

Как отмечалось выше, для EPIC 204376071 в архиве миссии Кеплер имеются данные 2-х кампаний наблюдений. Наша обработка была аналогична проводимой нами ранее для других объектов из архива космического телескопа Кеплер и подобна описанной в [3]. Наибольшее внимание мы уделили данным кампании C15, содержащим ослабление блеска и менее зашумленным, по сравнению с измерениями кампании C2. На рис.1а, б, с представлены: кривая блеска EPIC 204376071, соответствующий спектр мощности и фазовая диаграмма. Хорошо заметна периодическая модуляция блеска, обладающая заметной переменностью амплитуды. В течение сета наблюдений звезда не меняла свою активность. На шкале времени порядка длительности наблюдений в сете C15 форма фазовой кривой и положения максимумов и минимумов не претерпели изменений (рис.1с), что, вероятно, свидетельствует о сравнительно устойчивом положении холодных областей на поверхности звезды. Такая стабильная конфигурация пятен достаточно характерна для маломассивных, полностью конвективных звезд. EPIC 204376071 является маломассивным M-карликом ($0.16 M_{\odot}$) с радиусом $0.63 R_{\odot}$. Большой радиус по сравнению с характерным радиусом для звезды ГП с аналогичной массой, по мнению и оценкам [2], указывает на то, что вероятно звезда еще не достигла ГП. Примером может служить M4 карлик V374 Peg с массой $0.3 M_{\odot}$ и периодом 0.5 сут, для которого кривая блеска обладает малыми изменениями и остается практически стабильной на протяжении почти 16-и лет ([4]).

На построенных нами спектрах мощности имеется характерный пик, соответствующий величине периода вращения звезды $P = 1.627 \pm 0.030$ сут (погрешность оценена по полуширине пика). Авторами [1] была приведена совпадающая с полученной нами величина периода вращения EPIC 204376071 - 1.6268 сут.

Рассчитанные спектры мощности и вид фазовой кривой указывают на достаточно стабильный характер изменений блеска изучаемой звезды. Амплитуда переменности блеска составляет около 2% от уровня среднего блеска звезды. По стандартной методике (см. в [3]) нами были оценены величины параметра запятненности EPIC 204376071, которые достигают 5.5% от площади ее поверхности. Принимая оценку радиуса звезды $R = 0.631 \pm 0.042$ радиусов Солнца из [2], можно получить величину площади поверхности запятненности в абсолютной мере (в миллионных долях видимой полусферы Солнца, м.д.п.). На Солнце средние по размерам пятна имеют площадь

10-200 м.д.п. (детали см. в [5]). Площадь пятен на поверхности EPIC 204376071 превосходит максимальную площадь пятен на Солнце и составляет величину порядка 7900 м.д.п.

3. Температурные карты поверхности EPIC 204376071. Дальнейший анализ фотометрической переменности звезды был выполнен нами с фотометрическим периодом $P = 1.6270$ сут. Данные на фазовой кривой были разделены на 40 бинов, для каждого из которых были найдены средние величины. В каждом бине содержалось порядка 90-100 оценок блеска звезды.

Как и в наших предыдущих исследованиях карликов поздних спектральных классов, мы выполнили анализ кривой блеска с помощью программы iPH [6]. Программа решает обратную задачу восстановления температурных неоднородностей на поверхности звезды по кривой блеска в двухтемпературном приближении (интенсивность излучения от каждой элементарной площадки на поверхности звезды складывается из двух компонентов: фотосферы и холодного пятна). Полное описание программы, ее тесты представлены в [6]. Как указывалось выше, мы приняли температуру звезды равной 2960 К [2].

Авторами [7] методом доплеровского картирования были изучены пятна на поверхности двух холодных, полностью конвективных, M-карликов. Один из них, M4.5-карлик GJ791.2A, имеет температуру фотосферы $T_{\text{эфф}} = 3000$ К, сопоставимую с величиной для EPIC 204376071. По построенным доплеровским картам в [7] было получено, что температура пятен ниже температуры фотосферы на 300 К. Таким образом, в наших расчетах мы также приняли, что $T_{\text{spot}} = 2700$ К.

Согласно нашей методике, для каждой элементарной площадки размером $6^\circ \times 6^\circ$ на поверхности звезды был определен фактор заполнения f - доля поверхности элементарной площадки, занимаемой пятнами. На рис.2 представлены результаты восстановления температурных неоднородностей на поверхности EPIC 204376071. На рисунке приведены также наблюдаемая (усредненная

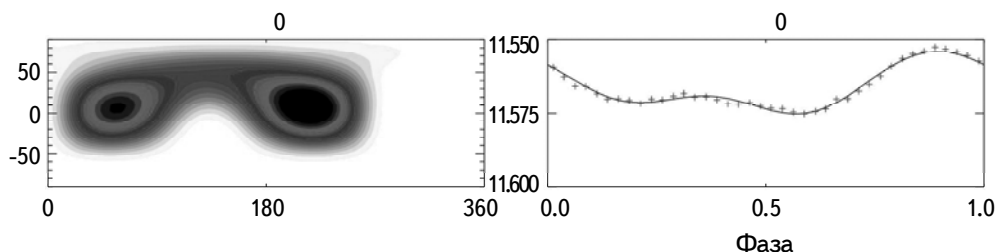


Рис.2. Результаты восстановления температурных неоднородностей на поверхности EPIC 204376071. Карты поверхности представлены в единой шкале, более темные области на рисунках соответствуют более высоким значениям факторов заполнения f . На этом же рисунке также приводятся наблюдаемая кривая блеска и теоретическая кривая блеска, построенные по восстановленной модели.

по бинам) и теоретическая (построенная по восстановленной модели) кривые блеска. Если на поверхностных картах имелись концентрации пятен на двух долготах, то их значения регистрировались нами, как две независимые активные долготы. Погрешность определений положений активных долгот составляет величину порядка около 0.06–0.08 в единицах фазы. Как отмечалось выше, кривая блеска EPIC 204376071 характеризуется наличием двух минимумов. В соответствии с этим, на построенной карте хорошо различимы две холодные области, разделенные по долготе примерно на 150° .

Как и в [2] величина угла i наклона оси вращения звезды к лучу зрения была принята равной 60° . Оказалось, в случае изменения величины параметра на 20° различия в картах не изменяют сделанных нами заключений о положении активных областей на поверхности звезды. Согласно нашим вычислениям (см. в [6] многочисленные тесты), построенные карты содержат преимущественно информацию о положении пятен по долготе, но не по широте. Заключения о наличии полярных пятен (как в [7] для GJ791.2A) мы сделать не можем.

4. *Вспышечная активность.* По мнению авторов [2] (рис.5 в их статье) на кривой блеска EPIC 204376071 присутствует ряд вспышек с амплитудой до 6%. Следует иметь в виду, что качество наблюдательного материала, полученного с продолжением миссии Кеплер K2, существенно ниже, чем для данных основной миссии. Нестабильное поведение космического телескопа приводит к появлению многочисленных артефактов на регистрируемых кривых блеска, которые, к сожалению, до конца не устраняются при редукции данных. В принципе, по форме многие артефакты существенно отличаются от характерной формы большинства вспышек (фаза возгорания, более плавная фаза затухания), но требуется осторожность при отборе явлений, похожих на вспышки.

На рис.1 приводятся два фрагмента кривой с артефактами, как вызванных возможно недостаточно точной редукцией данных, так и проявлением вероятных вспышек со структурой, характерной для вспышек звезд позднего спектрального класса – резкий подъем, пик, стадия затухания. В нашем исследовании мы ограничились рассмотрением одной наиболее достоверной вспышки, которая, несомненно, может дать представление о свойствах вспышечной активности EPIC 204376071. Амплитуда блеска вспышки составляет около 4%. Энергия излучения вспышки была вычислена нами по стандартной методике, принятой при анализе вспышечной активности звезд по наблюдениям с космическим телескопом Кеплер или миссией TESS (см. в [8,9]). Данная методика уже неоднократно использовалась для определений энергетики вспышек звезд по наблюдениям миссии TESS с учетом изменения полосы пропускания для

этой космической миссии - см., например, описание в [10]. Как и в [10], нами принималось, что вспышка характеризуется чернотельным излучением. Измеренная относительная энергия вспышки RE составила 212с. Вычисленная по формулам из [10] энергия вспышки E_{fl} оказалась равной - $1.1 \cdot 10^{34}$ эрг ($\log E_{\text{fl}} = 34.05$).

Результаты широкого круга исследований, включающих анализ свойств звездных вспышек, основанных на данных наблюдений с космическим телескопом TESS с июля 2018г. по октябрь 2020г., можно найти в [11]. Авторами [11] были проанализированы 60810 вспышек для 13478 звезд по наблюдениям TESS в секторах 1-30. В исследовании были рассмотрены объекты в диапазоне $T_{\text{эфф}}$ от 2500 К до 6500 К и с массами от 0.08 до 1.4 масс Солнца. Для сравнения с EPIC 204376071 укажем, что по данным [11] (рис.12) значения энергии вспышек для звезд с температурой около 3000 К лежат в диапазоне от $7 \cdot 10^{31}$ до $5 \cdot 10^{34}$ эрг. Найденная нами энергия вспышки для EPIC 204376071 выше средней, но в целом сопоставима с типичными максимальными величинами E_{fl} для M звезд с $T_{\text{эфф}} = 3000$ К.

Следуя идеи солнечно-звездной аналогии и на других звездах можно ожидать корональные выбросы массы СМЕ [10,12], которые могут проявляться в сопутствующих возмущениях плотности и скорости плазмы, ускорении энергичных частиц в областях ударов. Все эти факторы принимаются во внимание при изучении влияния СМЕ на экзопланеты и их атмосферы, но не исключена вероятность необходимости учета их влияния на малые тела экзопланетных систем (экзокометы и проч.) при условии совпадения направления СМЕ на объект. Планетарное влияние звездной активности СМЕ может варьироваться в зависимости от возраста звезды, ее активности, спектрального типа и орбитального расстояния планеты. Для оценки свойств СМЕ часто используется эмпирическая зависимость, связывающая энергию вспышки и массу СМЕ (см. подробнее в [10,12]). Применение зависимости к данным для EPIC 204376071 приводит к оценке, что для этой звезды вероятная величина массы СМЕ может достигать $4.1 \cdot 10^{20}$ г.

Для того, чтобы оценить величины максимально возможных масс СМЕ для самых холодных карликов, в [12] мы использовали данные [13] об энергиях супервспышек восьми карликов спектрального класса M. Энергии супервспышек этих объектов лежат в диапазоне величин $\log E_{\text{fl}}$ от 33.59 до 34.96. Возможно, что по энергии вспышка на EPIC 204376071 подобна супервспышкам объектов из [13]. Требуются дальнейшие наблюдения для подтверждения характеристик вспышечной активности EPIC 204376071. Масса соответствующих СМЕ у карликов из [13] в случае супервспышек может достигать до $2.2 \cdot 10^{20} - 1.5 \cdot 10^{20}$ г, что не только сопоставимо, но даже немного превосходит массы СМЕ звезд солнечного типа, установленные по средним

энергиям вспышек.

5. Заключение и обсуждение результатов. Авторы [2] сообщили об обнаружении значительного (на 80%) ослабления блеска молодой звезды EPIC 204376071 длительностью порядка суток. В остальном, кривая блеска объекта в течение интервала наблюдений с космическим телескопом Кеплер (миссия K2) длительностью в общей сложности около 160 сут во время кампаний C2 и C15 характеризуется изменениями вследствие вращательной модуляции, а также возможным наличием вспышек. EPIC 204376071 является маломассивным M-карликом ($0.16 M_{\odot}$) с радиусом $0.63 R_{\odot}$. Молодость звезды определяется ее принадлежностью к ассоциации Upper Scorpius с возрастом порядка 10 млн лет. Большой радиус по сравнению с характерным радиусом для звезды ГП с аналогичной массой указывает на то, что, вероятно, звезда еще сжимается и не достигла ГП. Период вращения $P = 1.6$ сут также соответствует предположению о молодости звезды.

По наблюдениям миссии K2 мы уточнили период вращения и амплитуду переменности блеска EPIC 204376071, а также по стандартной методике оценили величину параметра запятненности A в абсолютной мере. Из решения обратной задачи восстановления температурных неоднородностей звезды по усредненной кривой блеска получена карта поверхностных температурных неоднородностей. Для оценки свойств вспышечной активности EPIC 204376071 была рассмотрена одна наиболее достоверная вспышка. Амплитуда блеска вспышки составляет около 4%. Измеренная относительная энергия вспышки RE составила 212 с. Вычисленная энергия вспышки E_{fl} оказалась равной $1.1 \cdot 10^{34}$ эрг ($\log E_{fl} = 34.05$). По эмпирической зависимости, связывающей энергию вспышки и массу СМЕ, установлено, что для этой звезды вероятная величина массы СМЕ может достигать $4.1 \cdot 10^{20}$ г.

В [2] были исследованы два основных сценария проявления глубокого асимметричного затмения, подобного наблюдаемому в EPIC 204376071. В первом из них был рассмотрен пылевой диск около малого тела, вращающегося вокруг звезды. Диск наклонен к наблюдателю так, что в проекции он выглядит как эллипс. Параметры модели представлены в табл.4 в [2]. Возможные величины полуосей диска составляют 4.2 и 0.89 радиусов звезды, а наклон диска равен 22° . Масса диска равна $3 \cdot 10^{19}$ г, а масса малого тела, к которому принадлежит диск - 3 массы Юпитера. Во втором сценарии предлагался пылевой экран "неизвестного происхождения", возможно временного характера. В этой модели прозрачность экрана систематически уменьшается от резкой границы до противоположного края (см. рис.8 в [2]). По мнению авторов [2] обе модели достаточно хорошо описывают форму затмения (может быть, модель с диском несколько лучше). Возможность

существования кометного хвоста от малого тела в [2] была рассмотрена, но отвергнута по их мнению вследствие малого потока излучения (по сравнению с требуемым для формирования хвоста) от звезды со светимостью в $0.027 L_{\odot}$. Однако, принимая во внимание наличие высокой вспышечной активности звезды и сопутствующих СМЕ, не исключена необходимость дополнительного изучения этого вопроса (при условии подтверждения существования супервспышек, генерации СМЕ в требуемом направлении и проч.).

Поскольку EPIC 204376071 является членом ассоциации Upper Scorpions, для которой характерно большое число объектов, известных как дипперы, естественным является вопрос о том, не связано ли наблюдаемое явление ослабления блеска с проявлением природы диппера. В таком случае ослабление будет вызвано пылевой материей, находящейся вблизи радиуса коротации около звезды, однако в [2] были рассмотрены три возможных отличия EPIC 204376071 от остальных объектов - дипперов (см. подробности и соответствующие ссылки на литературу здесь и далее в [2]). Во-первых, для дипперов глубина ослабления блеска составляет всего 10-30%, возможным исключением является звезда HQ Tau, для которой глубина была сопоставима или превосходила величину для EPIC 204376071, а продолжительность затмения была более длительной. Во-вторых, активность дипперов, как правило, остается высокой в течение всего интервала наблюдений (десятки дней) и у них ослабления блеска наблюдаются гораздо чаще; правда, вопрос о возможности селекции наблюдений по частоте наблюдений до конца не решен. Наконец, в-третьих, большинство дипперов имеют ярко-выраженный избыток потока излучения в полосах WISE 3 и 4, тогда как EPIC 204376071 характеризуется слабой эмиссией в полосе WISE 3, а в полосе WISE 4 для объекта имеется лишь верхняя оценка потока.

Исследование EPIC 204376071 представляет интерес с точки зрения установления природы затмения блеска этого объекта. Остается открытым вопрос о характере затмевающего тела - это тело с эллипсообразной пылевой оболочкой, пылевой экран, экзокомета (если возможно образование ее хвоста вследствие супервспышек на звезде) или что-то еще? Необходимы новые наблюдения этого объекта, а также поиск звезд с аналогичными затмениями.

Исследование выполнено в рамках проекта "Исследование звезд с экзопланетами" по гранту Правительства РФ для проведения научных исследований, проводимых под руководством ведущих ученых (соглашение № 075-15-2019-1875, 075-15-2022-1109.).

ACTIVITY OF THE YOUNG STAR EPIC 204376071 FROM THE UPPER SCO ASSOCIATION

I.S.SAVANOV

Using the observations of the K2 mission of the Kepler Space Telescope we studied the activity of EPIC 204376071 - a young object in the Upper Sco association with the age of 11 ± 3 million years, whose light curve has a single occultation of daily duration with a depth of about 80%. EPIC 204376071 is a M-dwarf of mass $0.16 M_{\odot}$. On the base on the observations of the C15 campaign of the K2 mission we estimated the rotation period, amplitude of the variability of the brightness of the star and the spottedness parameter A in absolute measure using the standard method. The magnitude of the rotation period of the star P is 1.6270 ± 0.030 days. The area of spots on the surface of EPIC 204376071 exceeds the maximum area of spots on the Sun and is about 7900 MSH. The results of the restoration of temperature inhomogeneities on the surface of EPIC 204376071 are presented. Two cool regions separated in longitude by about 150° are clearly distinguishable on the constructed map. Characteristics stellar flare activity are estimated on the base of one of the most reliable flare. The flare amplitude is about 4%. The measured relative energy RE of the flare was 212 sec. The calculated energy of the flare E_{fl} equal to $1.1 \cdot 10^{34}$ erg ($\log E_{fl} = 34.05$). The corresponding probable value of the coronal mass ejection can reach $4.1 \cdot 10^{20}$ g. Possible explanations of a single occultation of 1-day duration with a depth of about 80% on the EPIC 204376071 light curve are discussed.

Keywords: *stars: activity: spots: photometry: variability: variability: flares: occultation*

ЛИТЕРАТУРА

1. *L.M.Rebull, J.R.Stauffer, A.M.Cody et al.*, Astron. J., **155**, 196, 2018.
2. *S.Rappaport, G.Zhou, A.Vanderburg et al.*, Mon. Not. Roy. Astron. Soc., **485**, 2681, 2019.
3. *I.S.Savanov*, Astrophysics, **64**, 178, 2021.
4. *K.Vida, L.Kriskovics, K.Olah et al.*, Astron. Astrophys., **590**, A11, 2016.
5. *Y.A.Nagovitsyn, A.A.Pevtsov*, Astrophys. J., **906**, id. 27, 2021.
6. *I.S.Savanov, K.G.Strassmeier*, Astron. Nachr., **329**, 364, 2008.
7. *J.R.Barnes, S.V.Jeffers, H.R.A.Jones et al.*, Astrophys. J., **812**, 42, 2015.

8. *S.Okamoto, Y.Notsu, H.Maebara et al.*, *Astrophys. J.*, **906**, 72, 2021.
9. *Z.-L.Tu, M.Yang, H.-F.Wang et al.*, *Astrophys. J. Suppl. Ser.*, **253**, 35 2021.
10. *M.N.Gunther, Z.Zhan, S.Seager*, *Astron. J.*, **159**, 60, 2020.
11. *Z.Yang, L.Zhang, G.Meng et al.*, *Astron. Astrophys.*, **669**, A15, 2023.
12. *I.S.Savanov*, *Astron. Lett.*, **46**, 831, 2020.
13. *H.-Y.Chang, C.-L.Lin, W.-H.Ip et al.*, *Astrophys. J.*, **867**, 78, 2018.

АСТРОФИЗИКА

ТОМ 66

АВГУСТ, 2023

ВЫПУСК 3

DOI: 10.54503/0571-7132-2023.66.3-385

PLANE SYMMETRIC STRING COSMOLOGICAL MODEL WITH ZERO MASS SCALAR FIELD IN $f(R)$ GRAVITY

KALPANA PAWAR¹, A.K.DABRE¹, PALLAVI MAKODE²

Received 23 March 2023

Accepted 18 August 2023

In this article, an anisotropic Locally Rotationally Symmetric (LRS) Bianchi type I metric in the presence of cloud string fluid and zero mass scalar field in reference to $f(R)$ gravity have been investigated. To obtain the deterministic solutions we assumed the weak field limit for a point-like source $f(R) = R^{3/2}$ and the very well-known expansion-shear scalar proportionality relation. Furthermore, some physical and kinematical parameters have been calculated to study the astrophysical consequences of obtained model, which shows a good resemblance to the recent observational data.

Keywords: *cosmic string: scalar field: Bianchi type I metric: $f(R)$ gravity*

1. Introduction. Observational evidence and measurements from high redshift supernovae observed by cosmologists [1-3] at various redshift ranges suggest that the universe is in its accelerating phase, and this acceleration is assumed to be the effect of dark energy, which is due to the universe's negative pressure. Two solutions have been brought forth to address this problem; one is to develop a viable dark energy model, and the other is to modify Einstein's theory of gravity. Among these non-Einsteinian theories, one of the theories is $f(R)$ gravity, this modification is one of the oldest and was originally proposed by Buchdahl [4]. Modified theories of gravitation received growing attention lately but the scientific curiosity of cosmologists for the universe gave them new inspiration to study the universe hugely in new ways. Despite the many shortcomings conferred to modified gravities, various cosmologist gave their tremendous efforts. Nojiri and Odintsov, [5] reconstructed cosmological methods i.e. inverse problems in view of cosmic time or e-folding in $f(R)$ gravity. Katore and Hatkar, [6] examined interacting as well as non-interacting scenarios of two fluids considering FRW space-time in $f(R)$ theory of gravity. Bahamonde et al., [7] studied modified teleparallel gravitational theories and derived the particular unification case of teleparallel equivalent to $f(R)$ gravitational theory which is invariant under local Lorentz transformation. Ferraro, [8] concisely reviewed the $f(R)$, and $f(T)$ gravity theories and showed some remarkable applications to cosmology and cosmic strings. De La Cruz-Dombriz and Dobado, [9] considered the possibility of

describing the current evolution of the universe, without the introduction of any cosmological constant or dark energy, by modifying the Einstein-Hilbert action. Nojiri and Odintsov, [10] suggested the new model of modified gravity which contains positive and negative powers of the curvature in which the Lagrangian appears to be $L = R + R^m + 1/R^n$ where m and n are positive numbers. Again Nojiri and Odintsov, [11] suggested two realistic $f(R)$ and one $f(G)$ modified gravities which are consistent with local tests and cosmological bounds. Guendelman and Herrera, [12] analyzed unification: emergent universe followed by inflation and dark epochs from multi-field theory. Capozziello et al., [13] considered the tree-level effective gravitational action of bosonic string theory coupled with the dilaton field. Bari and Bhattacharya, [14] presented the full treatment of scalar and vector cosmological perturbations in a non-singular bouncing universe in the context of metric $f(R)$ cosmology. Sadeghi et al., [15] studied some cosmological parameters in a logarithmic corrected $f(R)$ gravitational model with swampland conjectures.

The investigation of yet unsolved interacting fields in reference to modified gravitation theories assuming one of the fields is a massless scalar field is a basic attempt to study the unification of the quantum and gravitational theories. In recent years, there has been a lot of interest in the set of field equations that represent a zero-mass scalar field coupled with gravitational theories. Venkateswarlu et al. [16-18], Godani and Samanta [19], Singh et al. [20], Singh [21], Patra [22], Adhav et al. [23], Dixit et al. [24], Katore et al. [25], Cadoni and Franzin [26], Pawar et al., [27], are some of the authors who have vigorously studied interacting fluid with one matter content as a zero mass scalar field.

In accordance with the study of strings, these are widely receiving significant interest from researchers as they play an important role in explaining the early phase of cosmic evolution. Nojiri et al., [28] studied string-inspired models, inflation, bounce, and late-time evolution in reference to modified gravity. Freidel et al., [29] discussed the formulation and dynamics of string theory and looks for string solutions. Pawar et al. [30-32] have studied string-coupled cosmological models using Bianchi type V and VI₀ space-time in the context of teleparallel gravity. Mishra et al., [33] investigated the string cosmological model using spatially homogeneous and anisotropic Bianchi type V space-time. The viscous string cosmological model explaining the cosmic accelerated expansion has been investigated by Vinutha et al., [34]. Darabi et al., [35] obtained string cosmological solutions via Hojman symmetry using FRW line element. Chirde et al., [36] have studied the LRS Bianchi type I cosmological model having the source as perfect fluid and a string of clouds using three different $f(T)$ formalisms. In modern cosmology, the substantial theoretical development of string theory [37-47], has been done using different types of gravitation theories.

Motivated by the situations discussed above in this paper, we have considered

anisotropic LRS Bianchi type I space-time to construct a string cosmological model coupled with zero mass scalar field within the context of $f(R)$ gravity. This paper is divided into several sections: Sec. 2 deals with $f(R)$ gravity formalism. In Sec. 3 considering Bianchi type I metric, we have obtained the corresponding field equations. In Sec. 4, we obtained the exact solution of highly non-linear field equations along with different physical and kinematical quantities and presented them with 3D graphs. Lastly, in Sec. 5, we have concluded the investigations.

2. $f(R)$ gravity formalism. The $f(R)$ theory of gravitation is a modification of the general theory of relativity. The action for $f(R)$ gravity is given by

$$S = \int \sqrt{-g} (f(R) + L_m) d^4x, \quad (1)$$

where $f(R)$ is a general function of Ricci Scalar R and L_m is the matter Lagrangian. It is worth mentioning that the standard Einstein-Hilbert action can be recovered when $f(R) = R$.

The corresponding field equations are obtained by varying the action with respect to the metric $g_{\mu\nu}$ as

$$F(R)R_{\mu\nu} - \frac{1}{2} f(R)g_{\mu\nu} - \nabla_\mu \nabla_\nu F(R) + g_{\mu\nu} \nabla^\mu \nabla_\mu F(R) = T_{\mu\nu}, \quad (2)$$

where $F(R) \equiv df(R)/dR$, ∇_μ denotes covariant differentiation, $T_{\mu\nu}$ is the standard matter energy-momentum tensor derived from the matter Lagrangian L_m .

3. Metric and field equations. We consider an anisotropic LRS Bianchi type I metric of the form as

$$ds^2 = dt^2 - A^2 dx^2 - B^2 (dy^2 + dz^2), \quad (3)$$

where A and B are functions of cosmic time t only.

The energy-momentum tensor for a one-dimensional cosmic string coupled with a zero mass scalar field is given by

$$T_{\mu\nu} = \rho u_\mu u_\nu - \lambda x_\mu x_\nu + \left(\Psi_{,\mu} \Psi_{,\nu} - \frac{1}{2} g_{\mu\nu} \Psi_{,m} \Psi^{,m} \right), \quad (4)$$

where λ and ρ are respective the tension density and rest energy density of string cloud fluid. u_μ denotes four time-like velocity vectors and x_μ denotes a unit space-like vector which represents the anisotropic direction of cloud string and satisfies the conditions,

$$g^{\mu\nu} u_\mu u_\nu = -x_\mu x_\nu = 1, \quad u_\mu x_\mu = 0. \quad (5)$$

In the comoving coordinate system, components of the energy-momentum tensor from equation (4) are given by

$$T_1^1 = -\lambda + \frac{1}{2}\dot{\psi}^2, \quad T_2^2 = T_3^3 = \frac{1}{2}\dot{\psi}^2 \quad \text{and} \quad T_4^4 = \rho - \frac{1}{2}\dot{\psi}. \quad (6)$$

Taking consideration of (6), the field equations (2) for the metric (3) are obtained as

$$\ddot{F} + 2\left(\frac{\dot{B}}{B}\right)\dot{F} + \left(\frac{\ddot{A}}{A} + 2\frac{\dot{A}\dot{B}}{AB}\right)F - \frac{1}{2}f = -\lambda + \frac{1}{2}\dot{\psi}^2, \quad (7)$$

$$\ddot{F} + \left(\frac{\dot{A}}{A} + \frac{\dot{B}}{B}\right)\dot{F} + \left(\frac{\ddot{B}}{B} + \frac{\dot{B}^2}{B^2} + \frac{\dot{A}\dot{B}}{AB}\right)F - \frac{1}{2}f = \frac{1}{2}\dot{\psi}^2, \quad (8)$$

$$\left(\frac{\dot{A}}{A} + 2\frac{\dot{B}}{B}\right)\dot{F} + \left(\frac{\ddot{A}}{A} + 2\frac{\ddot{B}}{B}\right)F - \frac{1}{2}f = \rho - \frac{1}{2}\dot{\psi}^2, \quad (9)$$

where the overhead dot (\cdot) denotes the derivative with respect to cosmic time t .

Here we have three non-linear differential field equations with six unknowns, namely; f , A , B , ρ , λ and ψ . The solution of these unknowns is discussed in the next section.

Also, we define some kinematical space-time quantities of physical interest in cosmology, as follows:

The average scale factor a and the spatial volume V are respectively defined as

$$a = \sqrt[3]{AB^2} \quad \text{and} \quad V = a^3. \quad (10)$$

The volumetric expansion rate of the universe is described by the generalized mean Hubble's parameter H given by

$$H = \frac{1}{3} \sum_{i=1}^3 H_i = \frac{1}{3}(H_1 + H_2 + H_3), \quad (11)$$

in which $H_1 = \dot{A}/A$, and $H_2 = H_3 = \dot{B}/B$ denotes the directional Hubble's parameters.

Using (10) and (11), we have obtained the expansion scalar Θ , the mean anisotropy parameter Δ , the shear scalar σ^2 , and the deceleration parameter q respectively as

$$\Theta = \frac{\dot{A}}{A} + 2\frac{\dot{B}}{B} = 3H, \quad (12)$$

$$\Delta = \frac{1}{3} \sum_{i=1}^3 \left(\frac{H_i - H}{H} \right)^2, \quad (13)$$

$$\sigma^2 = \frac{1}{2} \left(\sum_{i=1}^3 H_i^2 - \Theta^2 \right), \quad (14)$$

$$q = -\frac{a\ddot{a}}{\dot{a}^2} = -1 + \frac{d}{dt} \left(\frac{1}{H} \right). \quad (15)$$

4. *Solution of field equations.* To solve the nonlinear differential field equations (7)-(9) and obtain the exact solution, we consider the weak field limit for a point-like source of $f(R)$ gravity model as presented by Capozziello et al. [48] and given by

$$f(R) = R^{3/2}. \quad (16)$$

For the deterministic solutions, we consider the expansion scalar Θ is proportional to the shear scalar σ^2 which leads to the following analytic relation

$$A = B^\zeta, \quad (17)$$

where ζ is a constant.

Also, as described by Yadav [49] we consider the average scale factor in the form

$$a(t) = (nDt)^{1/n}, \quad (18)$$

where n is a non-negative constant and D is an arbitrary constant.

We obtained the metric coefficients A and B as

$$A = (nDt)^{3\zeta/n(\zeta+2)}, \quad B = (nDt)^{3/n(\zeta+2)}. \quad (19)$$

Substituting values of A and B from (19) in (3), we get

$$ds^2 = dt^2 - (nDt)^{6\zeta/n(\zeta+2)} dx^2 - (nDt)^{6/n(\zeta+2)} (dy^2 + dz^2). \quad (20)$$

The metric coefficients of the model obtained in (20) are constant for any type of t , and hence it is free from any type of singularity.

In the following, we have determined the spatial volume V , the mean Hubble's parameter H , the expansion scalar Θ , the mean anisotropy parameter Δ , the shear scalar σ^2 , and the deceleration parameter q respectively as

$$V = (nDt)^{3/n}, \quad (21)$$

$$H = \frac{1}{nt}, \quad (22)$$

$$\Theta = \frac{3}{nt}, \quad (23)$$

$$\Delta = \frac{2(\zeta-1)^2}{(\zeta+2)^2}, \quad (24)$$

where $\zeta \neq 1$, and $\zeta \neq -2$

$$\sigma^2 = \frac{3(\zeta-1)^2}{n^2 t^2 (\zeta+2)^2}, \quad (25)$$

where $\zeta \neq 1$, and $\zeta \neq -2$

$$q = n-1. \quad (26)$$

The ratio

$$\frac{\sigma^2}{\Theta^2} = \frac{1}{3} \frac{(\zeta - 1)^2}{(\zeta + 2)^2}. \quad (27)$$

where $\zeta \neq 1$, and $\zeta \neq -2$.

It is observed from Fig.1 that the spatial volume is zero at the beginning of time and increases asymptotically with an increase in cosmic time for the range

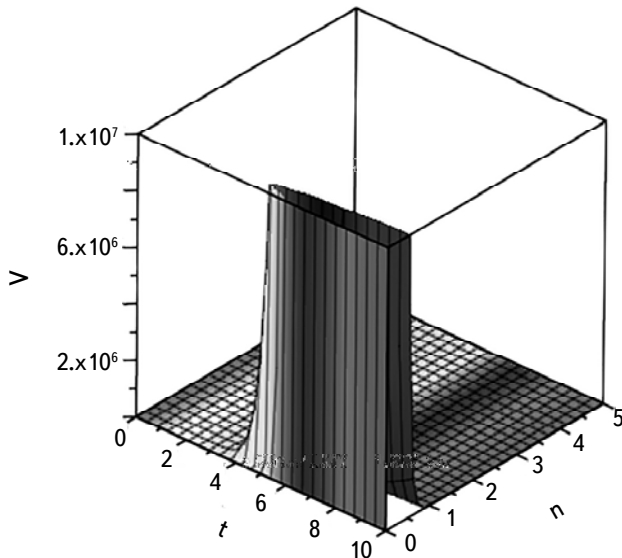


Fig.1. Plot of V vs t for $\zeta = -0.875$ and $D = 3$.

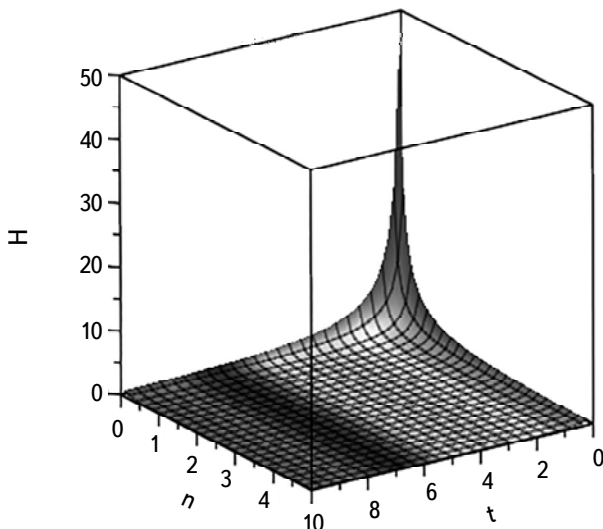


Fig.2. Plot of H vs t .

$0 < n < 1$ showing the expansion of the universe but for $n > 1$ the volume is found to be stable and flat, while the Hubble's parameter which is an inverse function of cosmic time decreases monotonically (Fig.2) with both the increase in cosmic time t and varying constant n and hence the rate of expansion of the universe also decreases. The ratio $\sigma^2/\Theta^2 \neq 0$ shows the discussed model doesn't approach isotropy. Also, the sign of q determines the accelerating or decelerating phase of the universe. The positive sign of q i.e. for $n > 1$ corresponds to a plain decelerating cosmological model although the deceleration parameter in range $-1 \leq q < 0$ corresponds to an accelerating universe and for $q = 0$ i.e. for $n = 1$ corresponds to the evolution with a constant rate. The observational SN Ia data [1,2] supports cosmic acceleration i.e $-1 \leq q < 0$.

The scalar field

$$\psi = -6t \left\{ -\frac{2[(2n+3)\zeta + 4n][(n-2)\zeta + 2n-1][(n-3)\zeta^2 + 2(2n-3)\zeta + 4n-9]}{n^3(\zeta+2)^3 t^3 [-6(n-3)\zeta^2 - 12(2n-3)\zeta - 6(4n-9)]^{1/2}} \right\}^{1/2}. \quad (28)$$

The behaviour of the scalar field observed in Fig.3 determines that the value of ψ that is negative throughout the evolution and is an asymptotically increasing function of cosmic time t .

The energy density

$$\rho = -\frac{9[(2n^2-5n-3)\zeta^2 + (8n^2-20n-15)\zeta + 4n(2n-5)][(n-3)\zeta^2 + 2(2n-3)\zeta + 4n-9]}{n^3(\zeta+2)^3 t^3 [-6(n-3)\zeta^2 - 12(2n-3)\zeta - 6(4n-9)]^{1/2}}. \quad (29)$$

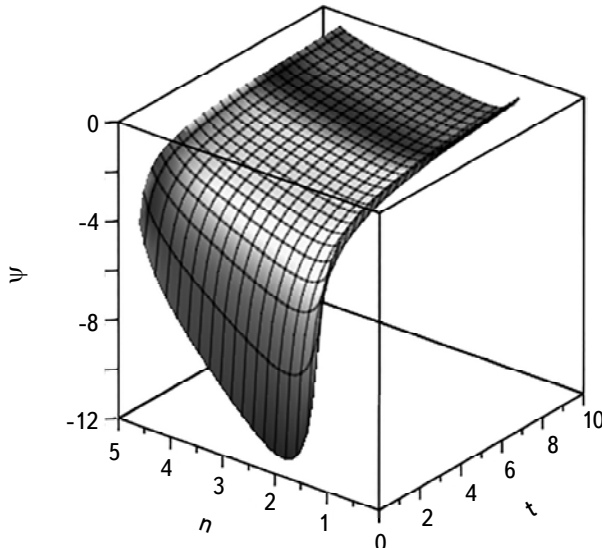


Fig.3. Plot of ψ vs t for $\zeta = -0.875$.

The string tension density

$$\lambda = \frac{81(\zeta-1)[(n-3)\zeta^2 + 2(2n-3)\zeta + 4n-9]}{n^3(\zeta+2)^3 t^3 [-6(n-3)\zeta^2 - 12(2n-3)\zeta - 6(4n-9)]^{1/2}}. \quad (30)$$

It is observed from Fig.4 as well as from Fig.5 that as the cosmic time t

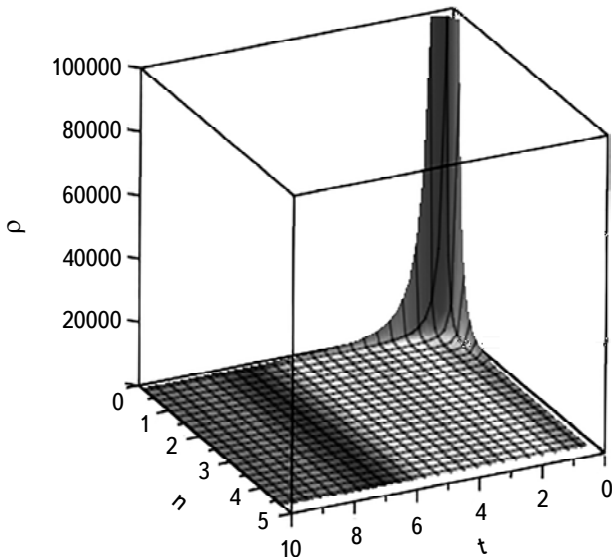


Fig.4. Plot of ρ vs t for $\zeta = -0.875$.

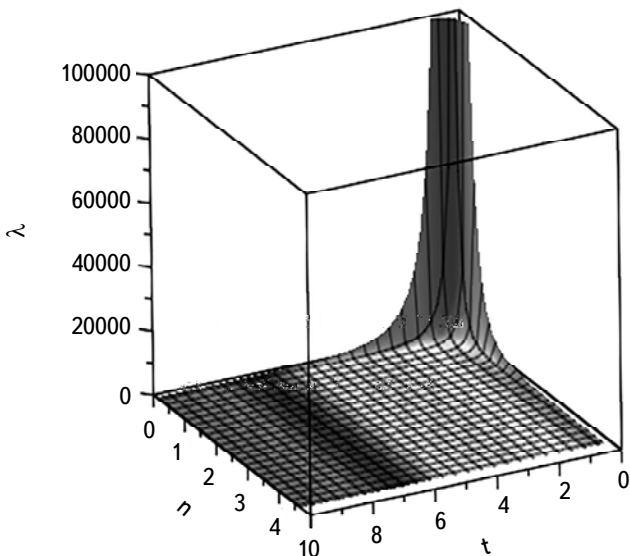


Fig.5. Plot of λ vs t for $\zeta = -0.875$.

and the value of constant n increases the energy density and the tension density both decreases to approach zero when $t \rightarrow \infty$. Furthermore, we observed that the presence of string as compared to the energy particles is quite larger which indicates the string dominance over energy particles. Letelier [44] studied the possibility that during the evolution of the universe, the strings disappear leaving only particles, and pointed out that the string tension density λ can be positive or negative. In our model, $\lambda > 0$ throughout the evolution, not only shows the presence of strings in the universe but also the string dominance over particles. Additionally, as both densities are positive, decrease with increasing cosmic time, and both approach zero when $t \rightarrow \infty$ indicates that the universe is expanding and expansion will keep forever which is in good agreement with [50].

The equation of state (EoS) for string fluid is given by

$$\rho = \varepsilon \lambda. \quad (31)$$

Then the EoS parameter can be obtained as

$$\varepsilon = -\frac{(2n^2 - 5n - 3)\zeta^2 + (8n^2 - 20n - 15)\zeta + 4n(2n - 5)}{9(\zeta - 1)(\zeta + 2)}. \quad (32)$$

The EoS parameter is observed to be a constant function and hence evolves constantly with increasing cosmic time. However, it should be noted that for $n \leq 1$ the value of the EoS parameter decreases while with increasing $n > 1$ the value of the EoS parameter increases positively (Fig.6).

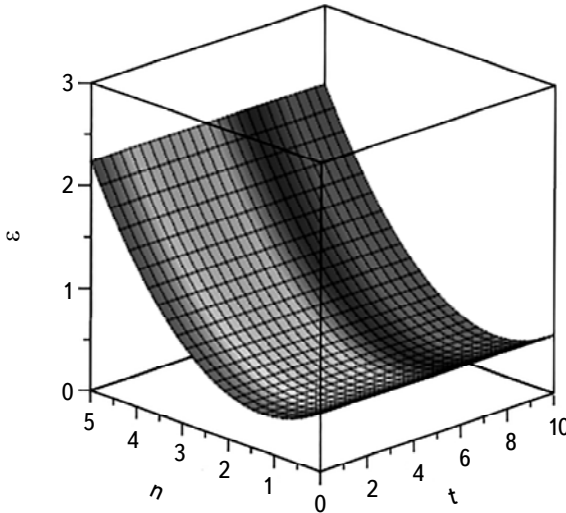


Fig.6. Plot of ε vs t for $\zeta = -0.875$.

The overall density parameter

$$\Omega = -\frac{3[(2n^2-5n-3)\zeta^2 + (8n^2-20n-15)\zeta + 4n(2n-5)][(n-3)\zeta^2 + 2(2n-3)\zeta + 4n-9]}{n(\zeta+2)^3 t[-6(n-3)\zeta^2 - 12(2n-3)\zeta - 6(4n-9)]^{1/2}}. \quad (33)$$

The graphical representation of the overall density parameter has been depicted in Fig.7 showing the complete positive epoch of the density parameter. It is observed that Ω decreases with an increase in cosmic time t and the value of constant n expressing the status for a flat universe which is supported by WMAP observations.

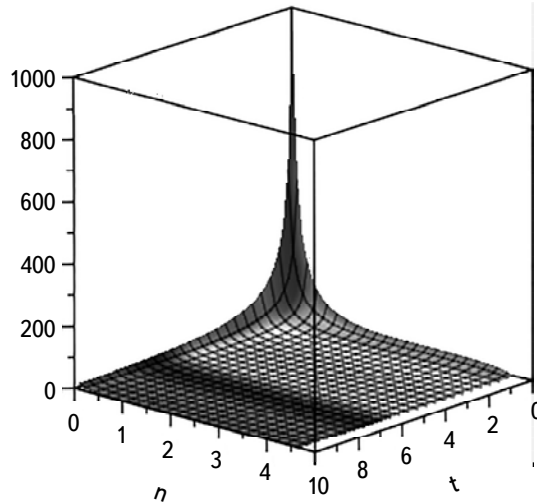


Fig.7. Plot of Ω vs t for $\zeta = -0.875$.

5. Concluding remarks. Zero mass scalar field and a string of clouds plays an vital role in understanding the early stages of cosmic evolution. In this present work, we have studied an anisotropic LRS Bianchi type I line element in the presence of one-dimensional cosmic string coupled with zero mass scalar field in reference to $f(R)$ gravity. The exact solutions to the field equations have been obtained by using the weak field limit for a point-like source of $f(R)$ gravity as presented by Capozziello et al. [48] and the average scale factor as described by Yadav [49]. It is observed that the constructed model is free from any type of singularity, expanding and showing acceleration or deceleration depending on the special choice of constant n which is in good agreement with recent observational data. The zero-mass scalar field is found to be negative which grows asymptotically in accordance with cosmic time t . The energy density and the tension density have finite values in the beginning which vanishes with an increasing cosmic time. Additionally, the obtained universe shows the string

dominance over energy particles. Furthermore, the constructed model is flat which is supported by WMAP observations, having constant EoS parameter and showing the never-ending expansion which is in good agreement with [50].

Acknowledgements. The authors would like to express their deep sense of gratitude towards the respected editor and the anonymous referees for their helpful remarks and illuminating suggestions, which substantially improved the quality of our research work and presentation.

¹ Department of Mathematics, Shri R. R. Lahoti Science College, Morshi, Dist. Amravati (M.S.), India, e-mail: kalpanapawar31@rediffmail.com
ankitdabre@live.com

² Department of Mathematics, SGB Amravati University, Amravati (M.S.), India, e-mail: pallavimakode@hotmail.com

ПЛОСКО-СИММЕТРИЧНАЯ СТРУННАЯ КОСМОЛОГИЧЕСКАЯ МОДЕЛЬ СО СКАЛЯРНЫМ ПОЛЕМ НУЛЕВОЙ МАССЫ В $f(R)$ ГРАВИТАЦИИ

К.ПАВАР¹, А.К.ДАБРЕ¹, П.МАКОДЕ²

В этой статье исследована анизотропная локально вращательно-симметрическая (LRS) метрика Бьянки типа I в присутствии жидкости облачной струны и скалярного поля нулевой массы относительно гравитации $f(R)$. Чтобы получить детерминированные решения, мы приняли предел слабого поля для точечного источника $f(R)=R^{3/2}$ и хорошо известное скалярное соотношение расширение-сдвиг. Кроме того, были рассчитаны некоторые физические и кинематические параметры для изучения астрофизических последствий полученной модели, которая показывает хорошее согласие с недавними наблюдательными данными.

Ключевые слова: *космическая струна: скалярное поле: метрика Бьянки типа I: гравитация $f(R)$*

REFERENCES

1. *A.G.Riess et al.*, Astron. J., **116**, 1009, 1998.
2. *S.Perlmutter et al.*, Astrophys. J., **517**, 565, 1999.
3. *R.A.Knop et al.*, Astrophys. J., **598**, 102, 2003.
4. *H.A.Buchdahl*, Mon. Not. Roy. Astron. Soc., **150**, 1, 1970.
5. *S.Nojiri, S.D.Odintsov*, Phys. Rep., **505**, 59, 2011.
6. *S.D.Katore, S.P.Hatkar*, Indian J. Phys., **90**, 243, 2016.
7. *S.Bahamonde, C.G.Böhmer, M.Wright*, Phys. Rev. D, **92**, 104042, 2015.
8. *R.Ferraro*, AIP Conf. Proc., **1471**, 103, 2012.
9. *A. De La Cruz-Dombriz, A.Dobado*, Phys. Rev. D, **74**, 087501, 2006.
10. *S.Nojiri, S.D.Odintsov*, arXiv preprint hep-th/0307288 68, 2003.
11. *S.Nojiri, S.D.Odintsov*, Phys. Lett. B, **657**, 238, 2007.
12. *E.Guendelman, R.Herrera*, arXiv preprint arXiv:2301.10274, 2023.
13. *S.Capozziello, S.J.Gabriele Gionti, D.Vernieri*, J. Cosmol. Astropart. Phys., **2016**, 015, 2016.
14. *P.Bari, K.Bhattacharya*, J. Cosmol. Astropart. Phys., **2019**, 019, 2019.
15. *J.Sadeghi, E.N.Mezerji, S.N.Gashti*, Mod. Phys. Lett. A, **36**, 2150027, 2021.
16. *R.Venkateswarlu, K.P.Kumar*, Int. J. Theor. Phys., **49**, 1894, 2010.
17. *R.Venkateswarlu, K.Sreenivas*, Int. J. Theor. Phys., **53**, 2051, 2014.
18. *R.Venkateswarlu, J.Satish*, Int. J. Theor. Phys., **53**, 1879, 2014.
19. *N.Godani, G.C.Samanta*, Int. J. Mod. Phys. A, **35**, 2050186, 2020.
20. *N.I.Singh, S.S.Singh, S.R.Devi*, Astrophys. Space Sci., **334**, 187, 2011.
21. *K.M.Singh*, Astrophys. Space Sci., **325**, 293, 2010.
22. *R.Patra*, Int. J. Math. Trends Technol., **54**, 11, 2018.
23. *K.S.Adhav, S.D.Katore, R.S.Rane et al.*, Astrophys. Space Sci., **323**, 87, 2009.
24. *A.Dixit, D.C.Maurya, A.Pradhan*, New Astron., **87**, 101587, 2021.
25. *S.D.Katore, M.M.Sancheti, N.K.Sarkate*, Prespacetime J., **2**, 1860, 2011.
26. *M.Cadoni, E.Franzin*, Phys. Rev. D, **91**, 104011, 2015.
27. *D.D.Pawar, S.P.Shahare, Y.S.Solanke et al.*, Indian J. Phys., **95**, 1563, 2021.
28. *S.Nojiri, S.D.Odintsov, V.K.Oikonomou*, Phys. Rep., **692**, 1, 2017.
29. *L.Freidel, R.G.Leigh, D.Minic*, Int. J. Mod. Phys. D, **23**, 1442006, 2014.
30. *K.Pawar, A.K.Dabre*, Int. J. Sci. Res. Phy. App. Sci., **10**, 8, 2022.
31. *K.Pawar, A.K.Dabre, N.T.Katre*, Int. J. Sci. Res. Phy. App. Sci., **10**, 1, 2022.
32. *K.Pawar, A.K.Dabre*, Astrophysics, **66**, 114, 2023.
33. *B.Mishra, S.K.Tripathy, P.P.Ray*, Astrophys. Space Sci., **363**, 86, 2018.
34. *T.Vinutha, V.U.M.Rao, G.Bekele et al.*, Indian J. Phys., **95**, 1933, 2021.
35. *F.Darabi, M.Golmohammadi, A.Rezaei-Aghdam*, Int. J. Geom. Methods Mod. Phys., **17**, 2050175, 2020.
36. *V.R.Chirde, S.P.Hatkar, S.D.Katore*, Int. J. Mod. Phys. D, **29**, 2050054, 2020.
37. *D.D.Pawar, G.G.Bhuttampalle, P.K.Agrawal*, New Astron., **65**, 1, 2018.
38. *R.Zia, D.C.Maurya, A.Pradhan*, Int. J. Geom. Methods Mod. Phys., **15**, 1850168, 2018.

39. *M.Sharif, Q.Ama-Tul-Mughani*, Mod. Phys. Lett. A, **35**, 2050091, 2020.
40. *A.K.Yadav*, Eur. Phys. J. Plus, **129**, 179, 2014.
41. *T.Vinutha, V.U.M.Rao, M.Mengesha*, Can. J. Phys., **99**, 168, 2021.
42. *A.R.P.Moreira, J.E.G.Silva, D.F.S.Veras et al.*, Int. J. Mod. Phys. D, **30**, 2150047, 2021.
43. *R.Consiglio, O.Sazhina, G.Longo et al.*, Mon. Not. Roy. Astron. Soc., **439**, 3213, 2014.
44. *P.S.Letelier*, Phys. Rev. D, **28**, 2414, 1983.
45. *H.Bernardo, R.Brandenberger, G.Franzmann*, Phys. Rev. D, **103**, 43540, 2021.
46. *P.Berglund, T.Hübsch, D.Minić*, Phys. Lett. B, **798**, 134950, 2019.
47. *P.S.Letelier*, Nuovo Cim. B, **63**, 519, 1981.
48. *S.Capozziello, E.Piedipalumbo, C.Rubano et al.*, Astron. Astrophys., **505**, 21, 2009.
49. *A.K.Yadav*, Eur. Phys. J. Plus, **129**, 194, 2014.
50. *A.Dixit, R.Zia, A.Pradhan*, Pramana, J. Phys., **94**, 25, 2020.

АСТРОФИЗИКА

ТОМ 66

АВГУСТ, 2023

ВЫПУСК 3

DOI: 10.54503/0571-7132-2023.66.3-399

MODIFIED TSALLIS HOLOGRAPHIC DARK ENERGY

J.BHARALI¹, K.DAS²

Received 30 March 2023

Accepted 18 August 2023

In this work we propose Modified Tsallis Holographic Dark Energy (MTHDE) in General Relativity (GR) in the framework of Bianchi type III space-time. Einstein's field equations are solved by using a special law of variation of Hubble parameter H proposed by Berman which yields constant deceleration parameter (DP). Interestingly, for the two different constant values of deceleration parameter, we have obtained two different cosmological models. The model 1 behaves like a quintessence dark energy model whereas model 2 behaves like a cosmological constant model. A correspondence between model 1 and quintessence scalar field is established. The quintessence dynamics of the potential and scalar field are reconstructed which illustrates the accelerating phase of the Universe. Various parameters like deceleration parameter, Hubble parameter, anisotropy parameter, equation of state (EOS) parameter, etc. for both the cosmological models are thoroughly discussed. The results obtained are found to be consistent with the recent observations on the present-day Universe.

Keywords: *MTHDE: GR: Hubble parameter: deceleration parameter DP*

1. Introduction. Recent astrophysical observational data [1-6] show that our Universe is going through a phase of accelerated expansion which put new avenues in modern cosmology. A class of people are making attempts to accomodate this observational fact by choosing some exotic matter (known as dark energy) in the framework of general relativity. Dark energy (DE) is believed to dominate over the matter content of the Universe by 70%. In all theories and models, the cosmological constant model is the most natural and simplest candidate of DE with the equation of state (EOS) parameter $\omega = -1$ but it suffers from cosmic coincidence and fine-tuning problem [7,8]. To relieve such problems, various dark energy models have been suggested in literature such as quintessence [9], phantom [10], k -essence [11], tachyon [12], HDE [13], etc.

Despite of many efforts from different observational and theoretical ways, the problem of DE is still not well settled due to its unknown nature. In order to justify the source of accelerating expansion (i.e. the nature of DE) of the Universe, two different approaches have been adopted. One way is to modify the geometric part of Einstein-Hilbert action (termed as modified theories of gravity) for the discussion of expansion phenomenon [14-18]. The second approach is to propose the different forms of DE called dynamical DE models. Up to now, different dynamical DE models have been proposed in two different contexts such as

quantum gravity and GR. Holographic dark energy have been proposed in the framework of quantum gravity on the basis of holographic principle [19]. The density of HDE model has the following form $\rho_{DE} = 3c^2 M_p^2 L^{-2}$ where c is a specific constant, $M_p = (8\pi G)^{-1/2}$ termed as reduced Planck mass and L represent the infrared (IR) cutoff described the size of the Universe. By considering horizon entropy of a black hole, Tsallis and Cirto assumed some quantum modification for HDE given by (Tsallis and Cirto [20]) $S_\delta = \gamma A^\delta$ with γ being an unknown constant and δ represents the non-additivity parameter chosen to have a positive value. The Bekenstein entropy is a particular case when $\delta=1$ and $\gamma=1/4G$ [21]. Considering the holographic hypothesis, Cohen et al. [22] proposed the relation among the system entropy S , the IR (L) and UV (Λ) cutoffs as $L^3 \Lambda^3 \leq S^{3/4}$ which after combining with $S_\delta = \gamma A^\delta$ gives $\Lambda^4 \leq \gamma(4\pi)^\sigma L^{2\delta-4}$. Using this inequality, the THDE density is obtained as $\rho_T = DL^{2\delta-4}$ where D is an unknown parameter [23-25]. It is worthy to mention that for $\delta=1$, the standard HDE is recovered. Furthermore, for $\delta=2$, the cosmological constant model is retrieved. Using the Hubble horizon H^{-1} as the IR cutoff L , $\rho_T = DH^{-2\delta+4}$ is obtained.

Since DE occupies almost 70% of the content of the Universe today, it is rational to assume that the density of DE is a function of the Hubble parameter H and its derivative w.r.t. cosmic time [26]. In this paper, we have modified the THDE by assuming $\rho_{MT} = DH^{-2\delta+4} + E\dot{H}$. In the above expression dot(.) denotes differentiation w.r.t. cosmic time t and E is the arbitrary dimensionless parameter. The early Universe inflation can be considered as the primordial DE because DE is merely the substitute for the accelerating expansion of the Universe [27]. So, our constructed model is a good candidate to describe the inflationary stage.

Bianchi type spaces play an important role in constructing spatially homogeneous and anisotropic cosmological models to describe the behaviour of the Universe at its early stages of its evolution. The anomalies found in the cosmic microwave background (CMB) and large-scale structure (LSS) observations stimulated a growing interest in anisotropic cosmological model of the Universe. Here we confine ourselves to Bianchi type III models.

Several researchers have investigated various cosmological models in the framework of THDE. Two Tsallis Agegraphic DE (TADE) models have been proposed by using the age of the Universe and the conformal time as the IR cut-offs and study their effects on the evolution of the Universe [28]. THDE in FRW Universe with time varying deceleration parameter (DP) in the framework of FRW Universe have been investigated by [29]. Mamon [30] has studied the evolution of a fractal Universe with THDE in presence of an interacting scenario. Sadeghi et al. [31] have explored THDE by considering the complex form of the quintessence model in the framework of Brans-Dicke cosmology. Pradhan et al. [32] have discussed THDE in the modified $f(R, T)$ gravity framework with

Granda-Oliveros (GO) cutoff. Mamon et al. [33] have studied THDE in presence of interacting scenario. Dubey et al. [34] have discussed the axially symmetric space-time in THDE. Korunur [35] have explored THDE in Bianchi type III space-time. Yadav [36] has worked out THDE in Brans-Dicke cosmology. Santhi and Sobhanbabu [37] have explained THDE in Saez-Ballester theory of gravitation. Dubey et al. [38] have investigated THDE using hybrid expansion law (HEL) with k -essence. Dubey et al. [39] have examined THDE in the non-flat Universe. Motivated by the above aforesaid works, we have modified THDE in GR in the framework of Bianchi type III space-time.

The organisation of the paper is as follows: In Section 2, we formulate the metric and field equations for MTHDE model. In Section 3, we have obtained the solutions of field equations of Bianchi type III space-time. In Section 4, we have studied the cosmological model 1 and the correspondence between model 1 and quintessence scalar field. In Section 5 we have studied the cosmological model 2. The model 1 behaves like a quintessence dark energy model whereas the model 2 behaves like a cosmological constant model. Various parameters for both the models are discussed graphically in Sections 6 and 7 respectively. The paper ends with concluding remarks in Section 8.

2. Metric and field equations. We consider the anisotropic Bianchi type III space-time

$$ds^2 = dt^2 - I^2 dx^2 - J^2 e^{-2x} dy^2 - K^2 dz^2 \quad (1)$$

where the scale factors I , J and K are functions of cosmic time t only.

The Einstein's field equations are given by

$$R_{ij} - \frac{1}{2} g_{ij} R = -\left(T'_{ij} + \bar{T}_{ij}\right), \quad (2)$$

where R_{ij} is the Ricci tensor and R is the Ricci scalar.

The energy momentum tensor $T_j^{i'}$ for dark matter (DM) is

$$T_j^{i'} = \text{diag}[\rho_m, 0, 0, 0], \quad (3)$$

where ρ_m is the energy density of DM.

The energy momentum tensor $\bar{T}_j^{i'}$ for MTHDE is

$$\begin{aligned} \bar{T}_j^{i'} &= \text{diag}[\rho_{MT}, -p_{MT_x}, -p_{MT_y}, -p_{MT_z}] = \text{diag}[1, -\omega_x, -\omega_y, -\omega_z]\rho_{MT} \\ &= \text{diag}[1, -\omega_{MT}, -\omega_{MT}, -\omega_{MT}]\rho_{MT}, \end{aligned} \quad (4)$$

where ρ_{MT} is the energy density of MTHDE, p_{MT} is the pressure of MTHDE and $\omega_x = \omega_{MT}$, $\omega_y = \omega_{MT}$ and $\omega_z = \omega_{MT}$ are the directional equation of state (EOS) parameters on x , y and z axes respectively and $\omega_{MT}\rho_{MT} = p_{MT}$.

The Einstein's field equations (2) for the metric (1) using Eqs. (3) and (4)

takes the form

$$\frac{\ddot{J}}{J} + \frac{\ddot{K}}{K} + \frac{J\dot{K}}{JK} = -\omega_{MT}\rho_{MT} \quad (5)$$

$$\frac{\ddot{I}}{I} + \frac{\ddot{K}}{K} + \frac{I\dot{K}}{IK} = -\omega_{MT}\rho_{MT} \quad (6)$$

$$\frac{\ddot{I}}{I} + \frac{\ddot{J}}{J} + \frac{\dot{IJ}}{IJ} - \frac{1}{I^2} = -\omega_{MT}\rho_{MT} \quad (7)$$

$$\frac{\dot{IJ}}{IJ} + \frac{\dot{JK}}{JK} + \frac{\dot{KI}}{KI} - \frac{1}{I^2} = \rho_m + \rho_{MT} \quad (8)$$

$$\frac{\dot{J}}{J} - \frac{\dot{I}}{I} = 0. \quad (9)$$

Eq. (9) on integration and taking integrating constant to be unity, we obtain
 $J = I.$ (10)

Using Eq. (10) in Eqs. (5)-(8), we get

$$\frac{\ddot{I}}{I} + \frac{\ddot{K}}{K} + \frac{I\dot{K}}{IK} = -\omega_{MT}\rho_{MT} \quad (11)$$

$$2\frac{\ddot{I}}{I} + \frac{\dot{I}^2}{I^2} - \frac{1}{I^2} = -\omega_{MT}\rho_{MT} \quad (12)$$

$$\frac{\dot{I}^2}{I^2} + 2\frac{I\dot{K}}{IK} - \frac{1}{I^2} = \rho_m + \rho_{MT}. \quad (13)$$

The energy conservation equation is

$$\dot{\rho}_m + \dot{\rho}_{MT} + \left(2\frac{\dot{I}}{I} + \frac{\dot{K}}{K} \right) (\rho_m + \rho_{MT} + p_{MT}) = 0, \quad (14)$$

where overhead dot (.) denotes differentiation w.r.t. cosmic time t .

We assume that there is no interaction between DM and MTHDE throughout the study.

3. Solutions of field equations. The average scale factor $a(t)$ and the spatial volume V are defined as

$$V = a^3 = I^2 K. \quad (15)$$

The directional Hubble's parameters H_x , H_y and H_z in the direction of x , y and z axes respectively are given by

$$H_x = H_y = \frac{\dot{I}}{I}, \quad H_z = \frac{\dot{K}}{K}. \quad (16)$$

The mean Hubble's parameter H is

$$H = \frac{\dot{a}}{a} = \frac{\dot{V}}{3V} = \frac{H_x + H_y + H_z}{3} = \frac{1}{3} \left(2 \frac{\dot{I}}{I} + \frac{\dot{K}}{K} \right). \quad (17)$$

The deceleration parameter q is defined as

$$q = -\frac{a\ddot{a}}{\dot{a}^2}. \quad (18)$$

The anisotropy parameter A_p is defined as

$$A_p = \frac{1}{3} \sum_{i=1}^3 \left(\frac{H_i - H}{H} \right)^2. \quad (19)$$

Field equations (11)-(13) forms a system of three independent equations with five unknowns I , K , ω_{MT} , ρ_{MT} and ρ_m . So, we use two extra relations to solve the system of field equations completely. These are as follows:

(i) Following Chen and Jing [26] and Bharali and Das [40], we define MTHDE density ρ_{MT} as a function of Hubble parameter H and its derivative w.r.t. cosmic time t as follows

$$\rho_{MT} = DH^{-2\delta+4} + E\dot{H}, \quad (20)$$

where E is the arbitrary dimensionless parameter and the other symbols have their usual meanings.

(ii) A special law of variation for Hubble's parameter H proposed by Berman [41] is defined as

$$H = ka^{-m}, \quad (21)$$

where $k > 0$ and $m \geq 0$ are constants.

Using Eqs. (17) and (21), we have obtained two models

$$a = (mkt + k_1)^{1/m}, \quad q = m-1, \quad m < 1, \quad (22)$$

where k_1 is a constant of integration.

$$a = \exp \{k(t - k_2)\}, \quad q = -1, \quad m = 0, \quad (23)$$

where k_2 is a constant of integration.

From Eqs. (11) and (12), we get

$$\frac{\dot{K}}{K} - \frac{\dot{I}}{I} = \frac{u_0}{V} \exp \left(\int -\frac{1}{I^2} \left(\frac{\dot{K}}{K} - \frac{\dot{I}}{I} \right)^{-1} dt \right), \quad (24)$$

where u_0 is a constant of integration.

Following Adhav [42], we assume

$$\frac{\dot{K}}{K} - \frac{\dot{I}}{I} = \frac{1}{I^2}. \quad (25)$$

Using Eq. (25) in Eq. (24), we get

$$\frac{\dot{K}}{K} - \frac{\dot{I}}{I} = \frac{u_0}{V} e^{-t}. \quad (26)$$

Integrating Eq. (26), we obtain

$$K = u_1 I \exp \left[u_0 \int \frac{e^{-t}}{V} dt \right], \quad (27)$$

where u_1 is a constant of integration.

4. Model 1. When $a = (mkt + k_1)^{1/m}$, $m < 1$. Eq. (27) with $a = (mkt + k_1)^{1/m}$ implies

$$K = u_1 I \exp \left[u_0 \int \frac{e^{-t}}{(mkt + k_1)^{3/m}} dt \right] \quad (28)$$

$$V = I^2 K = a^3 = (mkt + k_1)^{3/m}. \quad (29)$$

Eqs. (28) and (29) together implies

$$I = (mkt + k_1)^{1/m} u_1^{-1/3} \exp \left[-\frac{u_0}{3} \int \frac{e^{-t}}{(mkt + k_1)^{3/m}} dt \right] \quad (30)$$

$$K = (mkt + k_1)^{1/m} u_1^{2/3} \exp \left[\frac{2u_0}{3} \int \frac{e^{-t}}{(mkt + k_1)^{3/m}} dt \right]. \quad (31)$$

Both the cosmic scale factors I and K increases as the age of the Universe increases (Fig.1, 2). The Hubble parameter H and the MTHDE density ρ_{MT} are calculated as

$$H = \frac{k}{mkt + k_1}. \quad (32)$$

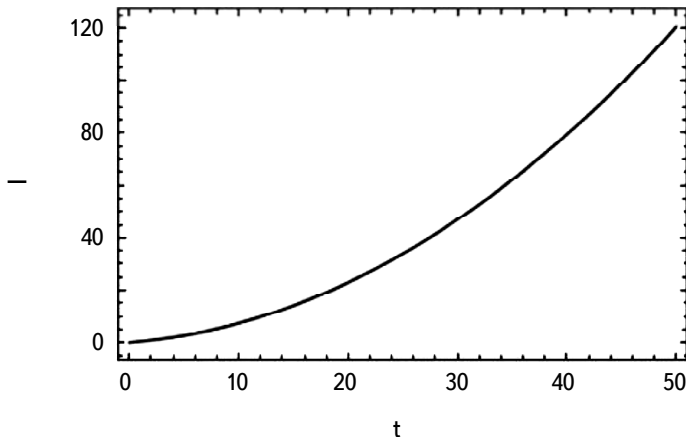


Fig.1. The plot of I versus cosmic time t for $m = 0.5$, $k = 0.3$, $k_1 = 0.5$, $u_0 = 0.03$ and $u_1 = 0.15$.

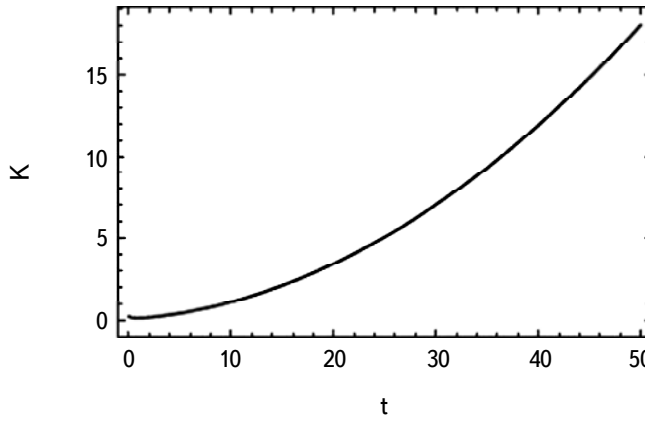


Fig.2. The variation of K against cosmic time t for $m = 0.5$, $k = 0.3$, $k_1 = 0.5$, $u_0 = 0.03$ and $u_1 = 0.15$.

The Hubble parameter H is a decreasing function of t and tends to a small value with the passage of cosmic time.

$$\rho_{MT} = D \left(\frac{k}{mkt + k_1} \right)^{-2\delta+4} + E \left[\frac{-mk^2}{(mkt + k_1)^2} \right]. \quad (33)$$

Fig.3 shows that ρ_{MT} decreases and tends to a constant value as cosmic time evolves. The anisotropy parameter A_p is calculated as

$$A_p = \frac{2}{9} \left(\frac{mkt + k_1}{k} \right)^2 \left[\frac{u_0^2 e^{-2t}}{(mkt + k_1)^{6/m}} \right]. \quad (34)$$

$A_p \rightarrow 0$ as observed from Fig.4. Thus, our Universe approaches isotropy at late

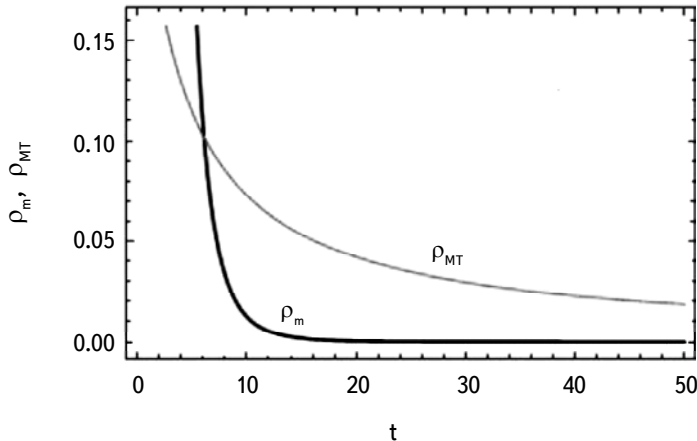


Fig.3. The variation of ρ_m and ρ_{MT} versus cosmic time t for $m = 0.5$, $k = 0.3$, $k_1 = 0.5$, $\rho_0 = 0.8$, $D = 0.5$, $\delta = 1.5$ and $E = 0.2$.

times. The energy conservation equation for dark matter is

$$\dot{\rho}_m + 3H\rho_m = 0. \quad (35)$$

Using Eq. (32) in Eq. (35), the energy density of dark matter ρ_m is found as

$$\rho_m = \frac{\rho_0}{(mkt + k_1)^{3/m}} \quad (36)$$

ρ_0 is a constant of integration.

From Fig.3, we see that ρ_m diminishes as cosmic time evolves and ultimately approaches to zero.

The energy conservation equation for MTHDE is

$$\dot{\rho}_{MT} + 3H(\rho_{MT} + p_{MT}) = 0. \quad (37)$$

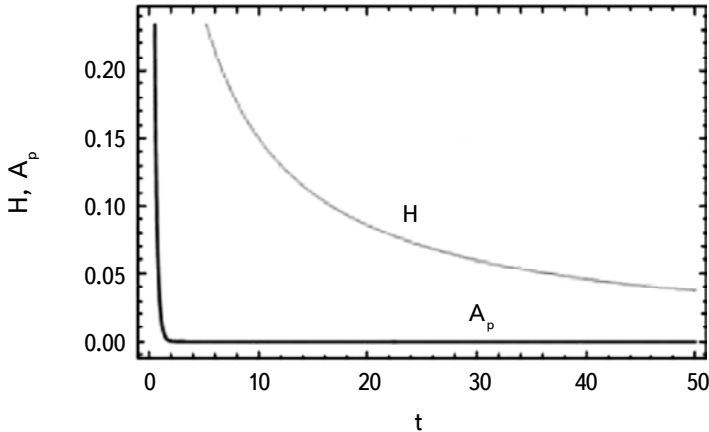


Fig.4. The evolution of H and A_p against cosmic time t for $m=0.5$, $k=0.3$, $k_1=0.5$ and $u_0=0.03$.

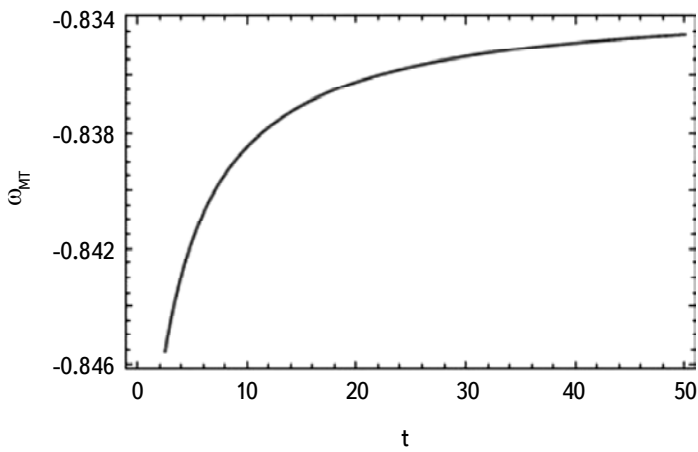


Fig.5. The plot of ω_{MT} versus t for $m=0.5$, $k=0.3$, $k_1=0.5$, $\delta=1.5$, $D=0.5$, $\rho_0=0.8$ and $E=0.2$.

The EOS parameter of MTHDE ω_{MT} is obtained by the use of Eqs. (32), (33) and (37) as

$$\omega_{MT} = -1 - \left(\frac{mkt + k_1}{3k} \right) \left\{ \frac{2D(\delta - 2) \left(\frac{k}{mkt + k_1} \right)^{-2\delta+3} \left[\frac{mk^2}{(mkt + k_1)^2} \right] + \frac{2m^2k^3E}{(mkt + k_1)^3}}{D \left(\frac{k}{mkt + k_1} \right)^{-2\delta+4} + E \left[\frac{-mk^2}{(mkt + k_1)^2} \right]} \right\}. \quad (38)$$

From Fig.5, it is observed that $\omega_{MT} > -1$. Thus, our model 1 behaves like a quintessence dark energy model. The present value of the EOS is calculated as $\omega_0 = -0.834$ [43-45] and this concludes that the model 1 is a quintessence dark energy model.

Correspondence between model 1 and quintessence scalar field.

The pressure and energy density for quintessence scalar field [46] are given by

$$p_\phi = \frac{\dot{\phi}^2}{2} - V(\phi) \quad (39)$$

$$\rho_\phi = \frac{\dot{\phi}^2}{2} + V(\phi), \quad (40)$$

where ϕ denotes the scalar field and $V(\phi)$ is the scalar field potential.

The EOS parameter ω_ϕ is defined as

$$\omega_\phi = \frac{p_\phi}{\rho_\phi} = \frac{\dot{\phi}^2 - 2V(\phi)}{\dot{\phi}^2 + 2V(\phi)}. \quad (41)$$

Eqs. (33) and (40) together implies

$$D \left(\frac{k}{mkt + k_1} \right)^{-2\delta+4} + E \left[\frac{-mk^2}{(mkt + k_1)^2} \right] = \frac{\dot{\phi}^2}{2} + V(\phi). \quad (42)$$

Eqs. (38) and (41) together implies

$$\frac{\dot{\phi}^2}{2} = \left(\frac{1 + \omega_{MT}}{1 - \omega_{MT}} \right) V(\phi). \quad (43)$$

Using Eq. (43) in Eq. (42), we obtain the scalar field potential $V(\phi)$ as

$$V(\phi) = \left(\frac{1 - \omega_{MT}}{2} \right) \left\{ D \left(\frac{k}{mkt + k_1} \right)^{-2\delta+4} - \frac{Emk^2}{(mkt + k_1)^2} \right\}. \quad (44)$$

The scalar field ϕ is calculated by using Eqs. (43) and (44) and then integrating, we get

$$\phi = \phi_0 + \int \left[(1 + \omega_{MT}) \left\{ D \left(\frac{k}{mkt + k_1} \right)^{-2\delta+4} - \frac{Emk^2}{(mkt + k_1)^2} \right\} \right]^{1/2} dt, \quad (45)$$

where ϕ_0 is the constant of integration.

Both the scalar field potential $V(\phi)$ and the scalar field ϕ diminishes and ultimately tends to a small value during the evolution of the Universe as seen from Fig.6 and 7.

5. Model 2. When $a = \exp\{k(t - k_2)\}$, $m = 0$. Eq. (27) with $a = \exp\{k(t - k_2)\}$ implies

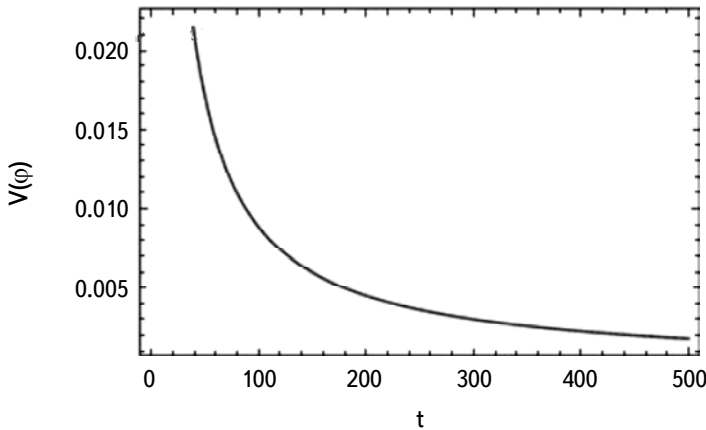


Fig.6. The plot of $V(\phi)$ versus t for $m = 0.5$, $k = 0.3$, $k_1 = 0.5$, $\delta = 1.5$, $\rho_0 = 0.8$, $D = 0.5$ and $E = 0.2$.

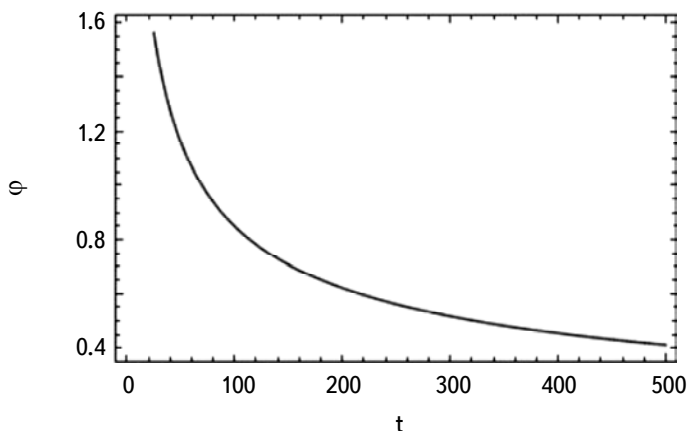


Fig.7. The evolution of ϕ against cosmic time t for $m = 0.5$, $k = 0.3$, $k_1 = 0.5$, $\delta = 1.5$, $\rho_0 = 0.8$, $D = 0.5$, $E = 0.2$ and $\phi_0 = 0.05$.

$$K = u_1 I \exp \left[u_0 \int \frac{e^{-t}}{\exp \{3k(t-k_2)\}} dt \right] \quad (46)$$

$$V = I^2 K = a^3 = \exp \{3k(t-k_2)\}. \quad (47)$$

Eqs. (46) and (47) together implies

$$I = u_1^{-1/3} \exp \left[\frac{-u_0}{3} \int \frac{e^{-t}}{\exp \{3k(t-k_2)\}} dt \right] \exp \{k(t-k_2)\} \quad (48)$$

$$K = u_1^{2/3} \exp \left[\frac{2u_0}{3} \int \frac{e^{-t}}{\exp \{3k(t-k_2)\}} dt \right] \exp \{k(t-k_2)\}. \quad (49)$$

Fig.8 demonstrates that the cosmic scale factors I and K increases as cosmic time evolves. The Hubble parameter H and the MTHDE density ρ_{MT} are calculated as

$$H = k \quad (50)$$

$$\rho_{MT} = Dk^{-2\delta+4}. \quad (51)$$

From Eqs. (50) and (51), we can conclude that both Hubble parameter H and MTHDE density ρ_{MT} are constant.

The energy conservation equation for dark matter is

$$\dot{\rho}_m + 3H\rho_m = 0. \quad (52)$$

Using Eq. (50) in Eq. (52), ρ_m is found as

$$\rho_m = \rho'_0 e^{-3kt}, \quad (53)$$

where ρ'_0 is a constant of integration.

From Fig.9, we can conclude that $\rho_m \rightarrow 0$ as cosmic time evolves.

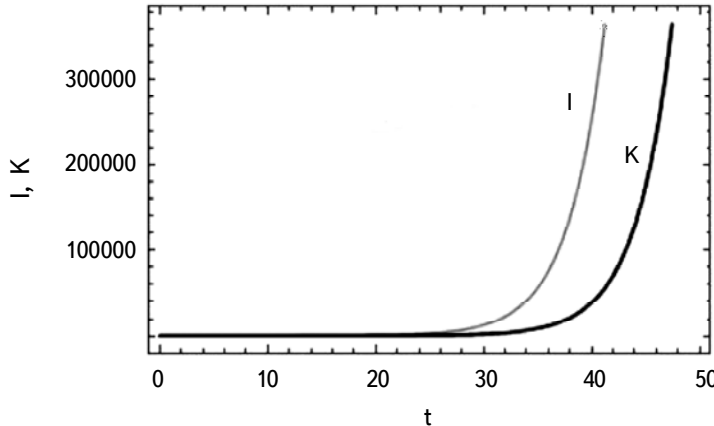


Fig.8. The plot of I and K versus cosmic time t for $k = 0.3$, $k_2 = 0.6$, $u_0 = 0.03$ and $u_1 = 0.15$.

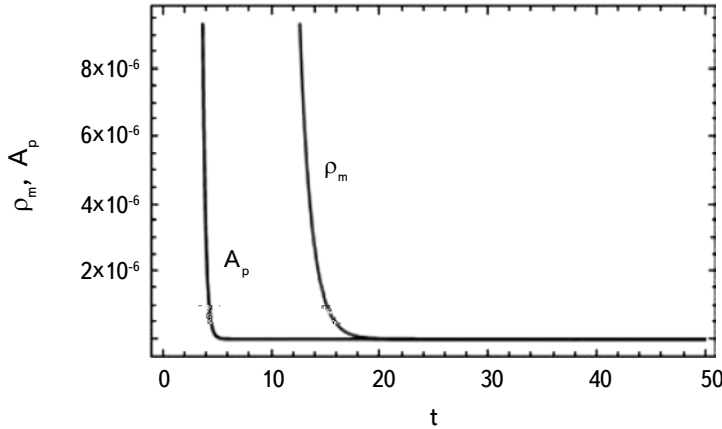


Fig.9. The graph of ρ_m and A_p versus cosmic time t for $\rho'_0 = 0.8$, $k = 0.3$ and $k_2 = 0.6$.

The energy conservation equation for MTHDE is

$$\dot{\rho}_{MT} + 3H(\rho_{MT} + p_{MT}) = 0. \quad (54)$$

Using Eqs. (50) and (51) in Eq. (54), we have obtained ω_{MT} as

$$\omega_{MT} = -1. \quad (55)$$

Thus, our Model 2 behaves like a cosmological constant model. Recent studies [5,47-50] indicate that our model 2 approaches to Λ CDM ($\omega_{MT} = -1$) served as an excellent model to describe the cosmological evolution. Hence our model 2 is in good agreement with these observations.

The anisotropy parameter A_p is obtained as

$$A_p = \frac{2}{9k^2} e^{-\{2t+6k(t-k_2)\}}. \quad (56)$$

Fig.9 indicates that as $t \rightarrow 0$, $A_p \rightarrow \infty$ and as $t \rightarrow \infty$, $A_p \rightarrow 0$. Hence, the anisotropy of our Universe dies out with the passage of cosmic time.

In all the graphs, t denotes cosmic evolution time, generally measured in giga years ($1 \text{ Gyr} = 10^9 \text{ y}$) along x axis. Along y axis, all physical quantities like the matter energy density ρ_m , MTHDE density ρ_{MT} , EOS parameter ω_{MT} , etc. are measured in geometrized units, where the speed of light $c=1$ and the gravitational constant $G=1$.

6. Graphical discussions of model 1.

I and K are increasing functions of t as observed from Fig.1 and 2.

Both H and A_p are decreasing functions of t as observed from the above figure.

H tends to a small value whereas $A_p \rightarrow 0$ at the later age of the Universe.

Both ρ_m and ρ_{MT} decreases with the passage of t . ρ_m approaches to zero whereas ρ_{MT} approaches to small value at the later epoch.

From the above figure, we can conclude that $\omega_{MT} > -1$ at the late times. This indicates that our model 1 behaves like a quintessence dark energy model.

The scalar field potential $V(\phi)$ decreases and ultimately approaches to a small value as cosmic time evolves.

ϕ tends to a small value at the later age of the Universe as observed from the above figure.

7. Graphical discussions of model 2.

I and K increases with the passage of cosmic time as observed from Fig.8.

Both ρ_m and A_p are decreasing functions of t and tends to zero at the later age of the Universe.

8. *Conclusions.* In this paper we have studied a Bianchi type III Universe filled with dark matter and MTHDE in General Relativity. To determine the solutions of the field equations completely, we make use of a special law of variation of Hubble parameter H proposed by Berman that yields constant DP. Interestingly, we have obtained two different cosmological models for two different constant values of DP. The EOS parameter of MTHDE also behaves like quintessence DE for model 1. Using these results, we have established a correspondence between MTHDE model with the quintessence scalar field. Quintessence potential and the dynamics of the quintessence scalar field are reconstructed for this anisotropic accelerating model of the Universe. Furthermore, it is observed from Eq. (55) that for large cosmic time the EOS parameter of the MTHDE for model 2 becomes -1. Therefore, in the late time evolution of the Universe, our model 2 behaves like a cosmological constant model. Also, the deceleration parameter appears with negative sign which implies accelerating expansion of the Universe. Perlmutter et al. [3] and Riess et al. [1,51,52] proved that the deceleration parameter of the Universe is in the range $-1 \leq q \leq 0$, and the present-day Universe is undergoing an accelerated expansion. From Fig.4 and 9, we see that the anisotropy parameter $A_p \rightarrow 0$ as $t \rightarrow \infty$. Hence, for sufficiently large time, our MTHDE models predict that the anisotropic nature vanishes and it will become isotropic at late times. This implies that our MTHDE models become isotropic at late times even though the space-time is anisotropic. Our results show that the Universe is anisotropic in the early stage and at the late time dynamics anisotropy of the Universe damps out and the present day Universe becomes isotropic as suggested by different observational data. We have found that the results are consistent with current cosmological observational data. The models presented in this paper could give an appropriate description of the evolution of the Universe.

¹ Department of Mathematics, Handique Girls' College, Assam (India),
e-mail: jumibharali2@gmail.com

² Department of Mathematics, Gauhati University, Assam (India),
e-mail: kallol@gauhati.ac.in

МОДИФИЦИРОВАННАЯ ГОЛОГРАФИЧЕСКАЯ ТЕМНАЯ ЭНЕРГИЯ ЦАЛЛИСА

Дж.БХАРАЛИ, К.ДАС

В данной работе мы предлагаем модифицированную голографическую темную энергию (MTHDE) Цаллиса в общей теории относительности (OTO) в рамках пространства-времени типа Бьянки III. Уравнения поля Эйнштейна решаются с использованием специального закона вариации параметра Хаббла H , предложенного Берманом, который приводит к постоянному параметру замедления (DP). Интересно, что для двух разных постоянных значений параметра замедления мы получаем две различные космологические модели. Модель 1 ведет себя как модель квинтэссенции темной энергии, тогда как модель 2 ведет себя как модель космологической постоянной. Устанавливается соответствие между моделью 1 и квинтэссенциальным скалярным полем. Проводится реконструкция кинематики квинтэссенции потенциала и скалярного поля, иллюстрирующая ускоряющуюся фазу Вселенной. Тщательно обсуждаются различные параметры, такие как параметр замедления, параметр Хаббла, параметр анизотропии, параметр уравнения состояния (EOS) и др. для обеих космологических моделей. Полученные результаты оказываются согласованными с последними наблюдениями современной Вселенной.

Ключевые слова: *MTHDE: OTO: параметр Хаббла: параметр замедления DP*

REFERENCES

1. *A.G.Riess et al.*, Astron. J., **116**, 1009, 1998.
2. *S.Perlmutter et al.*, Nature, **391**, 51, 1998.
3. *S.Perlmutter et al.*, Astrophys. J., **517**, 565, 1999.
4. *C.L.Bennett et al.*, Astrophys. J. Suppl. Ser., **148**, 1, 2003.
5. *D.N.Spergel et al.*, Astrophys. J. Suppl. Ser., **148**, 175, 2003.
6. *M.Tegmark et al.*, Phys. Rev. D, **69**, 103501, 2004.
7. *S.Weinberg*, Rev. Mod. Phys., **61**, 1, 1989.
8. *J.M.Overduin, F.I.Cooperstock*, Phys. Rev. D, **58**, 043506, 1998.
9. *T.Barreiro, E.J.Copeland, N.J.Nunes*, Phys. Rev. D, **61**, 127301, 2000.
10. *R.R.Caldwell, M.Kamionkowski, N.N.Weinberg*, Phys. Rev. Lett., **91**, 071301, 2003, arXiv: astro-ph /0302506v1.
11. *C.Armendariz-Picon, V.Mukhanov, P.J.Steinhardt*, Phys. Rev. D, **63**, 103510, 2001.

12. *J.S.Bagla, H.K.Jassal, T.Padmanabhan*, Phys. Rev. D, **67**, 063504, 2003.
13. *M.Li*, Phys. Lett. B, **603**, 1, 2004.
14. *M.Sharif, S.Rani*, Astrophys. Space Sci., **345**, 217, 2013.
15. *M.Sharif, S.Rani*, Astrophys. Space Sci., **346**, 573, 2013.
16. *E.V.Linder*, Phys. Rev. D, **81**, 127301, 2010.
17. *C.Brans, R.H.Dicke*, Phys. Rev., **124**, 925, 1961.
18. *S.Dutta, E.N.Saridakis*, JCAP, **1005**, 013, 2010.
19. *L.Susskind*, J. Math. Phys., **36**, 6377, 1995.
20. *C.Tsallis, L.J.L.Cirto*, Eur. Phys. J. C, **73**, 2487, 2013.
21. *M.Tavayef et al.*, Phys. Lett. B, **781**, 195, 2018.
22. *A.G.Cohen, D.B.Kaplan, A.E.Nelson*, Phys. Rev. Lett., **82**(25), 4971, 1999.
23. *B.Guberina, R.Horvat, H.Nikolić*, JCAP, **01**, 012, 2007.
24. *S.Ghaffari, M.H.Dehghani, A.Sheykhi*, Phys. Rev. D, **89**, 123009, 2014.
25. *A.S.Jahromi et al.*, Phys. Lett. B, **780**, 21, 2018.
26. *S.Chen, J.Jing*, Phys. Lett. B, **679**, 144, 2009.
27. *S.V.Ketov*, arXiv: 1909.05599v1 [hep-th], 2019.
28. *M.A.Zadeh, A.Sheykhi, H.Moradpour*, Mod. Phys. Lett. A, **34**, 1950086, 2019.
29. *A.Dixit, U.K.Sharma, A.Pradhan*, New Astron., **73**, 101281, 2019.
30. *A.A.Mamon*, arXiv: 2007.01591 [gr-qc], 2020.
31. *J.Sadeghi, S.N.Gashti, T.Azizi*, arXiv: 2203.04375v1 [gr-qc], 2022.
32. *A.Pradhan, G.Varshney, U.K.Sharma*, Can. J. Phys., **99**, 866, 2021.
33. *A.A.Mamon, A.H.Ziaie, K.A.Bamba*, Eur. Phys. J. C, **80**, 974, 2020.
34. *V.C.Dubey et al.*, Int. J. Geom. Methods Mod. Phys., **17**(1), 2050011, 2020.
35. *M.Korunur*, Mod. Phys. Lett. A, **34**(37), 1950310, 2019.
36. *A.K.Yadav*, Eur. Phys. J. C, **81**, 8, 2021.
37. *M.V.Santhi, Y.Sobhanbabu*, Eur. Phys. J. C, **80**, 1198, 2020.
38. *V.C.Dubey et al.*, Pramana, **93**(5), 1-10, 2019.
39. *V.C.Dubey, U.K.Sharma, A.Beesham*, Int. J. Mod. Phys. D, **28**(15), 1950164, 2019.
40. *J.Bharali, K.Das*, Astrophysics, **64**, 512, 2021.
41. *M.S.Berman*, Nuovo Cimento B, **74**, 182, 1983.
42. *K.S.Adhav*, Int. J. Astron. Astrophys., **1**, 204, 2011.
43. *A.A.Mamon, K.Bamba, S.Das*, Eur. Phys. J. C, **77**, 29, 2017.
44. *Ö.Akarsu et al.*, JCAP, **01**, 022, 2014.
45. *G.Hinshaw et al.*, ApJS, **208**, 19, 2013.
46. *A.Sangwan, A.Mukherjee, H.K.Jassal*, JCAP, **01**, 018, 2018.
47. *A.G.Riess et al.*, Astrophys. J., **659**, 98, 2007.
48. *D.J.Eisenstein et al.*, Astrophys. J., **633**, 560, 2005.
49. *P.Astier et al.*, Astron. Astrophys., **447**, 31, 2006.
50. *K.Bamba et al.*, Astrophys. Space Sci., **342**, 155, 2012.
51. *A.G.Riess et al.*, Astron. J., **117**, 707, 1999.
52. *A.G.Riess et al.*, Astrophys. J., **607**, 665, 2004.

АСТРОФИЗИКА

ТОМ 66

АВГУСТ, 2023

ВЫПУСК 3

DOI: 10.54503/0571-7132-2023.66.3-415

RENYI HOLOGRAPHIC DARK ENERGY AND ITS BEHAVIOUR IN $f(G)$ GRAVITY

M.K.ALAM, S.S.SINGH, L.A.DEVI

Received 10 April 2023

Accepted 18 August 2023

In this work, the Renyi holographic dark energy (RHDE) and its behaviour has been explored with the anisotropic and spatially homogeneous Bianchi type-I Universe in the framework of $f(G)$ gravity. We use IR cutoff as the Hubble and Granda-Oliveros (GO) horizons. To find a consistent solutions of the field equations of the models, it is assumed that the deceleration parameter is defined in terms of function of Hubble parameter H . With reference to current cosmological data, the behaviors of the cosmological parameters relating to the dark energy model are evaluated and their physical significance is examined. It is observed that for both the models, the equation of state parameter approaches to -1 at late times. However, the RHDE model with the Hubble horizon exhibits stability from the squared sound speed, but the RHDE model with the GO horizon exhibits instability. In both the models, deceleration parameter and statefinder diagnostic confirm the accelerated expansion of the Universe and also correspond to the Λ CDM model at late times.

Keywords: *Bianchi type-I metric: $f(G)$ gravity: Renyi holographic dark energy: cosmology*

1. Introduction. General relativity (GR) is regarded as a key theory to comprehend several complexities of gravitational influences that offer a fundamental explanation of astrophysical events as well as the cosmos. The most significant truth that the Universe suffers early inflation as well as late-time accelerated expansion has been revealed by a number of observational findings in recent years [1-6]. The exotic substance of extremely high negative pressure known as dark energy (DE) which is the cause of the Universe's expansion at an accelerated rate that accounts for 68 percent of the known Universe total density. Its nature continues to be a mystery still. The cosmological constant Λ , which Einstein incorporated into the field equations in General Relativity, provides the straightforward argument for DE. This cosmological constant is thought to be extremely compatible with the observational data and has an equation of state (EoS) parameter of $\omega = -1$. Some dynamic models of DE, such as quintessence [7,8], phantom [9], k -essence [10], tachyons [11], Chaplygin gas [12], etc, have been proposed in response to the challenges associated with its theoretically expected order of magnitude with respect to that of the vacuum energy [13]. Another categories of dynamic DE models allow us to accelerate the expansion without

introducing any form of energy. These categories are known as modified gravity theories, which give an accelerated expansion through a modification in the action such as $f(T)$ gravity, $f(R, T)$ gravity, $f(R, G)$ gravity, $f(T, T)$ gravity and $f(R, T, R_{\mu\nu}, T^{\mu\nu})$ gravity where T is the trace of the energy-momentum tensor, $R_{\mu\nu}$ is the Ricci tensor and G is the Gauss-Bonnet (GB) invariant [14-17]. Modified GB gravity, also known as $f(G)$ gravity, is one of the modified forms of GR that uses an arbitrary function of G , a quadratic invariant of the Gauss-Bonnet equation in the Einstein-Hilbert action [18]. The motivation for $f(G)$ theory is mostly based on string theory via low energy effective scale [19]. Nojiri and Odintsov [20] studied the cosmological reconstruction of different modified gravities in detail and the occurrence of Big Rip and other finite-time future singularities in modified gravity was found. This approach effectively explains the accelerated expansion of the Universe which change from the decelerating to accelerating phase, satisfactory system tests, essential for Sadjadi's explanation of thermodynamics [21] and characterization of all possible four types of future singularities by Bamba et al. [22]. Thus one can construct feasible and consistent general theory of relativity models with local constraints by using $f(G)$. Myrzakulov et al. [23] investigated this theory to examine the DE as well as the inflationary era. The reconstruction scenario of the most recent agegraphic dark energy (NADE) model and the $f(G)$ theory within the flat FRW space-time was taken into consideration by Jawad et al. [24]. Shamir [25] reviewed the anisotropic space-time in $f(G)$ gravity. Sharif and Fatima [26] studied energy conditions in $f(G)$ theory. Shaikh et al. [27] studied LRS Bianchi type-I models with holographic dark energy (HDE) within $f(G)$ theory of gravity using different scale factors. Nojiri et al. [28] reviewed the latest developments of modified gravity in cosmology, emphasizing on inflation, bouncing cosmology and late-time acceleration era. Koussour et al. [29] compared HDE in $f(G)$ gravity within Bianchi type-I space-time with the Λ CDM model by analysing the jerk parameter.

Particularly among the different dynamical DE models, the HDE model has recently emerged as an effective method for researching the DE riddle. It was put forth based on the quantum characteristics of black holes (BH), which have been thoroughly studied in the literature to research quantum gravity [30,31]. By holographic principle, we know that in a system with size L , bound on the vacuum energy Λ must be under the limit of same size of the BH mass because of the formation of BH in quantum field theory. The energy density of HDE is defined as $\rho_\Lambda = 3d^2 m_p^2 L^{-2}$ where m_p is the reduced Planck mass, $3d^2$ numerical constant and L is IR-cutoff (Cohen et al. [32]). In the literature, various types of IR-cutoff have been investigated, for example Hubble horizon H^{-1} , particle horizon, event horizon, Ricci scalar radius, conformal Universe age and Granda-Oliveros cutoff [33-36]. Several HDE models with different IR-cutoffs may provide the

recent accelerated expansion of the Universe and demonstrate that transition from early decelerated epoch ($q > 0$) to current accelerated epoch ($q < 0$) is in consistent with recent observational data. It can also resolve the problem of cosmic coincidence [37]. Number of studies suggested that the HDE model and observational data are in a fair amount of agreement [38-41]. By using generalized HDE and phantom cosmology, Nojiri and Odintsov [42] suggested a method to unify the early phase as well as late-time epochs of Universe, and they also advocate for generalized concept as Hinflation [43]. Based on several formalism of entropy, HDE models are formulated such as Tsallis HDE (THDE) [44], Sharma-Mittal HDE (SMHDE) [45] and Renyi HDE model (RHDE) [46]. Among these models, the new dark energy model proposed by Moradpour et al. [46] named the Renyi holographic dark energy (RHDE) model for the cosmological and gravitational investigations shows more stability by itself. Several researchers have discussed RHDE in different theories of gravity. Using the Renyi entropy, the modified Friedmann equations are obtained [47-49]. The inflation may be found in the Renyi formalism suggested by Ghaffari et al. [50]. THDE model is unstable at the classical level, whereas SMHDE and RHDE are stable in the case of non-interacting cosmos. Prasanthi and Aditya [51] studied RHDE in Bianchi type VI0 space-time and found that the Hubble cutoff is stable whereas the Granda-Oliveros cutoff is unstable. They also constrained the observational values of RHDE in Kantowski-Sachs Universe [52]. Shekh [53] studied holographic and Renyi holographic dark energy models with the help of FLRW line element in $f(Q)$ gravity. Nojiri et al. [54] investigated the holographic approach to describe the early-time acceleration and the late-time acceleration eras of our Universe in a unified manner. Nojiri et al. [55] showed that the Barrow entropic DE model is equivalent to the generalized HDE where the respective holographic cutoff is determined by two ways (a) in terms of particle horizon and its derivative and (b) in terms of future horizon and its derivative.

Since anisotropy was crucial in the early stages of cosmic evolution, the anisotropic Universe has recently caught the interest of many physicists. Additionally, the cosmic microwave background (CMB) anomalies from the Planck data [18], which were acquired, supported the notion of an anisotropy phase at the beginning of the Universe followed by an isotropy phase. The Bianchi type-I model has been examined by a number of researchers [56-59]. Based on the aforementioned studies, we investigate the Renyi holographic model of DE with $f(G)$ gravity in the Bianchi type-I Universe in this paper. In order to solve the field equations and determine various physical variables, we shall assume that the deceleration parameter (DP) is a function of the Hubble parameter H . Following is the breakdown of the paper. The introduction is found in Sect. 1. We construct the action of $f(G)$ gravity and the field equation in Sect. 2. We have developed

the Bianchi type-I metric and provided a few physical and geometrical parameters in Sect. 3. In Sect. 4, we studied the models of Renyi holographic dark energy Sect. 5 explain about the cosmological parameters. In Sect. 6, we examine the equivalence between the Granda-Oliveros HDE of the present work and the generalized HDE. A conclusion is included in the final section 7.

2. Formulation of Gauss-Bonnet gravity. The $f(G)$ gravity's modified Einstein-Hilbert action is configured [60] as follows

$$S = \frac{1}{2\kappa^2} \int d^4x \sqrt{-g} [R + f(G)] + S_M(g^{\mu\nu}, \psi). \quad (1)$$

In this case, g denotes the determinant of metric tensor $g^{\mu\nu}$, κ is the coupling constant, $f(G)$ is a general differentiable function of GB invariant, R is the Ricci scalar, S_M stands for a matter action which is a function of a space-time metric $g_{\mu\nu}$ and matter fields ψ . The equation of invariant GB quantity is given as

$$G = R^2 - 4R_{\mu\nu}R^{\mu\nu} + 4R_{\mu\nu\alpha\beta}R^{\mu\nu\alpha\beta}. \quad (2)$$

By varying the action (1) w.r.t. $g_{\mu\nu}$ shows the resulting equation

$$\begin{aligned} G_{\mu\nu} + 8[R_{\mu\rho\nu\sigma} + R_{\rho\nu}g_{\sigma\mu} - R_{\rho\sigma}g_{\nu\mu} - R_{\mu\nu}g_{\sigma\rho} + R_{\mu\sigma}g_{\nu\sigma\mu} \\ + \frac{1}{2}R(g_{\mu\nu}g_{\sigma\rho} - g_{\mu\sigma}g_{\nu\rho})] \nabla^\rho \nabla^\sigma f_G + (Gf_G - f)g_{\mu\nu} = \kappa^2 T_{\mu\nu}, \end{aligned} \quad (3)$$

where ∇_μ denotes covariant differentiation, the Einstein tensor, $G_{\mu\nu} = R_{\mu\nu} - Rg_{\mu\nu}/2$, $T_{\mu\nu}$ is the usual energy momentum tensor of matter fluid and f_G stands for the derivation of f with respect to G .

3. Field equations and solutions. As observations highlight the possibility of anisotropic behavior of Universe, the geometry of the spatially homogenous and anisotropic Bianchi type-I space-time, represented by the following metric is considered

$$ds^2 = dt^2 - A^2(t)dx^2 - B^2(t)(dy^2 + dz^2). \quad (4)$$

Here A and B are time dependent functions. Thus for this LRS Bianchi type-I metric, the Ricci scalar R and GB invariant are respectively obtained as

$$R = -2 \left[\frac{\ddot{A}}{A} + 2 \frac{\ddot{B}}{B} + 2 \frac{\dot{A}\dot{B}}{AB} + \frac{\dot{B}^2}{B^2} \right], \quad (5)$$

$$G = 8 \left[\frac{\ddot{A}\dot{B}^2}{AB^2} + 2 \frac{\dot{A}\dot{B}\ddot{B}}{AB^2} \right]. \quad (6)$$

The matter and holographic dark energy have the energy momentum tensors in the form

$$T_{\mu\nu} = \rho_m u_\mu u_\nu + g_{u_\mu u_\nu} p_\Lambda . \quad (7)$$

and

$$\tilde{T}_{\mu\nu} = (\rho_\Lambda + p_\Lambda) u_\mu u_\nu + g_{u_\mu u_\nu} p_\Lambda . \quad (8)$$

where ρ_m and ρ_Λ are the energy densities of matter and holographic dark energy respectively and p_Λ is the pressure of the HDE. In this Bianchi type-I metric (4), the field equations (3) with the (7) and (8) give us the system of field equations given below

$$-2\frac{\ddot{B}}{B} - \frac{\dot{B}^2}{B^2} + 16\frac{\dot{B}\ddot{B}}{B^2} \dot{f}_G + 8\frac{\dot{B}^2}{B^2} \ddot{f}_G - Gf_G + f = \kappa^2 p_\Lambda , \quad (9)$$

$$-\frac{\ddot{A}}{A} - \frac{\ddot{B}}{B} - \frac{\dot{A}\dot{B}}{AB} + 8\left(\frac{\dot{A}\dot{B}}{AB} + \frac{\ddot{A}\dot{B}}{AB}\right) \dot{f}_G + 8\frac{\dot{A}\dot{B}}{AB} \ddot{f}_G - Gf_G + f = \kappa^2 p_\Lambda , \quad (10)$$

$$2\frac{\dot{A}\dot{B}}{AB} + \frac{\dot{B}^2}{B^2} - 24\frac{\dot{A}\dot{B}^2}{AB^2} \dot{f}_G + Gf_G - f = \kappa^2 (\rho_m + \rho_\Lambda) , \quad (11)$$

As we know, a dot (.) denote the derivation of the time t . The average scale factor $a(t)$ and the spatial volume V are defined by

$$V = a^3 = AB^2 . \quad (12)$$

The general form of average Hubble parameter H is defined as

$$H = \frac{\dot{a}}{a} = \frac{1}{3}(H_1 + 2H_2) . \quad (13)$$

Here $H_1 = \dot{A}/A$ and $H_2 = H_3 = \dot{B}/B$ are directional Hubble parameter along x , y and z axes respectively.

The continuity equation can be obtained as

$$\dot{\rho}_m + \dot{\rho}_\Lambda + 3H(\rho_m + \rho_\Lambda + p_\Lambda) = 0 . \quad (14)$$

The continuity equations of the matter and HDE are respectively obtained as

$$\dot{\rho}_m + 3H\rho_m = 0 \quad (15)$$

and

$$\dot{\rho}_\Lambda + 3H(\rho_\Lambda + p_\Lambda) = 0 . \quad (16)$$

Applying the relation $p_\Lambda = \omega_\Lambda \rho_\Lambda$, the barotropic equation of state, the EoS HDE parameter can be found from (16) as

$$\omega_\Lambda = -1 - \frac{\dot{\rho}_\Lambda}{3H\rho_\Lambda} . \quad (17)$$

In this work, we assume that the function $f(G)$ obeys the power law models introduced by Cognola et al. [19]

$$f(G) = \eta G^{n+1} , \quad (18)$$

where η and n are arbitrary constants. The possibility of disappearing Big Rip singularity and the ability to anticipate the occurrence of a transient phantom epoch that is consistent with the observational data are the main factors for choosing this power law $f(G)$ model. For the Bianchi type-I Universe (4), deceleration parameter q , the scalar expansion θ , the shear scalar σ^2 and the average anisotropy parameter A_m have the form

$$q = -\frac{a\ddot{a}}{\dot{a}^2} = \frac{d}{dt}\left(\frac{1}{H}\right) - 1, \quad (19)$$

$$\theta = 3H = \frac{\dot{A}}{A} + 2\frac{\dot{B}}{B}, \quad (20)$$

$$\sigma^2 = \frac{1}{2} \left[\sum_{i=1}^3 H_i^2 - 3H^2 \right], \quad (21)$$

$$A_m = \frac{1}{3} \sum_{i=1}^3 \left(\frac{H_i - H}{H} \right)^2. \quad (22)$$

Here, we take into account the expansion scalar θ is directly proportional to the shear scalar σ , which results for following relationship between the metric potentials:

$$A = B^m. \quad (23)$$

Here, positive constant m accounts for the anisotropic evolution of space-time. When $m = 1$, the model is isotropic; else it is anisotropic. Logic behind this condition is described with reference to [61]. Observational evidence indicates the current isotropic expansion of Universe by about $\approx 30\%$ [62]. More specifically, redshift studies set the limit at $\sigma/H \leq 0.3$, in the neighbourhood of our present day galaxy. According to Collins et al. [63], the normal congruence follows the above condition (σ/H is constant) for a spatially homogenous space-time. In accordance with recent data, we are also interested in finding an acceptable cosmological explanations that show a transition from early deceleration to late acceleration. To solve this problem, a number of different assumptions can be used. Observations demonstrate the advance of Universe through a phase change from the earlier decelerating expansion to the present accelerating one, which is the reason for accounting for the time-dependent deceleration parameter q . The q is a geometrical parameter that, depending on its sign, depicts the Universe acceleration or deceleration. For this scenario, we understand that the Universe experiences accelerating expansion for $q < 0$; when $q > 0$, the Universe experiences decelerating expansion; when $q = 0$, constant expansion of Universe is shown whereas $q < -1$ stands for super-exponential expansion. As a result of the foregoing, we decided to use deceleration parameter q as a function of the Hubble parameter

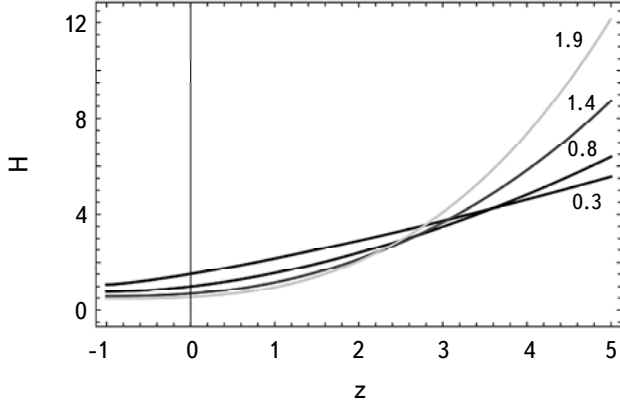


Fig.1. Hubble parameter H versus redshift z for $k_1 = 0.5$, $\beta = 1.4$ and $\alpha = 0.3, 0.8, 1.4, 1.9$.

H as proposed by Tiwari [64]

$$q = \alpha - \frac{\beta}{H}, \quad (24)$$

where α and β are constants. The desired transition from positive to negative is achieved by this form of the deceleration parameter. The scale factor and Hubble parameter can be calculated using equation (24) as follows

$$a = k_1 (e^{\beta t} - 1)^{1/(1+\alpha)}, \quad (25)$$

where k_1 is the integration constant. From equation (25), in order to have an expanding Universe, we can deduce that $\alpha > -1$, $\beta > 0$. Also the scale factors vanishes at $t = 0$, hence our model has a point type singularity at the early Universe. From this above equation, we can immediately derive the spatial volume as $V = k_1^3 (e^{\beta t} - 1)^{3/(1+\alpha)}$, which has value zero in the beginning and increases with increase of t , which shows that our model is expanding with time. And

$$H = \frac{\beta e^{\beta t}}{(1 + \alpha)(e^{\beta t} - 1)}. \quad (26)$$

From this equation, we can understand that at the beginning, H is infinite and with the passage of time it decreases to a constant value $\beta/(1 + \alpha)$. Using equations (23) and (25) in equation (12), the metric potentials A and B are found as

$$A = k_1^{3m/(m+2)} (e^{\beta t} - 1)^{3m/(1+\alpha)(m+2)}, \quad (27)$$

$$B = k_1^{3/(m+2)} (e^{\beta t} - 1)^{3/(1+\alpha)(m+2)}. \quad (28)$$

With the use of above metric potentials, the metric (4) can now be expressed as

$$ds^2 = dt^2 - \left[k_1 (e^{\beta t} - 1)^{1/(1+\alpha)} \right]^{6m/(m+2)} dx^2 - \left[k_1 (e^{\beta t} - 1)^{1/(1+\alpha)} \right]^{6/(m+2)} (dy^2 + dz^2). \quad (29)$$

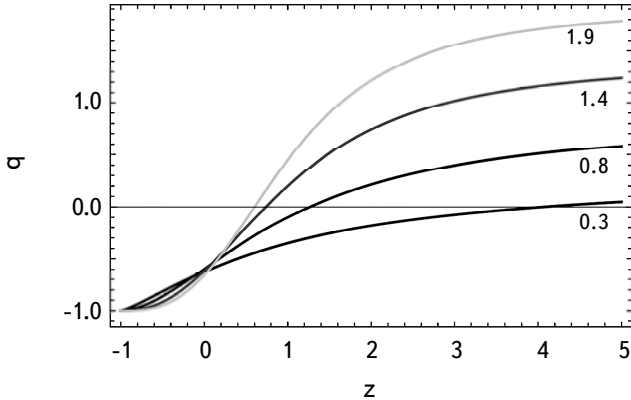


Fig.2. Deceleration parameter q versus redshift z for $k_1 = 0.5$, and $\alpha = 0.3, 0.8, 1.4, 1.9$.

Equation (29) represents the spatially homogeneous and anisotropic Bianchi type-I RHDE model in the context of $f(G)$ gravity with the following properties together with the physical parameters described below. Using equation (26) in equation (24), we have

$$q = -1 + \frac{1+\alpha}{e^{\beta t}}. \quad (30)$$

From this equation we can deduce that at the beginning, $q = \alpha$, a constant and with the increase of time, it approaches to -1 at late times, which shows that our model has a transition to acceleration. The relation $\alpha(t) = 1/(1+z)$, where z is the redshift, yield us the relationship as below

$$t(z) = \frac{1}{\beta} \log \left[1 + \frac{1}{\{k_1(1+z)\}^{1+\alpha}} \right]. \quad (31)$$

Additionally, redshift z can be used to express the Hubble parameter H as

$$H(z) = \frac{\beta}{1+\alpha} \left[1 + \{k_1(1+z)\}^{1+\alpha} \right]. \quad (32)$$

Fig.1 depicts the behavior of the Hubble parameter as a function of redshift at various α values (i.e. $\alpha \geq 0.3$). According to this graph, the Hubble parameter has a positive relationship with redshift. At the present, when ($z=0$), the Hubble parameter is strictly positive, and for the early Universe, when ($z > 0$), it increases as z increases. Also for $\alpha = 1.4$, the current value of H has been noted as $70.71 \text{ Kms}^{-1} \text{ Mpc}^{-1}$ which is in agreement with the observational value [65]. Similarly, we get the deceleration parameter q in terms of redshift z as

$$q(z) = -1 + \frac{(1+\alpha)\{k_1(1+z)\}^{1+\alpha}}{1 + \{k_1(1+z)\}^{1+\alpha}}. \quad (33)$$

The $q(z)$ exhibits two epochs throughout the Universe: the initial deceleration phase and the current acceleration phase, as shown in Fig.2, which depicts the parameter's behaviour in terms of redshift. In this study, $\alpha \geq 0.3$ is required to produce both phases. The change from the initial deceleration phase to the present accelerated phase is also accomplished with a specific redshift, called the transition redshift z . According to the graph, the transition redshift for $\alpha = 1.4$ is $z_{tr} = 0.73$. Also the value of q is found to be -0.6 in present time. Therefore, the results of our findings are in agreement with the observational values [65].

The expressions of scalar expansion θ , shear scalar σ^2 and the average anisotropy parameter A_m are therefore obtained as

$$\theta = \frac{3\beta e^{\beta t}}{(1+\alpha)(e^{\beta t}-1)}, \quad (34)$$

$$\sigma^2 = \frac{3\beta^2 e^{2\beta t}}{(1+\alpha)^2 (e^{\beta t}-1)^2} \frac{(m-1)^2}{(m+2)^2}, \quad (35)$$

$$A_m = \frac{2(m-1)^2}{(m+2)^2}. \quad (36)$$

From equations (34) and (35), we can deduce that the scalar expansion and the shear scalar diverge at $t \rightarrow 0$, then tends to respective constant values $\theta = 3\beta/(1+\alpha)$ and $\sigma^2 = 3\beta^2(m-1)^2/(1+\alpha)^2(m+2)^2$ when $t \rightarrow \infty$. From equation (36) it is observed that the anisotropic parameter remains constant during cosmic evolution which suggests that our model is uniformly anisotropic for $m \neq 1$. We also observe

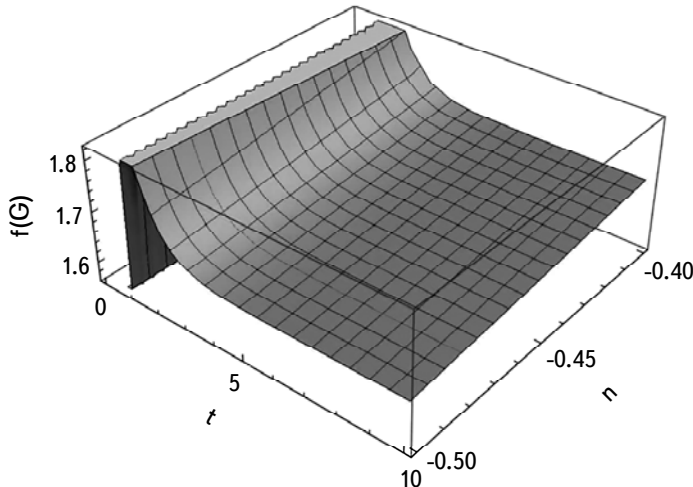


Fig.3. Evolution of $f(G)$ versus n and t for $\alpha = \beta = \eta = 1.4$.

from the equations (35) and (36) that when $m=1$, shear scalar $\sigma^2=0$ and anisotropic parameter $A_m=0$, the model becomes shear free and isotropic.

Also the GB invariant G and Ricci scalar R behave as

$$G = \frac{648m\beta^4 e^{3\beta t}}{(m+2)^3(1+\alpha)^4(e^{\beta t}-1)^4} \{e^{\beta t} - (1+\alpha)\}, \quad (37)$$

$$R = \frac{6\beta^2 e^{2\beta t}}{(1+\alpha)^2(e^{\beta t}-1)^2} \left[\frac{1+\alpha}{e^{\beta t}} - \frac{3(m^2+2m+3)}{(m+2)^2} \right]. \quad (38)$$

Equations (18) and (37) are used to derive the function $f(G)$ given by

$$f(G) = \eta \left[\frac{648m\beta^4 e^{3\beta t}}{(m+2)^3(1+\alpha)^4(e^{\beta t}-1)^4} \{e^{\beta t} - (1+\alpha)\} \right]^{n+1}. \quad (39)$$

Fig.3 depicts the $f(G)$ as a function of time $n < 0$. It demonstrates that the function $f(G)$ has a transitory behaviour and is positive throughout cosmic time. $f(G)$ is very large at the beginning of evolution, approaches zero, then increases and ultimately takes a constant value as $\lim f(G) \rightarrow \eta [648m\beta^4 / (m+2)^3(1+\alpha)^4]^{n+1}$ when $t \rightarrow \infty$.

4. Renyi holographic dark energy models. We have consider a system with n discrete states having probability distribution P_i which satisfies the condition $\sum_{i=1}^n P_i = 1$. Renyi entropy is a recognized generalized entropy parameter defined as [66]

$$S = \frac{1}{\delta} \ln \sum_i^n P_i^{1-\delta}, \quad S_T = \frac{1}{\delta} \sum_{i=1}^n (P_i^{1-\delta} - P_i), \quad (40)$$

where $\delta \equiv 1 - U$ and U is a real parameter and $T = 1/2\pi L$ and L is the IR cutoff. By using equation (40), we obtain the relation

$$S = \frac{1}{\delta} \ln (1 + \delta S_T). \quad (41)$$

In equation (41), the Bekenstein entropy is given in the form $S_T = A/4$, where $A = 4\pi L^2$. This gives the Renyi entropy of the system as

$$S = \frac{1}{\delta} \ln (1 + \pi \delta L^2). \quad (42)$$

Using the following assumption $\rho_\Lambda dV \propto TdS$, we can get RHDE as

$$\rho_\Lambda = \frac{3d^2}{8\pi L^2} (1 + \pi \delta L^2)^{-1}. \quad (43)$$

4.1. Model-1: RHDE model with Hubble horizon cutoff. Here, the Renyi holographic dark energy density is calculated by using the Hubble horizon

as a candidate for the IR cutoff i.e. $L = H^{-1}$ and $8\pi = 1$ is found to be

$$\rho_\Lambda = \frac{3d^2H^4}{H^2 + \pi\delta}. \quad (44)$$

Using equation (26) in equation (44), we obtain energy density of RHDE in this model as

$$\rho_\Lambda = \frac{3d^2(\beta e^{\beta t})^4}{\{\beta(1+\alpha)e^{\beta t}(e^{\beta t}-1)\}^2 + \pi\delta(1+\alpha)(e^{\beta t}-1)^4}. \quad (45)$$

From this expression for ρ_Λ , we can deduce that it is a positive decreasing function of time and when $t \rightarrow \infty$, it tends to a constant value $\frac{3d^2}{\beta^2(1+\alpha)^2 + \pi\delta(1+\alpha)^4}$ which shows that this dark energy component will remain uniformly at late epoch. This phenomenon highlights the behavior of accelerated expansion of Universe. Also using equation (26) in (15), we found the matter energy density as

$$\rho_m = c_1 k_1^{-3} (e^{\beta t} - 1)^{-3/(1+\alpha)}. \quad (46)$$

The coincidence parameter \bar{r} is defined as the ratio between the HDE density ρ_Λ and the matter energy density ρ_m , therefore from equations (45) and (46) the coincidence parameter is found to be

$$\bar{r} = \frac{\rho_\Lambda}{\rho_m} = \frac{3d^2k_1^3}{c_1} \frac{(\beta e^{\beta t})^4 (e^{\beta t} - 1)^{3/(1+\alpha)}}{\{\beta(1+\alpha)e^{\beta t}(e^{\beta t}-1)\}^2 + \pi\delta(1+\alpha)(e^{\beta t}-1)^4}. \quad (47)$$

The Renyi holographic dark energy density is plotted against time in Hubbles cutoff with appropriate values of constants as shown in Fig.4. It is shown that it remains positive and decrease with increase of time and the contribution of α ,

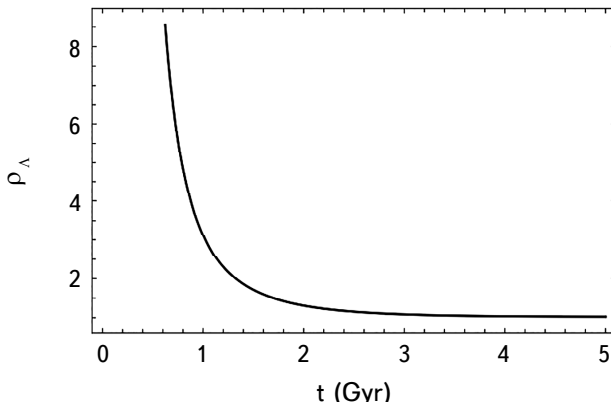


Fig.4. Holographic dark energy density ρ_Λ versus time t (Hubble horizon cutoff) for $\alpha = \beta = 1.4$, $d = 7$ and $\delta = 5.2$.

β and δ remains negligible in its behavior. From equation (46), we can observed that the evolution of the matter energy density ρ_m begins with a positive value, but disappears later, which denotes the expansion of the Universe. It is also noted that the coincidence parameter \bar{r} initially changes at a very early stage of development, but after a finite time, it converges to a constant value and stays constant throughout the evolution, avoiding the coincidence problem (unlike Λ CDM). Equation of state parameter for RHDE in Hubble cutoff is

$$\omega_\Lambda = -1 + \frac{2}{3} \frac{(1+\alpha) \left[\beta^2 e^{2\beta t} + 2\pi\delta(1+\alpha)^2 (e^{\beta t} - 1)^2 \right]}{e^{\beta t} \left[\beta^2 e^{2\beta t} + \pi\delta(1+\alpha)^2 (e^{\beta t} - 1)^2 \right]}. \quad (48)$$

From this expression, we can deduce that the value of ω_Λ converges to -1 at late times, indicating the Λ CDM model, which coincides with observational data. The RHDE pressure is obtained as

$$\begin{aligned} \rho_\Lambda &= \frac{3d^2(\beta e^{\beta t})^4}{\left\{ \beta(1+\alpha)e^{\beta t}(e^{\beta t}-1) \right\}^2 + \pi\delta(1+\alpha)(e^{\beta t}-1)^4} \\ &\times \left[-1 + \frac{2}{3} \frac{(1+\alpha) \left[\beta^2 e^{2\beta t} + 2\pi\delta(1+\alpha)^2 (e^{\beta t} - 1)^2 \right]}{e^{\beta t} \left[\beta^2 e^{2\beta t} + \pi\delta(1+\alpha)^2 (e^{\beta t} - 1)^2 \right]} \right]. \end{aligned} \quad (49)$$

4.2. Model-2: RHDE model with Granda-Oliveros horizon cutoff.

For this model, we consider RHDE model with GO horizon cut off i.e. $L = (\gamma_1 H^2 + \gamma_2 \dot{H})^{-1/2}$ and $8\pi = 1$. Substituting this value of L in (43), we have

$$\rho_\Lambda = \frac{3d^2(\gamma_1 H^2 + \gamma_2 \dot{H})^2}{\pi\delta + (\gamma_1 H^2 + \gamma_2 \dot{H})}. \quad (50)$$

Using equation (26) in equation (50), we found energy density of RHDE as

$$\rho_\Lambda = \frac{3d^2 \beta^4 e^{2\beta t} \left\{ \gamma_1 e^{\beta t} - \gamma_2 (1+\alpha) \right\}^2}{\pi\delta \left\{ (1+\alpha)(e^{\beta t} - 1) \right\}^4 + e^{\beta t} \left\{ \beta(1+\alpha)(e^{\beta t} - 1) \right\}^2 \left\{ \gamma_1 e^{\beta t} - \gamma_2 (1+\alpha) \right\}}. \quad (51)$$

From this expression, we can derive that the value of ρ_Λ is very large in the beginning and decreases with the increase of time. Also for this model, the matter energy density will be same as that of the RHDE with Hubble cutoff. Now from equations (45) and (51) the coincidence parameter becomes

$$\bar{r} = \frac{\rho_\Lambda}{\rho_m} = \frac{3d^2 k_1^3}{c_1} \frac{\beta^4 e^{2\beta t} \left\{ \gamma_1 e^{\beta t} - \gamma_2 (1+\alpha) \right\}^2 (e^{\beta t} - 1)^{3/(1+\alpha)}}{\pi\delta \left\{ (1+\alpha)(e^{\beta t} - 1) \right\}^4 + e^{\beta t} \left\{ \beta(1+\alpha)(e^{\beta t} - 1) \right\}^2 \left\{ \gamma_1 e^{\beta t} - \gamma_2 (1+\alpha) \right\}}. \quad (52)$$

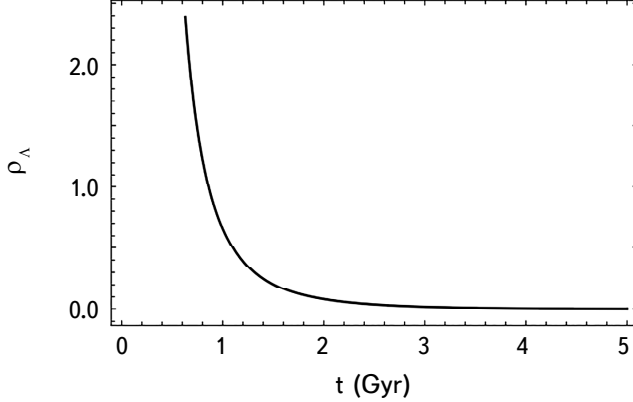


Fig.5. Holographic dark energy density ρ_Λ versus time t (GO cutoff) for $\alpha = \beta = 1.4$, $d = 7$, $\delta = 5.2$, $\gamma_1 = 1.065$ and $\gamma_2 = 0.4$.

The behavior of Renyi holographic dark energy density is plotted against time in Granda-Oliveros cutoff with the acceptable values of constant as shown in Fig.5. From the figure, it is observed that the energy density of the model is constantly a positive function of time and decreases with increase of time. As we know from equation (46), evolution of the matter energy density ρ_m starts at a positive value, but disappears at late times. As in the RHDE Hubble cutoff, it is observed that the coincidence parameter \bar{r} initially changes at a very early stage of development, but after a finite time, it converges to a constant value and stays constant throughout the evolution, avoiding the coincidence problem (unlike Λ CDM).

Equation of state parameter for RHDE in Granda-Oliveros cutoff is

$$\begin{aligned} \omega_\Lambda &= -1 - \frac{(2\gamma_1 H \dot{H} + \gamma_2 \ddot{H})(2\pi\delta + \gamma_1 H^2 + \gamma_2 \dot{H})}{3H(\gamma_1 H^2 + \gamma_2 \dot{H})(\pi\delta + \gamma_1 H^2 + \gamma_2 \dot{H})} \\ &= -1 + \frac{(1+\alpha)\{2\gamma_1 e^{\beta t} - \gamma_2(1+\alpha)(e^{\beta t} + 1)\}}{3e^{\beta t}\{\gamma_1 e^{\beta t} - \gamma_2(1+\alpha)\}} \\ &\quad \times \frac{\left[2\pi\delta(1+\alpha)^2(e^{\beta t} - 1)^2 + \beta^2 e^{\beta t}\{\gamma_1 e^{\beta t} - \gamma_2(1+\alpha)\}\right]}{\left[\pi\delta(1+\alpha)(e^{\beta t} - 1)^2 + \beta^2 e^{\beta t}\{\gamma_1 e^{\beta t} - \gamma_2(1+\alpha)\}\right]}. \end{aligned} \quad (53)$$

From this expression also, we can deduce that the value of ω_Λ converge to -1 at late times, indicating the Λ CDM model, which coincides with the observational data. The RHDE pressure is obtained as

$$\begin{aligned}
p_{\Lambda} = \rho_{\Lambda} & \left[-1 + \frac{(1+\alpha)\{2\gamma_1 e^{\beta t} - \gamma_2(1+\alpha)(e^{\beta t}+1)\}}{3e^{\beta t}\{\gamma_1 e^{\beta t} - \gamma_2(1+\alpha)\}} \right. \\
& \times \left. \frac{\left[2\pi\delta(1+\alpha)^2(e^{\beta t}-1)^2 + \beta^2 e^{\beta t}\{\gamma_1 e^{\beta t} - \gamma_2(1+\alpha)\} \right]}{\left[\pi\delta\{(1+\alpha)(e^{\beta t}-1)\}^2 + \beta^2 e^{\beta t}\{\gamma_1 e^{\beta t} - \gamma_2(1+\alpha)\} \right]} \right] \quad (54)
\end{aligned}$$

5. Cosmological parameters. This section investigates how the Universe expands using the cosmological parameters including equation of state (EoS), squared sound speed v_s^2 , density parameter Ω , state finder parameter (r, s) and the energy conditions for both the derived anisotropic RHDE models.

5.1. EoS parameter. The various phases of the expanding Universe are commonly categorised using the equation of state parameter ω . Particularly, the transition between the decelerated and accelerated phases has phases where radiation and DE predominate. EoS parameter is defined as $\omega = p/\rho$ where p is pressure and ρ is energy density of matter distribution. The eras that make up the decelerated and accelerated phases are as follows: decelerated phase (cold dark matter or dust fluid $\omega = 0$, radiation era $0 < \omega < 1/3$ and stiff fluid $\omega = 1$) and accelerated phase (cosmological constant or vacuum era $\omega = -1$, quintessence $-1 < \omega < -1/3$ and quintom era). Fig.6 displays the graphical behavior of the Renyi holographic dark energy equation of state parameter versus redshift z in Hubble cutoff for the proper choice of constants. This figure makes it abundantly clear that the equation of state parameter changes to negative values inside the proper range ($-1 \leq \omega_{\Lambda} \leq 0$), which is in good agreement with astronomical data. As a result our research model is realistic. Fig.6 shows that the equation of state

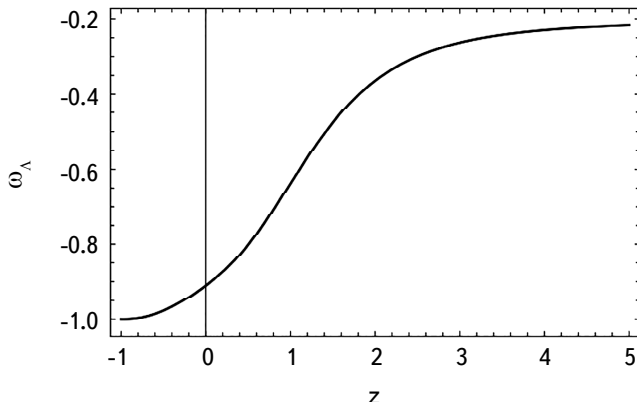


Fig.6. Equation of state parameter ω versus redshift z (Hubble horizon cutoff) for $k_1 = 0.5$, $\alpha = \beta = 1.4$, $d = 7$ and $\delta = 5.2$.

parameter begins near to zero at the beginning of cosmic time (i.e., the Universe is dominated by matter) and progresses to a close negative value of -1 at the end of cosmic time (i.e. when the Universe dominated by the HDE). Additionally, we can see that in the current Universe, ω_Λ tends to -1, indicating the model Λ CDM, whereas in the early Universe, $-1 < \omega_\Lambda < 0$ suggests the quintessential model. Our model produces a $\omega_\Lambda = -0.90$ at the current epoch, which is near to the Λ CDM model i.e. $\omega_\Lambda = -1$ which is compatible with the observational bounds [65]. Fig.7 displays the graphical behaviour of the Granda-Oliveros cutoff equation of state parameter of Renyi holographic dark energy vs redshift z for the proper choice of constants. We observed that the value of ω_Λ is differed as compared to with the results obtained in the RHDE with Hubble cutoff. In this case, ω_Λ deviates from its initial positive value to function as a pure cosmological constant in the last phases of cosmic time. This model produces a $\omega_\Lambda = -0.72$ value at the current epoch, which is relatively close to the value produced by the Λ CDM model ($\omega_\Lambda = -1$), which is compatible with the observational bounds [65].

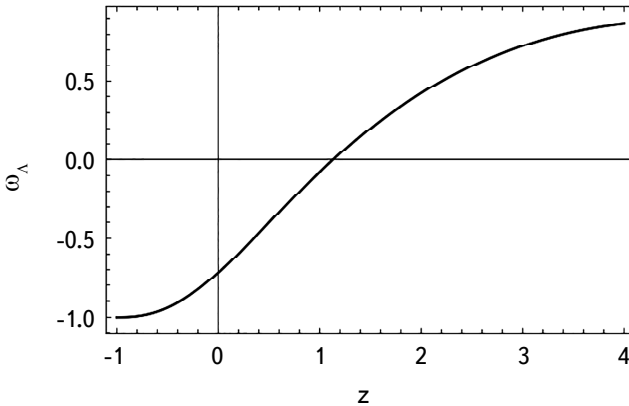


Fig.7. Equation of state parameter ω versus redshift z (GO cutoff) for $k_1 = 0.5$, $\alpha = \beta = 1.4$, $d = 7$, $\delta = 5.2$, $\gamma_1 = 1.065$ and $\gamma_2 = 0.4$.

5.2. Squared sound speed. The squared sound speed parameter is given by

$$v_s^2 = \frac{\dot{p}_\Lambda}{\dot{\rho}_\Lambda} = \omega_\Lambda + \frac{\rho_\Lambda}{\dot{\rho}_\Lambda} \dot{\omega}_\Lambda \quad (55)$$

This parameter can be used to discuss how the stability of DE models is affected by its sign. If v_s^2 has a positive signature, the DE model is stable; otherwise, the model is unstable. Using equations (45), (48) and (51), (53) in the expression of squared sound speed v_s^2 equation (55), we analyze v_s^2 graphically or both models -1 and 2. Fig.8 displays the stability of RHDE with the Hubble cutoff for the proper choice of constants. It can be seen from the figure that the value of the δ has no effect on the stability of the Universe. Also $v_s^2 > 0$ for

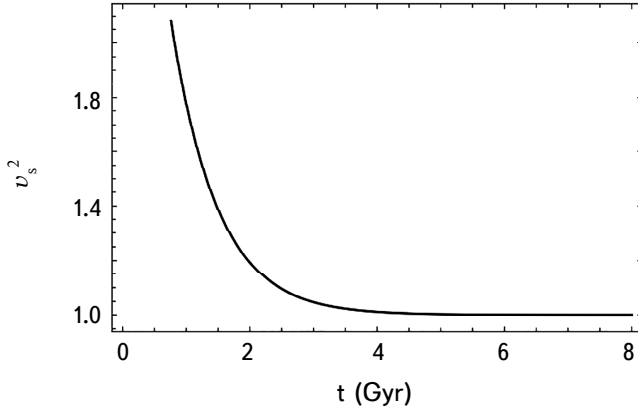


Fig.8. Square speed sound parameter v_s^2 versus time t (Hubble horizon cutoff) for $\alpha = \beta = 1.4$, $d = 7$ and $\delta = 5.2$.

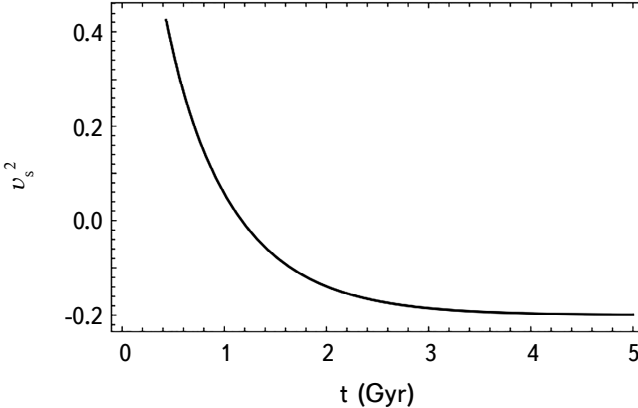


Fig.9. Square speed sound parameter v_s^2 versus time t (GO cutoff) for $k_1 = 0.5$, $c_1 = 1$, $\alpha = \beta = 1.4$, $d = 7$, $\delta = 5.2$, $\gamma_1 = 1.065$ and $\gamma_2 = 0.4$.

all epoch and tends to a small value. Hence in all Universe our model is stable. Fig.9 shows the stability of RHDE in the Granda-Oliveros cutoff of the model over time for the proper choice of constants. The model is stable during the beginning epoch, as can be seen in the figure. But after $t > 1.17$ Gyr, the trajectory of the graph becomes negative, which shows that our model is classically unstable at current epoch.

5.3. Density parameter. Total energy density parameter is given by

$$\Omega = \Omega_m + \Omega_\Lambda , \quad (56)$$

where $\Omega_m = \rho_m / 3H^2$ is the matter density parameter and $\Omega_\Lambda = \rho_\Lambda / 3H^2$ is the holographic dark energy density parameter. The total energy density parameters $\Omega > 1$, $\Omega = 1$, and $\Omega < 1$ correspondingly represent the open, flat, and closed

Universes. Now the total energy density parameter for RHDE with Hubble cutoff is found to be

$$\Omega = \frac{c_1 k^{-3} (1+\alpha)^2 (e^{\beta t} - 1)^{(-1+2\alpha)/(1+\alpha)}}{3\beta^2 e^{2\beta t}} + \frac{d^2 \beta^2 e^{2\beta t}}{\beta^2 e^{2\beta t} + \pi\delta(1+\alpha)^2 (e^{\beta t} - 1)^2}. \quad (57)$$

And the total energy density parameter for RHDE with Granda-Oliveros cutoff is found as

$$\Omega = \frac{c_1 k^{-3} (1+\alpha)^2 (e^{\beta t} - 1)^{(-1+2\alpha)/(1+\alpha)}}{3\beta^2 e^{2\beta t}} + \frac{d^2 \beta^2 \left\{ \gamma_1 e^{\beta t} - \gamma_2 (1+\alpha) \right\}^2}{\pi\delta(1+\alpha)^2 (e^{\beta t} - 1)^2 + \beta^2 e^{\beta t} \left\{ \gamma_1 e^{\beta t} - \gamma_2 (1+\alpha) \right\}^2}. \quad (58)$$

The total energy density parameter for the RHDE with the Hubble cutoff is shown in Fig.10. Here, it is demonstrated that the energy density parameter's value

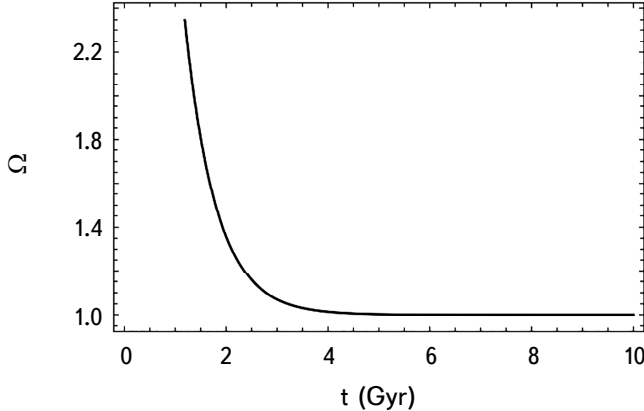


Fig.10. Total energy density parameter Ω versus time t (Hubble horizon cutoff) for $k_1 = 0.5$, $c = 1$, $\alpha = \beta = 1.4$, $d = 7$ and $\delta = 5.2$.

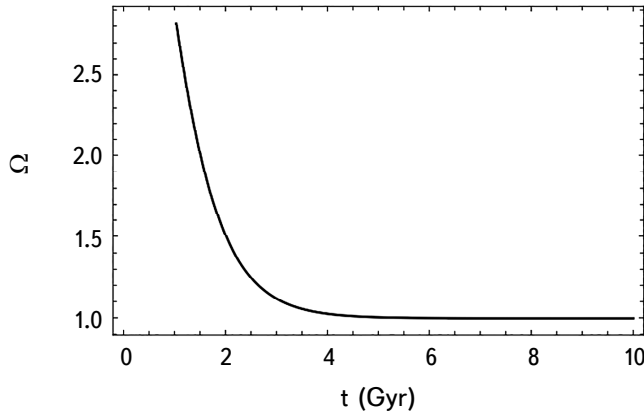


Fig.11. Total energy density parameter Ω versus time t (GO cutoff) for $k_1 = 0.5$, $c = 1$, $\alpha = \beta = 1.4$, $d = 7$, $\delta = 5.2$, $\gamma_1 = 1.065$ and $\gamma_2 = 0.4$.

was high in the early period of the Universe but is currently approaching 1. So for very large times, the model predicts a flat Universe. The resultant model is consistent with the observations because the Universe as it currently exists is very close to flat. The total energy density parameter for RHDE with Granda-Oliveros cutoff is shown in Fig.11. Here the graph is almost same as that of the Hubble cutoff. Hence the model predicts a flat Universe for large time.

5.4. Statefinder parameters. Hubble and deceleration parameters can be used to accurately explain the known Universe expanding nature. The values of these parameters, however, are the same in many dynamical DE models at the present. As a result, these parameters were unable to choose the best-fitting model out of a variety of dynamical DE models. With this objective, Sahni et al. [67] developed statefinder parameters, which are dimensionless cosmological parameters and are defined as follows:

$$r = \frac{\ddot{a}}{aH^3}, \quad s = \frac{r-1}{3(q-1/2)}. \quad (59)$$

For $(r, s) = (1, 0)$ and $(r, s) = (1, 1)$, respectively, these statefinders establish a connection with the Λ CDM and CDM models. In contrast to the Chaplygin gas model, which occurs for $r > 1$ with $s < 0$, if the trajectories of $r-s$ correspond to the region $s > 0$ and $r < 1$, the model belongs to the phantom and quintessence phases. These statefinders are same for both the models and are obtained as

$$r = 1 - \frac{3(1+\alpha)}{e^{\beta t}} + \frac{(1+\alpha)^2}{e^{2\beta t}} (e^{\beta t} + 1), \quad (60)$$

$$s = \frac{2(1+\alpha)[-3e^{\beta t} + (1+\alpha)(e^{\beta t} + 1)]}{3e^{\beta t}[(1+\alpha) - 3e^{\beta t}]} . \quad (61)$$

Fig.12 shows the graph of (r, s) parameter in $r-s$ plane. The parameter s

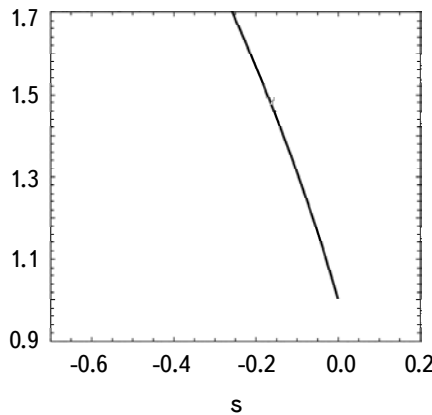


Fig.12. Plot of $r-s$ plane for $\alpha = \beta = 1.4$, $d = 7$.

is seen to remain negative for all values of r at the early epoch. This suggests that the RHDE models were able to correspond to the Chaplygin gas model. Additionally, at late times, the $r-s$ plane corresponds to the Λ CDM.

5.5. Energy conditions. The energy conditions namely, null energy conditions (NEC), strong energy conditions (SEC) and dominant energy conditions (DEC), are respectively given by

- (i) $\rho_\Lambda + p_\Lambda \geq 0$,
- (ii) $\rho_\Lambda + 3p_\Lambda \geq 0$,
- (iii) $\rho_\Lambda - p_\Lambda \geq 0$.

Now the energy conditions for RHDE with Hubble cutoff are

NEC:

$$\begin{aligned} & \frac{3d^2(\beta e^{\beta t})^4}{\{\beta(1+\alpha)e^{\beta t}(e^{\beta t}-1)\}^2 + \pi\delta\{(1+\alpha)(e^{\beta t}-1)\}^4} \\ & \times \frac{2}{3} \frac{(1+\alpha)\left[\beta^2 e^{2\beta t} + 2\pi\delta(1+\alpha)^2(e^{\beta t}-1)^2\right]}{e^{\beta t}\left[\beta^2 e^{2\beta t} + \pi\delta(1+\alpha)^2(e^{\beta t}-1)^2\right]} \geq 0. \end{aligned} \quad (62)$$

SEC:

$$\begin{aligned} & \frac{3d^2(\beta e^{\beta t})^4}{\{\beta(1+\alpha)e^{\beta t}(e^{\beta t}-1)\}^2 + \pi\delta\{(1+\alpha)(e^{\beta t}-1)\}^4} \\ & \times \left[\frac{2(1+\alpha)\left[\beta^2 e^{2\beta t} + 2\pi\delta(1+\alpha)^2(e^{\beta t}-1)^2\right]}{e^{\beta t}\left[\beta^2 e^{2\beta t} + \pi\delta(1+\alpha)^2(e^{\beta t}-1)^2\right]} - 2 \right] \geq 0. \end{aligned} \quad (63)$$

DEC:

$$\begin{aligned} & \frac{3d^2(\beta e^{\beta t})^4}{\{\beta(1+\alpha)e^{\beta t}(e^{\beta t}-1)\}^2 + \pi\delta\{(1+\alpha)(e^{\beta t}-1)\}^4} \\ & \times \left[2 - \frac{(1+\alpha)\left[\beta^2 e^{2\beta t} + 2\pi\delta(1+\alpha)^2(e^{\beta t}-1)^2\right]}{3e^{\beta t}\left[\beta^2 e^{2\beta t} + \pi\delta(1+\alpha)^2(e^{\beta t}-1)^2\right]} \right] \geq 0. \end{aligned} \quad (64)$$

Also the energy conditions for RHDE with Granda-Oliveros cutoff are found to be

NEC:

$$\begin{aligned} & \frac{3d^2\beta^4 e^{2\beta t} \left\{ \gamma_1 e^{\beta t} - \gamma_2(1+\alpha) \right\}}{\pi\delta \left\{ (1+\alpha)(e^{\beta t}-1) \right\}^4 + e^{\beta t} \left\{ \beta(1+\alpha)(e^{\beta t}-1) \right\}^2 \left\{ \gamma_1 e^{\beta t} - \gamma_2(1+\alpha) \right\}} \\ & \times \frac{(1+\alpha) \left\{ 2\gamma_1 e^{\beta t} - \gamma_2(1+\alpha)(e^{\beta t}+1) \right\}}{3e^{\beta t} \left\{ \gamma_1 e^{\beta t} - \gamma_2(1+\alpha) \right\}} \\ & \times \frac{2\pi\delta(1+\alpha)^2 (e^{\beta t}-1)^2 + \beta^2 e^{\beta t} \left\{ \gamma_1 e^{\beta t} - \gamma_2(1+\alpha) \right\}}{\left[\pi\delta \left\{ (1+\alpha)(e^{\beta t}-1) \right\}^2 + \beta^2 e^{\beta t} \left\{ \gamma_1 e^{\beta t} - \gamma_2(1+\alpha) \right\} \right]} \geq 0. \end{aligned} \quad (65)$$

SEC:

$$\begin{aligned} & \frac{3d^2\beta^4 e^{2\beta t} \left\{ \gamma_1 e^{\beta t} - \gamma_2(1+\alpha) \right\}^2}{\pi\delta \left\{ (1+\alpha)(e^{\beta t}-1) \right\}^4 + e^{\beta t} \left\{ \beta(1+\alpha)(e^{\beta t}-1) \right\}^2 \left\{ \gamma_1 e^{\beta t} - \gamma_2(1+\alpha) \right\}} \\ & \times \left[\frac{(1+\alpha) \left\{ 2\gamma_1 e^{\beta t} - \gamma_2(1+\alpha)(e^{\beta t}+1) \right\}}{e^{\beta t} \left\{ \gamma_1 e^{\beta t} - \gamma_2(1+\alpha) \right\}} \right. \\ & \left. \times \frac{2\pi\delta(1+\alpha)^2 (e^{\beta t}-1)^2 + \beta^2 e^{\beta t} \left\{ \gamma_1 e^{\beta t} - \gamma_2(1+\alpha) \right\}}{\left[\pi\delta \left\{ (1+\alpha)(e^{\beta t}-1) \right\}^2 + \beta^2 e^{\beta t} \left\{ \gamma_1 e^{\beta t} - \gamma_2(1+\alpha) \right\} \right]} - 2 \right] \geq 0. \end{aligned} \quad (66)$$

DEC:

$$\begin{aligned} & \frac{3d^2\beta^4 e^{2\beta t} \left\{ \gamma_1 e^{\beta t} - \gamma_2(1+\alpha) \right\}^2}{\pi\delta \left\{ (1+\alpha)(e^{\beta t}-1) \right\}^4 + e^{\beta t} \left\{ \beta(1+\alpha)(e^{\beta t}-1) \right\}^2 \left\{ \gamma_1 e^{\beta t} - \gamma_2(1+\alpha) \right\}} \\ & \times \left[2 - \frac{(1+\alpha) \left\{ 2\gamma_1 e^{\beta t} - \gamma_2(1+\alpha)(e^{\beta t}+1) \right\}}{3e^{\beta t} \left\{ \gamma_1 e^{\beta t} - \gamma_2(1+\alpha) \right\}} \right. \\ & \left. \times \frac{2\pi\delta(1+\alpha)(e^{\beta t}-1)^2 + \beta^2 e^{\beta t} \left\{ \gamma_1 e^{\beta t} - \gamma_2(1+\alpha) \right\}}{\left[\pi\delta \left\{ (1+\alpha)^2 (e^{\beta t}-1) \right\}^2 + \beta^2 e^{\beta t} \left\{ \gamma_1 e^{\beta t} - \gamma_2(1+\alpha) \right\} \right]} \right] \geq 0. \end{aligned} \quad (67)$$

Fig.13 shows the graph of energy conditions for RHDE with Hubble cutoff for our model. From the graph, it is observed that $\rho_\Lambda + p_\Lambda \geq 0$ and $\rho_\Lambda - p_\Lambda > 0$ but $\rho_\Lambda + 3p_\Lambda \geq 0$ at early times but becomes negative after some time and stays in the negative domain. So, NEC and DEC are satisfied whereas SEC is violated. Fig.14 shows the graph of energy conditions for RHDE with Granda-Oliveros cutoff for our model. From the graph, it is observed that $\rho_\Lambda + p_\Lambda \geq 0$ and $\rho_\Lambda - p_\Lambda > 0$ but $\rho_\Lambda + 3p_\Lambda < 0$. This shows that NEC and DEC are satisfied whereas SEC is violated. So in both the model NEC and DEC are satisfied

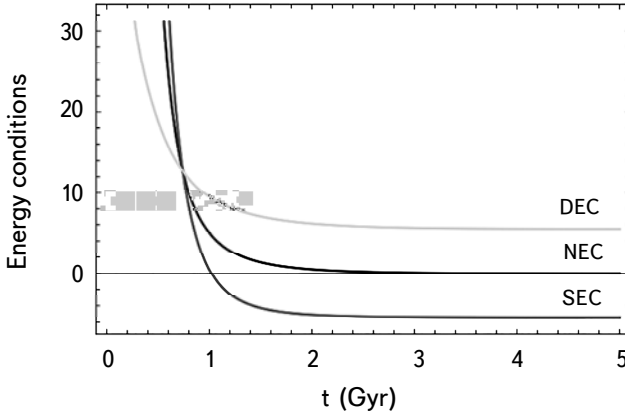


Fig.13. Energy conditions versus time t (Hubble horizon cutoff) for $\alpha = \beta = 1.4$, $d = 7$ and $\delta = 5.2$.

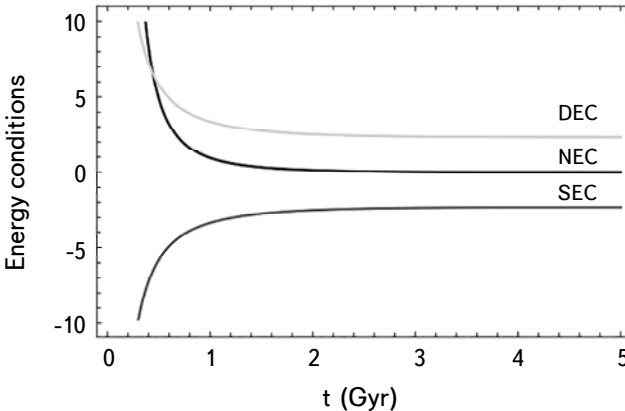


Fig.14. Energy conditions versus time t (GO horizon cutoff) for $\alpha = \beta = 1.4$, $d = 7$, $\delta = 5.2$, $\gamma_1 = 1.065$ and $\gamma_2 = 0.4$.

whereas SEC is violated in the present and future. Therefore, the Universe accelerates as a result of the SEC violation. Our model shows the shift from an early decelerating to a current accelerating Universe as a result of the violation of SEC, which causes an anti-gravitational effect that causes the Universe to jerk. Our model therefore fits the most recent cosmological observations.

6. Generalized holographic dark energy. In this section, we effort to establish that our dark energy model has a direct equivalence to the generalized holographic dark energy model. In the holographic principle, the holographic energy density is proportional to the inverse squared infrared cutoff L_{IR} , which could be related to the causality given by the cosmological horizon:

$$\rho_{hol} = \frac{3c^2}{\kappa^2 L_{IR}^2}, \quad (68)$$

where c is a numerical constant which acts as a free parameter and $\kappa^2 = 8\pi G$ is the gravitational constant. The IR cutoff is supposed to be the particle horizon L_p or the future event horizon L_F , which are determined respectively as [54,55,68]

$$L_p \equiv a \int_0^t \frac{dt}{a}, \quad L_F \equiv a \int_t^\infty \frac{dt}{a}. \quad (69)$$

Differentiating both sides of the above expressions leads to the Hubble parameter in terms of L_p , \dot{L}_p or in terms of L_F , \dot{L}_F as

$$H(L_p, \dot{L}_p) = \frac{\dot{L}_p}{L_p} - \frac{1}{L_p}, \quad H(L_F, \dot{L}_F) = \frac{\dot{L}_F}{L_F} + \frac{1}{L_F}. \quad (70)$$

The general form of the cutoff was proposed in the work [68]

$$L_{IR} = L_{IR}(L_p, \dot{L}_p, \ddot{L}_p, \dots, L_F, \dot{L}_F, \ddot{L}_F, \dots, a). \quad (71)$$

Actually, the other dependency of L_{IR} , particularly on the Hubble parameter, the Ricci scalar and their derivatives, can be transformed to either L_p and their derivatives or L_F and their derivatives via Eq. (71). The above cutoff could be chosen to be equivalent to a general covariant gravity model:

$$S = \int d^4 \sqrt{-g} F(R, R_{\mu\nu} R^{\mu\nu}, R_{\mu\nu\rho\sigma} R^{\mu\nu\rho\sigma}, \square R, \square^{-1} R, \nabla_\mu R \nabla^\mu R, \dots). \quad (72)$$

In the following, using the above expressions and with the help of the generalized cutoff, we will show that the Granda-Oliveros HDE of the present work has direct equivalence to the generalized HDE model. The comparison of Eq. (68) with Eq. (50) and using Eq. (70) immediately conduct to the equivalence holographic cut-off L_R (in terms of L_p and its derivatives or in terms of L_F and its 19 derivatives) corresponds to the HDE as

$$\begin{aligned} \frac{3c^2}{\kappa^2 L_R^2} &= \frac{3d^2 \left[\gamma_1 \left(\frac{\dot{L}_p}{L_p} - \frac{1}{L_p} \right)^2 + \gamma_2 \left(\frac{\ddot{L}_p}{L_p} - \frac{\dot{L}_p^2}{L_p^2} + \frac{\dot{L}_p}{L_p^2} \right) \right]^2}{\pi\delta + \left[\gamma_1 \left(\frac{\dot{L}_p}{L_p} - \frac{1}{L_p} \right)^2 + \gamma_2 \left(\frac{\ddot{L}_p}{L_p} - \frac{\dot{L}_p^2}{L_p^2} + \frac{\dot{L}_p}{L_p^2} \right) \right]^2} \\ &= \frac{3d^2 \left[\gamma_1 \left(\frac{\dot{L}_F}{L_F} + \frac{1}{L_F} \right)^2 + \gamma_2 \left(\frac{\ddot{L}_F}{L_F} - \frac{\dot{L}_F^2}{L_F^2} - \frac{\dot{L}_F}{L_F^2} \right) \right]^2}{\pi\delta + \left[\gamma_1 \left(\frac{\dot{L}_F}{L_F} + \frac{1}{L_F} \right)^2 + \gamma_2 \left(\frac{\ddot{L}_F}{L_F} - \frac{\dot{L}_F^2}{L_F^2} - \frac{\dot{L}_F}{L_F^2} \right) \right]^2}. \end{aligned} \quad (73)$$

The equation of state parameter can be derived from the conservation equation corresponds to the HDE density ρ_{hol}

$$\omega_{hol}^{(R)} = -1 + \frac{2}{3H L_R} \frac{dL_R}{dt}, \quad (74)$$

where L_R is given by Eq. (73). Hence, we conclude that $\omega_{hol}^{(R)}$ is equivalent to ω_Λ as derived in Eq. (53).

7. Conclusion. In this work, we investigate RHDE with a homogeneous and anisotropic Universe of Bianchi type-I, in the context of $f(G)$ gravity. We also consider RHDE with the IR cutoffs of both the Hubble and the Granda-Oliveros horizons. We make the assumption that the deceleration parameter (DP) is a function of Hubble parameter H in order to determine exact solutions to the field equations. With the use of this analysis, we found that the deceleration parameter changes from negative to positive with respect to redshift z , indicating that the Universe transitions from an earlier deceleration phase to the present acceleration phase. Our model's transition redshift value is $z_{tr} = 0.73$, which is in accordance with the observational data. Scalar expansion and shear scalar both have infinitely large value at $t \rightarrow 0$ and become finite at $t \rightarrow \infty$. Since the anisotropic parameter doesn't change throughout the cosmic evolution, our model is fully anisotropic from the early Universe to the end of the Universe for $m \neq 1$ whereas the model is isotropic for $m = 1$. For investigations in model I, it has been found that the energy density of the model is consistently a positive function of time, and that these parameters have no effect on the behavior of the model for any $\alpha \geq 0.3$. Also, the RHDE density in Hubble's cutoff is positive for all Universe and is decreasing to a small value at later times. The RHDE Universe in the Hubble's cutoff is stable, and the value of δ has no effect on the stability of the Universe, which is approaching to a small value. From the evolution of the EoS parameter, we understand that in the early Universe, it indicates the quintessential model, while in the current Universe, ω_Λ tends to -1, i.e. the model Λ CDM, which is well in agreement with recent observational data. Additionally, the NEC and DEC energy conditions are satisfied, however the SEC is violated at later times. The acceleration of the Universe results from this SEC violation. Again in the study of model II, the energy density of the model is rigorously a positive function of time and is a decreasing function and approaches to a small positive value at later times. Even if it is stable in the early Universe, the behavior of the stability of the RHDE Universe in the Granda-Oliveros cutoff is not stable at later times. In this model, the EoS parameter falls from a positive value in the early phase of cosmic time to act as a pure cosmological constant, or $\omega_\Lambda = -1$, in the late phase. The NEC and DEC energy conditions are also satisfied, while the SEC is violated in the present and the future, which causes the Universe to accelerate.

Additionally, for both models, the (r, s) plane provides a correspondence with the Chaplygin gas model and, at late times, with the Λ CDM. Finally, the exact solutions described in the study can be one of the decent candidates to describe the observable Universe. In order to comprehend the characteristics of the anisotropic Bianchi type-I model in the development of the Universe, it may be helpful to consider the solutions presented in this study.

Department of Mathematics, National Institute of Technology Manipur-795004,
India, e-mail: alamkhurshid96@gmail.com ssuren.mu@gmail.com
anjnlam@gmail.comg

ГОЛОГРАФИЧЕСКАЯ ТЕМНАЯ ЭНЕРГИЯ РЕНЬИ И ЕЕ ПОВЕДЕНИЕ В $f(G)$ ГРАВИТАЦИИ

М.Х.АЛАМ, С.С.СИНГХ, Л.А.ДЕВИ

В данной работе исследуется голографическая темная энергия Ренни (RHDE) и ее поведение в анизотропной и пространственно однородной Вселенной типа Бьянки-I в рамках гравитации $f(G)$. Мы используем инфракрасное обрезание как горизонт Хаббла и Гранда-Оливероса (GO). Для нахождения согласованных решений уравнений поля моделей предполагается, что параметр замедления определен в терминах функции параметра Хаббла H . С учетом современных космологических данных оценивается поведение космологических параметров, связанных с моделью темной энергии, и исследуется их физическая значимость. Отмечается, что для обеих моделей параметр уравнения состояния приближается к -1 в позднюю эпоху. Однако модель RHDE с горизонтом Хаббла проявляет стабильность по отношению к квадрату скорости звука, тогда как модель RHDE с горизонтом GO нестабильна. В обеих моделях параметр замедления и диагностический показатель состояния подтверждают ускоренное расширение Вселенной и также соответствуют модели Λ CDM в позднюю эпоху.

Ключевые слова: метрика Бьянки-I: гравитация $f(G)$: голографическая темная энергия Ренни: космология

REFERENCES

1. *S.Perlmutter et al.*, *Astrophys. J.*, **517**, 565, 1999.
2. *A.G.Riess et al.*, *Astron. J.*, **116**, 1009, 1998.
3. *Z.Y.Huang et al.*, *JCAP*, **0605**, 013, 2006.
4. *D.J.Eisenstein et al.*, *Astrophys. J.*, **633**, 560, 2005.
5. *C.Fedeli et al.*, *Astron. Astrophys.*, **500**, 667, 2009.
6. *T.Koivisto, D.F.Mota*, *Phys. Rev. D*, **73**, 083502, 2006.
7. *S.M.Carroll*, *Phys. Rev. Lett.*, **81**, 3067, 1998.
8. *M.S.Turner*, Making sense of the new cosmology, in: 2001: A Spacetime Odyssey, p.180196, 2002.
9. *R.R.Caldwell*, *Phys. Lett. B*, **545**, 2329, 2002.
10. *T.Chiba, T.Okabe, M.Yamaguchi*, *Phys. Rev. D*, **62**, 023511, 2000.
11. *T.Padmanabhan*, *Phys. Rev. D*, **66**, 021301, 2002.
12. *A.Kamenshchik, U.Moschella, V.Pasquier*, *Phys. Lett. B*, **511**, 265268, 2001.
13. *I.Zlatev, L.Wang, P.J.Steinhardt*, *Phys. Rev. Lett.*, **82**, 896, 1999.
14. *R.Myrzakulov*, *Eur. Phys. J. C*, **71**, 18, 2011.
15. *E.V.Linder*, *Phys. Rev. D*, **81**, 127301, 2010.
16. *M. De Laurentis, M.Paoletta, S.Capozziello*, *Phys. Rev. D*, **91**, 083531, 2015.
17. *T.Harko, F.S.Lobo, S.I.Nojiri et al.*, *Phys. Rev. D*, **84**, 024020, 2011.
18. *S.Nojiri, S.D.Odintsov, O.G.Gorbunova*, *J. Phys. A, Math. Gen.*, **39**, 6627, 2006.
19. *G.Cognola, E.Elizalde, S.Nojiri et al.*, *Phys. Rev. D*, **73**, 084007, 2006.
20. *S.Nojiri, S.D.Odintsov*, *Phys. Rept.*, **505**, 59-144, 2011.
21. *H.M.Sadjadi*, *Phys. Scr.*, **83**, 055006, 2011.
22. *K.Bamba, S.D.Odintsov, L.Sebastiani et al.*, *Eur. Phys. J. C*, **67**, 295310, 2010.
23. *R.Myrzakulov, D.Sáez-Gómez, A.Tureanu*, *Gen. Relativ. Gravit.*, **43**, 16711684, 2011.
24. *A.Jawad, S.Chattopadhyay, A.Pasqua*, *Eur. Phys. J. Plus*, **128**, 88, 2013.
25. *M.F.Shamir*, *Astrophys. Space Sci.*, **361**, 147, 2016.
26. *M.Sharif, H.I.Fatima*, *Astrophys. Space Sci.*, **353**, 259265, 2014.
27. *A.Y.Shaikh, S.V.Gore, S.D.Katore*, *New Astron.*, **80**, 101420, 2020.
28. *S.Nojiri, S.D.Odintsov, V.K.Oikonomou*, *Phys. Rept.*, **692**, 1-104, 2017.
29. *M.Koussour, H.Filali, S.H.Shekhh et al.*, *Nucl. Phys. B*, **978**, 115738, 2022.
30. *M.Li*, *Phys. Lett. B*, **603**, 1, 2004.
31. *L.Susskind*, *J. Math. Phys.*, **36**, 6377, 1995.
32. *A.Cohen, D.Kaplan, A.Nelson*, *Phys. Rev. Lett.*, **82**, 4971, 1999.
33. *Z.K.Gao et al.*, *Phys. Rev. D*, **74**, 127304, 2006.
34. *L.N.Granda, A.Oliveros*, *Phys. Lett. B*, **669**, 275, 2008.
35. *L.N.Granda, A.Oliveros*, *Phys. Lett. B*, **671**, 199, 2009.
36. *H.Weii, R.G.Cai*, *Phys. Lett. B*, **660**, 113, 2009.
37. *W.Zimdahl, D.Pavon*, *Quantum Grav.*, **24**, 5461, 2007.
38. *L.Xu, Y.Wang*, *J. Cosmol. Astropart. Phys.*, **06**, 002, 2010.

39. *X.Zhang*, Phys. Rev. D, **79**, 103509, 2009.
40. *Y.Wang, L.Xu*, Phys. Rev. D, **81**, 083523, 2010.
41. *I.Duran, D.Pavon*, Phys. Rev. D, **83**, 023504, 2011.
42. *S.Nojiri, S.D.Odintsov*, Gen. Relativ. Grav., **38**, 1285, 2006.
43. *S.Nojiri et al.*, Phys. Lett. B, **797**, 134829, 2019.
44. *C.Tsallis, L.J.L.Cirto*, Eur. Phys. J. C, **73**, 2487, 2013.
45. *A.S.Jahromi et al.*, Phys. Lett. B, **780**, 21, 2018.
46. *H.Moradpour et al.*, Eur. Phys. J. C., **78**, 829, 2018.
47. *H.Moradpour, Bonilla et al.*, Phys. Rev. D, **96**(12), 123504, 2017.
48. *H.Moradpour*, Implications, Int. J. Theor. Phys., **55**(9), 4176, 2016.
49. *N.Komatsu*, Eur. Phys. J. C, **77**(4), 229, 2017.
50. *S.Ghaffari, A.H.Ziaie et al.*, Phys. Lett. A, **35**(1), 1950341, 2020.
51. *U.Y.D.Prasanthi, Y.Aditya*, Results Phys., **17**, 103101, 2020.
52. *U.Y.D.Prasanthi, Y.Aditya*, Phys. Dark Universe, **31**, 100782, 2021.
53. *S.H.Shekhar*, Phys. Dark Universe, **33**, 100850, 2021.
54. *S.Nojiri, S.D.Odintsov, V.K.Oikonomou et al.*, Phys. Rev. D, **102**, 023540, 2020.
55. *S.Nojiri, S.D.Odintsov, T.Paul*, Phys. Lett. B, **825**, 136844, 2022.
56. *M.S.Singh, S.S.Singh*, New Astron., **72**, 36, 2019.
57. *M.S.Singh, S.S.Singh*, Gravit. Cosmol., **25**, 8289, 2019.
58. *S.S.Singh, L.A.Devi*, New Astron., **90**, 101656, 2022.
59. *M.K.Alam, S.S.Singh, L.A.Devi*, Adv. High Energy Phys., **2022**, 5820222, 2022.
60. *S.Nojiri, S.D.Odintsov*, Phys. Lett. B, **631**(1-2), 12-6, 2005.
61. *K.S.Thorne*, Astrophys. J., **148**, 51, 1967.
62. *J.Kristian, R.K.Sachs*, Astrophys. J., **143**, 379, 1966.
63. *C.B.Collins*, Phys. Lett. A, **60**, 397, 1977.
64. *R.K.Tiwari, D.Sofuoğlu, V.K.Dubey*, Int. J. Geom. Methods Mod. Phys., **17**, 2050187, 2020.
65. *N.Aghanim et al.*, (Planck Collaboration), Planck 2018 results. VI. Cosmological parameters. Astron. Astrophys., **641**, A6, 2020.
66. *A.Jawad et al.*, Symmetry, **10**, 635, 2018.
67. *V.Sahni, T.D.Saini, A.A.Starobinsky et al.*, JETP Lett., **77**, 201206, 2003.
68. *S.Nojiri, S.D.Odintsov, T.Paul*, Symmetry, **13**, 928, 2021.

АСТРОФИЗИКА

ТОМ 66

АВГУСТ, 2023

ВЫПУСК 3

DOI: 10.54503/0571-7132-2023.66.3-441

ДВИЖЕНИЕ ЧАСТИЦЫ В ПОЛЕ БЕСКОНЕЧНОГО ПЛОСКОГО СЛОЯ

Р.М.АВАКЯН, А.А.СААРЯН, С.С.ДЖИБИЛИАН

Поступила 25 мая 2023

В настоящей работе в рамках общей теории относительности исследуется движение светового сигнала и пробной частицы в поле бесконечного плоского слоя. Рассмотрены оба случая внешнего решения для гравитационного поля в вакууме, соответствующие метрикам Риндлера и Тауба. Определяются время движения и путь, пройденный частицей до ее остановки. Показано, что в геометрии Тауба, в отличие от светового сигнала, материальная частица не достигает сингулярности. Определено минимальное расстояние от сингулярности в зависимости от энергии частицы. Для сравнения приводятся результаты в рамках специальной теории относительности.

Ключевые слова: *плоско-симметричное гравитационное поле: метрика Тауба: метрика Риндлера*

1. *Введение.* Плоско-симметричные решения уравнений Эйнштейна играют важную роль в различных задачах гравитационной физики. В качестве примера отметим доменные стенки, разделяющие различные фазы физической системы. Они являются топологическими дефектами, которые могут образоваться в результате фазовых переходов в ранних стадиях расширения Вселенной (см., например, [1,2] и приведенные там ссылки). Другим примером являются браны в различных фоновых геометриях. В теории струн такие объекты являются фундаментальными составляющими наряду со струнами. В настоящее время широко обсуждаются также феноменологические модели с бранами в различных фоновых геометриях. В частности, ведутся активные исследования в рамках бран-моделей типа Рандалла-Сундрума с дополнительными пространственными измерениями в пространстве-времени анти-де Ситтера [3].

Наряду с решением Шварцшильда, плоско-симметричные вакуумные решения уравнений гравитационного поля в общей теории относительности являются одними из первых точных решений. Впервые такие решения рассматривались в работе [4]. В дальнейшем аналогичные решения в различных координатных системах исследовались во многих работах (см., например, [5-7] и приведенные в [5] ссылки). Важной составляющей рассмотренных задач являются решения гравитационного поля внутри плоскопараллельной пластины, которые сшиваются с внешним решением. В литературе рассмат-

ривались различные внутренние решения, которые включают нестатические решения, решения с космологической постоянной, а также решения с ненулевым электромагнитным полем (см. работы [5,8-23] и приведенные там ссылки). Они имеют интересные особенности, которые, несмотря на многочисленные работы, обсуждаются до сих пор.

Многие особенности поля гравитирующих масс проявляются в движении свободной частицы в соответствующей геометрии. В настоящей работе рассмотрено движение в плоскосимметричном гравитационном поле пластины. Статья построена следующим образом. В следующем разделе приведена постановка задачи и рассмотрено движение частицы в рамках специальной теории относительности (СТО). В разделе 3 рассматривается движение в однородном статическом гравитационном поле, описываемом метрикой Риндлера. Исследованию движения в гравитационном поле Тауба посвящен раздел 4. В разделе 5 подытожены основные результаты работы.

2. Решение в рамках СТО. Геометрия рассматриваемой задачи изображена на рис.1. Координатная плоскость $z=0$ совмещена с правой боковой поверхностью слоя. Поверхностная плотность массы равна σ , а распределение вещества в слое не зависит от координат x и y . Вначале рассмотрим задачу движения частицы в рамках СТО в неподвижной относительно слоя инерциальной системе отсчета. Из точки O в момент $t=0$ в направлении оси z вылетает частица со скоростью v_0 . Необходимо определить время t_n до полной остановки и пройденное за это время расстояние z_n . Для корректного сравнения во всех задачах предполагаются одинаковые значения поверхностной плотности σ и начальной скорости $v_0 = c\beta_0$ (c - скорость света в вакууме).

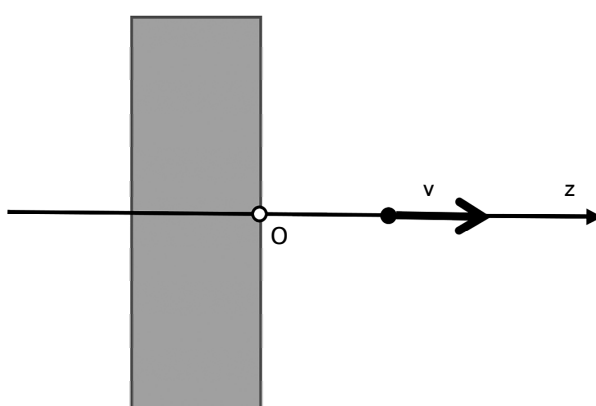


Рис.1. Геометрия задачи.

Если в качестве нулевого уровня принять плоскость $z = 0$, то для потенциала поля будем иметь:

$$\phi = 2\pi k \sigma z = wz, \quad w = 2\pi k \sigma, \quad (1)$$

где k - гравитационная постоянная, величина w имеет размерность ускорения. О его смысле будет сказано позднее. В нерелятивистской механике частица совершает равнозамедленное движение и w есть модуль ускорения. За время $t'_n = v_0/w$ частица проходит путь $z'_n = v_0^2/2w$. В релятивистском случае движение в инерциальной системе не является равнозамедленным. Сила, действующая на частицу, направлена противоположно скорости и по модулю равна mw , где m - масса покоя частицы.

Релятивистский закон движения в инвариантной форме таков:

$$\frac{dP^i}{ds} = F^i, \quad i = 0, 3, \quad (2)$$

где $ds = cdt/\gamma$, $\gamma = 1/\sqrt{1-\beta^2}$, $\beta = v/c$, а $P^i = mcu^i$ импульс частицы. В обычных обозначениях уравнение с $i = 3$ в безразмерных величинах имеет вид:

$$\frac{d}{dt} \frac{P}{mc} = \frac{d}{dt} (\beta\gamma) = -\frac{w}{c} = -\frac{1}{T}, \quad T = \frac{1}{2\pi k \sigma}. \quad (3)$$

Здесь постоянная T имеет размерность времени. С учетом начальных условий ($t=0$, $\beta = \beta_0$) решение уравнения (3) будет $\beta\gamma = \beta_0\gamma_0 - t/T$, где $\gamma_0 = 1/\sqrt{1-\beta_0^2}$. Из условия $\beta = 0$ найдем время движения до остановки: $t_n = T\beta_0\gamma_0 > t'_n$. Зависимость безразмерной скорости $\beta(t)$ определяется формулой

$$\beta = \frac{1}{c} \frac{dz}{dt} = \frac{\beta_0\gamma_0 - t/T}{\sqrt{1 + (\beta_0\gamma_0 - t/T)^2}}. \quad (4)$$

Отсюда с учетом $z = 0$ при $t = 0$, получим закон движения

$$\frac{z}{cT} = \gamma_0 - \sqrt{1 + \left(\beta_0\gamma_0 - \frac{t}{T} \right)^2}. \quad (5)$$

Подставив в (5) $t = t_n$, найдем максимальное значение z_n :

$$\frac{z_n}{cT} = \gamma_0 - 1 > \frac{\beta_0^2}{2} = \frac{z'_n}{cT}. \quad (6)$$

Отметим, что это выражение для z_n можно получить из (2) при $i = 0$ (закон сохранения энергии).

Остается выяснить смысл величины w . Отличные от нуля компоненты четырехмерной скорости имеют вид $u^0 = \gamma$, $u^3 = \beta\gamma$. Компоненты четырехмерного ускорения легко вычисляются и равны $w^0 = \beta\gamma^4\dot{\beta}/c^3$ и $w^3 = \gamma^4\dot{\beta}/c^2$, где точка означает производную по времени. Из инвариантности $w_i w^i$

получим $\gamma^6 \dot{\beta}^2 / c^2 = w^2$. Отсюда следует, что в каждый момент времени в инерциальной системе отсчета, относительно которой частица покоятся, ускорение равно w . Такое движение частицы называется релятивистски равноускоренным.

3. Движение в статическом однородном гравитационном поле в рамках ОТО. Далее мы рассмотрим движение на фоне плоско-симметричного вакуумного решения уравнений Эйнштейна. Известно, что существуют два класса таких решений. Для решений из первого класса пространство-время является плоским в рассматриваемой области. В работе [24] было показано, что общий вид плоско-симметричного статического интервала с таким свойством имеет вид

$$ds^2 = f(z) c^2 dt^2 - dx^2 - dy^2 - (\sqrt{f'(z)} / \alpha)^2 dz^2, \quad (7)$$

где α - постоянная, $f(z)$ - произвольная действительная функция, ограниченная только условием нерелятивистского предела $f(z) \approx 1 + 2\alpha z$. Автор статьи [24] называет такое поле статическим однородным гравитационным полем. В литературе в основном рассматривается частный случай $f(z) \approx (1 + 2\alpha z)^2$ с метрическим тензором, задаваемым линейным элементом

$$ds^2 = (1 + \alpha z)^2 c^2 dt^2 - dx^2 - dy^2 - dz^2, \quad (8)$$

и называемым также метрикой Риндлера. Линейный элемент (8) описывает часть пространства-времени Минковского в неинерциальной системе отсчета, совершающей релятивистское равноускоренное движение. Это является проявлением принципа эквивалентности. Метрика (8) является одной из популярных геометрий в квантовой теории поля в искривленном пространстве-времени для исследования зависимости понятия вакуума квантового поля от системы отсчета. Вакуумное состояние, реализуемое модами квантового поля в метрике (8), отличается от вакуума инерциального наблюдателя в пространстве-времени Минковского и называется вакуумом Фуллинга-Риндлера. Локальные свойства этого вакуума при наличии равноускоренной плоской границы исследованы в работах [25-29].

Обозначим через (t_M, x_M, y_M, z_M) координаты пространства-времени Минковского в инерциальной системе отсчета K . Они связаны с риндлеровскими координатами соотношениями

$$ct_M = (z + 1/\alpha) \sinh t, \quad x_M = x, \quad y_M = y, \quad z_M = (z + 1/\alpha) \cosh t, \quad \tau = \alpha ct. \quad (9)$$

Заметим, что координаты (t, x, y, z) покрывают часть пространства-времени Минковского $z_M > |ct_M|$. В переменных Минковского для границы $z = 0$ имеем $z_M^2 - c^2 t_M^2 = 1/\alpha^2$. При фиксированных значениях x_M и y_M соответствующая мировая линия представляет гиперболу с асимптотами $x_M = \pm ct_M$.

Это соответствует равнускоренному движению в инерциальной системе отсчета с собственным ускорением $w = c^2/\alpha$.

Рассмотрим движение частицы на фоне геометрии (8). Пусть в момент $t=0$ из точки O движется частица вдоль оси z с начальной скоростью v_0 в инерциальной системе K . В этой системе для мировой линии частицы имеем $x_M = y_M = 0$, $z_M = 1/\alpha + \beta_0 ct_M$. Подставляя сюда ct_M и x_M из (9) для закона движения частицы в системе отсчета (8) получим

$$\alpha z(t) = \frac{1}{\cosh t - \beta_0 \sinh t} - 1. \quad (10)$$

Максимальное значение координаты z получается из условия $dz/dt = 0$. Для соответствующих значений времени $t = t_m$ и координаты $z = z_m$ имеем

$$\tanh(\alpha ct_m) = \beta_0, \quad z_m = \frac{\gamma_0 - 1}{\alpha}. \quad (11)$$

Закон движения теперь запишется в виде

$$\alpha z(t) = \frac{\cosh(\alpha ct_m)}{\cosh[\alpha c(t - t_m)]} - 1. \quad (12)$$

Отсюда следует, что функция $z(t)$ симметрична относительно $t = t_m$. Время движения частицы равно $2t_m$. В координатах пространства-времени Минковского максимальному удалению частицы от границы $z = 0$ соответствуют значения

$$ct_m^{(m)} = \frac{\gamma_0^2}{\alpha} \beta_0, \quad z_m^{(m)} = \frac{\gamma_0^2}{\alpha}. \quad (13)$$

Проекция скорости частицы, измеренная наблюдателем с фиксированными координатами (x, y, z) равна

$$v_{(p)} = \frac{dz}{dt_{(p)}} = \frac{1}{1 + \alpha z} \frac{dz}{dt} = c \tanh[\alpha c(t_m - t)]. \quad (14)$$

Модуль этой скорости всегда меньше скорости света.

Из формул (11) следует, что величины t_m и z_m являются монотонно возрастающими функциями начальной скорости частицы и стремятся к бесконечности в пределе $v_0 \rightarrow c$. В этом пределе для временной зависимости координаты z получим

$$z(t) = \frac{e^{\alpha ct} - 1}{\alpha}. \quad (15)$$

В этом случае определенная согласно (14) скорость равна скорости света. На рис.2 приведены графики функции (10) для различных значений параметра β_0 (числа возле кривых).

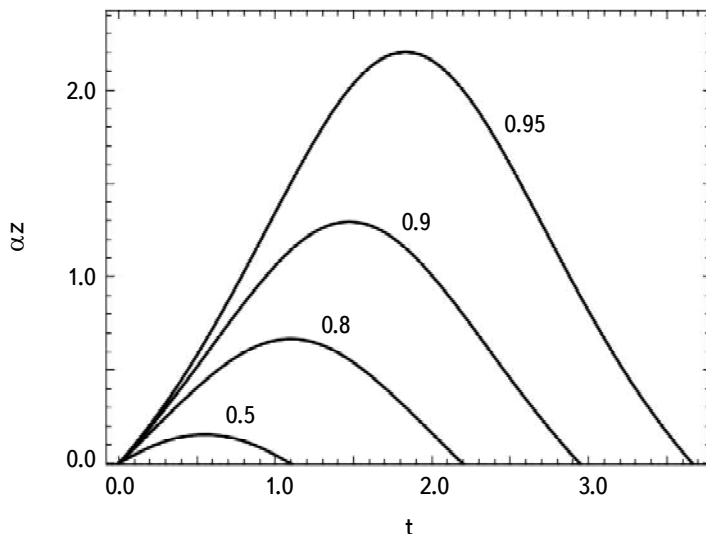


Рис.2. Зависимость координаты частицы от времени в метрике (8) для различных значений параметра β_0 (числа возле кривых).

4. *Движение в гравитационном поле Тауба.* В этом разделе рассмотрено движение на фоне второго класса плоско-симметричных решений уравнений Эйнштейна с искривленной геометрией. Свойства этих решений подробно обсуждались в литературе (см., например, приведенные во *Введении* ссылки). Переопределением координат линейный элемент (см. [4,6,7]) приводится к виду

$$ds^2 = \frac{c^2 dt^2}{\sqrt[3]{(1-z/z_s)^2}} - \sqrt[3]{(1-z/z_s)^4} (dx^2 + dy^2) - dz^2, \quad (16)$$

где z_s - постоянная. Определяемая этим линейным элементом метрика обычно называется метрикой Тауба. Соответствующий тензор Римана R_{iklm} отличен от нуля и геометрия искривлена. Для инварианта тензора кривизны имеем $R_{iklm} R^{iklm} = 64(z_s - z)^{-4}/27$ и метрика сингулярна в точке $z = z_s$. Природа этой сингулярности широко обсуждалась в литературе (см., например, [5,20,21]).

Рассмотрим сначала распространение света вдоль направления z на фоне геометрии (16). Воспользуемся уравнением эйконала ψ в виде $g^{ik} \partial_i \psi \partial_k \psi = 0$, где $\partial_i = \partial/\partial x^i$. В рассматриваемом частном случае движения производные по x и y равны нулю и уравнение примет вид

$$\frac{1}{c^2} \sqrt[3]{(1-z/z_s)^2} (\partial_t \psi)^2 - (\partial_z \psi)^2 = 0. \quad (17)$$

Это уравнение не содержит время явным образом и производная ψ по времени равна со знаком минус сохраняющейся частоте ω_0 . Это позволяет сделать разделение переменных $\psi = -\omega_0 t + \psi_0(z)$. В итоге получим $\psi'_0(z) = -(\omega_0/c) \sqrt[6]{(1-z/z_s)^2}$. После интегрирования имеем

$$\psi = -\omega_0 t - s(z) \frac{3\omega_0 z_s}{4c} \sqrt[3]{(1-z/z_s)^4} + \text{const}, \quad (18)$$

где $s(z) = \text{sgn}(1-z/z_s)$. Зависимость $z = z(t)$ получаем из уравнения $\partial\psi/\partial\omega_0 = \text{const}$:

$$\frac{z}{z_s} = 1 - s(z) \left[4s(z)c \frac{t_0 - t}{3z_s} \right]^{3/4}, \quad s(z)c \frac{t_0 - t}{3z_s} > 0. \quad (19)$$

Заметим, что точка сингулярности соответствует конечному моменту времени $t = t_0$. Проекция скорости, измеренная наблюдателем с фиксированными координатами (x, y, z) , определяется формулой

$$v_{(p)} = \sqrt[6]{(1-z/z_s)^2} \frac{dz}{dt}, \quad (20)$$

и по модулю всегда равна c . Общая формула (19) включает различные частные случаи, включая положительные и отрицательные значения параметра z_s .

Рассмотрим, например, случай, когда границе плоскопараллельного материального слоя соответствует $z = L$, где $L < z_s$ и $z_s > 0$. Полагая, что световой сигнал выходит из точки $z = L$ в момент времени $t = 0$ из (19), находим момент времени, когда сигнал достигнет сингулярности

$$t_0 = \frac{3z_s}{4c} \left(1 - \frac{L}{z_s} \right)^{4/3}. \quad (21)$$

Перейдем теперь к задаче движения материальной частицы с массой покоя m . Воспользуемся уравнением Гамильтона-Якоби

$$\frac{1}{c} \sqrt[3]{(1-z/z_s)^2} (\partial_t S)^2 - (\partial_z S)^2 = m^2 c^2, \quad (22)$$

где S - действие. Здесь учтено, что компоненты импульса P_x и P_y равны нулю. Уравнение (22) не содержит время явным образом. Это позволяет сделать разделение переменных. Частная производная действия по времени - это сохраняющаяся энергия E и поэтому $S = -Et + S_0(z)$. Уравнение для функции $S_0(z)$ следует из (22). После интегрирования действие запишется в виде

$$S = -Et + \int dz \sqrt{\frac{E^2}{c^2} \left(1 - \frac{z}{z_s} \right)^{2/3} m^2 c^2}. \quad (23)$$

Продифференцировав S по энергии и приравняв результат постоянной, получим зависимость $z = z(t)$. В параметрическом виде эта зависимость дается соотношениями

$$\frac{z}{z_s} = 1 - \frac{s(z)}{\gamma^3} y^3, \\ t - t_0 = -\frac{9s(z)z_s}{8c\gamma^4} \left[y \left(1 + \frac{2}{3} y^2 \right) \sqrt{y^2 - 1} + \ln \left(y + \sqrt{y^2 - 1} \right) \right], \quad (24)$$

где параметром является величина $y \geq 1$ и $\gamma = E/mc^2$. Для скорости частицы, определяемой согласно (20), получим

$$v_{(p)} = c \frac{\sqrt{y^2 - 1}}{y}. \quad (25)$$

Из формулы (24) следует, что материальная частица никогда не падает на сингулярность. Минимальное расстояние соответствует моменту времени $t = t_0$, когда $y = 1$. Расстояние от сингулярности равно $|z - z_s|_{min} = z_s / \gamma^3$ и оно уменьшается с ростом энергии частицы.

Рассмотрим предельные случаи общей формулы (24). При заданном γ и для $c|t - t_0|/z_s \ll 1$ имеем

$$\frac{z}{z_s} \approx 1 - \frac{s(z)}{\gamma^3} - s(z) \frac{\gamma^5}{6} \left(c \frac{t - t_0}{z_s} \right)^2, \quad v_{(p)} \approx -\gamma^4 \frac{c^2(t - t_0)}{3s(z)z_s}. \quad (26)$$

При $s(z) = -1$ и $c|t - t_0|/z_s \gg 1$ асимптотическое поведение имеет вид

$$\frac{z}{z_s} \approx \left(\frac{4c}{3} \frac{t - t_0}{z_s} \right)^{3/4}, \quad v_{(p)} \approx c \left[1 - \frac{1}{4\gamma^2} \left(c \frac{t - t_0}{3z_s} \right)^{-1/2} \right]. \quad (27)$$

Для больших значений γ и y , при фиксированном значении отношения y/γ , в первом приближении получим

$$\frac{z}{z_s} \approx 1 - s(z) \left[4s(z)c \frac{t_0 - t}{3z_s} \right]^{3/4}. \quad (28)$$

Этот результат совпадает с точной формулой (19) для движения светового сигнала. Этого, конечно, следовало ожидать для ультраквантитативистских частиц.

На рис.3 и 4 приведены зависимости координаты частицы от времени для различных значений параметра γ (энергия частицы в единицах энергии покоя). Числа около кривых соответствуют значениям этого параметра. Пунктирные линии соответствуют распространению светового сигнала. Рис.3 и 4 представляют случаи $z < z_s$ и $z > z_s$, соответственно.

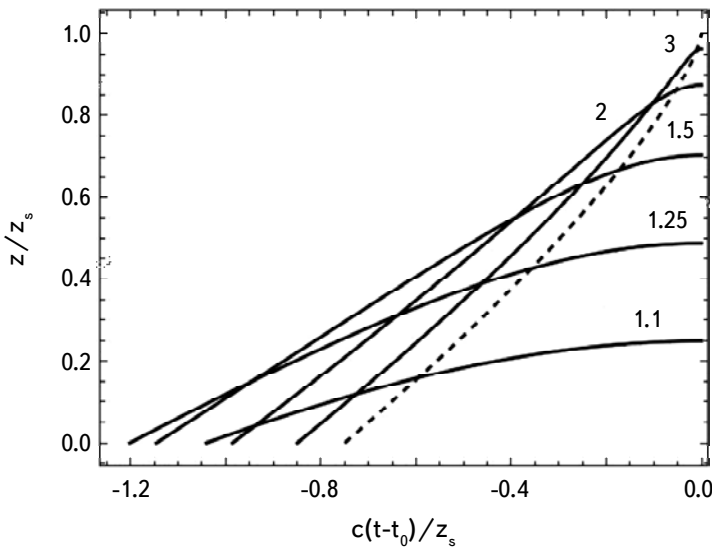


Рис.3. Зависимость координаты частицы от времени в геометрии (16) с $z < z_s$ для различных значений параметра γ (числа около кривых).

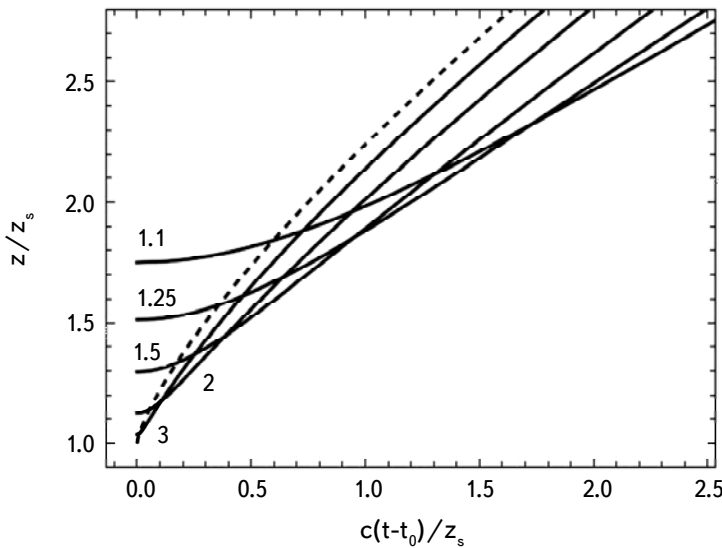


Рис.4. То же самое, что и на рис.3 при $z > z_s$.

5. Заключение. В работе исследовано движение светового сигнала и материальной частицы в поле бесконечного плоского слоя. Для сравнения сначала рассмотрено движение в рамках СТО, где сила, действующая на частицу, описывается потенциалом (1). Временные зависимости скорости и

координаты частицы даются формулами (5) и (6), где величина T определяется поверхностью плотностью слоя и связана с собственным ускорением соотношением $T = c/w$.

В геометрии плоского бесконечного слоя возможны два класса вакуумных решений уравнений Эйнштейна. Первый из них соответствует однородному статическому гравитационному полю, описываемому метрикой (8), частной реализацией которого является метрика Риндлера (9). Последний соответствует части пространства-времени Минковского, описываемой в равноускоренной неинерциальной системе отсчета. В этой геометрии временные зависимости координаты и скорости частицы, измеренные наблюдателем с фиксированными координатами (x, y, z) , даются соотношениями (12) и (14), где $t = t_m$ соответствует времени максимального удаления частицы от границы слоя. В отличие от материальной частицы, координата z для светового сигнала является монотонно возрастающей функцией времени и описывается формулой (15). Второму классу вакуумного гравитационного поля плоского слоя в ОТО соответствует решение Тауба, которое переопределением координат приводится к виду (16), где параметр z_s определяется поверхностью плотностью слоя. Распространение светового сигнала в этой геометрии описывается формулой (19) и за конечное время сигнал достигает точки сингулярности. Для материальной частицы с сохраняющейся энергией $E = \gamma mc^2$ закон движения дается параметрической формулой (24). Частица никогда не достигает сингулярности и минимальное расстояние равно z_s/γ^3 .

Работа выполнена в научно-исследовательской лаборатории теоретической физики Института физики ЕГУ, финансируемой комитетом по науке Министерства образования, науки, культуры и спорта Республики Армения. Работа Р.М.Авакяна и А.А.Сааряна выполнена в рамках программы 21AG-1C047 комитета по науке Министерства образования, науки, культуры и спорта Республики Армения.

Институт физики, Ереванский государственный университет, Армения
e-mail: rolavag@ysu.am saharian@ysu.am jibilyan2014@gmail.com

MOTION OF A PARTICLE IN THE FIELD OF AN INFINITE FLAT SLAB

R.M.AVAGYAN, A.A.SAHARIAN, S.S.JIBILYAN

In this paper we investigate the motion of a light signal and a test particle in the field of an infinite flat slab within the framework of the general relativity. Both cases of the external solution for the gravitational field in the vacuum, corresponding to the Rindler and Taub metrics, are considered. The time of motion and the path traveled by the particle before it stops are determined. It is shown that in the Taub geometry, in contrast to the light signal, a material particle does not reach a singularity. The minimum distance from the singularity is determined depending on the energy of the particle. For comparison, results are given within the framework of the special relativity.

Keywords: *plane symmetric gravitational field: Taub metric: Rindler metric*

ЛИТЕРАТУРА

1. *A.Vilenkin, E.P.S.Shellard*, Cosmic strings and other topological defects, Cambridge University Press, Cambridge, U.K., 1994.
2. *M.Cvetiu, S.Griffies, H.H.Soleng*, Phys. Rev. D, **48**, 2613, 1993.
3. *R.Maartens, K.Koyama*, Living Rev. Relativity, **13**, 5, 2010.
4. *T.Levi-Civita*, Atti Accad. Naz. Rend., **27**, 240, 1918.
5. *P.A.Amundsen, Ø.Grøn*, Phys. Rev. D, **27**, 1731, 1983.
6. *E.Kasner*, Trans. Amer. Math. Soc., **27**, 155, 1925.
7. *A.H.Taub*, Ann. Math., **53**, 472, 1951.
8. *A.H.Taub*, Phys. Rev., **103**, 454, 1956.
9. *R.Tabensky, A.H.Taub*, Commun. Math. Phys., **29**, 61, 1973.
10. *J.S.Shikin*, Gen. Relativ. Gravit., **433**, 411, 1979.
11. *R.M.Avakyan, J.Horský*, Astrophysics, **11**, 454, 1975.
12. *J.Horský, E.V.Chubaryan, V.V.Papoyan*, Bull. Astron. Inst. Czech. **27**, 115, 1976.
13. *J.Horský, E.V.Chubaryan*, Bull. Astron. Inst. Czech., **27**, 133, 1976.
14. *G.G.Arutyunyan, Ya.Gorskii, E.V.Chubaryan*, Astrophysics, **12**, 77, 1976.
15. *J.Novotný, J.Kuuera, J.Horský*, Gen. Rel. Grav., **19**, 1195, 1987.
16. *A.D.Dolgov, I.B.Khriplovich*, Gen. Rel. Grav., **21**, 13, 1989.
17. *M.L.Bedran, M.O.Calvão, F.M.Paiva et al.*, Phys. Rev. D, **55**, 3431, 1997.
18. *R.M.Avakyan, E.V.Chubaryan, A.H.Yeranyan*, arXiv:gr-qc/0102030.

19. *H.Zhang, H.Noha, Z.-H.Zhu*, Phys. Lett. B, **663**, 291, 2008.
20. *P.Jones, G.Muñoz, M.Ragsdale et al.*, Am. J. Phys., **76**, 73, 2008.
21. *S.A.Fulling, J.D.Bouas, H.B.Carter*, Phys. Scr., **90**, 088006, 2015.
22. *A.J.Silenko, Yu.A.Tsalkou*, Int. J. Mod. Phys. A, **34**, 1950228, 2019.
23. *A.Yu.Kamenshchik, T.Vardanyan*, Phys. Lett. B, **792**, 430, 2019.
24. *F.Rohrlich*, Ann. Phys., **22**, 169, 1963.
25. *P.Candelas, D.Deutsch*, Proc. R. Soc. London, A**354**, 79, 1977.
26. *A.A.Saharian*, Class. Quantum Grav., **19**, 5039, 2002.
27. *R.M.Avagyan, A.A.Saharian, A.H.Yeranyan*, Phys. Rev. D, **66**, 085023, 2002.
28. *A.A.Saharian, R.S.Davtyan, A.H. Yeranyan*, Phys. Rev. D, **69**, 085002, 2004.
29. *A.A.Saharian, R.M.Avagyan, R.S.Davtyan*, Int. J. Mod. Phys. A, **21**, 2353, 2006.

АСТРОФИЗИКА

ТОМ 66

АВГУСТ, 2023

ВЫПУСК 3

DOI: 10.54503/0571-7132-2023.66.3-453

SWAMPLAND CRITERIA AND NEUTRINO GENERATION IN A NON-COLD DARK MATTER UNIVERSE

M.KHURSHUDYAN^{1,2}

Received 15 May 2023

Accepted 18 August 2023

In this paper, the implications of string Swampland criteria for a dark energy-dominated universe, where we have a deviation from the cold dark matter model, will be discussed. In particular, we have considered two models. One of them is one parameter model, while the second one has been crafted to reveal the dynamics in the deviation. The analysis has been obtained through the use of Gaussian processes (GPs) and $H(z)$ expansion rate data (a 30-point sample deduced from a differential age method and a 10-point sample obtained from the radial BAO method). We learned that the tension with the Swampland criteria still will survive as in the cases of the models where dark matter is cold. In the analysis besides mentioned 40-point $H(z)$ data, we used the latest values of H_0 reported by the Planck and Hubble missions to reveal possible solutions for the H_0 tension problem. Finally, the constraints on the neutrino generation number have been obtained revealing interesting results to be discussed yet. This and various related questions have been left to be discussed in forthcoming papers.

Keywords: *Swampland criteria: non-cold dark matter model: Gaussian processes*

1. Introduction. The discovery of the accelerated expansion of the universe significantly changed our understanding of the universe [1-7]. It brought new knowledge and imposed new tasks to be solved yet and modification of General Relativity (GR) is one of the direct outcomes of this. On the other hand, quantum corrections also have a central role in crafting viable and advanced modified theories of gravity [8-13] (to mention a few). By modifying GR we search to find an effective way to deal with dark energy, dark matter, inflation, and other relevant problems [14-37] and references therein. Moreover, in light of the most common view GR can not be the ultimate theory of the universe, allowing the modification of GR to be one of the most discussed topics in recent literature. But we can still assume that yet unknown high-energy UV-complete theory can be reduced to GR (low-energy limit). The string theory plays the role of the mentioned unknown UV-complete theory. On the other hand, here we have an interesting situation related to the de Sitter (dS) vacua. In particular, until now no dS vacuum has been constructed, owing to numerous problems [38-48]. We took this as a hint indicating that in a consistent quantum theory of gravity, dS does not exist. The mentioned problem allows forming of the Swampland region

where inconsistent semi-classical effective field theories should inhabit. On the other hand, we have a Landscape provided by string theory where a vast range of choices fitting our universe in a consistent quantum theory of gravity exists. Therefore, it is not excluded that dS vacua may reside in the Swampland [49-50]. Recently two Swampland criteria have been proposed

1. *SC1*: The scalar field net excursion in reduced Planck units should satisfy the bound [49]

$$\frac{|\Delta\phi|}{M_p} < \Delta \sim O(1), \quad (1)$$

2. *SC2*: The gradient of the scalar field potential is bounded by [50]

$$M_p \frac{|V'|}{V} > c \sim O(1), \quad (2)$$

or [51]

$$M_p^2 \frac{V''}{V} < -c \sim O(1). \quad (3)$$

demanding the field to traverse a larger distance, in order to have the domain where the validity of the effective field theory will be fulfilled. Here, GR in the presence of a quintessence field ϕ has been considered to be the effective field theory. In the above-given formulation of the Swampland criteria, both Δ and c are positive constants of order one, while the prime denotes derivative with respect to the scalar field ϕ , and $M_p = 1/\sqrt{8\pi G}$ is the reduced Planck mass.

On the other hand, GR in the presence of a quintessence field ϕ (dark energy) has been used often to explain the accelerated expansion (including cosmic inflation too) of the universe. In this regard, it is highly reasonable to investigate/understand 1) how the constraints on the dark energy model affect the Swampland constraints, and 2) what are conditions to be satisfied in order not to end up in the Swampland. Different attempts in this direction had been taken already (see [52-61]). Even, it appears that with the GPs (Gaussian processes), it is possible to study and obtain the constraints on the Swampland criteria in a model-independent way [18]. In other words, with the GPs, it is possible to study the Swampland criteria for a dark energy model without using any explicit model describing the potential of the quintessence field ϕ and using a dark energy model to constrain the parameters of that potential.

Actually, GP is a machine learning tool intensively used in the recent literature to study various cosmology-related problems. A significant part of those studies indicates that with machine learning we can explore unseen and yet unknown physics of our universe in a more efficient way than can be done with traditional tools. One such problem to be mentioned here is the H_0 tension

problem. Basically, the H_0 tension problem requires explaining why the Planck CMB data analysis and a local measurement from the Hubble Space Telescope give different values for H_0 . We need to understand why in the Λ CDM scenario the Planck CMB data analysis gives $H_0 = 67.4 \pm 0.5$ km/s/Mpc, while local measurements from the Hubble Space Telescope yield $H_0 = 73.52 \pm 1.62$ km/s/Mpc (see [1,2]). Recently by Bayesian machine learning various interesting results have been learned about this problem. In particular, a deviation from cold dark matter has been learned giving a solution to the H_0 tension problem [17]. Moreover, another recent study confirms a deviation from the cold dark matter where the GPs and expansion rate data have been used. Even, a hint has been found that the deviation can have a dynamic nature [19]. We refer readers to the references of this paper to gain more about the problem and what are the alternative options to solve it. Above mentioned results indicate the existence of new knowledge requiring future analysis using new data and statistical tools.

The goal of this study is twofold given the above-mentioned problems and recently learned new hints. In particular, in this study, we will explore the impact of the deviation from the cold dark matter model on the Swampland tension using GPs. Moreover, we will learn how the Swampland tension and the deviation from the cold dark matter model affect the constraints on the neutrino generation number. To our knowledge, this will be the first work trying to do this using GPs. Given the nature of the problem and the tool we applied, some data-related artificial constraints have been imposed which hopefully can be lifted in the near future using other machine learning tools. However, obtained results are in great agreement with other results intensively discussed in the recent literature indicating that the impact of constraints with high precision can be neglected.

The paper is organized as follows. In Sect. II we present the data and discuss the strategy we follow. In Sect. III we will discuss the method. In Sect. IV we discuss the results obtained from the reconstruction for various scenarios based on three kernels. Moreover, in our analysis, one of the values of H_0 has been estimated with the GP method and using high-redshift data for $H(z)$, while the other two are taken to be the values from the Planck [1] and Hubble [2] missions, respectively. This strategy has been adopted to make the link between the H_0 tension problem, Swampland criteria tension, and deviation from the cold dark matter model more transparent. The discussion of our results can be found in Sect. V.

2. Gaussian processes and data. The GPs have two key ingredients and the goal of this section is to give a very brief presentation of them. Mainly, the goal here is to develop some intuition about the method which is using two-point covariance function $K(x, x')$ and a mean $\mu(x)$ to get a continuous realization of

$$\xi(x) \propto GP(\mu(x), K(x, x')) \quad (4)$$

and uncertainty $\Delta\xi(x)$ to get the posterior $\xi(x) \pm \Delta\xi(x)$. It is formed through a Bayesian iterative process allowing the reconstruction of the function representing the data. Using the data directly the GPs allow us to find a form of the function representing the data. It is possible because we consider the observational data to be a realization of the GPs, too. However, the method does not indicate how to choose the kernel and it should be done manually. In the recent literature, various kernel candidates have been considered and one of them is the squared exponent

$$K(x, x') = \sigma_f^2 \exp\left(-\frac{(x-x')^2}{2l^2}\right). \quad (5)$$

Table 1

$H(z)$ AND ITS UNCERTAINTY σ_H IN UNITS OF $\text{km s}^{-1} \text{Mpc}^{-1}$

z	$H(z)$	σ_H	z	$H(z)$	σ_H
0.070	69	19.6	0.4783	80.9	9
0.090	69	12	0.480	97	62
0.120	68.6	26.2	0.593	104	13
0.170	83	8	0.680	92	8
0.179	75	4	0.781	105	12
0.199	75	5	0.875	125	17
0.200	72.9	29.6	0.880	90	40
0.270	77	14	0.900	117	23
0.280	88.8	36.6	1.037	154	20
0.352	83	14	1.300	168	17
0.3802	83	13.5	1.363	160	33.6
0.400	95	17	1.4307	177	18
0.4004	77	10.2	1.530	140	14
0.4247	87.1	11.1	1.750	202	40
0.44497	92.8	12.9	1.965	186.5	50.4
0.24	79.69	2.65	0.60	87.9	6.1
0.35	84.4	7	0.73	97.3	7.0
0.43	86.45	3.68	2.30	224	8
0.44	82.6	7.8	2.34	222	7
0.57	92.4	4.5	2.36	226	8

with σ_f and l hyperparameters to be determined from the minimization of the GP marginal likelihood. The Cauchy kernel

$$K_C(x, x') = \sigma_f^2 \left[\frac{l}{(x-x')^2} + l^2 \right], \quad (6)$$

and the Matern ($v = 9/2$) kernel

$$K_M(x, x') = \sigma_f^2 \exp\left(-\frac{3|x-x'|}{l}\right) \\ \times \left[1 + \frac{3|x-x'|}{l} + \frac{27(x-x')}{7l^2} + \frac{18|x-x'|^3}{7l^3} + \frac{27(x-x')^4}{35l^4} \right], \quad (7)$$

are among the intensively used ones, too. The l parameter in the above three equations represents the correlation length along which the successive $\xi(x)$ values are correlated. The σ_f parameter, on the other hand, is used to control the variation in $\xi(x)$ relative to the mean of the process. The readers can follow [17-20] and references therein for a better understanding of the key aspects of the approach and how it can be used in cosmology. The dataset we have used can be found in Table 1, where the upper panel consists of thirty samples deduced from the differential age method. The lower panel corresponds to ten samples obtained from the radial baryon acoustic oscillation (BAO) method. The table is according to [62-75]. We use 30-point samples of $H(z)$ deduced from the differential age method. Then, we add 10-point samples obtained from the radial BAO method. This allowed us to have good data up to $z = 2$ and extend the data range up to $z = 2.4$ where still

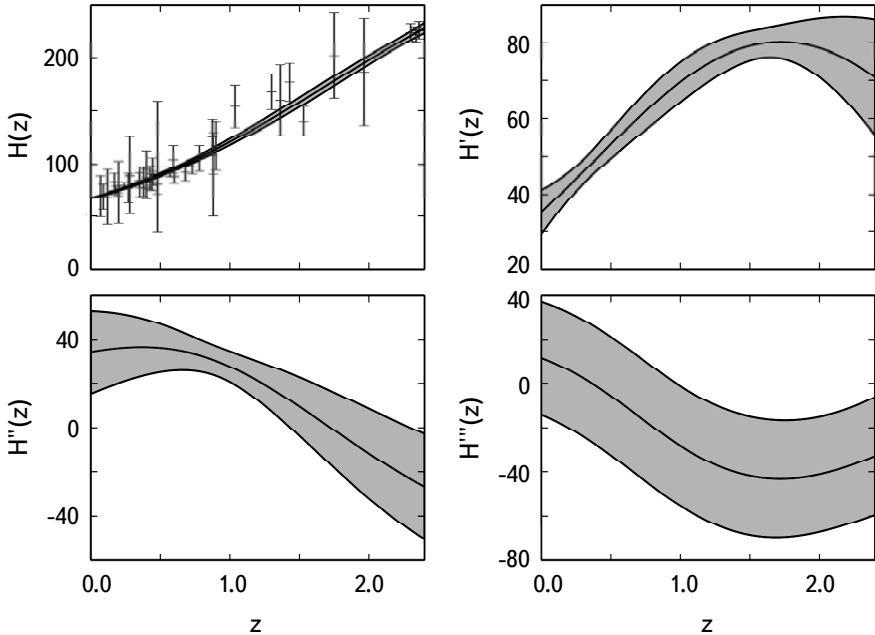


Fig.1. GP reconstruction of $H(z)$, $H'(z)$, $H''(z)$, and $H'''(z)$, for the 40-point sample deduced from the differential age method, with the additional 10-point sample obtained from the radial BAO method, when $H_0 = 67.66 \pm 0.42$ reported by the Planck mission. The ' means derivative with respect to the redshift variable z . The kernel is the Matern ($v = 9/2$) kernel given by Eq. (7).

the value of the Hubble parameter at $z = 0$ has not been taken into account. In this study, we will consider three different values for H_0 . In particular, first of all, we allowed the process to guess what the H_0 should be using the data given in Table 1. Then, in the other two scenarios, $H_0 = 67.66 \pm 0.42$ and $H_0 = 73.52 \pm 1.62$ reported from the Planck and Hubble missions, respectively, have been merged to the available data given in Table 1. Therefore, we could craft two datasets with two different H_0 values to be used in the reconstruction process. To save space we refer to the upper part of Table 2 to find more about the estimated H_0 value for considered kernels¹.

To end this section we present the reconstructions of $H(z)$ function and its higher order derivatives for $H_0 = 67.66 \pm 0.42$ and $H_0 = 73.52 \pm 1.62$ for the Matern ($\nu = 9/2$) kernel, Eq. (7). They can be found in Fig.1 and Fig.2, respectively. The reconstruction of the other cases used in this paper can be found in the references of this paper and they are not presented here only to save our place.

In the next section, we will revise how we can estimate the bounds of SC2 in a model-independent way and how to infer the constraints on the neutrino number

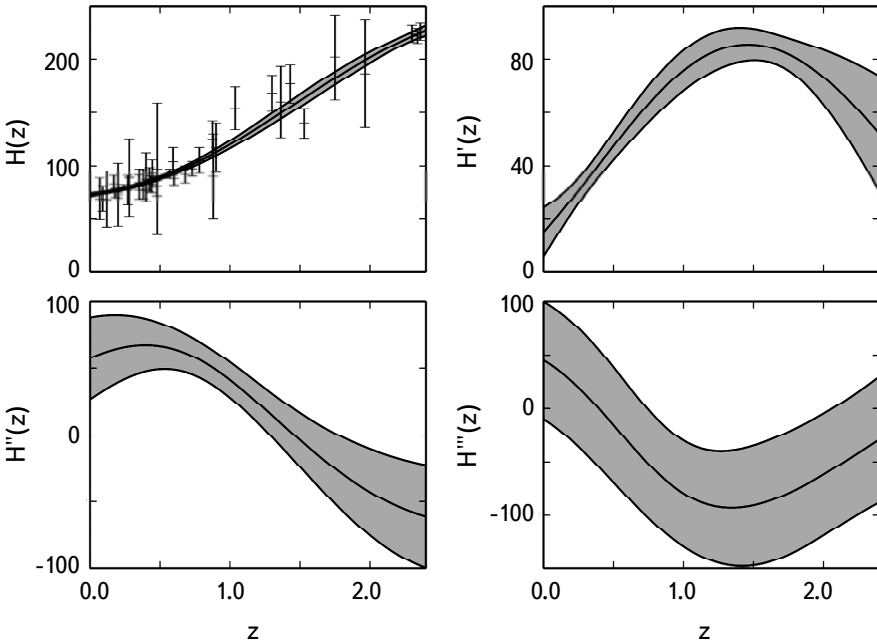


Fig.2. GP reconstruction of $H(z)$, $H'(z)$, $H''(z)$ and $H'''(z)$ for the 40-point sample deduced from the differential age method, with the additional 10-point sample obtained from the radial BAO method, when $H_0 = 73.52 \pm 1.62$ reported by the Hubble mission. The ' means derivative with respect to the redshift z . The kernel is the Matern ($\nu = 9/2$) kernel given by Eq. (7).

¹ We have used the GaPP (Gaussian Processes in Python) package developed by Seikel et al [76].

generation when we have certain deviations from the cold dark matter model.

3. Model. Here we consider GR in the presence of a quintessence field ϕ to be the effective field theory described by the following action (see for instance [18])

$$S = \int d^4x \sqrt{-g} \left(\frac{M_p^2}{2} R - \frac{1}{2} \partial_\mu \phi \partial^\mu \phi - V(\phi) \right) + S_m, \quad (8)$$

where S_m corresponds to the matter, $M_p = 1/\sqrt{8\pi G}$ is the reduced Planck mass, R is the Ricci scalar and $V(\phi)$ is the field potential. According to this scenario when we consider the FRWL universe, the dynamics of the scalar field's dark energy and matter will be described by the following equations

$$\dot{\rho}_\phi + 3H(\rho_\phi + P_\phi) = 0, \quad (9)$$

$$\dot{\rho}_{dm} + 3H(\rho_m + P_m) = 0, \quad (10)$$

where ρ_ϕ and P_ϕ are the energy density and pressure describing the quintessence field ϕ , while ρ_m and P_m are the energy density and pressure of the matter, respectively. We know also that they are related to each other through the Friedmann equations, as follows

$$H^2 = \frac{1}{3}(\rho_\phi + \rho_m), \quad (11)$$

and

$$\dot{H} + H = -\frac{1}{6}(\rho_\phi + \rho_m + 3(P_\phi + P_m)). \quad (12)$$

with $H = \dot{a}/a$ to be the Hubble parameter. On the other hand, for the spatially homogeneous scalar field, the energy density and pressure are of the following form

$$\rho_\phi = \frac{1}{2}\dot{\phi}^2 + V(\phi), \quad (13)$$

and

$$P_\phi = \frac{1}{2}\dot{\phi}^2 - V(\phi), \quad (14)$$

where the dot is the derivative w.r.t. the cosmic time. But it is easy to see that from Eqs. (13) and (14) we have

$$\dot{\phi}^2 = \rho_\phi + P_\phi, \quad (15)$$

while

$$V(\phi) = \frac{\rho_\phi - P_\phi}{2}. \quad (16)$$

After the discussion given above, it is easy to see that we can use Eqs. (11)

and (12), and the model of the matter to constrain Swampland criteria, Eq. (1) and Eq. (2) (or Eq. (3)), respectively, because Eq. (1) and Eq. (2) (or Eq. (3)), can be expressed in terms of the Hubble function and its higher order derivatives which will be reconstructed using GPs from the expansion rate data. In other words, we are in the position to reconstruct *SC2* and estimate its upper bound in a model-independent way using directly observational data. Coming back to the form of *SC2* we need take into account that $dV(\phi)/d\dot{\phi} = (dV/dz)/(d\phi/dz)$, where $d\phi/dz$ should be calculated from Eq. (15), and that $\dot{\phi} = -(1+z)H\phi'$. The results of the study, for the strategies discussed in Sect. II are presented in the next section.

To end this section, we need to define the last element required to perform the analysis and it is the matter model. In particular, we consider two models where the matter part differs from the cold dark matter described by $P_{dm} = \omega_{dm}\rho_{dm}$ equation. As the first model, we consider the case when ω_{dm} is a non-zero constant, while we consider $\omega_{dm} = \omega_0 + \omega_1 z$ to be the second model, respectively. In both models ω_0 and ω_1 are the model parameters to be learned. Moreover, in our analysis, we included neutrinos through radiation

$$\rho_r = 3H_0^2\Omega_r^{(0)}(1+z)^4, \quad (17)$$

where

$$\Omega_r^{(0)} = \Omega_\gamma^{(0)}\left(1 + 0.68(N_{eff}/3)\right) \quad (18)$$

following the very well-known strategy used in modern cosmology, with $\Omega_\gamma^{(0)}$ and N_{eff} free parameters to be constrained too. Here N_{eff} is the neutrino generation number.

4. The reconstruction results. In this section, we present and discuss the key aspects we have inferred from the reconstruction using the GP. The starting point in our analysis is based on the assumptions we have used for ρ_m to define the energy density of the scalar field, ρ_ϕ , Eq. (11). In this paper, we have considered two models only, but the discussion given in the previous section is applicable to any other model describing deviations from the cold dark matter model. Obtained results indicate a need to continue research in this direction involving new data and tools to reveal the true nature of learned phenomena and their impact on various fundamental problems of modern cosmology. We need to stress that for the dark energy-dominated universe the first Swampland criteria, Eq. (1) is always satisfied therefore we will not present the reconstruction of it in the discussion below.

A. Model with $\omega_{dm} = \omega_0$. The first model we consider is the model where the dark matter equation is $P_{dm} = \omega_0\rho_{dm}$ with $\omega_0 \neq 0$ to be learned.

The dynamics of the energy density of this model according to Eq. (10) will

be given by the following equation [17]

$$\rho_{dm} = 3H_0^2 \Omega_{dm}^{(0)} (1+z)^{3(1+\omega_0)}, \quad (19)$$

where H_0 and $\Omega_{dm}^{(0)}$ are the Hubble parameter and the fraction of the dark matter at $z=0$, respectively. Therefore, for ρ_{de} we will have (see Eq. (11))

$$\rho_{de} = 3H^2 - \rho_{dm} - \rho_r = 3H^2 - 3H_0^2 \Omega_{dm}^{(0)} (1+z)^{3(1+\omega_0)} - 3H_0^2 \Omega_r^{(0)} (1+z)^4. \quad (20)$$

Using the above-given equation and some simple algebra, eventually for $\rho'_{de} = d\rho_{de}/dz$ we will get

$$\rho'_{de} = 6HH' - 9H_0^2(1+\omega_0)\Omega_{dm}^{(0)}(1+z)^{3\omega_0+2} - 12H_0^2\Omega_r^{(0)}(1+z)^3. \quad (21)$$

It is not hard to see that after some algebra for P_{de} we will get

$$P_{de} = -3H^2 - 3H_0^2\omega_0\Omega_{dm}^{(0)}(1+z)^{3(1+\omega_0)} - H_0^2\Omega_r^{(0)}(1+z)^4 + 2(1+z)HH'. \quad (22)$$

On the other hand, using Eq. (22) we can calculate dP/dz used to estimate SC2, Eq. (2). The constraints on the parameters for this case we have obtained can be found in Table 2. From where we see that when the H_0 has been estimated using available expansion rate data we got a model of the universe where $\Omega_{dm}^{(0)} \approx 0.262$ according to the mean of the reconstruction when the kernel is given by Eq. (5). We estimated $\Omega_{dm}^{(0)} \approx 0.266$ when the kernels are given by Eq. (6) and Eq. (7), respectively. In all three cases, the deviation from the cold dark matter model has been learned (see the upper panel of Table 2). On the other hand, when $H_0 = 73.52 \pm 1.62$ km/s/Mpc has been merged to the expansion rate data and used in the reconstruction we estimated that $\Omega_{dm}^{(0)} \approx 0.273$ when the kernel is given by Eq. (5). On the other hand, when the kernel has been given by Eq. (6) we estimated $\Omega_{dm}^{(0)}$ to be about 0.278 according to the mean of the reconstruction. Finally, we got $\Omega_{dm}^{(0)} \approx 0.281$ when the kernel is given by Eq. (7) indicating a huge impact of the kernel on the estimations of dark matter fraction $\Omega_{dm}^{(0)}$ in our universe. The results corresponding to this case can be found in the middle panel of Table 2. The bottom panel of Table 2 represents the case when $H_0 = 67.66 \pm 0.42$ km/s/Mpc from the Planck CMB data analysis has been merged together with available expansion rate data given in Table 1 and used in the reconstruction. From the obtained results we infer a very important result indicating that to solve the H_0 tension problem a strong deviation from the cold dark matter model is required. Moreover, this will affect the constraints on $\Omega_\gamma^{(0)}$. However, the constraints on N_{eff} indicate that in all cases the neutrino generation number will be three.

The model-independent reconstruction of the SC2 given by Eq. (2) can be found in Fig.3. In particular, two plots of Fig.3 represent the reconstruction when the squared exponent kernel given by Eq. (5) has been used. In the case of the left-hand side plot, we have the reconstruction when the $H_0 = 73.52 \pm 1.62$ km/s/Mpc from the

TABLE 2

CONSTRAINTS ON THE PARAMETERS FOR THE COSMOLOGICAL
MODEL WHERE THE DEVIATION FROM THE COLD DARK MATTER
IS GIVEN BY Eq. (19) AND $\omega_0 \neq 0$

Kernel	$\Omega_{dm}^{(0)}$	H_0 km/s/Mpc	ω_0	$\Omega_\gamma^{(0)}$	N_{eff}
Squared Exponent	0.262±0.011	71.286±3.743	-0.071±0.011	0.00023±0.00002	2.98±0.08
	0.266±0.012	71.472±3.879	-0.075±0.011	0.00022±0.00002	2.95±0.08
	0.266±0.011	71.119±3.867	-0.076±0.011	0.00021±0.00002	2.97±0.08
Cauchy	0.273±0.011	73.52±1.62	-0.075±0.011	0.00022±0.00005	2.94±0.11
	0.278±0.011	73.52±1.62	-0.083±0.012	0.00019±0.00007	2.92±0.15
	0.281±0.012	73.52±1.62	-0.088±0.013	0.00015±0.00005	2.96±0.11
Matern ($v = 9/2$)	0.293±0.013	67.66±0.42	-0.051±0.017	0.00015±0.00005	3.04±0.12
	0.291±0.013	67.66±0.42	-0.045±0.012	0.00013±0.00002	3.02±0.13
	0.291±0.011	67.66±0.42	-0.049±0.015	0.00015±0.00002	2.95±0.11

The constraints have been obtained for three kernels, Eq. (5), Eq. (6), and Eq. (7), respectively. In particular, the upper part of the table stands for the case when the H_0 value has been predicted from the GP. The middle part of the table stands for the case when the $H_0 = 73.52 \pm 1.62$ km/s/Mpc from the Hubble Space Telescope has been merged with available expansion rate data given in Table I to reconstruct the $H(z)$ and $H'(z)$. Finally, the lower part of the table stands for the case when the $H_0 = 67.4 \pm 0.5$ km/s/Mpc from the Planck CMB data analysis has been merged together with available expansion rate data given in Table I and used in the reconstruction.

Hubble Space Telescope has been merged with the $H(z)$ data depicted in Table 1 and used in the reconstruction process. On the other hand, the right-hand side plot represents the reconstruction of the $|V'|/V$, Eq. (2), when the $H_0 = 67.4 \pm 0.5$ km/s/Mpc from the Planck CMB data analysis has been merged with the $H(z)$ data and used in the reconstruction process. To save our place we did not present the reconstruction results corresponding to the other kernels. Because in all cases we have obtained similar qualitative results indicating that in the dark energy dominated universe the recent form of the Swampland criteria is in huge tension with the expansion rate data and future development in this direction is a must. Moreover, we see that the deviation from the cold dark matter model is unable to reduce the tension. Here we confirm that the non-gravitational interaction is also not able to reduce this tension confirming previously obtained results. However, we see clearly that even a theory not residing in Swampland can end up or not end up in Swampland. Moreover, a theory residing in Swampland can end up or not end up in Swampland. In other words, we have four possibilities indicating that inferring a solution for the H_0 tension problem from the Swampland criteria is also possible but is an extremely hard problem. In other words,

the conclusion about the H_0 tension problem from the Swampland criteria is not unique. The constraints on the N_{eff} inferred from the Swampland criteria indicates that we should expect three generations of neutrinos in our universe even if we have a deviation from the cold dark matter model, Eq. (19). We need to stress again that the model-independent reconstruction means that we did not use any specific form of scalar field potential and dark energy model to constrain its parameters.

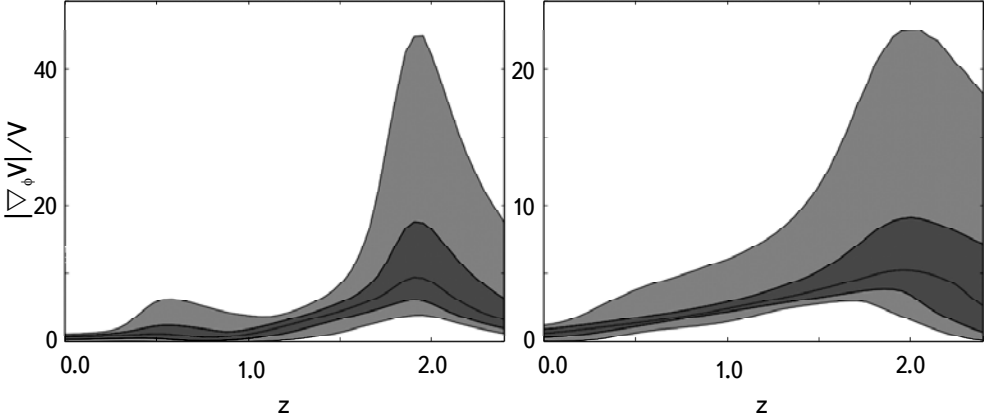


Fig.3. The left-hand side plot represents the reconstruction of the $|V'|/V$, Eq. (2), when the $H_0 = 73.52 \pm 1.62$ km/s/Mpc from the Hubble Space Telescope has been merged with the $H(z)$ data depicted in Table I and used in the reconstruction process. The right-hand side plot represents the reconstruction of the $|V'|/V$, Eq. (2), when the $H_0 = 67.4 \pm 0.5$ km/s/Mpc from the Planck CMB data analysis has been merged with the $H(z)$ data depicted in Table I and used in the reconstruction process. In both cases the squared exponent kernel given by Eq. (5) has been used. The solid line is the mean of the reconstruction and the shaded blue regions are the 68% and 95% C.L. of the reconstruction, respectively. The model is given by Eq. (19) and $\omega_0 \neq 0$.

B. Model with $\omega_m = \omega_0 + \omega_1 z$. The second model we consider here is another simple model that can reveal possible dynamics in the deviations from the cold dark matter model. The linear model we have crafted is given below [19]

$$\omega_m = \omega_0 + \omega_1 z \quad (23)$$

providing the dynamics of dark matter to be

$$\rho_{dm} = 3H_0^2 \Omega_{dm}^{(0)} e^{3\omega_1 z} (1+z)^{3(1+\omega_0-\omega_1)}, \quad (24)$$

because $P_{dm} = (\omega_0 + \omega_1 z)\rho_{dm}$, where ω_0 and ω_1 are the free parameters to be learned. It is easy to see that in this case

$$\frac{d\rho_{dm}}{dz} = 9H_0^2 \Omega_{dm} e^{3\omega_1 z} (1+z)^{3\omega_0-3\omega_1+2} (1+\omega_0 + \omega_1 z), \quad (25)$$

$$\rho_{de} = 3H^2 - \rho_{dm} = 3H^2 - 3H_0^2 \Omega_{dm}^{(0)} e^{3\omega_1 z} (1+z)^{3(1+\omega_0-\omega_1)} - 3H_0^2 \Omega_r^{(0)} (1+z)^4, \quad (26)$$

and

$$\frac{dP_{de}}{dz} = 6HH' - 9H_0^2\Omega_{dm}^{(0)}e^{3\omega_1 z}(1+z)^{3\omega_0-3\omega_1+2}(1+\omega_0+\omega_1 z) - 12H_0^2\Omega_r^{(0)}(1+z)^3, \quad (27)$$

respectively. Therefore, after some algebra for the dark energy, we will have

$$\omega_{de} = -\frac{3H^2 + 3H_0^2\Omega_{dm}^{(0)}e^{3\omega_1 z}(\omega_0 + \omega_1 z)(1+z)^{3(1+\omega_0-\omega_1)} + H_0^2\Omega_r^{(0)}(1+z)^4 - 2(1+z)HH'}{3H^2 - 3H_0^2\Omega_{dm}^{(0)}e^{3\omega_1 z}(1+z)^{3(1+\omega_0-\omega_1)} - 3H_0^2\Omega_r^{(0)}(1+z)^4}, \quad (28)$$

allowing to reconstruct the equation of state dynamics for dark energy since for the pressure P_{de} we have

$$P_{de} = -3H^2 - 3H_0^2\Omega_{dm}^{(0)}e^{3\omega_1 z}(\omega_0 + \omega_1 z)(1+z)^{3(1+\omega_0-\omega_1)} - H_0^2\Omega_r^{(0)}(1+z)^4 + 2(1+z)HH'. \quad (29)$$

The constraints on $\Omega_{dm}^{(0)}$, ω_0 and ω_1 we obtained can be found in Table 3. The upper part of Table 3 represents the constraints when the H_0 has been estimated using only the expansion rate data given in Table 1. The middle part of Table 3 represents the constraints when we merged the $H_0 = 73.52 \pm 1.62$ km/s/Mpc with the available $H(z)$ data. While the constraints we have obtained when the $H_0 = 67.4 \pm 0.5$ km/s/Mpc with the available $H(z)$ data has been merged, can be found in the lower part of Table 3. A closer look at obtained results indicates that the deviation from the cold dark matter solving the H_0 tension problem is not able to reduce the existing tension with the Swampland criteria.

Table 3

CONSTRAINTS ON THE PARAMETERS FOR THE COSMOLOGICAL MODEL WHERE THE DEVIATION FROM THE COLD DARK MATTER IS DESCRIBED BY Eq. (23) AND Eq. (24), RESPECTIVELY

Kernel	$\Omega_{dm}^{(0)}$	ω_0	ω_1	$\Omega_\gamma^{(0)}$	N_{eff}
Squared Exponent	0.267 \pm 0.011	-0.074 \pm 0.011	-0.015 \pm 0.003	0.00021 \pm 0.00002	2.89 \pm 0.09
	0.263 \pm 0.011	-0.074 \pm 0.011	-0.0015 \pm 0.011	0.00021 \pm 0.00002	2.89 \pm 0.09
	0.267 \pm 0.011	-0.074 \pm 0.011	-0.0027 \pm 0.0015	0.00019 \pm 0.00002	2.96 \pm 0.03
Cauchy	0.272 \pm 0.012	-0.065 \pm 0.012	-0.014 \pm 0.011	0.00017 \pm 0.00002	2.99 \pm 0.03
	0.271 \pm 0.011	-0.065 \pm 0.011	-0.009 \pm 0.005	0.00017 \pm 0.00002	2.99 \pm 0.05
	0.271 \pm 0.012	-0.068 \pm 0.012	-0.009 \pm 0.007	0.00021 \pm 0.00002	2.91 \pm 0.08
Matern (v = 9/2)	0.271 \pm 0.013	-0.022 \pm 0.014	-0.009 \pm 0.007	0.00021 \pm 0.00003	2.94 \pm 0.05
	0.273 \pm 0.013	-0.028 \pm 0.017	-0.008 \pm 0.007	0.00019 \pm 0.00002	2.85 \pm 0.04
	0.273 \pm 0.012	-0.027 \pm 0.015	-0.009 \pm 0.007	0.00018 \pm 0.00002	2.91 \pm 0.03

The constraints have been obtained for three kernels, Eq. (5), Eq. (6), and Eq. (7), respectively. In particular, the upper part of the table stands for the case when the H_0 value has been predicted from the GP. The middle part of the table stands for the case when the $H_0 = 73.52 \pm 1.62$ km/s/Mpc from the Hubble Space Telescope has been merged together with available expansion rate data given in Table 1. Finally, the lower part of the table stands for the case when the $H_0 = 67.4 \pm 0.5$ km/s/Mpc from the Planck CMB data analysis has been merged together with available expansion rate data given in Table 1 and used in the reconstruction.

The reconstruction of the Swampland criteria, Eq. (2), when the squared exponent kernel is given by Eq. (5) can be found in Fig.4. It clearly indicates that using only the Swampland criteria, Eq. (2), a unique solution for the H_0 tension problem can not be found. Here we also have four possibilities indicating that, for instance, we can craft effective theories not residing in the Swampland region that can end up or not end up in Swampland at $z=0$. Besides this, we see that similar transitions are possible during the whole evolution of the universe where the deviation from the cold dark matter is given by Eq. (23) and Eq. (24). The constraints on N_{eff} inferred from the Swampland criteria, expansion rate data, and GPs with three different kernels indicate that we should expect three generations of neutrinos in this universe.

On the other hand, we learned that including neutrino strongly affects the constraints on the ω_1 parameter. The last means that the study of the early universe can impose strong constraints on the dynamics in the deviations from the cold dark matter model. It could have a strong impact on various processes and the physics of the early universe requiring additional analysis that has been left to be tackled in the forthcoming papers. One of the initial results already shows that non-linear dynamics in the deviation can strongly affect the N_{eff} indicating the existence of more than three neutrino generations in such models of the universe.

To end the section we need to indicate that the cases we have analyzed allowed also to reproduce the Λ model of dark energy. The reconstruction results indicated

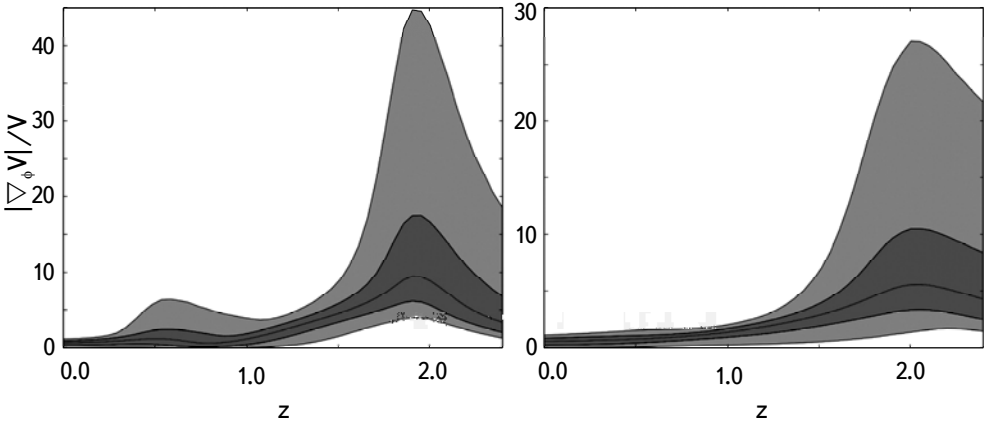


Fig.4. The left-hand side plot represents the reconstruction of the $|V'|/V$, Eq. (2), when the $H_0 = 73.52 \pm 1.62$ km/s/Mpc from the Hubble Space Telescope has been merged with the $H(z)$ data depicted in Table 1 and used in the reconstruction process. The right-hand side plot represents the reconstruction of the $|V'|/V$, Eq. (2), when the $H_0 = 67.4 \pm 0.5$ km/s/Mpc from the Planck CMB data analysis has been merged with the $H(z)$ data depicted in Table 1 and used in the reconstruction process. In both cases the squared exponent kernel given by Eq. (5) has been used. The solid line is the mean of the reconstruction and the shaded blue regions are the 68% and 95% C.L. of the reconstruction, respectively. The model is given by Eq. (23) and Eq. (24).

that phantom and quintessence universes can be obtained too. Moreover, the phantom divide from the above and the bottom can also be realized. We refer readers to [19] where a detailed discussion of the behavior of the dark energy equation of state parameter ω_{de} recently appeared. To save our place we do not reproduce them here again.

5. Discussion. The H_0 tension problem is one of the recent problems of modern cosmology attracting a lot of attention. Various attempts to solve it including solutions based on the interacting and early dark energy models already have been discussed and appeared in the literature. In this problem, it is required to explain why the Planck CMB data analysis and a local measurement from the Hubble Space Telescope give different values for H_0 . We need to understand why in the Λ CDM scenario the Planck CMB data analysis gives $H_0 = 67.4 \pm 0.5$ km/s/Mpc, while local measurements from the Hubble Space Telescope yield $H_0 = 73.52 \pm 1.62$ km/s/Mpc. Nowadays even there is a huge hint that the problem challenges the Λ CDM model itself and it does not have an observational origin. Actually, the Λ CDM model has two components that over the years have been challenged. Indeed, various dark energy models already have been crafted and analyzed giving a good motivation to build modified GR theories, too. The second component is the cold dark matter and the challenge of it mainly started with the introduction of non-gravitational interaction between it and dark energy models. Because on the mathematical level, when non-gravitational interaction is introduced we modify the energy density dynamics of both components. Therefore in this scenario, the background dynamics will be described by some effective dark energy and dark matter models where the effective dark matter is not cold anymore. On the other hand, since observations do not exclude interacting dark energy scenarios, we seriously need to consider the possibility that on the cosmological scales, dark matter is not cold. Indeed, recently Bayesian machine learning a deviation from the cold dark matter has been learned. Moreover, the deviation has been confirmed using GP and expansion rate data. Detailed analysis showed that the stronger deviation from cold dark matter solves the H_0 tension problem. Some initial hints that the deviation has dynamic nature also has been revealed to be analyzed yet. On the other hand, Bayesian machine learning and GP already have been used to study the Swampland criteria in a dark energy-dominated universe. In particular, tension with the recent form of the Swampland criteria had been learned when the GP has been applied. In other words, we arrived at a point where using machine learning tools we have various interesting and promising results, but how they are connected to each other has not been analyzed yet. The goal of this work is to use GP and reveal how they are interconnected and what sort of new knowledge we can infer from them.

Therefore, in this paper, we used GP to study the Swampland criteria for the

scenarios where we have a deviation from the cold dark matter model. Moreover, we constrained the neutrino generation number and found that the tension with the recent form of the Swampland criteria still survives. This is another indication that interacting dark energy models and including neutrinos in analysis can not reduce the Swampland tension. We found also that considered cosmological models where the deviations from the cold dark matter are given by Eq. (19) and Eq. (24), respectively, have three neutrino generations (perfect agreement with the predictions followed from GR). However, when the deviation has non-linear nature then there is a hint that more neutrino generations could exist. More detailed analyses of such scenarios have been left to be reported in the forthcoming papers. We found also that the Swampland criteria alone do not offer a unique solution to the H_0 tension problem which confirms previously obtained results. Another important result capturing our attention is the constraints we have obtained on ω_1 free parameter for the second model given by Eq. (24). In particular, we learned that including neutrino significantly reduced the numerical value of this parameter indicating that the studies of the early universe will help us understand better what is the nature behind the deviations from the cold dark matter model. This is an important question requiring a serious study since with a deviation from cold dark matter our aim is to exclude non-gravitational interactions, however, we still need to understand how to do it correctly.

To end we need to stress that in this paper only some steps are taken to collect the Swampland criteria, neutrino physics, the H_0 tension, and the deviation from the cold dark matter under the same umbrella using machine learning techniques. However, obtained results are very promising giving a hint that some fundamental problems of modern cosmology can be treated from a different point of view. Various questions still should be answered yet and their connections with learned results still should be established. Some of them, we have already mentioned and they have been left to be tackled in the forthcoming papers.

Acknowledgements. M.K. has been supported by a Juan de la Cierva-incorporacion grant (IJC2020-042690-I). This work has been partially supported by MICINN (Spain), project PID2019-104397GB-I00, of the Spanish State Research Agency program AEI/10.13039/501100011033, by the Catalan Government, AGAUR project 2021-SGR-00171, and by the program Unidad de Excelencia MarÍa de Maeztu CEX2020-001058-M.

¹ Consejo Superior de Investigaciones Científicas, ICE/CSIC-IEEC, Campus UAB, Carrer de Can Magrans s/n, 08193 Bellaterra (Barcelona), Spain, e-mail: martiros.khurshudyan@csic.es

² International Laboratory for Theoretical Cosmology, Tomsk State University of Control Systems and Radioelectronics (TUSUR), 634050 Tomsk, Russia

КРИТЕРИИ "БОЛОТА" И ГЕНЕРАЦИЯ НЕЙТРИНО ВО ВСЕЛЕННОЙ С НЕХОЛОДНОЙ ТЕМНОЙ МАТЕРИЕЙ

М.ХУРШУДЯН

В статье рассмотрены критерии "струнного болота" для Вселенной с преобладанием темной энергии, где наблюдается отклонение от модели холодной темной материи. В частности, были рассмотрены две модели. Одна из них является однопараметрической, а вторая предложена для выявления динамики отклонения. Анализ был проведен с использованием гауссовских процессов (GPs) и данных о скорости расширения $H(z)$ (выборка из 30 точек, полученная с помощью метода дифференциального возраста, и выборка из 10 точек, полученная с помощью радиального метода ВАО). Выяснено, что как и в случаях моделей с холодной темной материей, проблема с критериями "болота" по-прежнему сохранится. В анализе, для выявления возможных решений проблемы постоянной Хаббла H_0 , помимо упомянутых 40 точек данных $H(z)$, были использованы последние значения H_0 , полученные космическими телескопами "Планк" и "Хаббл". Наконец, были получены ограничения на число генераций нейтрино, которые привели к интересным результатам. Эти и другие связанные вопросы оставлены для обсуждения в последующих статьях.

Ключевые слова: *критерии "болота": нехолодные модели темной материи; Гауссовые процессы*

REFERENCE

1. *N.Aghanim et al.* (Planck), Astron. Astrophys., **641**, A6, 2020, 1807.06209.
2. *A.G.Riess et al.*, Astrophys. J., **861**, 126, 2018, 1804.10655.
3. *A.G.Riess et al.*, Astron. J., **116**, 1009, 1998.
4. *S.Perlmutter et al.*, Astrophys. J., **517**, 565, 1999.
5. *G.Hinshaw et al.* [WMAP Collaboration], Astrophys. J. Suppl., **208**, 19, 2013.
6. *P.A.R.Ade et al.* [Planck Collaboration], Astron. Astrophys., **571**, A16, 2014.
7. *P.A.R.Ade et al.* [Planck Collaboration], Astron. Astrophys., **594**, A13, 2016.
8. *S.Nojiri et al.*, Phys. Rept., **692**, 1, 2017.
9. *S.Nojiri, S.D.Odintsov*, eConf C, 0602061, 06, 2006, [Int. J. Geom. Meth. Mod. Phys., **4**, 115, 2007].
10. *S.Nojiri, S.D.Odintsov*, Phys. Rept., **505**, 59, 2011.

11. *E.Elizalde et al.*, Eur. Phys. J. C, **70**, 351, 2010.
12. *E.Elizalde et al.*, Class. Quant. Grav., **27**, 095007, 2010.
13. *G.Cognola et al.*, Phys. Rev. D, **77**, 046009, 2008.
14. *S.Weinberg*, Rev. Mod. Phys., **61**, 1, 1989.
15. *H.E.S.Velten et al.*, Eur. Phys. J. C, **74**, 3160, 2014.
16. *N.Sivanandam*, Phys. Rev. D, **87**, 083514, 2013.
17. *E.Elizalde et al.*, arXiv:2104.01077.
18. *E.Elizalde, M.Khurshudyan*, Phys. Rev. D, **99**, 10, 103533, 2019.
19. *M.Khurshudyan, E.Elizalde*, Constraints on prospective deviations from the cold dark matter model using a Gaussian Process, submitted, 2023.
20. *Y.F.Cai et al.*, Astrophys. J., **888**, 62, 2020.
21. *E.Elizalde, M.Khurshudyan*, Eur. Phys. J. C, **82**, 9, 81, 2022.
22. *E.Elizalde et al.*, arxiv:2203.06767.
23. *M.Aljaf et al.*, Eur. Phys. J. C, **82**, 12, 1130, 2022.
24. *K.Yerzhanov et al.*, Mod. Phys. Lett. A, **36**, 31, 2150222, 2021.
25. *M.Aljaf et al.*, Int. J. Mod. Phys. A, **37**, 34, 2250211, 2022.
26. *E.Elizalde, M.Khurshudyan*, Eur. Phys. J. C, **81**, 4, 335, 2021, Eur. Phys. J. C, **81**, 5, 438, 2021, (erratum).
27. *E.Elizalde, M.Khurshudyan*, Phys. Dark Univ., **37**, 101114, 2022.
28. *E.Elizalde et al.*, Phys. Rev. D, **102**, 12, 123501, 2020.
29. *E.Elizalde et al.*, Int. J. Mod. Phys. D, **28**, 1950019, 2019.
30. *M.Khurshudyan, R.Myrzakulov*, Eur. Phys. J. C, **77**, 65, 2017.
31. *C.Li et al.*, Phys. Lett. B, **80**, 135141, 2020.
32. *M.Khurshudyan*, Symmetry, **8**, 110, 2016.
33. *S.D.Odintsov et al.*, Phys. Rev. D, **96**, 044022, 2017.
34. *K.Bamba et al.*, Astrophys. Space Sci., **342**, 155, 2012.
35. *E.Elizalde, M.Khurshudyan*, Int. J. Mod. Phys. D, **27**, 1850037, 2018.
36. *M.Aljaf et al.*, Eur. Phys. J. C, **80**, 112, 2020.
37. *E.Sadri et al.*, Eur. Phys. J. C, **80**, 393, 2020.
38. *S.Kachru et al.*, Phys. Rev. D, **68**, 046005, 2003.
39. *M.Rummel, A.Westphal*, JHEP, **01**, 020, 2012.
40. *J.Blbck, U.Danielsson, G.Dibitetto*, JCAP, **1403**, 003, 2014.
41. *M.P.Hertzberg, S.Kachru, W.Taylor et al.*, JHEP, **12**, 095, 2007.
42. *C.Caviezel, T.Wrase, M.Zagermann*, JHEP, **04**, 011, 2010.
43. *B. de Carlos, A.Guarino, J.M.Moreno*, JHEP, **01**, 012, 2010.
44. *S.R.Green, E.J.Martinec, C.Quigley et al.*, Class. Quant. Grav., **29**, 075006, 2012.
45. *D.Junghans*, JHEP, **06**, 132, 2016.
46. *D.Andriot, J.Blbck*, JHEP, **03**, 102, 2017.
47. *J.Moritz, A.Retolaza, A.Westphal*, Phys. Rev. D, **97**, 046010, 2018.
48. *U.H.Danielsson, T. Van Riet*, arxiv:1804.01120.
49. *H.Ooguri, C.Vafa*, Nucl. Phys. B, **766**, 21, 2007.
50. *G.Obied et al.*, arXiv:1806.08362
51. *H.Ooguri, E.Palti, G.Shiu et al.*, Phys. Lett. B, **788**, 180, 2019.

52. *L.Heisenberg et al.*, Phys. Rev. D, **98**, 123502, 2018.
53. *P.Agrawal, G.Obied, P.J.Steinhardt et al.*, Phys. Lett. B, **784**, 271, 2018.
54. *D.Wang*, arXiv:1809.04854.
55. *S.Brahma*, Md. Wali Hossain, JHEP, **03**, 006, 2019.
56. *K.Dimopoulos*, Phys. Rev. D, **98**, 123516, 2018.
57. *S.Das*, Phys. Rev. D, **99**, 063514, 2019.
58. *W.H.Kinney et al.*, Class. Quant. Grav., **36**, 117001, 2019.
59. *S.D.Odintsov, V.K.Oikonomou*, EPL, **126**, 20002, 2019.
60. *L.Heisenberg et al.*, Sci. China Phys. Mech. Astron., **62**, 990421, 2019.
61. *Y.Akrami et al.*, Fortschr. Phys., 1800075, 2018.
62. *C.Zhang et al.*, Research in Astron. Astrophys., **14**, 1221, 2014.
63. *M.Moresco et al.*, JCAP, **05**, 014, 2016.
64. *R.Jimenez et al.*, Astrophys. J., **593**, 622, 2003.
65. *D.Stern et al.*, JCAP, **02**, 008, 2010.
66. *M.Moresco et al.*, JCAP, **08**, 006, 2012.
67. *J.Simon et al.*, Phys. Rev. D, **71**, 123001, 2005.
68. *M.Moresco*, Mon. Not. Roy. Astron. Soc. Lett., **450**, L16, 2015.
69. *E.Gaztanaga et al.*, Mon. Not. Roy. Astron. Soc., **399**, 1663, 2009.
70. *C.Blake et al.*, Mon. Not. Roy. Astron. Soc., **425**, 405, 2012.
71. *X.Xu et al.*, Mon. Not. Roy. Astron. Soc., **431**, 2834, 2013.
72. *T.Delubac et al.*, Astron. Astrophys., **552**, A96, 2013.
73. *T.Delubac et al.*, Astron. Astrophys., **574**, A59, 2015.
74. *L.Samushia et al.*, Mon. Not. Roy. Astron. Soc., **429**, 1514, 2013.
75. *A.Font-Ribera et al.*, JCAP, **05**, 027, 2014.
76. *M.Seikel et al.*, JCAP, **06**, 036, 2012.

CONTENTS

Surface photometry of 50 dwarf galaxies in the local volume <i>K.A.Kryzhanovsky, M.E.Sharina, I.D.Karachentsev, G.M.Karataeva</i>	317
On a possible mechanism for the start or resumption of activity of radio galaxies in clusters of galaxies <i>R.R.Andreasyan, H.V.Abrahamyan, G.M.Paronyan, G.A.Mikayelyan, A.M.Mickaelian</i>	331
The revisited BPT diagram from the self-consistent analysis <i>P.Privatus, C.Pappalardo, P.V.K.Rao, D.T.Mazengo</i>	339
Ephemeris updates for seven selected HATNet survey transiting exoplanets <i>A.Poro, F.A.Farahani, E.Jahangiri, A.Sarostad, M.Gozarandi, M.Haghgou, F.Abolhassani, A.Fakhrabadi, Y.Jongen, A.Wunsche, R.Naves, P.Guerra, A.Marchini, M.Salisbury, R.Ehrenberger, V-P.Hentunen</i>	353
Activity of the young star EPIC 204376071 from the Upper Sco association <i>I.S.Savanov</i>	373
Plane symmetric string cosmological model with zero mass scalar field in f(R) gravity <i>K.Pawar, A.K.Dabre, P.Makode</i>	385
Modified Tsallis holographic dark energy <i>J.Bharali, K.Das</i>	399
Renyi holographic dark energy and its behaviour in f(G) gravity <i>M.K.Alam, S.S.Singh, L.A.Devi</i>	415
Motion of a particle in the field of an infinite flat slab <i>R.M.Avagyan, A.A.Saharian, S.S.Jibilyan</i>	441
Swampland criteria and neutrino generation in a non-cold dark matter universe <i>M.Khurshudyan</i>	453

СОДЕРЖАНИЕ (продолжение)

ПЛОСКО-СИММЕТРИЧНАЯ СТРУННАЯ КОСМОЛОГИЧЕСКАЯ МОДЕЛЬ СО СКАЛЯРНЫМ ПОЛЕМ НУЛЕВОЙ МАССЫ В $f(R)$ ГРАВИТАЦИИ

К.Павар, А.К.Дабре, П.Макоде 385

МОДИФИЦИРОВАННАЯ ГОЛОГРАФИЧЕСКАЯ ТЕМНАЯ ЭНЕРГИЯ ЦАЛЛИСА

Дж.Бхарали, К.Дас 399

ГОЛОГРАФИЧЕСКАЯ ТЕМНАЯ ЭНЕРГИЯ РЕНЬИ И ЕЕ ПОВЕДЕНИЕ В $f(G)$ ГРАВИТАЦИИ

М.Х.Алам, С.С.Синх, Л.А.Деви 415

ДВИЖЕНИЕ ЧАСТИЦЫ В ПОЛЕ БЕСКОНЕЧНОГО ПЛОСКОГО СЛОЯ

Р.М.Авакян, А.А.Саарян, С.С.Джисибилиан 441

КРИТЕРИИ "БОЛОТА" И ГЕНЕРАЦИЯ НЕЙТРИНО ВО ВСЕЛЕННОЙ С НЕХОЛОДНОЙ ТЕМНОЙ МАТЕРИЕЙ

М.Хуршудян 453